Nanoscale Effects and Applications of Self-Organized Nanostructured Thin Films

Dissertation
zur Erlangung des Grades
'Doktor der Naturwissenschaft'

am Fachbereich Chemie, Pharmazie und Geowissenschaften
der Johannes Gutenberg-Universität Mainz

vorgelegt von
King Hang Aaron Lau
geboren in Hong Kong SAR PRC

Mainz, 2008

Tag der mündlichen Prüfung: 8, Jul. 2008

Die vorliegende Arbeit wurde unter Betreuung von Herrn Prof. Dr. W. Knoll im Zeitraum zwischen August 2005 bis Juli 2008 am Max-Planck-Institut für Polymerforschung, Mainz, angefergt.

Abstract

A nanostructured thin film is a thin material layer, usually supported by a (solid) substrate, which possesses subdomains with characteristic nanoscale dimensions (10 ~ 100 nm) that are differentiated by their material properties. Such films have captured vast research interest because the dimensions and the morphology of the nanostructure introduce new possibilities to manipulating chemical and physical properties not found in bulk materials. Block copolymer (BCP) self-assembly, and anodization to form nanoporous anodic aluminium oxide (AAO), are two different methods for generating nanostructures by self-organization. Using poly(styrene-block-methyl methacrylate) (PS-b-PMMA) nanopatterned thin films, it is demonstrated that these polymer nanopatterns can be used to study the influence of nanoscale features on protein-surface interactions. Moreover, a method for the directed assembly of adsorbed protein nanoarrays, based on the nanoscale juxtaposition of the BCP surface domains, is also demonstrated. Studies on protein-nanopattern interactions may inform the design of biomaterials, biosensors, and relevant cell-surface experiments that make use of nanoscale structures. In addition, PS-b-PMMA and AAO thin films are also demonstrated for use as optical waveguides at visible wavelengths. Due to the sub-wavelength nature of the nanostructures, scattering losses are minimized, and the optical response is amenable to analysis with effective medium theory (EMT). Optical waveguide measurements and EMT analysis of the films' optical anisotropy enabled the *in situ* characterization of the PS-b-PMMA nanostructure, and a variety of surface processes within the nanoporous AAO involving (bio)macromolecules at high sensitivity.

Zusammenfassung

Charakteristisch für einen nanostrukturierten, dünnen Film ist seine Zusammensetzung aus Subdomänen mit typischen lateralen Dimensionen im Bereich von 10- bis 100 nm, die sich durch unterschiedliche Materialeigenschaften auszeichnen.
Die Existenz solcher nanoskopischer Domänen führt zu einer hohen Anzahl an Grenzflächen, deren Eigenschaften das Verhalten des gesamten strukturierten Films bestimmen kann. Auch die Domänengröße an sich führt zu nanoskopischen Effekten bei der Wechselwirkung mit Objekten gleicher Größenordnung (z.B. Biomakromoleküle) bzw. physikalischen Phänomenen wie eingestrahltem Licht, dessen Wellenlänge im Vergleich zu der Größe der Domänen groß ist.
Die Strukturierung von Materialien auf der Nanoskala ermöglicht somit neue Möglichkeiten der gezielten Manipulation chemischer und physikalischer Eigenschaften, die zu neuartigen Anwendungen unter Ausnutzung nanoskaliger Effekte führen können.
Zwei Methoden zur einfachen Erzeugung von Nanostrukturierungen in dünnen Filmen auf festen Substraten sind die Selbstorganisation von Blockcopolymeren (BCP) und die anodische Oxidation von Aluminiumfilmen, die zur Ausbildung von nanoporösem anodischem Aluminiumoxid (AAO) führt.
In der vorliegenden Arbeit wird die Möglichkeit zur exakten Regulierung von Domängröße und Grenzflächendichte über die gesamte Nanoskala durch Selbstorganisation von Poly-(Styrol-block-Methylmethacrylat) Filmen gezeigt. Der Einfluss dieser nanoskaligen Effekte wird am Beispiel von Protein-Oberflächen Interaktionen untersucht. Es wird gezeigt, dass die Anzahl absorbierter Proteine durch Variieren der Gesamtlänge der Grenzflächen von Polystyrol- und Polymethylmethacrylat-Domänen an der Oberfläche reguliert werden kann. Desweiteren wird untersucht, wie durch ebenmäßige Strukturierung des Blockcopolymerfilms Adsorption von Proteinen zu geordneten Strukturen auf der Nanoskala erreicht werden kann.
Protein-Oberflächen Wechselwirkungen in nanostrukturierten Filmen sind wertvolle Grundlagenuntersuchungen für spätere Anwendungen in Biomaterialien, Biosensoren und bei Zell-Oberflächenexperimenten in nanoskalierter Umgebung.
Auch die Anwendung von PS-b-PMMA und AAO Filmen als optische Wellenleiter im sichtbaren Wellenlängenbereich wird in der vorliegenden Arbeit untersucht. Dazu wurden PS-b-PMMA Filme mit vertikalen, zylinderförmigen Domänen präpariert, deren Morphologie der nanoporösen Struktur von anodisch oxidiertem Aluminiumoxid gleicht. Aus dieser geordneten Morphologie resultiert eine optische Anisotropie. Durch die nanoskope Strukturierung, deren Domängröße weit unterhalb der Wellenlänge sichtbaren Lichts liegt, werden Streuverluste minimiert und die optische Antwort kann mithilfe der Effektiven Medium Theorie (EMT) analysiert werden.
Optische Wellenleiter Messungen und EMT Analyse der optischen Anisotropie des Films ermöglichen die in situ Charakterisierung der PS-b-PMMA Nanostruktur und die Untersuchung von Oberflächenprozessen in nanoporösen AAO mit hoher Genauigkeit und versprechen so vielfältige Anwendungsgebiete.

Contents

1. Introduction

As the physical size of engineered structures are reduced to the nanoscale (10 ~100 nm) material properties become size dependent and heavily influenced by the density of surfaces and interfaces relative to the bulk volumes of the nanostructures [1-3]. Moreover, consideration of the nanostructure's size relative to the length scale of other physical phenomena, such as the wavelength of incidence light [4], becomes important in evaluating material properties. In other words, the nanostructure of a material introduces additional possibilities to manipulating the chemical and physical properties, and may lead to new applications [1-4]. Advances in nanoscience has been fostered by the development of "top-down" lithographic tools for generating nanostructures [2, 5]. On the other hand, the high costs and resolution limits associated with these top-down methods [5] have spurred research aimed at developing bottom up technologies which employ the concept of self-organization to create nanostructures [2, 6-9].

Block copolymer self-assembly and the preparation of nanoporous alumina membranes by anodization are two convenient techniques for preparing periodic nanostructures by self-organization. Both technologies have been extensively investigated as nanoscale lithography masks [10-15], and for the nanoscale templating of a broad variety of materials [9, 11, 12, 16-18]. Ordered nanoporous anodic aluminium oxide (AAO) is produced by an electric field assisted process of simultaneous oxidation and dissolution of bulk Al, and has a fixed morphology consisting of straight cylindrical pores embedded in an alumina matrix [19-21]. The pore openings originate from the sample surface, and are hexagonally arrayed parallel to each other. The pores can be prepared with diameters 10 ~ 400 nm, and the thickness of the AAO layer is controlled by the duration of the anodization process. A block copolymer (BCP) is composed of chemically distinct polymer chains (blocks) covalently joined together. For nanotechnology applications, long, immiscible blocks are usually paired together such that the minimization of interfacial energies can induce microphase separation and the self-assembly of distinct chemical domains [11, 22-25]. Many morphologies can be achieved with BCP self organization, and their sophistication increases with the number of polymer blocks present. In the simplest case of a diblock copolymer, cylindrical, spherical, lamella, gyroid, and other morphologies can be prepared by varying the block volume ratio. The domain

periodicity, typically in the range of 10 ~ 100 nm, is principally defined by the molecular weight of the copolymer. Thin films of BCP can also be prepared on solid substrate supports, and the self-assembled morphologies, modified by substrate interfacial interactions, are manifested as different surface nanopatterns [11, 26, 27]. Hierarchical structures that incorporate BCP into AAO membranes as a 3D matrix on which BCP morphologies are self-assembled have also been demonstrated [28].

In this study, the emphasis is placed on exploring the properties that emerge from the nanoscale nature of BCP and AAO thin films, rather than to employ the self-organised nanostructures as physical templates for generating other nano-objects. As mentioned earlier, a high density of surface interfaces are introduced with nanostructures. In the case of BCP self-assembly, the domain sizes generated span the nanoscale [11, 22-25] down to the length-scale of individual proteins [29, 30], the biomacromolecules responsible for many cellular self-organised processes [31]. Therefore nanopatterned BCP surfaces may be a valuable, and conveniently accessible, platform for exploring the length-scale dependent properties of protein/cell-surface interactions. In a first series of studies, the high density of surface interfaces is exploited for inducing distinct protein adsorption behavior diblock copolymer surfaces of polystyrene-block-poly(methyl methacrylate) (PS-b-PMMA) nanopatterns. We demonstrate that the amount of protein adsorbed can be modulated by the length density of PS-b-PMMA surface interfaces. In addition, the high density of surface interfaces is exploited, together with the difference in protein adsorption affinities between PS and PMMA, for the directed assembly of adsorbed protein nanoarrays. Applications of the protein nanoarrays for biosensing, and for the nanoarraying of other biomolecules, are also demonstrated.

Light at visible or longer wavelengths cannot directly resolve the nanostructures of either BCP or nanoporous AAO films. However, the sub-wavelength nature of the nanostructures enables the description of the films' optical responses by effective medium theory (EMT) [4, 32, 33]. In fact, both the morphology and the volume fractions of the nanophases are reflected in the (anisotropic) refractive indices of the nanostructured films. The sub-wavelength nature of the nanostructured films also enables their use as optical waveguides [34], as intensity losses due to scattering are small. Therefore, in a second series of studies, the optical characterization of nanostructured BCP and AAO thin films by optical waveguide spectroscopy is investigated. The application of a BCP thin film as an optical waveguide, and the characterization of the nanostructure by its waveguide response, are unprecedented [35, 36]. The corresponding demonstration for a nanoporous AAO thin film has previously been reported by the present author [34], and other groups have since applied this approach to other nanoporous systems [37-41]. Here, the concept is extended to investigate, in the context of the AAO cylindrical nano-pore geometry: 1) the process of layer-by-layer dendrimer

polyelectrolyte deposition, 2) the development of anisotropic, surface grafted, polypeptide nanostructures, and 3) fluorescence detection.

In this report, following this introductory chapter, an account of the materials and methods used are given in Chapter 2. Introductions to BCP and AAO thin film formation, as well as the processing methods used and the subsequent nanostructure characterization, are then described in Chapter 3. In Chapter 4, investigations of protein adsorption on the nanopatterned BCP surfaces are presented, while in Chapter 5, waveguide studies of the BCP nanostructure and on the characterization of the aforementioned macromolecular nanostructures in the AAO film, are described. To facilitate understanding of the waveguide results, the principles of effective medium theory and optical waveguide spectroscopy are also discussed in Chapter 5. Lastly, conclusions drawn from the present studies, which have exploited some of the nanoscale effects associated with the BCP and AAO nanostructures for the investigation of nanoscale surface processes, are given in Chapter 6.

1.1. References

[1] Klabunde KJ ed: *Nanoscale Materials in Chemistry*, Wiley-Interscience: New York, 2001.

[2] Balzani V, Credi A, Venturi M: *Molecular Devices and Machines: A Journey into the Nanoworld*, Wiley-VCH: Weinheim, 2003.

[3] Lazzari M, Liu G, Lecommandoux S eds: *Block Copolymers in Nanoscience*, Wiley-VCH: Weinheim, 2006.

[4] Choy TC: *Effective Medium Theory: Principles and Applications* Oxford University Press: New York, 1999.

[5] ITRS: *The International Technology Roadmap for Semiconductors*, http://www.itrs.net/Links/2007ITRS/Home2007.htm, 2007 Edition.

[6] Stephan Förster MA: Amphiphilic Block Copolymers in Structure-Controlled Nanomaterial Hybrids. *Advanced Materials* **1998**, *10*, 195.

[7] Li AP, Muller F, Birner A, Nielsch K, Gosele U: Hexagonal Pore Arrays with a 50-420 Nm Interpore Distance Formed by Self-Organization in Anodic Alumina. *Journal of Applied Physics* **1998**, *84*, 6023.

[8] Park C, Yoon J, Thomas EL: Enabling Nanotechnology with Self Assembled Block Copolymer Patterns. *Polymer* **2003**, *44*, 6725.

[9] Lazzari M, López-Quintela MA: Block Copolymers as a Tool for Nanomaterial Fabrication. *Advanced Materials* **2003**, *15*, 1583.

[10] Park M, Harrison C, Chaikin PM, Register RA, Adamson DH: Block Copolymer Lithography: Periodic Arrays of ~10^11 Holes in 1 Square Centimeter. *Science* **1997**, *276*, 1401.

[11] Fasolka MJ, Mayes AM: Block Copolymer Thin Films: Physics and Applications. *Annual Review of Materials Research* **2001**, *31*, 323.

[12] Hamley IW: Nanostructure Fabrication Using Block Copolymers. *Nanotechnology* **2003**, R39.

[13] Crouse D, Lo Y-H, Miller AE, Crouse M: Self-Ordered Pore Structure of Anodized Aluminum on Silicon and Pattern Transfer. *Applied Physics Letters* **2000**, *76*, 49.

[14] Shingubara S, Okino O, Murakami Y, Sakaue H, Takahagi T: Fabrication of Nanohole Array on Si Using Self-Organized Porous Alumina Mask. *Journal of Vacuum Science & Technology B: Microelectronics and Nanometer Structures* **2001**, *19*, 1901.

[15] Lei Y, Cai W, Wilde G: Highly Ordered Nanostructures with Tunable Size, Shape and Properties: A New Way to Surface Nano-Patterning Using Ultra-Thin Alumina Masks. *Progress in Materials Science* **2007**, *52*, 465.

[16] Thurn-Albrecht T, Schotter J, Kastle GA, Emley N, Shibauchi T, Krusin-Elbaum L, Guarini K, Black CT, Tuominen MT, Russell TP: Ultrahigh-Density Nanowire Arrays Grown in Self-Assembled Diblock Copolymer Templates. *Science* **2000**, *290*, 2126.

[17] Segalman RA: Patterning with Block Copolymer Thin Films. *Materials Science and Engineering R-Reports* **2005**, *48*, 191.

[18] Li X, Lau KHA, Kim DH, Knoll W: High-Density Arrays of Titania Nanoparticles Using Monolayer Micellar Films of Diblock

Copolymers as Templates. *Langmuir* **2005**, *21*, 5212.

[19] Diggle JW, Downie TC, Goulding CW: Anodic Oxide Films on Aluminum. *Chemical Reviews* **1969**, *69*, 365.

[20] O'Sullivan JP, Wood GC: The Morphology and Mechanism of Formation of Porous Anodic Films on Aluminium. *Proceedings of the Royal Society of London. Series A, Mathematical and Physical Sciences (1934-1990)* **1970**, *317*, 511.

[21] Li F, Zhang L, Metzger RM: On the Growth of Highly Ordered Pores in Anodized Aluminum Oxide. *Chemistry of Materials* **1998**, *10*, 2470.

[22] Bates FS, Fredrickson GH: Block Copolymer Thermodynamics: Theory and Experiment. *Annual Review of Physical Chemistry* **1990**, *41*, 525.

[23] Fredrickson GH, Bates FS: Dynamics of Block Copolymers: Theory and Experiment. *Annual Review of Materials Science* **1996**, *26*, 501.

[24] Green PF, Limary R: Block Copolymer Thin Films: Pattern Formation and Phase Behavior. *Advances in Colloid and Interface Science* **2001**, *94*, 53.

[25] Matsen MW: The Standard Gaussian Model for Block Copolymer Melts. *Journal of Physics: Condensed Matter* **2002**, R21.

[26] Huinink HP, Brokken-Zijp JCM, van Dijk MA, Sevink GJA: Asymmetric Block Copolymers Confined in a Thin Film. *Journal of Chemical Physics* **2000**, *112*, 2452.

[27] Suh KY, Kim YS, Lee HH: Parallel and Vertical Morphologies in Block Copolymers of Cylindrical Domain. *Journal of Chemical Physics* **1998**, *108*, 1253.

[28] Xiang H, Shin K, Kim T, Moon SI, McCarthy TJ, Russell TP: Block Copolymers under Cylindrical Confinement. *Macromolecules* **2004**, *37*, 5660.

[29] Simon PFW, Ulrich R, Spiess HW, Wiesner U: Block Copolymer-Ceramic Hybrid Materials from Organically Modified Ceramic Precursors. *Chemistry of Materials* **2001**, *13*, 3464.

[30] Napoli A, Sebök D, Senti A, Meier W: *Potential Applications of Polymer Vesicles*. In *Block Copolymers in Nanoscience*, Massimo Lazzari; Guojun Liu; Sébastien Lecommandoux, eds.; Wiley-VCH: Weinheim, 2006, pp. 64.

[31] Lesk A: *Antibody Structure*. In *Introduction to Protein Science: Architecture, Function, and Genomics*; Oxford University Press: New York, 2004, pp. 270.

[32] Aspnes DE, Heller A, Porter JD: Microstructurally Engineered, Optically Transmissive, Electrically Conductive Metal Films. *Journal of Applied Physics* **1986**, *60*, 3028.

[33] Maldovan M, Bockstaller MR, Thomas EL, Carter WC: Validation of the Effective-Medium Approximation for the Dielectric Permittivity of Oriented Nanoparticle-Filled Materials: Effective Permittivity for Dielectric Nanoparticles in Multilayer Photonic Composites. *Applied Physics B: Lasers and Optics* **2003**, *76*, 877.

[34] Lau KHA, Tan LS, Tamada K, Sander MS, Knoll W: Highly Sensitive Detection of Processes Occurring inside Nanoporous Anodic Alumina Templates: A Waveguide Optical Study. *Journal of Physical Chemistry B* **2004**, *108*, 10812.

[35] Kim DH, Lau KHA, Robertson JWF, Lee OJ, Jeong U, Lee JI, Hawker CJ, Russell TP, Kim JK, Knoll W: Thin Films of Block Copolymers as Planar Optical Waveguides. *Advanced Materials* **2005**, *17*, 2442.

[36] Kim DH, Lau KHA, Joo W, Peng J, Jeong U, Hawker CJ, Kim JK, Russell TP, Knoll W: An Optical Waveguide Study on the Nanopore Formation in Block Copolymer/Homopolymer Thin Films by Selective Solvent Swelling. *Journal of Physical Chemistry B* **2006**, *110*, 15381.

[37] Cameron PJ, Jenkins ATA, Knoll W, Marken F, Milsom EV, Williams TL: Optical Waveguide Spectroscopy Study of the Binding of Cytochrome C in Mesoporous Titanium Dioxide Film Electrodes. *Chemistry of Materials* **2008**, *accepted for publication*.

[38] Durr M, Menges B, Knoll W, Yasuda A, Nelles G: Direct Measurement of Increased Light Intensity in Optical Waveguides Coupled to a Surface Plasmon Spectroscopy Setup. *Applied Physics Letters* **2007**, *91*, 021113.

[39] Awazu K, Rockstuhl C, Fujimaki M, Fukuda N, Tominaga J, Komatsubara T, Ikeda T, Ohki Y: High Sensitivity Sensors Made of Perforated Waveguides. *Optics Express* **2007**, *15*, 2592.

[40] Fujimakia M, Rockstuhla C, Wanga X, Awazua K, Tominagaa J, Ikedab T, Ohkib Y, Komatsubarac T: Nanoscale Pore Fabrication for High Sensitivity Waveguide-Mode Biosensors. *Microelectronic Engineering* **2007**, *84*, 1685.

[41] Reimhult E, Kumar K, Knoll W: Fabrication of Nanoporous Silicon Nitride and Silicon Oxide Films of Controlled Size and Porosity for Combined Electrochemical and Waveguide Measurements. *Nanotechnology* **2007**, 275303.

2. Material and methods

2.1. Materials

2.1.1. Copolymer materials

PS-b-PMMA with PS/PMMA number average molecular weights (M_n, in kg mol^{-1}) of 26.4/68, 106/99, and 868/857, and polydispersities of 1.18, 1.09, and 1.3, respectively, and atatic PMMA homopolymer with M_n = 13.8 kg/mol and polydispersity = 1.71, were purchased from Polymer Source Inc., Dorval, Canada, and used as received. The following copolymers were synthesised by collaborators at the University of Massachusetts at Amherst, USA:[*] PS-b-PMMA with PS/PMMA M_n ratio of 21.5/20.6 and 35.7/35.9, and polydispersities of 1.07 and 1.09, were synthesised by living anionic polymerization; PS-b-PMMA with PS/PMMA M_n ratio of 40.8/19.8 and polydispersity = 1.19 was prepared by atom transfer radical polymerization; crosslinkable, random copolymer of styrene, methyl methacrylate, and reactive benzocyclobutene (BCB) (P(S-r-BCB-r-MMA)), with M_n = 25 kg mol^{-1}, and polydispersity = 1.18, was synthesised by living free-radical polymerization [1]. The proportion of S:BCB:MMA in P(S-r-BCB-r-MMA) was controlled to a ratio of 56:2:42; hydroxy end-functionalised random copolymer of styrene and methyl methacrylate (P(S-*r*-MMA)) having a styrene fraction of 0.58, was synthesised in bulk also via living free radical polymerization [2]. The molecular weight was determined to be M_w = 9,600 with M_w/M_n = 1.80 by size exclusion chromatography.

2.1.2. Polyelectrolyte materials

N,N-disubstituted hydrazine phosphorus-containing dendrimers having 96 terminal functional groups (Figure 5.14) with either cationic (G4(NH+Et2Cl^-)96) or anionic (G4(CHCOO^- Na+)96) character were synthesised by collaborators at the Laboratoire de Chimie de Coordination CNRS, Toulouse [3-5]. Biotin functionalised poly(allylamine hydrochloride) (PAH-biotin) with 21% biotin functionalization was prepared by a collaborator[†] at the Max Planck Institute for Polymer Research, Mainz.

[*] From the group of Prof. T.P. Russell, in the Polymer Science and Engineering Department, by Dr. J.T. Goldbach, now at Arkema Inc., USA, and by Prof. Dr. Joona Bang, now at Korea University, Seoul, Republic of Korea.
[†] By Basit Yameen at the Max-Planck-Institute for Polymer Research, Mainz.

6-biotinyl-N-hydroxysuccinimide (NHS-biotin) and PAH (M_w~15,000) were purchased from Sigma-Aldrich, and the PAH amine side groups were reacted with NHS-biotin by active ester chemistry. The content of biotin was determined by ^{1}H-NMR. Powders of poly(sodium 4-styrenesulfonate) with an average M_w ~70,000 were purchased from Sigma-Aldrich, as was poly(allylamine hydrochloride) with an average M_w ~56,000.

2.1.3. Biomolecules

The following proteins were purchased from Sigma-Aldrich: whole goat anti-rabbit IgG (affinity purified); biotinylated whole goat anti-rabbit IgG (affinity purified); bovine serum albumin (essentially fatty acid and globulin free (≥99%)); and streptavidin (essentially salt-free, affinity purified). The following proteins were purchased from Pierce Biotechnology, Rockford, USA: avidin (affinity purified), whole mouse anti-goat IgG (affinity purified) and whole rabbit anti-mouse IgG (affinity purified). Streptavidin Alexa Fluor 647 conjugate and fibronectin isolated from bovine plasma were purchased from Invitrogen, Paisley, UK. Protein concentrations were verified by UV absorbance assay, measured using a BioPhotometer, Eppendorf, Germany. A peptide nucleic acid (PNA) probe was synthesised by collaborators at the MPI-P [6], and DNA targets were purchased from MWG-Biotech AG, Ebersberg, Germany. The PNA probe was biotinylated at the 5' end and had the following sequence: 5'-(TTT)5-TGTACATCACAACTA-3'. DNA targets M0 and M1 were Cy5 labeled at the 5' end, and had the sequences 5'-TAGTTGTGATGTACA-3' and 5'-TAGTTGTGACGTACA-3', respectively. All proteins were dissolved in phosphate buffered saline (PBS), and PNA and DNA were dissolved in PBS added with 0.01% Tween-20.

2.1.4. Other materials

Polished silicon (100) substrates (525 mm thick) were purchased from Si-Mat, Landsberg, Germany. Polished LaSFN9 high refractive index glass substrates were purchased from Hellma Optik GmbH, Jena, Germany. All solvents and PBS (10 mM phosphate buffer, 2.7 mM KCl and 137 mM NaCl, pH 7.4 (25 °C)) were purchased from Sigma-Aldrich Chemie Gmbh, Munich, Germany. 3-aminopropyl-dimethylethoxysilane (APDMES) and 3-aminopropyl-triethoxysilane (APTES), 3-mercaptopropyl trimethoxysilane (MPTES), tetramethyl orthosilicate (TMOS), and tetraethyl orthosilicate (TEOS) were also purchased from Sigma-Aldrich. The surfactant polyoxyethylenesorbitan monolaurate (Tween-20) was also purchased from Sigma-Aldrich. The N-carboxy anhydride (NCA) monomer of poly(γ-benzyl-L-glutamate) (PBLG) was synthesised by phosgenation of L-glutamic acid (Merck Biosciences) by collaborators at the MPI-P [7].

2.2. Atomic force microscopy (AFM)

In Chapter 3, AFM was used to characterise the BCP surface nanopatterns and the adsorbed protein nanopatterns in this study. Tapping mode AFM in air was used in most cases while contact mode AFM was also used in selected experiments to verify the tapping mode results.

In normal tapping mode AFM operation, a cantilever with a nanometer sharp tip constructed at one end is oscillated at its fundamental mechanical resonance frequency, and held with the tip pointed down towards the sample. The oscillation is driven by a vibrating piezoelectric crystal attached to the other end of the cantilever. The oscillating cantilever is brought close to the sample surface such that the tip repeatedly "taps" the surface, and the oscillation is damped. The oscillation amplitude is on the order of nanometers and is measured by a laser reflected off the mirror surface of back of the cantilever. The beam path of the reflected laser oscillates in synchrony with the cantilever, and the oscillation is detected by the projected spatial variation of the reflected intensity over a quadrant of photodiodes. Comparison of the input piezoelectric crystal oscillation and the measured laser/cantilever oscillation reveals the oscillation damping due to contact with the surface. Contact is defined by the electrostatic repulsion between the electron clouds belonging to the atoms on the cantilever tip and the sample surface. Feedback circuitry adjusts the vertical position of the cantilever to control the degree of tip-surface contact, in an attempt to restore the measured oscillation to the undamped amplitude. At the same time, the tip is laterally translated with respect to the surface to scan a defined area on the sample. The feedback circuitry continuously adjusts the cantilever vertical distance as the tip was brought into contact with different parts of the surface. Simultaneous recording of this vertical distance and the sample position maps the topography of the scanned area.

Although the cantilever oscillation amplitude can be maintained, there exists a phase lag between the driving and measured oscillations due to tip interactions with the surface. This phase contrast can be recorded simultaneously with the topography data, and is a measure of the energy dissipated during contact of tapping AFM tip with the surface [8-10]. Different materials have different mechanical responses, thus the phase data indicates the spatial arrangement of material compositions across a sample surface.

In contact mode AFM operation, the cantilever tip is brought towards the sample surface until contact with the surface pushes against the tip, and causes a desired amount of cantilever deflection that is also detected by the laser-photodiode setup. The total force acting against the cantilever is commonly adjusted to within a range of pico- to nanonewtons. As the tip is scanned across the sample surface, the sample topography is measured by the feedback circuitry as it adjusts the vertical position of the cantilever to maintain a constant cantilever deflection. Since the tip is in continuous contact with the surface as it scans the surface, it experiences a lateral

force caused by mechanical friction between the tip and surface. This lateral force causes a torsional twist about the long axis of the cantilever and induces a lateral deflection of the reflected laser beam. This signal can be simultaneously recorded with the height image. Since the frictional force sensitively depends on surface properties, the lateral deflection signal (lateral force AFM) can be used to identify the spatial distribution of surface chemical heterogeneity [8, 11].

AFM was performed with a Nanoscope IIIa Multimode (Digital Instruments/Veeco Metrology, USA) using a 15x15 μm scanner. For tapping mode AFM, two types of tetrahedral silicon micro cantilevers (Olympus, Japan) were used: 42 N/m, 300 kHz tips were used for general PS-b-PMMA phase contrast characterization; 1.8 N/m, 70 kHz tips were used for all surfaces decorated with biomolecules. For liquid-AFM, 0.38 N/m rectangular silicon nitride cantilevers (Olympus, Japan) were employed in the tapping mode at a damped resonance frequency of ~7 kHz in PBS. In all cases, the cantilever was oscillated vertically about its fundamental resonance frequency by a vibrating piezoelectric crystal attached to the cantilever. The same 0.38 N/m cantilevers were also used for contact mode and lateral force AFM.

2.3. Surface plasmon resonance spectroscopy (SPR) and Surface plasmon field-enhanced fluorescence spectroscopy (SPFS)

In Chapter 3, SPR was used to monitor, in situ, protein adsorption and antibody-antigen binging on nanopatterned BCP surfaces. Also in Chapter 3, SPFS was used to monitor, in situ, DNA-PNA hybridization on the nanoarrayed PS-b-PMMA/IgG-biotin-streptavidin-biotin-PNA sensing architecture.

In the context of SPR optical sensing, surface plasmons (SP's) are the collective and resonant excitations of unbound electrons on a metal surface, in response to an incidence optical field with propagation momentum matching the SP surface mode. SP's represent "electromagnetic surface waves that have their intensity maxima in the surface and exponentially decaying fields perpendicular to it" [12]. The propagation properties of the SP mode are sensitively dependent on the dielectric constants (ε) and thickness (h) of the metal and surrounding layers. Adsorption of molecules on the (suitably functionalised) metal surface changes the optical density of the system, and is detected as changes in the SP excitation conditions [12-14]. Moreover, the exponentially decaying nature of the SP away from the surface confers on the technique a high specificity to detecting surface processes, and filters out possible measurement artefacts in the bulk. Furthermore, fluorescent dyes can also be excited by this surface bound SP evanescent field. Because of the resonance character of the SP (i.e. field-enhancement), fluorescent-labelled molecules can be detected with an enhanced sensitivity (SP field-enhanced spectroscopy—SPFS). Over the past

two decades, SPR has become a popular and commercially available technique to monitor with high sensitivity the adsorption or deposition of (ultra)thin (molecular) layers on suitably functionalised metal (e.g. Au) surfaces [14].

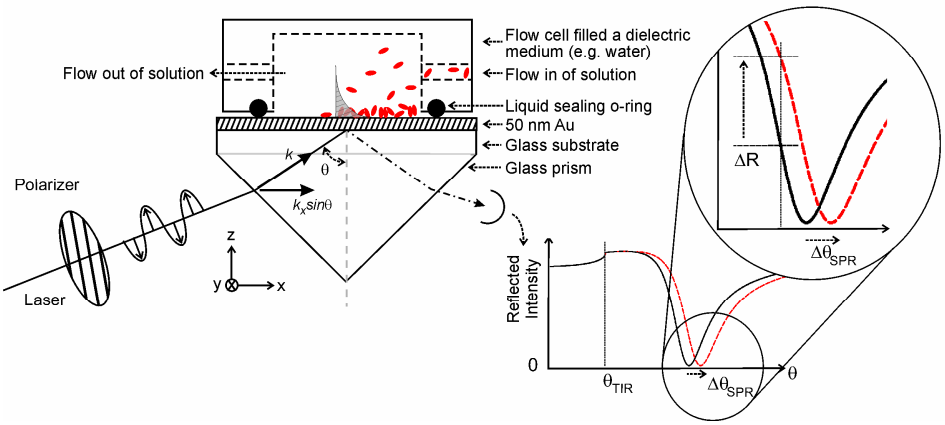

Figure 2.1. Schematic of a SPR sensor setup in the Kretschmann configuration. Light with electric field polarised perpendicular to the substrate surface is directed through the prism/substrate assembly and reflected off the back of the 50 nm thick Au film. At an incidence angle $\theta > \theta_{TIR}$, the SP is excited (decaying field shown on top of the Au surface) if the momentum of the incidence light in the x-direction (k_x) exactly matches the excitation conditions of the surface plasmon (SP) mode. At this resonance angle (θ_{SPR}) the energy of the incidence light is transferred to the SP and no light is reflected, resulting in a minimum in the R vs. θ measurement. Furthermore, a flow cell can be clamped on top of the Au film to allow solutions of adsorbing molecules to be introduced onto the Au surface. Adsorption of molecules on the Au then causes a change in the SP excitation condition, and a corresponding shift in θ_{SPR}.

The Kretschmann configuration, shown in Figure 2.1, is a commonly used SPR setup [12-14]. SP's are excited on a thin metal film vacuum deposited on a glass substrate via prism coupling. A laser is directed onto the substrate side of the metal film through the prism and substrate. (A λ = 632.8 nm He-Ne laser was used throughout this study.) At most incidence angles, the laser is reflected, either by simple reflection at the metal/prism interface, or by total internal reflection (TIR) at the same interface at angles $\theta > \theta_{TIR}$ (with reference to the refractive index combination between the prism and the medium on the other side of the metal film, e.g. air or aqueous buffer). However, a SP propagating on the metal surface can be excited at an angle θ_{SPR} within the range $\theta > \theta_{TIR}$ if there is a match in momentum (i.e. coupling) between the SP mode and the incidence light (referring to the component in the surface direction ($k_x \sin\theta$, Figure 2.1). At the same time, the symmetric prism arrangement leads to the immediate back-coupling of SP out into the prism. Destructive interference between the incidence and back-coupled waves leads to a minimum in the reflected intensity around the excitation angle (θ_{SPR}). A schematic of

the R vs. θ measurement showing the SP minimum is also shown in Figure 2.1. Surface plasmons are excited only for an incidence electric field with a component polarised normal to the surface, which can induce an electric displacement across the metal/medium interface. A Au layer (50 nm), or a Ag layer (40 nm), is commonly used. These metals have the lowest levels of optical damping and broadening of the reflected intensity minimum). The experimental precision in determining θ_{SPR} is therefore the highest for these surfaces [12, 13].

θ_{SPR} sensitively depends on the thickness of the Au layer and the dielectric constants of the system. (The dielectric constant, ε, is related to the refractive index, n, by $\varepsilon = n^2$.) If a thin layer of molecules is deposited on the Au surface, the optical density above the Au changes and induces a shift in θ_{SPR}. If the thin film induces an overall increase in optical density above the Au surface, then the surface plasmon is excited at a higher momentum and θ_{SPR} shifts to a higher angle. If a liquid flow cell is clamped on top of the Au surface, adsorption/surface processes occurring in a liquid medium can also be monitored in situ as the pure solvent is exchanged with one loaded with the adsorbing molecule (Figure 2.1). The θ_{SPR} shift can be tracked directly by repeated measurement of the R vs. θ response in order to determine the reflectivity minimum associated with θ_{SPR} (i.e. angle tracking), or by monitoring the increase in the reflected intensity at a fixed angle immediately to the left of θ_{SPR}, along the quasi-linear part of the R vs. θ response (i.e. reflectivity tracking, Figure 2.1). The change in θ_{SPR} is then directly proportional the measured change in R, with the proportionality constant given by the slope of the quasi-linear part of the R vs. θ response. The technique is sufficiently sensitive for the detection of molecular sub-monolayers. However, both the film thickness and dielectric constant affect the overall optical density, and the two parameters cannot be determined independently. Usually, the film's dielectric constant is determined by other techniques, such as by optical waveguide spectroscopy (see section 5.2) or by refractometry [15],and SPR is used to measure the film thickness.

The quantitative evaluation of θ_{SPR} shifts with respect to changes in the molecular layer's adsorbed thickness ($h_{molecule}$) and its dielectric constant ($\varepsilon_{molecule}$) is achieved by analysis with Fresnel equation calculations [12, 13]. These equations are the exact solutions to Maxwell's equations for the geometry of the prism-multilayer system and they express explicitly the reflected intensity at the Au-glass interface as a function of the thickness and dielectric constants of the entire system (i.e. the individual glass/Au/molecule/medium layers). Fresnel calculations have been implemented by the program WINSPALL, developed at the MPI-P [16]. In evaluating experimental data, the R vs. θ measurement is compared with the response calculated from the Fresnel equations based on trial values of h and ε. The best fit between the data and the calculation constitutes the measurement of the adsorbed molecular layer. Furthermore, for the measurement of biomolecule adsorption, the mass of material adsorbed can be calculated from the film thickness by the equation [15]:

Equation 2.1. $$mass = h_{molecule} \frac{n_{molecule} - n_{medium}}{dn/dc}$$

where h_{molecule} is the thickness of the adsorbed molecular layer, n_{molecule} and n_{medium} are the refractive indices of the "dry" molecule and the solvent medium, respectively, and dn/dc is the refractive index increment of the molecules in solution (c is the concentration). A value of $dn/dc = 0.182$ cm^3/g has been found to apply for a range of proteins and biomolecules [15].

Although SPR detection is highly sensitive, the magnitude of θ_{SPR} shift depends critically on the refractive index contrast between surface bound molecules and the medium above the sample (e.g. air, or aqueous buffer). Therefore, for the detection of surface processes that induce only small overall refractive index changes in the system, molecule labelling with fluorophores and subsequent fluorescence detection schemes that take advantage of the SP field enhancement, i.e. SP field-enhanced fluorescence spectroscopy (SPFS), may be considered [17].

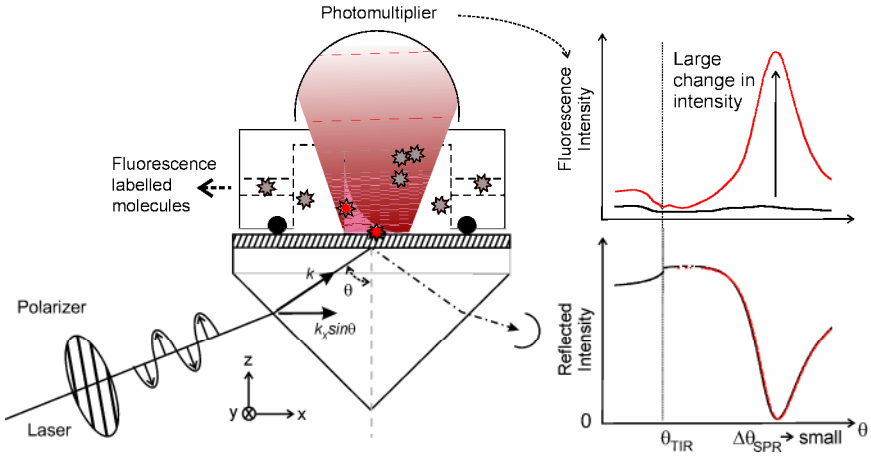

Figure 2.2. Schematic of the SPR setup configured for SPFS. At θ_{SPR}, the evanescent SP field can induce fluorescence emission of fluorophores bound onto the sample surface (or in solution immediately adjacent of the surface), if the wavelength of the incidence laser (hence the SP) overlap with the adsorption band of the fluorophores. The fluorescence intensity can be measured by a photomultiplier mounted directly on top of the sample, even if the induced refractive index change is too small to be measured in the angle shift of θ_{SPR}.

Assuming there is an overlap between the wavelength of the SP mode (i.e. of the incidence laser) and the adsorption band of the fluorophores, the evanescent SP field can excite fluorophores residing within its exponentially decaying tail above the metal surface, such as when the labelled molecules are bound on the sample surface. The radiated fluorescence emission at angle θ_{SPR} can then be measured by a photomultiplier placed directly on top of the sample surface (Figure 2.2). Since the intensity of fluorescence emission is directly proportional to number of excited

fluorophores, as long as the fluorophore density is not so high as to induce self-quenching, which is not encountered in high sensitivity sensing (i.e. small numbers of analyte), surface binding events can also be monitored in situ by following the change in the fluorescence intensity measured. Incidentally, during in situ real-time monitoring of a binding event, an attempt at measuring $\Delta\theta_{SPR}$, however small, is made by the aforementioned reflectivity tracking (Figure 2.1, right inset). The fluorescence intensity is then simultaneously recorded, but at an angle slightly lower than θ_{SPR} suitable for reflectivity tracking, and an off-peak fluorescence intensity is monitored. Also in SPFS, the fluorescence background due to unbound fluorophores away from the surface is minimised because the SP does not radiate into the bulk. However, care must be taken in designing the sensing molecular architecture so that the labelled analytes are placed some distance away from the metal surface (> 15~20 nm) [18]. Otherwise drastic quenching interactions with the metal surface will lead to the loss of the fluorescence signal [17, 18].

2.4. Scanning electron microscopy (SEM)

SEM characterization of the BCP and AAO films were performed on a LEO 1530 Gemini field emission scanning electron microscope. In SEM, a high-energy beam of electrons scans the sample surface in a raster pattern and produces scattered electrons, the intensity of which depends on the surface topography and composition. An acceleration voltage of 0.5 kV to 3 kV was typically used, and the intensity of the secondary electrons was typically used for imaging. SEM operation was performed by Dipl. Ing. Gunnar Glasser at the MPI-P.

2.5. References

[1] Ryu DY, Shin K, Drockenmuller E, Hawker CJ, Russell TP: A Generalized Approach to the Modification of Solid Surfaces. Science 2005, 308, 236.

[2] Mansky P, Liu Y, Huang E, Russell TP, Hawker C: Controlling Polymer-Surface Interactions with Random Copolymer Brushes. Science 1997, 275, 1458.

[3] Sebastián R-M, Magro G, Caminade A-M, Majoral J-P: Dendrimers with N,N-Disubstituted Hydrazines as End Groups, Useful Precursors for the Synthesis of Water-Soluble Dendrimers Capped with Carbohydrate, Carboxylic or Boronic Acid Derivatives. Tetrahedron 2000, 56, 6269.

[4] Loup C, Zanta M-A, Caminade A-M, Majoral J-P, Meunier B: Preparation of Water-Soluble Cationic Phosphorus-Containing Dendrimers as DNA Transfecting Agents. Chemistry - A European Journal 1999, 5, 3644.

[5] Launay N, Caminade A-M, Lahana R, Majoral J-P: A General Synthetic Strategy for Neutral Phosphorus-Containing Dendrimers. Angewandte Chemie International Edition 1994, 33, 1589.

[6] Park H. In Department of Chemistry and Pharmacy; Johannes Gutenberg-Universität Mainz 2005; Vol. PhD, pp. 54.

[7] Duran H, Lau KHA, Lübbert A, Jonas U, Steinhart M, Knoll W: Biopolymers for Biosensors: Polypeptide Nanotubes for Optical Biosensing. In Polymers for Biomedical Applications, Anil Mahapatro, ed.; Oxford University Press: New York, 2008; Vol. 977, pp. 371.

[8] Magonov SN, Reneker DH: Characterization of Polymer Surfaces with Atomic Force Microscopy. Annual Review of Materials Science 1997, 27, 175.

[9] McLean RS, Sauer BB: Tapping-Mode Afm Studies Using Phase Detection for Resolution of Nanophases in Segmented Polyurethanes and Other Block Copolymers. Macromolecules 1997, 30, 8314.

[10] Wang H, Djurišić AB, Chan WK, Xie MH: Factors Affecting Phase and Height Contrast of Diblock Copolymer Ps–B-Peo Thin Films in Dynamic Force Mode Atomic Force Microscopy Applied Surface Science 2005, 252, 1092.
[11] Sadaie M, Nishikawa N, Kumashiro Y, Ikezawa Y, Kumagai Y, Makino K, Ohnishi S, Tamada K, Hara M: Quantitative Friction Map on Surface Composed of B-Cyclodextrin Monolayer. Japanese Journal of Applied Physics 2007, 46, 7838.
[12] Raether H: Surface-Plasmons on Smooth and Rough Surfaces and on Gratings, Springer: Berlin / Heidelberg, 1988.
[13] Knoll W: Interfaces and Thin Films as Seen by Bound Electromagnetic Waves. Annual Review of Physical Chemistry 1998, 49, 569.
[14] Homola J: Surface Plasmon Resonance-Based Sensors, Springer: Berlin / Heidelberg, 2006.
[15] Voros J: The Density and Refractive Index of Adsorbing Protein Layers. Biophysical Journal 2004, 87, 553.
[16] Worm J; Max Planck Institute for Polymer Research: Mainz, 2001, pp. Implementation of Fresnel calculations for a layer system with anistropic dielectric and layer thickness values; and the graphical comparison with measured reflectivity data.
[17] Liebermann T, Knoll W: Surface-Plasmon Field-Enhanced Fluorescence Spectroscopy. Colloids and Surfaces A: Physicochemical and Engineering Aspects 2000, 171, 115.
[18] Kasry A: Ph.D. thesis. In Biology Department; Johannes Gutenberg-Universität Mainz 2006; pg. 16.

3. Nanostructure formation of block copolymer (BCP) and anodic aluminium oxide (AAO) thin films

3.1. PS-b-PMMA block copolymer thin films

3.1.1. Introduction to block copolymer thin film self-assembly

A block copolymer (BCP) is composed of two or more chemically distinct polymer chains (blocks) covalently bonded together. If these blocks are immiscible, microphase separation can drive their self-assembly into periodic morphologies, which consist of distinct domains with sizes and chemistries directly related to the corresponding copolymer blocks [1-6]. The corresponding domain centre-to-centre periodicity, $\lambda_{C\text{-}C}$, is in the range of 10 ~ 100 nm, which is a length scale directly relevant to applications in nanotechnology.

The BCP composition strongly determines the self-assembled morphology in thermodynamic equilibrium, the formation of which may be understood by considerations of the interfacial energies between the blocks and the conformation energy of the polymer chains ("stretching" energy) associated with their morphological arrangement [1-5]. The main parameters determining the self-assembly, then, are the segmental interaction parameter χ, the BCP degree of polymerization N, and the volumetric composition of each copolymer block, *f*. In particular, the product χN characterises the degree of immiscibility of unlike blocks and, therefore, the driving force for microphase separation.

There is a wide variety of self-assembled BCP morphologies and their range in complexity depends on the number of copolymer blocks present in the system [1-6]. The simplest example is the pure AB diblock copolymer. For the case of symmetric AB composition ($f_A = 1 - f_B = 0.5$), as χN increases beyond a value of ~10.5 [1, 2, 4, 5], the transition from a disordered polymer melt state ("weak segregation" limit) to the formation of alternating lamellae composed generally of the A and B blocks begins. As χN increases further, the block segregation becomes stronger and the AB interfaces become sharper, until for very large χN [2], the interfaces are well-defined and significant stretching of the chains occur [2, 4, 5]. At this final strong segregation limit, the scaling $\lambda_{C\text{-}C} \propto N^{2/3}$ becomes applicable, while in the transition between the weak and strong segregation limits, larger exponents for N have been predicted [2]. Although the scaling relation suggest that $\lambda_{C\text{-}C}$ may be adjusted simply by changing N,

and that the degree of segregation is enhanced at higher block molecular weights, the kinetics of the self-assembly decreases as the BCP molecular weight increases [7-9]. Although the chain dynamics may be improved by increasing the temperature, the strength of the unfavourable block interactions is diminished as the order-disorder transition temperature is approached [4, 10]. Improving the frictional properties between the blocks [2] (e.g. via the tacticity) may also improve the dynamics, but its control may have a limited range and may involve major changes in the polymerization route [11]. Thus the chain dynamics for high molecular weights may be too slow for the equilibrium morphology to be reached [2, 7], and $\lambda_{C\text{-}C}$ larger than ~100 nm is in general difficult to achieve.

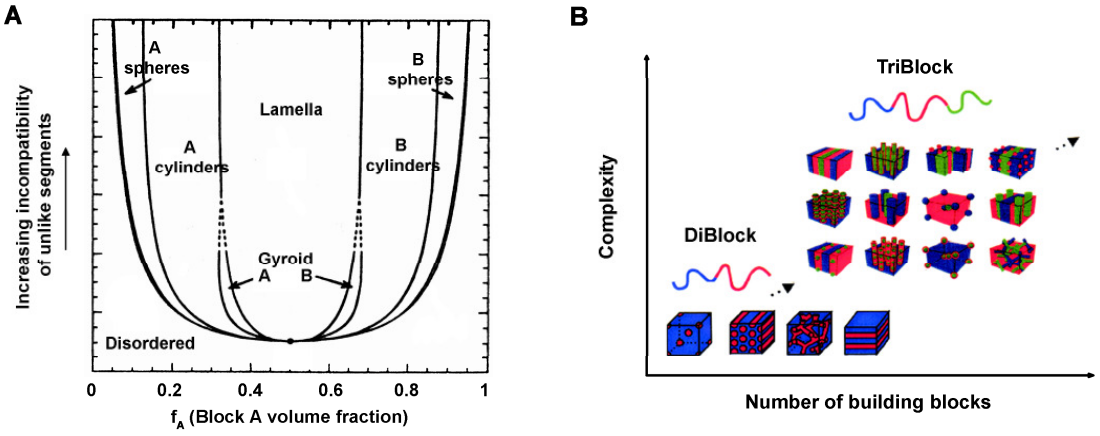

Figure 3.1. Basic morphologies resulting from BCP self-assembly. (A) shows schematically the phase diagram of a pure AB diblock BCP as functions of the block volume fraction and the degree of incompatibility of the unlike segments. Only the major phases—lamella, gyroid, close packed cylindrers and spheres—are shown. (Adapted from Ref. [5].) (B) shows schematically the increase in complexity in the morphological phase space as the number of copolymer blocks is increased from two to three (and beyond). Only the major equilibrium morphologies are shown (e.g. only the four morphologies from (A) for the diblock BCP are drawn). (Adapted from Ref. [12].)

Other than lamellae phases, morphologies with other symmetries may be accessed in BCP's by varying the block volume fraction. The most prominent morphologies formed are the gyroid, the hexagonally packed cylinders, and the sphere phases, as the asymmetry of the AB composition is increased (Figure 3.1a). Other phases, such as modulated lamellae, perforated lamellae, and close packed spheres, may also exist over sharply limited ranges in composition [1, 2, 5]. As mentioned above, as the number of copolymer blocks increase, the system becomes correspondingly more complex; some additional morphologies for ABC tri-block copolymers are shown in Figure 3.1b [12].

In the case of BCP thin films prepared on solid supports, surface interaction energies and the interplay between $\lambda_{C\text{-}C}$ and the film thickness (h) both heavily

influence the equilibrium morphology [3, 14, 15]. For example, the BCP block with preferential interaction with the substrate material would self-segregate to the substrate surface while, depending on the match between the h and $\lambda_{C\text{-}C}$, one or both blocks may be exposed on the top surface of the BCP film to minimise the free energy of the system. Some common film morphologies for the symmetric diblock BCP [3, 13] are shown in Figure 3.2. In general, a morphology with lamellae parallel to the substrate surface would form due to preferential wetting of the substrate with one of the blocks (Figure 3.2a and b). In particular, terraces may be observed if the amount of BCP material deposited on the substrate is insufficient to form a film with a thickness that is commensurate with $\lambda_{C\text{-}C}$ (Figure 3.2a). On the other hand, if neither polymer block has a preferential interaction with the substrate, lamellae perpendicular to the surface is the predicted equilibrium morphology for a certain values of h and range of surface interactions (Figure 3.2c). Hybrid structures(Figure 3.2b) may also be thermodynamically stable for film thickness < $\lambda_{C\text{-}C}$. However, an ultrathin surface skin layer of one polymer block masking the underlying nanostructure may also form depending on the specific combination of interfacial interactions [3, 16].

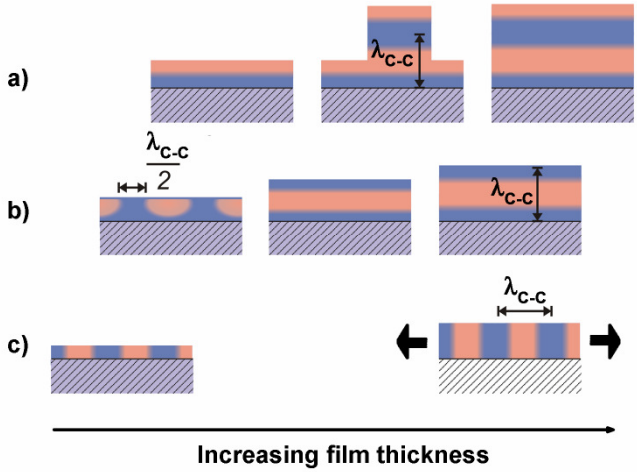

Figure 3.2. Schematics of some basic thin film morphologies resulting from symmetric diblock BCP self-assembly on wetting substrates as a function of film thickness (h). $\lambda_{C\text{-}C}$ is the domain centre-to-centre periodicity. The substrate is indicated as the hatched rectangular areas. The concentrations of the blocks (pink and blue) are indicated by the colour shading. Lamella morphologies in (a) and (b) dominate due to preferential substrate wetting of the blue block with the blue-hatched substrate. Preferential interactions at the top-surface with the pink and blue blocks are shown in (a) and (b), respectively. Note that at intermediate h incommensurate with $\lambda_{C\text{-}C}$, terraces may form, as illustrated in (a). In (b), as h decreases, the chain stretching and mixed phases may be observed to satisfy both block segregation and h. Although not shown explicitly, corresponding terraces, chain stretching, and mixed morphologies may occur for both cases (a) and (b). Morphologies perpendicular to the substrate surface are shown in (c). The black/white substrate hatching indicates a balanced interfacial interaction with both blocks. Perpendicular morphologies may exist for very thin films dominated by packing frustration, or for thicker films in the case of top-surface and substrate interfacial energy neutral conditions. The thick arrows in the latter case indicate some latitude in permitted h for the morphology to exist. (Adapted from Refs. [3, 13].)

In chapter 4, protein adsorption on nanopatterned surfaces is investigated, and BCP surfaces with chemically distinct nanodomains are desired. Thus BCP films with morphologies perpendicular to the substrate surface without any skin layer are needed. As indicated in Figure 3.2, the perpendicular morphology with a flat top surface may be achieved by thickness confinement for limited combinations of preferential surface interactions and film thickness [3, 13-15, 17-19]. However, the required precision in thickness control at the nanometer level is not easy to achieve reproducibly over large areas [3, 13, 19]. The perpendicular morphology may also be produced by applying an external driving force to overcome the substrate/top surface interfacial interactions for the alignment of the domains. For example, solvent annealing [20, 21] or the application of an electric field at a high potential (10^6 – 10^8 V/m) [22-24] have been demonstrated. In an alternate strategy, the interface interactions at the substrate interface may be effectively removed by balancing them for the different copolymer blocks in the form of interfacial energy "neutral" surfaces. Such substrates may be obtained by surface functionalization with finely tuned mixed self-assembled monolayers [25-27], or appropriate surface chemical treatments [8, 28]. In addition, a random copolymer layer composed of the same monomers as the pattern-forming BCP with a suitably adjusted composition may be immobilised on the substrate to provide a neutral energy surface [29, 30]. The interactions at the "free" top surface of the BCP film may be modified by placing the sample in an atmosphere spiked with appropriate solvents, or by simply choosing a BCP with equal block affinities with air.

In chapter 5, thick BCP films of $h >> \lambda_{C\text{-}C}$, with a structural anisotropy between the directions parallel and normal to the substrate surface (the perpendicular morphologies) are desired for optical waveguide studies. Using the surface energy neutral substrates described above, the thickness confinement constraint is in theory relaxed for the formation of perpendicular morphologies. Nonetheless, demonstrations of the extension of the perpendicular morphology for $h > \lambda_{C\text{-}C}$ without a strong external alignment force has been sparse [3, 11]. Nonetheless, blending of an asymmetric BCP with a homopolymer identical to the minor copolymer block has been exploited to promote self-assembly of the perpendicular cylindrical morphology with $h \sim 10\ \lambda_{C\text{-}C}$ or higher [11, 31, 32]. Homopolymer blends with BCP's have been more commonly applied to modify the domain sizes and $\lambda_{C\text{-}C}$ of a BCP morphology [4, 21, 33, 34]. Up to moderate homopolymer additions, microphase separation leading to the self-assembly of the original BCP morphology is preserved [33, 35]. The molecular weight of the homopolymer relative to the copolymer block with more similar segmental interactions (the "like-block") has been shown to control the homopolymer distribution within the BCP morphology [4, 21, 33, 35]. In particular, in the "dry brush" state where the homopolymer molecular weight is approximately equal or slightly higher than the like-block, segregation of the homopolymer to the centre of the cylindrical domains comprised of the like-blocks is observed [21, 33, 34, 36]. This morphology is favoured because the energy penalty due to chain stretching

required to accommodate the homopolymer amongst the like-blocks, is higher than the loss in translational entropy due to demixing of the homopolymer [4, 21, 35]. For the purpose of extending the perpendicular cylinder film morphology for $h9 > \lambda_{C\text{-}C}$, segregation of the homopolymer to the centre of the minor domains has been shown to be essential. In addition to the energetics of the BCP chain conformation, the mechanism of extended perpendicular phase formation has been argued in terms of the relaxation of the homopolymer chain along the cylindrical domain axis [11]. This promotes the formation of contiguous cylinders, with the perpendicular orientation templated by balanced interfacial interactions at the air/film and (modified) substrate surfaces.

In this study, polystyrene-block-poly(methyl methancrylate) (PS-b-PMMA) diblock copolymers have been chosen for the preparation of the BCP thin film nanostructures. Both lamellae and cylindrical morphologies perpendicular to the substrate surface have been prepared. The PS-b-PMMA system was chosen because the surface energy difference between PS and PMMA in air is small (values of $\gamma_{PMMA}/\gamma_{PS} = 1.004$ [29] to $\gamma_{PMMA}/\gamma_{PS} = 1.01$ [37] have been reported), which essentially balances the interfacial energies at the top "free" surface of the BCP films, and minimises the likelihood of skin layer formation [38]. A balanced substrate interfacial energy was achieved with the aid of poly(styrene-random-methyl methacrylate) (P(S-r-MMA)) copolymer neutral surface energy thin film layers ($\gamma_{PS/PS\text{-}r\text{-}PMMA} \sim \gamma_{PS/PS\text{-}r\text{-}PMMA} \sim 0.41 \pm 0.01$ mN/m) [29, 30]. The copolymer surface modification approach was chosen because the identical copolymer substrate modification layer could be prepared on both glass and Si substrates, to be used for optical and routine AFM measuresurements, respectively. This was especially convenient with the use of a crosslinkable version of the P(S-r-MMA) [30], although an equivalent brush variant of the copolymer that can be anchored on SiO_2 surfaces [29] was also used. The glass transition temperature for both PS and PMMA are ~100°C, with variations depending on the tacticity and molecular weight [39, 40]. To impart sufficient chain mobility for PS-b-PMMA self-assembly into their equilibrium morphologies, PS-b-PMMA were thermally annealed at temperatures from 165°C to 200°C for 2 days, depending on the molecular weight. Annealing was usually carried out in vacuum at 10^{-2} mbar to avoid possible thermal degradation to PS-b-PMMA. For the study of protein adsorption on surface nanopatterns, symmetric PS-b-PMMA was used to prepare the perpendicular lamellae morphology, and asymmetric PS-b-PMMA with a 3:7 PS:PMMA block volume ratio was used to prepare the cylindrical morphology with the PS cylinder axes oriented normal to the substrate surface. These morphologies resulted in, respectively, striped nanopatterns with approximately equal PS and PMMA surface fractions, and hexagonally arranged PS nanodomains set in a PMMA matrix. PS-b-PMMA with a range of M_n and $\lambda_{C\text{-}C}$ were used to prepared PS/PMMA surface nanopatterns with a range of surface domain centre-to-centre periodicity, $\lambda_{C\text{-}C}$, spanning an order of magnitude from 29 nm to ~300 nm. The film thickness was

controlled to $h \sim \lambda_{C\text{-}C}$ to guarantee the formation of perpendicular morphologies. Thicker films with perpendicular cylindrical morphologies of $h > 10\ \lambda_{C\text{-}C}$ were also prepared for optical waveguide experiments. These were prepared by self-assembly of a PS-b-PMMA with 7:3 PS:PMMA volume ratio, blended with a PMMA homopolymer of average molecular weight 1.3 times that of the copolymer PMMA block. The aforementioned neutral surface energy modified substrates were also used. The homopolymer addition approach was chosen because of the experimental convenience of self-assembly without the use of an external alignment fields.

3.1.2. PS-b-PMMA thin film preparation

PS-b-PMMA with film thickness (h) corresponding to the intrinsic BCP microphase separation periodicity ($\lambda_{C\text{-}C}$) were prepared on a ~10 nm thick, crosslinked P(S-r-BCB-r-MMA) surface modification layer with balanced PS/PMMA interfacial interactions. To prepare the P(S-r-BCB-r-MMA) ultrathin surface layer, the P(S-r-BCB-r-MMA) random copolymer was spin coated on either gold-coated LaSFN9 glass substrates or silicon (3000 rpm using 0.3 wt% polymer solution in benzene) and was annealed in vacuum (220°C, overnight) to activate crosslinking. Subsequently, the crosslinked layer was rinsed with toluene. Film thickness was measured by a surface profiler (model P-10, KLA Tencor, USA). PS-b-PMMA films were then prepared on top of the coated substrates by spin-coating polymer solutions in toluene. The concentration (1 to 2.5 wt%) and spin speed (1800 to 4500 rpm) were used to control the film thickness. (25 nm, 25 nm, 51 nm, and 64 nm, for copolymers of total M_n = 42.1 kg mol-1, 94.4 kg mol-1, 205 kg mol-1, and 1725 kg mol-1, respectively.) Figure 3.3 summarises the spin coating conditions to achieve different film thicknesses. The samples were then annealed in vacuum (180 °C for 2 days for copolymers of total Mn = 42.1 kg/mol and 94.4 kg/mol, and at 200 °C for 2 days for copolymers of total M_n = 205 kg/mol and 1725 kg/mol). The samples were quenched to room temperature and rinsed in ethanol and then in deionised water before use. LaSFN9 substrates were coated with 45 nm gold, with a 2 nm Cr adhesion layer, by thermal evaporation (Autolab 306, BOC Edwards, UK).

Films with $h > \lambda_{C\text{-}C}$ and the perpendicular cylindrical PMMA morphology were prepared for optical waveguide experiments together by collaborators at the MPI-P.[*] The samples were prepared from a blend of the 7:3 block volume ratio PS-b-PMMA (M_n = 40.8/19.8 kg/mol) and the PMMA homopolymer (M_n = 13.8 kg/mol) in the following ratio: PS-block:PMMA-block:homoPMMA = 65:7:28. They were prepared on Au- or Ag-coated LaSFN9 substrates modified with either the crosslinkable P(S-r-BCB-r-MMA), or with a hydroxyl-terminated P(S-r-MMA) copolymer brush surface energy neutral layer. The P(S-r-MMA) brush was also used

[*] Prof. Dr. Juan Peng, now at Fudan University, Shanghai, PRC; and Prof. Dr. Dong Ha Kim, now at Ewha Women's Univeristy, Seoul, Republic of Korea.

because the P(S-r-BCB-r-MMA) was not always available at the time of the experiment. Films using the crosslinkable P(S-r-BCB-r-MMA) neutral energy layer were prepared using the same procedure as the thin films described above with $h \leq \lambda_{C\text{-}C}$. Films using the P(S-r-MMA) copolymer brush were prepared with additional adhesion layers to anchor the hydroxyl terminated brush to the metal surface according to a previously published protocol [31, 32]. Briefly, to create a silicon oxide surface for the covalent coupling of the hydroxyl-terminated copolymer brush, the metal-coated glass surface was functionalised first with a $\leq$ 2 nm layer of siloxane terminated thiol (20 mM of distilled MPTES in dry ethanol), followed by a ~30 nm layer of SiO_x prepared from a TMOS sol-gel precursor (H_2O:methanol:0.1M HCl:TMOS with volume ratio = 163:55:81:20). The P(S-r-MMA) surface energy neutral copolymer brush was then prepared by spin coating onto the oxide-functionalised metal surface (2 wt% in toluene, 1000 rpm, 60s) and annealing under vacuum at 165ºC for 2 days. After rinsing in toluene, a ~5 nm thick copolymer brush layer is produced, on which the PS-b-PMMA can be prepared according to the regular spin-coating/anneal procedure described earlier.

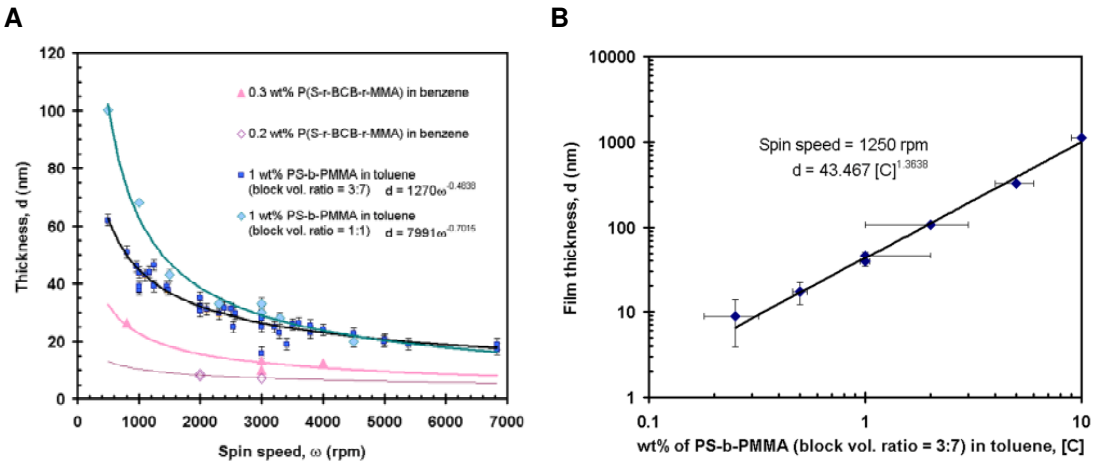

Figure 3.3. Spin coating conditions for PS-b-PMMA copolymers. (A) shows the fine tuning of copolymer film thickness obtained by varying the spin speeds for different copolymers, and (B) shows coarse adjustment of the copolymer film thickness by varying the copolymer solution concentration while keeping the spin speed constant. (Results for the copolymer with PS:PMMA block volume ratio = 3:7 and total Mn = 104.4 kg/mol is shown in B.)

3.1.3. AFM characterization of PS-b-PMMA surface nanopatterns

In this section, AFM characterization of the surface nanopatterns prepared by PS-b-PMMA self-assembly on the P(S-r-MMA) modified energy neutral substrates is presented. The film thickness, measured by a line profiler, was controlled to within the range $h \leq \lambda_{C\text{-}C}$. AFM tapping mode measurements of the PS-b-PMMA surface

nanopatterns are shown in Figure 3.4, 3.5 and 3.6. The nanopatterns are labelled by the M_n, $\lambda_{C\text{-}C}$, and *h* corresponding to each sample. Figure 3.4 shows the striped nanopatterns resulting from the perpendicular lamella morphology, Figure 3.5 shows a symmetric PS-b-PMMA with such a high M_n (1725k g/mol), and Figure 3.6 shows the samples with PS cylindrical phases resulting from the perpendicular cylindrical morphology. In Figure 3.5, although the copolymer was not expected to self-assemble into ordered structure due to its high molecular weight, microphase separation did produce a perpendicular morphology with an average pattern $\lambda_{C\text{-}C}$. Varying *h* in the range 68 nm - 220 nm for this large PS-b-PMMA produced no noticeable difference in the average $\lambda_{C\text{-}C}$. Thicker films commensurate with the observed $\lambda_{C\text{-}C}$ were not prepared because they would be incompatible with the surface plasmon measurements that the nanopatterns were intended for (Chapter 4). The exact values of *h* for the other samples were also not found to be essential for pattern formation as long as it is controlled to around $\lambda_{C\text{-}C}$.

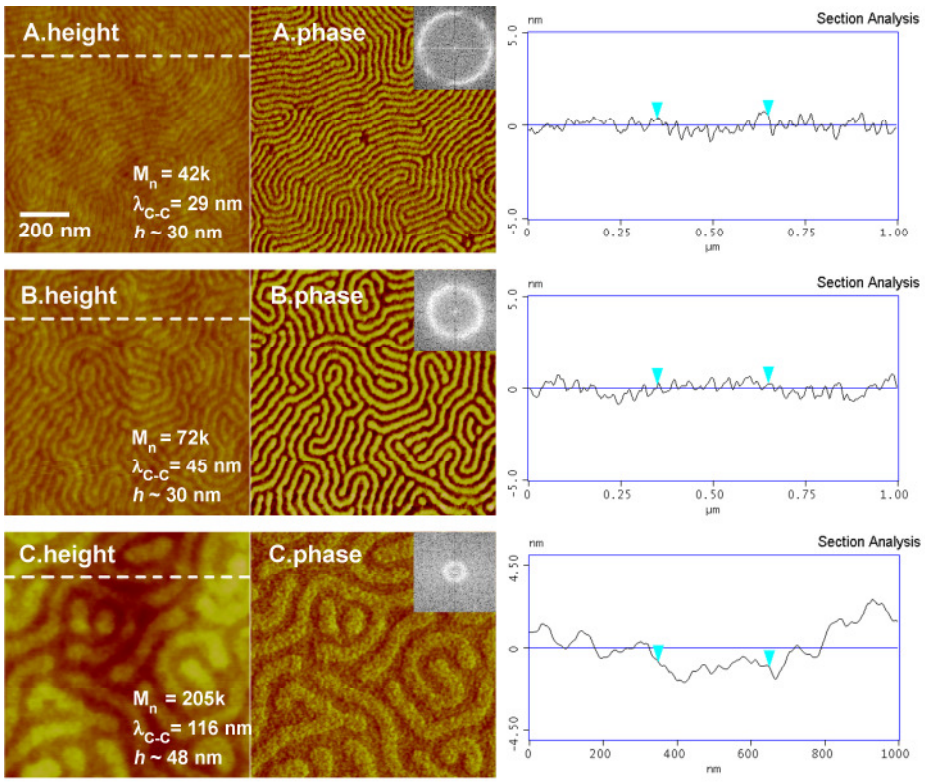

Figure 3.4. Tapping mode AFM height, phase and cross-section measurements of striped surface nanopatterns self-assembled from PS-b-PMMA with approximately 1:1 block volume ratios. The height scale is 10 nm and the phase scale is 20°. All images show a 1x1 μm^2 scan area. As discussed in the text, PS surfaces appear as darker areas in the phase measurement. (A), (B) and (C) differ in the M_n (in g/mol) of the sample. The greyscale insets show the fast fourier transforms of the phase images, from which $\lambda_{C\text{-}C}$ was measured. The white dashed lines in the height data indicate where the cross-sections were taken along.

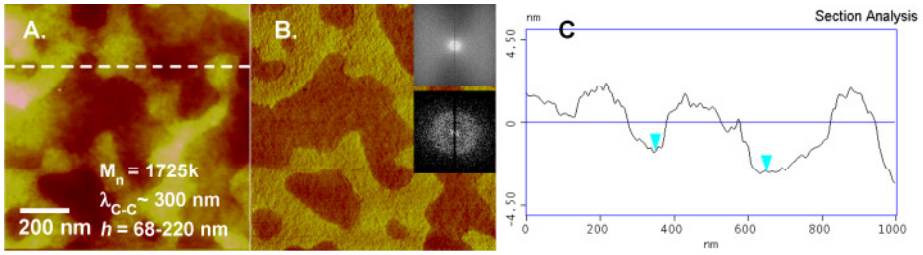

Figure 3.5. Tapping mode AFM height (A), phase (B) and cross-section (C) measurements of the PS-b-PMMA (total M_n = 1725 kg/mol) surface nanopattern (1x1 μm^2; height scale = 10 nm; phase scale = 20º). PS surfaces appear as darker areas in the phase measurement. The white dashed line in (A) indicates where the cross-sections (C) was taken. The grayscale insets show the fast fourier transforms of the phase image (measured from the original data scanning a 5x5 μm^2 area), from which λ_{C-C} was measured. The lower FFT is an expanded, contrast enhanced view of the upper inset.

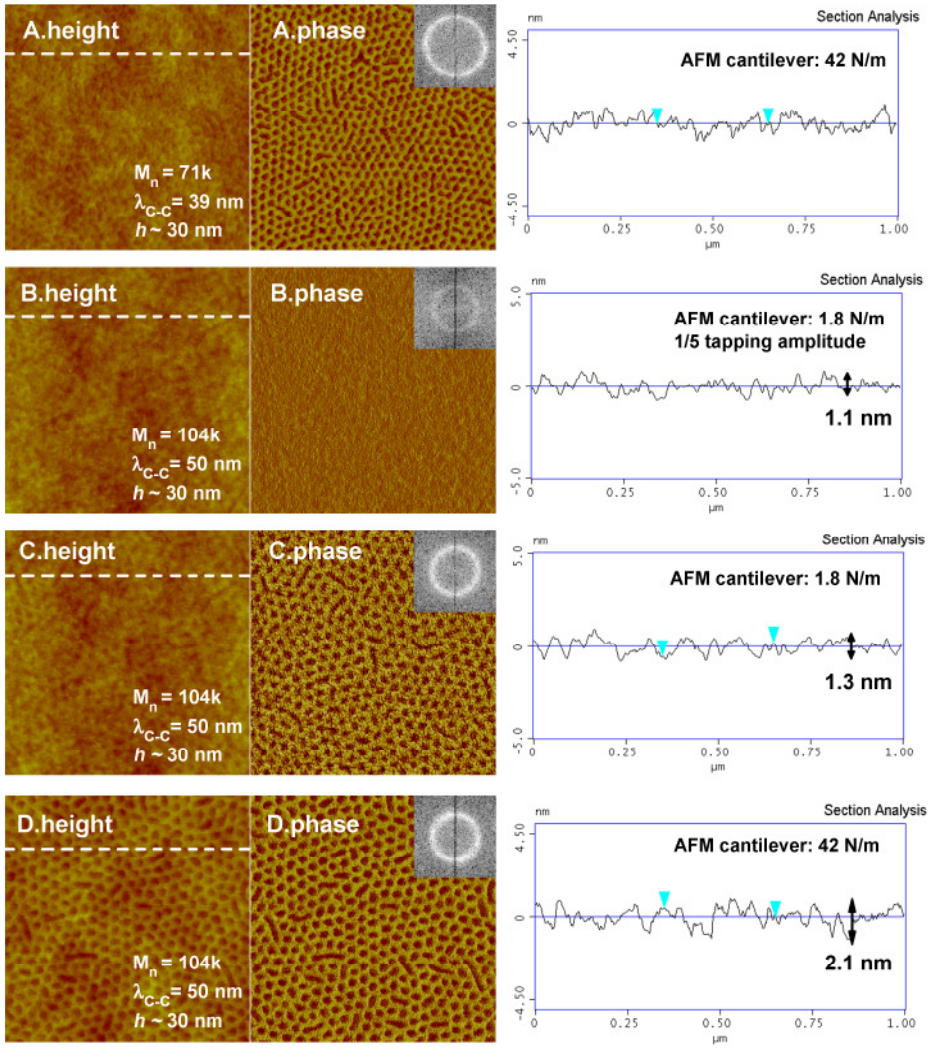

Figure 3.6. Tapping mode AFM measurements (1x1 μm^2) of surface nanopatterns with hexagonally ordered PS domains, self-assembled from PS-b-PMMA with approximately 3:7 block volume ratios. (Height scale is 10 nm; phase scale is 20º.) PS surfaces appear as darker areas in the phase measurement. (A) shows a sample with M_n = 71 kg/mol, while (B), (C) and (D) show samples with M_n = 104 kg/mol. In (B), (C) and (D), different AFM cantilevers were used for the measurements (as indicated in the section analysis on the right), and resulted in different heights in the topography measured, but the lateral dimensions remained unaffected. The greyscale insets show the fast fourier transforms of the phase images, from which λ_{C-C} was measured. The white dashed lines in the height data indicate where the cross-sections were taken.

In Figure 3.4, 3.5 and 3.6, the height and phase images, as well as a line cross-section for each sample, are shown for comparison. As discussed in section 2.2, AFM tapping mode phase contrast can reveal the spatial arrangement of domains with different material compositions on a surface due to differences in mechanical properties. In the case of PS-b-PMMA, the PS domains appear as regions with a lower phase offset (darker areas) than PMMA domains and the self-assembled nanopatterns are revealed at high spatial resolution. $\lambda_{C\text{-}C}$ was measured by identifying the intensity maxima in the frequency transforms of the phase images (greyscale insets). These measurements are plotted in Figure 3.7 against the BCP degree of polymerization calculated from M_n. The $\lambda_{C\text{-}C}$ data for the symmetric PS-b-PMMA samples was also fitted to power law profiles to estimate the segregation regime of the self-assembly. In Figure 3.7a the fit over all data for the samples shown in Figure 3.4 and Figure 3.5 shows a remarkable correspondence of the fitted exponent—0.631—to the theoretical value of 0.667 at the strong segregation limit. Nonetheless, the degree of segregation may be different for the samples with lower molecular weights, and a separate fit excluding the highest molecular weight sample was performed (Figure 3.7b). A higher exponent of 0.788 was found in this range of N, which indicated that the degree of segregation was in an intermediate regime [2].

The height images and cross-sections in Figure 3.4, 3.5 and 3.6 show that all the nanopatterns had relatively flat topographies and no terracing. In particular, all samples had $\leq$ 2 nm height variations across all PS/PMMA surface interface. In fact, the measured height differences should be taken as an upper bound of the actual topography variation, because AFM tip-surface interactions can induce mechanical deformation of the polymer surface [41-44]. For example, Figure 3.6b, c and d show that the height variation measured on the same PS-b-PMMA sample can be different depending on the contact force applied during AFM operation. Figure 3.6b and c show the same 1x1 μm^2 area measured with the same AFM cantilever with a low spring constant (1.8 N/m) but with different cantilever oscillation amplitudes applied. For the same AFM cantilever oscillating at a constant frequency, larger oscillation amplitudes imply higher cantilever oscillation velocities, thus higher contact forces and larger surface deformations. Figure 3.6b shows a maximum height variation of 1.1 nm, and Figure 3.6c shows that the height variation increased by ~15% to 1.3 nm at 5 times larger tapping amplitude. Figure 3.6d shows that the measured height variation can be exaggerated even more to 2.1 nm, by using a stiffer cantilever with a 20 times higher spring constant of 42 N/m. AFM contact mode measurements, which exert a continuous pressure on the surfaces, did not produce less topography variations than that shown in Figure 3.6b with the AFM cantilevers available in our laboratory (0.05 N/m).

Although the surface topography can be measured with a lower degree of deformation-induced artefact by reducing the tip-surface contact force during AFM operation, the measured phase contrast useful for delineating the PS-b-PMMA

microphase separation is also reduced at lower contact forces, as also shown in Figure 3.6b, c and d. Thus the PS-b-PMMA nanopatterns were normally characterised with stiff 42 N/m AFM cantilevers.

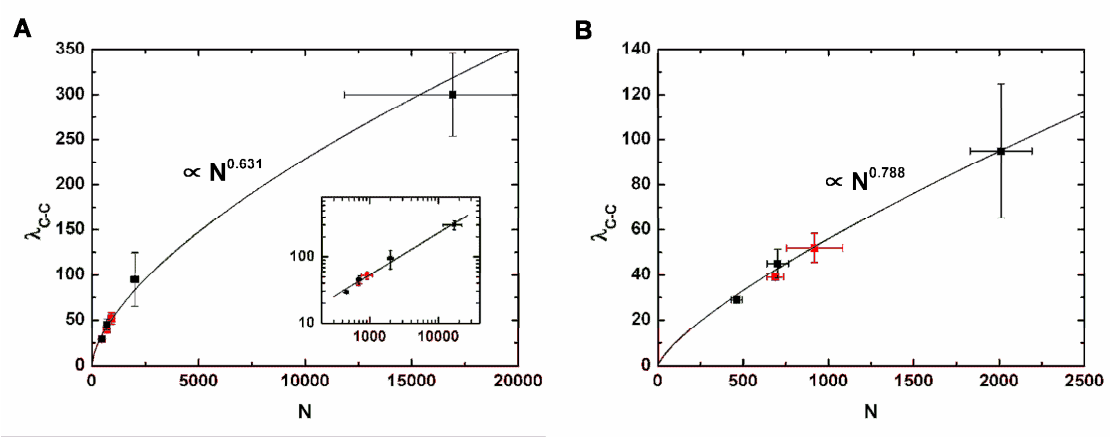

Figure 3.7. λ_{C-C} measured from the frequency transforms of the AFM phase images plotted against the degree of polymerization (N). The symbols are measurements (black: 1:1 symmetric PS-b-PMMA; red: 3:7 PS-b-PMMA), and the curves are least mean squared power law fits (fitted only over the symmetric samples). A) Data points for all samples prepared. B) Data points and fit only for lower molecular weight samples. The Y-error bars show ±2 SD (4 SD in total). The X-error bars indicate ± polydispersity.

Other than λ_{C-C}, the PS-b-PMMA surface nanopatterns were also characterised by the surface area fractions of PS and PMMA, $f_{PS} = 1 - f_{PMMA}$, the characteristic width of the surface domains, $w_{PS} = \lambda_{C-C} - w_{PMMA}$ (referring to the PS domain diameter, or the stripe width, depending on the nanopattern morphology), and the surface length density of the PS/PMMA surface interface, $l_{interf.}$. These parameters were measured from the AFM phase images by computer image analysis (see Appendix A), and are listed in Table 3.1.

M_n (kg/mol) (polydispersity)	PS:PMMA v/v ratio	λ_{C-C} (nm)	f_{PS}	w_{PS} (nm)	$l_{interf.}$ ($\mu m/\mu m^2$)
42 (1.07)	48:52	29	0.45	13	84
72 (1.09)	53:47	45	0.56	25	65
205 (1.09)	49:51	116±15	0.50±0.04	50±5	20±1
1725 (1.3)	47:53	~300±50	0.56±0.02	~200±50	8±1
71 (1.07)	26:74	39±1	0.37±0.03	26±1	62±1
104 (1.18)	26:74	50±3	0.35±0.06	30±2	48±5

Table 3.1. Surface nanopattern parameters of the PS-b-PMMA thin films prepared. The uncertainties indicate ± 1 standard deviation from multiple AFM measurements and across multiple samples. Uncertainties are not given in the first two rows because only one sample was made for each of the block copolymers, but they are expected to be similar to other samples with comparable molecular weights.

3.1.4. Verification of surface composition of self-assembled PS-*b*-PMMA thin films with $h \leq \lambda_{C\text{-}C}$

As described in section 3.1.1, PS and PMMA have almost identical surface energies at the polymer-air interface that differ by less than 1% (0.4 mN/m). Thus given our P(S-r-BCB-r-MMA) modified substrates with balanced PS and PMMA interfacial energies, PS-*b*-PMMA self-assembly during thermal annealing in vacuum should produce surface nanopatterns with both PS and PMMA microdomain surfaces exposed [38]. In other words, unlike other block copolymer thin films, such as polystyrene-*block*-poly(tert-butyl acrylate) [45], no skin layers should be formed under the present PS-b-PMMA preparation conditions.

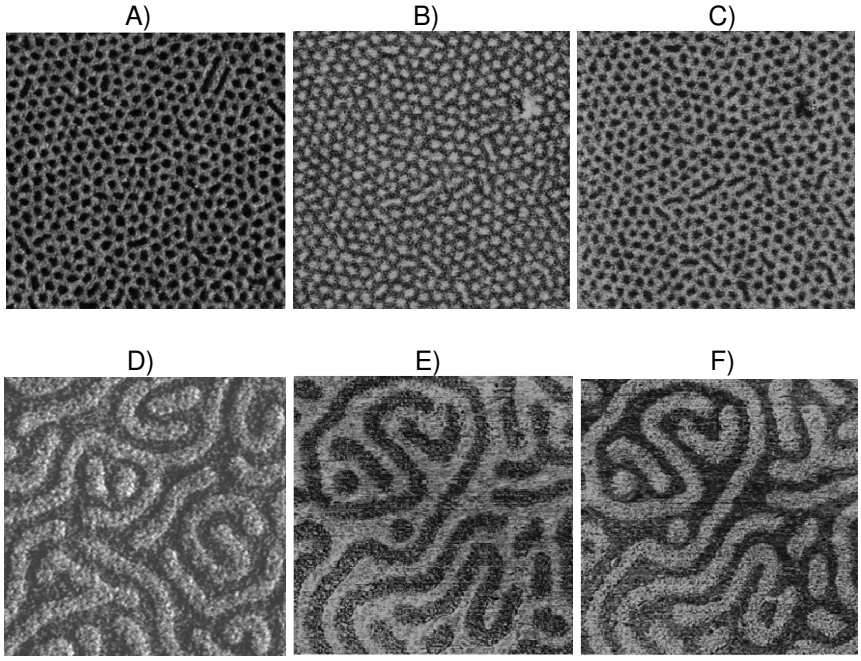

Figure 3.8. PS-b-PMMA nanopatterns revealed by AFM phase and lateral force measurements. All images show 1x1 μm^2 scan areas, (A)-(C): Measurements on PS-b-PMMA with M_n = 104 kg/mol. (D)-(F): on PS-b-PMMA with M_n = 205 kg/mol. (A),(D) are phase measurements. (B),(E) are lateral force images measured as the AFM tip was scanned from right to left; (C),(F) were measurements for scans from left to right.

Although tapping mode AFM phase measurements are frequently used to characterise block copolymer nanopatterns, because the tip interaction volume extends a few nanometers below the sample surface, the technique is not sensitive to the presence of skin layers. We verified the presence of nanopatterned surface chemical heterogeneity inferred from AFM phase measurements by comparing them with lateral force (friction) AFM measurements. Lateral force AFM operating under low contact force conditions can be uniquely surface sensitive, and has been used to map, e.g., chemical patterns of different self-assembled monolayers differing only in

the surface head group [41, 46]. As examples, Figure 3.8 compares the nanopatterns as measured by the two techniques for PS-b-PMMA nanopatterns corresponding to Figure 3.4c and b, respectively. Excellent agreement is found, thus verifying that the phase images shown in Figure 3.4 to Figure 3.6 truly reflect the surface chemistry of PS-b-PMMA nanopatterns.

3.1.5. Nanostructure characterization of self-assembled PS-*b*-PMMA/PMMA waveguiding films

Thicker films with $h >> \lambda_{C\text{-}C}$ and the perpendicular cylindrical morphologies were prepared by self-assembly from a blend of an asymmetric PS-b-PMMA with 7:3 PS:PMMA volume, with a PMMA homopolymer (homoPMMA), following the protocol reported by Jeong et al. [11] M_n of the homoPMMA used was 13.8 kg/mol, and that of the PS-b-PMMA was 55.5 kg/mol. A final block volume ratio of 65:28:7 PS:PMMA:homoPMMA was used. As opposed to the thin films described in section 3.1.3 , here the PS was the major block, and forms the continuous matrix with hexagonally-packed arrays of cylindrical PMMA microdomains embedded. Therefore a surface nanopattern with hexagonally arranged PMMA surface domains set in a PS matrix was expected. Figure 3.9 shows the AFM measurement of the top surface of a PS-b-PMMA/homoPMMA film with h = 380 nm. As discussed in section 3.1.3, the darker and brighter areas are PS and PMMA, respectively. The $\lambda_{C\text{-}C}$ of the PMMA nanodomains shown is 46 nm.

AFM by itself can only reveal surface information. Characterization of thin film internal structures on the nanoscale is a continuing challenge. Conventional approaches such as electron microscopy and neutron scattering have drawbacks in terms of sample preparation, limited sensitivity, or the limited availability of synchrotron source [43, 47, 48]. For example, Figure 3.10 shows the SEM cross sections of typical PS-b-PMMA/PMMA thick film samples. The samples were exposed to UV radiation, followed by acetic acid rinsing, to preferentially remove the PMMA content and facilitate the identification of the BCP nanostructure [31, 49]. Figure 3.10a shows a fortunate instance when cracking of the underlying Si substrate revealed the cross section of a 200 nm thick sample. The cylindrical morphology is clearly revealed by the elliptical cross sections at the cleavage plane. However, the amount of PMMA removed and the pore (PMMA domain) size of the original film cannot be characterised by SEM due to limited resolution and e-beam degradation of the polymers. Figure 3.10b shows the more usual case when cracking of the substrate, in this case LaSFN9 glass, caused large scale deformation of the polymer film, and obscured the nanostructure. The potential for nanostructure characterization by non-destructive waveguide analysis is demonstrated in chapter 5 with the examples of PS-*b*-PMMA/PMMA and nanoporous AAO films.

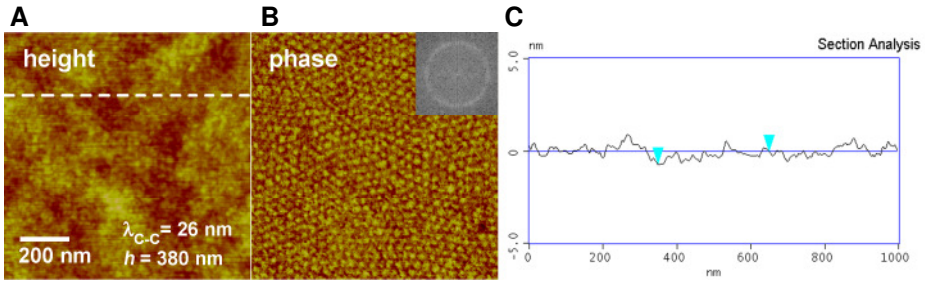

Figure 3.9. AFM height (A), phase (B), and cross-section (C) measurements of the surface nanopattern self-assembled from PS-b-PMMA/homoPMMA blend with total PS-b-PMMA M_n = 56 kg/mol and homoPMMA M_n = 13.8 kg/mol. The height scale is 10 nm and the phase scale is 20º. As discussed in the text, PS surfaces appear as darker areas in the phase measurement. The white dashed line in (A) indicates where the cross-sections (C) was taken along (also 10 nm full scale). The greyscale insets show the fast fourier transforms of the phase image (measured from the original data scanning a 5x5 μm^2 area), from which λ_{C-C} (46 nm) was measured. (The sample was obtained courtesy of Prof. Dr. Juan Peng, now at Fudan University, Shanghai, China.)

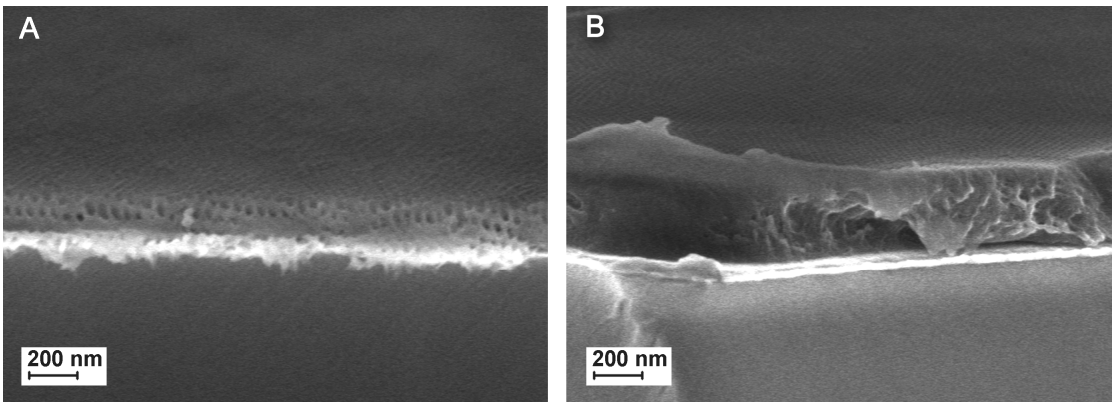

Figure 3.10. SEM cross section images of thick PS-b-PMMA/PMMA films after the PMMA components were preferentially removed by UV exposure and acetic acid rinsing. (A) shows a fortunate instance when cracking of the underlying Si substrate revealed the cross section of a 200 nm thick sample. The slanting arrangements of the pores indicate misoriented "grains" of the perpendicular cylindrical PMMA domains. (B) shows the more usual case when cracking of the substrate, in this case LaSFN9 glass, caused large scale deformation of the polymer film, and obscured the nanostructure. (Samples shown were prepared by Prof. Dr. Peng Juan, now at Fudan University, Shanghai, China.)

3.2. Nanoporous anodic aluminium oxide (AAO) thin films

3.2.1. Introduction to nanoporous alumina preparation by anodization

Anodization refers to the conversion from Al into an aluminium oxide surface layer, when the Al is made the anode in an electrolytic cell. It is an easily reproducible but complex electric field assisted, simultaneous oxidation and dissolution process [50-54]. Nanoporous anodic alumina layers are characterised by cylindrical pores of a high aspect ratio that run straight through the film thickness, and a narrow distribution of pore diameters. Anodization is commonly prepared in sulphuric, oxalic and

phosphoric acids (Table 3.2) [52, 54, 55]. Non-porous "barrier" type films may also be produced by anodization in electrolytes with a near neutral pH [50, 53]. Moderate voltage potentials (10^1 ~ 10^2 V) over a nanoscale effective oxide thickness (10^1 ~ 10^2 nm) are generally applied, leading to very high local electric field strengths (10^6 ~ 10^7 V/cm). Both the pore centre to centre distance ($\lambda_{C\text{-}C}$) and the native pore diameters (ϕ_{native}) obtained after anodization vary in direct proportion to the voltage applied during anodization [51, 54, 56]. Therefore, anodization at a constant voltage is used for generating regular pore arrays with well-defined pore geometries. The pores can also be subsequently enlarged to the desired pore diameter (ϕ_{pore}) by additional isotropic etching without an electric field applied [52, 57-60].

Electrolyte (concentration)	Anodization voltage	Electrolyte temperature	$\lambda_{C\text{-}C}$	ϕ_{native}
H_2SO_4 (0.3M)	25 V	1ºC	~ 60 nm	~ 20 nm
$COOH_2$ (0.3M)	40 V	1ºC	~ 100 nm	~ 30 nm
H_3PO_4 (0.1M)	195 V	1ºC	~ 500 nm	~ 160 nm

Table 3.2. Standardised anodization conditions giving optimal pore ordering. (Adapted from Nielsch et al. [55])

Current research interest has been spurred in part by advances made since the early 1990s that has enabled the preparation of hexagonal pore arrays with exceptional lattice perfection spanning very large areas. Self-organization was initially exploited in processes such as 2-step anodization [61, 62] and high-field anodization [56, 63, 64], and proceeds at two levels: the formation of uniformly sized pores with a fixed $\lambda_{C\text{-}C}$; and long range ordering into hexagonal pore arrays. Later, lithography-assisted methods such as mechanical imprinting [61, 65, 66] and lithographies [58, 67] were also used. Figure 3.11 shows the pore arrangement obtained by 2-step anodization in oxalic acid both before and after pore widening by etching in phosphoric acid.

In the anodization process, when the electric potential is first applied, a thin barrier alumina layer is quickly formed on top of the Al surface as the metal is electrolytically converted into Al cations and combined with oxygen containing anions that are driven towards the Al metal electrode. Therefore, the maximum thickness of this barrier layer is determined by the electric potential applied (i.e., the anodization voltage, U) and the mobility of ions through the oxide layer. At the same time, the field-assisted oxidation process is not completely efficient, and some of the Al cations are ejected into the electrolyte [50, 52-55]. Since there is a lattice

expansion accompanying Al conversion into alumina, as oxygen atoms are incorporated into the oxide, compressive mechanical stress is also expected to be generated at the Al metal/oxide interface, and the level of stress is dependent on the ratio of Al atoms incorporated into the oxide and those dissolved in the electrolyte. As will be discussed below, this compressive stress is believed to be a significant driving force responsible for long range pore ordering [52, 54-56]. While oxide is formed at the metal/oxide interface, etching of the barrier layer takes place at the oxide/electrolyte interface, whereby electric field assisted oxide dissolution [50-54] is caused by the polarization of the alumina lattice and the electric field enhanced association of hydrogen ions to, and solvation by water molecules of, respectively, the oxygen and Al atoms in the oxide [51]. The steady state balance between the oxidation, etching, and the Al conversion efficiency, together determine the thickness of the barrier layer ($d_{barrier}$) finally formed, which is an essential parameter intimately connected with $\lambda_{C\text{-}C}$ [51].

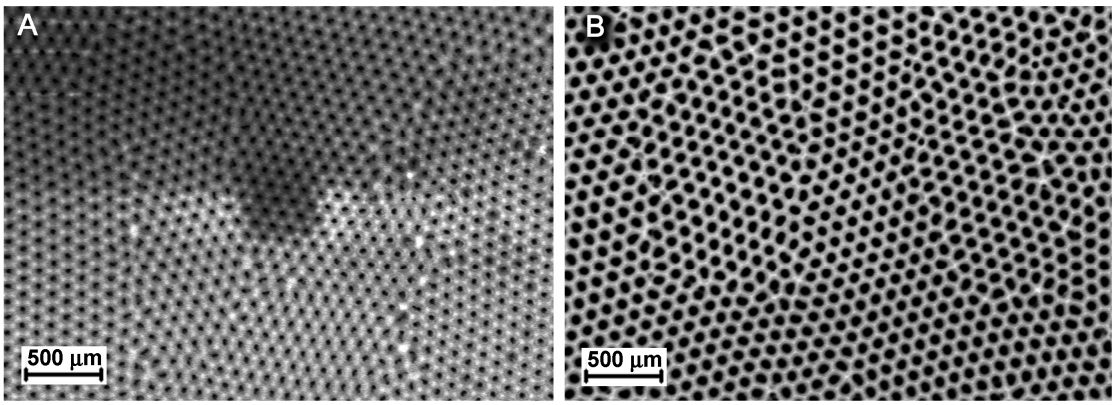

Figure 3.11. SEM images of the top surface of AAO obtained by 2-step anodization in oxalic acid, according to the recipes provided in Table 3.2. (A) shows the pores directly after the second anodization. (B) shows the pores after 50 min etching in 5 wt.% H_3PO_4. The average pore size and $\lambda_{C\text{-}C}$ in (A) are, respectively, 31 nm and 107 nm, and those in (B) are, respectively, 69 nm and 108 nm. These measurements were obtained by computer image analysis (Appendix A). (The pre-pore-widened sample was obtained courtesy of the Steinhart group at the Max Planck Institute for Microstructure Physics, Halle.)

In Figure 3.12, the pore nucleation process on the barrier oxide layer formed when the anodization potential was initially switched on is shown [50, 51, 53]. Since atomic and topographic defects necessarily exist on the original Al surface, barrier layer formation is not uniform over the Al surface. Crucially, electric field concentrations exist where the barrier layer is thinnest (E = U/d). At these locations of field concentration, both oxide formation and dissolution proceed at the highest rates, and lead to surface depressions [51, 53]. These quickly deepen to form pores due to further field enhancement reinforced by the hemispherical geometry imposed by the developing constant barrier thickness. As anodization continues, the pores that

developed first quickly dominate, which, because of the coalescence of their barrier oxide layers, close off further growth of the smaller (later formed) pores. Once the pores grow away from the top surface, electric field enhanced oxidation and etching are completely localised at the pore growth front at the metal/oxide interface. Regular etching of the already formed pore walls by the acid electrolyte above the etching front is minimised by anodization at low temperatures and in moderate acid concentrations (Table 3.2) [51, 53, 55].

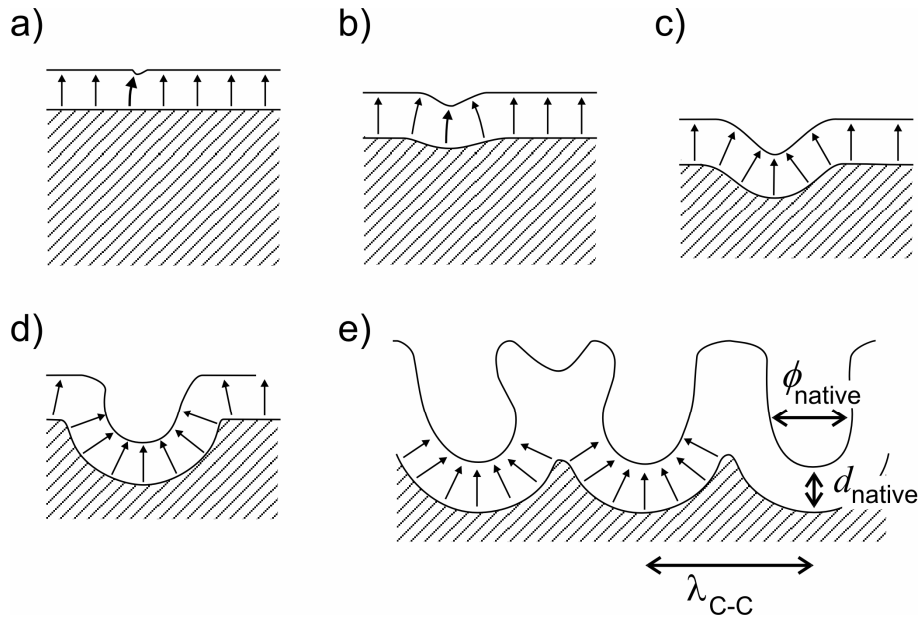

Figure 3.12. Schematic of the pore nucleation process on the barrier oxide layer formed at the start of the anodization process. The Al substrate is shown as the hatched bottom areas. The barrier oxide layer is shown as the layer marked with arrows indicating the electric field orientation. (A) shows the initial field concentration effect around a defect on the oxide layer. (B) through (D) show how this field concentration promotes etching and oxidation around the initial defect site, and lead to pore formation. (E) shows the emergence of a constant $\lambda_{C\text{-}C}$ between the pores as the sides of neighbouring pores merge to form pore walls and pores with a diameter ϕ_{native}. A partially formed pore is also shown: it was terminated by neighbouring pores which nucleated at an earlier stage. Note the constant barrier layer thickness at the oxidation front that characterises porous anodic alumina formation. (Adapted from Ref. [51].)

As the pores deepen and the oxide growth front advances, both geometric considerations [51, 53] and mechanical stress [52, 54-56] contribute to the development of a uniform $\lambda_{C\text{-}C}$ and a hexagonal ordering of the pores into a close-packed array. The uniform $\lambda_{C\text{-}C}$ emerges because, first, as the dominant pores grow towards each other after pore initiation, they are prevented from merging due to a steady state balance between the oxidation and etching rates (which together determine both $d_{barrier}$ and the areal ratio between the pore and the oxidation fronts). Second, a geometry imposed feedback mechanism ensures that all growth fronts advance at the highest rate commensurate with $d_{barrier}$: if a particular pore front grows

larger than adjacent pores, given a constant $d_{barrier}$, the pore front curvature is correspondingly reduced, and the field concentration is also reduced, leading to a reduction in the growth rate, and vice versa [51]. At the same time, it has been found experimentally that the conversion efficiency of Al into oxide increases with increasing U, which, as discussed earlier, would increase the volume expansion and is expected to increase the compressive mechanical stress incorporated into the oxide layer formed. Since the strain energy is proportional to the square of the stress [68], mechanical stress can provide a strong driving force to eliminating stress concentrations in the pore structure, thus promoting an efficient and uniform (hexagonal) pore packing arrangement. A certain value of U and a corresponding compressive stress level that accompany an Al metal to oxide volume expansion of 1.2 ~ 1.4 or higher is found to be optimal for promoting long range ordering of the pore array [52, 54, 55]. Very low conversion efficiency, possibly leading to volume contraction and tensile stresses, was not found to induce stable development of pore order [52]. Higher U's and the accompanying higher volume expansion has been demonstrated to further improve pore ordering [56, 63, 64], but this effect has not been universally observed[52] and higher stresses may also lead to lattice defect strain relaxation. Moreover, acid burning and/or the alumina barrier layer breakdown easily occurs at high field-strengths [56, 63, 64]. All in all, the anodization voltage, U, is the principal parameter for controlling $\lambda_{C\text{-}C}$, while ϕ_{pore} can be adjusted by subsequent isotropic pore etching. However, 1) the lower $\phi_{pore} > \phi_{native}$ limit cannot be controlled independently from $\lambda_{C\text{-}C}$ by adjusting U for a given electrolyte, 2) each electrolyte has a critical U above which acid burning occurs, and 3) a certain level of volume expansion dependent on U must accompany anodization for long range pore ordering. Therefore, in practice, anodization in specific acids and U are employed to generate optimally ordered pore arrays with a given range of $\phi_{native} < \phi_{pore} < \lambda_{C\text{-}C}$ at standardised $\lambda_{C\text{-}C}$'s (Table 3.2) [54, 55].

An important inference drawn from the preceding discussion is that, because pore initiation at the original Al metal surface is random, pore ordering emerges only at the pore front as it progresses deeper into the bulk Al. Hexagonal pore ordering beyond the nearest neighbour is observed only when the pore depth vs. ϕ_{native} ratio becomes larger than ~100, and the domain size over which a perfect hexagonal lattice extends increases with pore depth [53] until electrolyte conditions at the pore front are changed for extremely deep pores [53, 55]. This behaviour is exploited for 2-step anodization [61, 62], whereby a thick (10^4 ~ 10^5 nm) sacrificial layer of porous alumina with well developed pore ordering is first prepared and then preferentially etched away to leave behind an imprint of the scalloped oxide growth front on the Al surface. Subsequent anodization on this scalloped Al surface with hexagonally arrayed depressions spaced $\lambda_{C\text{-}C}$ apart then leads to directed pore initiation at the centre of the depressions and the immediate realization of an optimizing hexagonal pore array.

The relatively slow development of the hexagonally ordered pore growth front also means that good pore ordering cannot be achieved by self-organization for thin film AAO supported by heterogeneous substrates. For integrated optics or integrated electronics applications, it may be desirable to prepare micrometer thick thin film AAO on a silicon or glass substrate [60]. Since the physical handling of such thin films is extremely challenging, it is desirable to directly anodize a thin layer of Al that has been deposited on the substrate by vacuum techniques. The pore initiation process on the vacuum deposited Al is identical to that of bulk Al, but because high quality vacuum deposited Al typically do not exceed 10^2 ~ 10^3 nm in thickness [69-72], there is simply not enough Al material to take advantage of 2-step anodization. Therefore highly ordered AAO thin films can be prepared only by lithographic approaches [61, 65, 66].

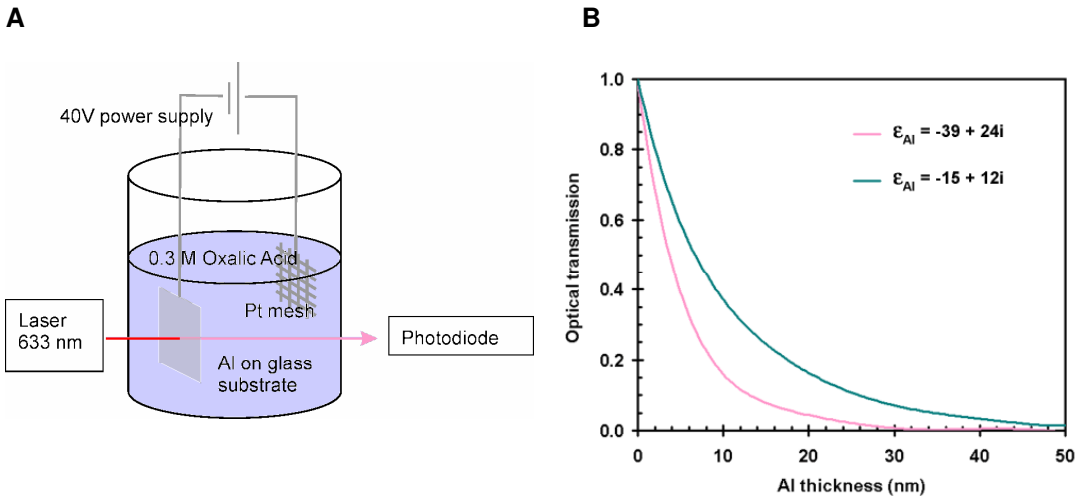

Figure 3.13. (A) Schematic of the Al anodization setup with final Al layer thickness control by a laser-photodiode setup. The photodiode measures the transmission of the laser light (633 nm) through the AAO/Al sample on LaSFN9 glass substrates. (B) The original 1 μm thick Al layer does not transmit the laser light. But as Al is oxidised to form nanoporous AAO, which is transparent, the Al layer thickness decreases and the layer becomes semi-transparent to the laser. The final Al layer thickness can then be sensitively measured at the nanometer level by the transmittance. Depending on the Al sputtering conditions and the surface structure of the Al film, the dielectric constant of the deposited film may vary widely. ε_{Al} = -39 + 24i refers to the bulk crystalline Al value. -15 + 12i refers to an effective value of ε_{Al} plus 10% alumina content according to effective medium theory (see section 5.1).

The chemical composition of the AAO is complex and depends sensitively on the anodization conditions. The AAO structure is amorphous with significant incorporations of water, in the forms of both hydroxide and the hydrate oxide [50, 51, 53], and the conjugate base anion of the acid electrolyte [50, 51, 53, 73-75], which has been suggested to replace O^{2-} in the oxide [53]. The level of acid anion incorporation depends on the nature of the acid electrolyte, and goes in the order H_2SO_4 > $(COOH)_2$

> H_3PO_4. Moreover, higher incorporation is found for higher anodization voltages. An incorporation of as much as 8 wt% [50] to 10 wt% [74] to 20 wt% [53] has been measured for H_2SO_4. Interestingly, no acid anion incorporation is usually found for anodization in chromic acid, which does not have a conjugate base ion [53]. It should also be noted there is a gradation in acid anion incorporation through the wall thickness of the oxide pore structure, with the highest concentrations at the pore surfaces, and essentially no incorporation for a distinct thin layer of oxide near the metal/oxide interface and at the centres of the vertical pore walls [53, 73-75]. The thickness of this pure alumina layer depends, again, on the anodizing acid (in the order $H_2SO_4 < (COOH)_2 < H_3PO_4$) [53, 73, 74] and the anodization voltage [74]. This layered distribution has been explained in terms of the difference in the charge and mobilities of the various acid anions [74, 76], and has been linked to differences in the pore growth rate in difference acids [73]. A consequence of the amorphous nature of the AAO is its inferior chemical stability compared with crystalline Al_2O_3: significant etching occurs at pH < 5.0 and pH > 8.2 [60, 75]. The gradation of acid anion incorporation also means that the details of the surface chemistry can be expected to be different, not just for AAO anodized in different acids, but also for the same template pore widened to different diameters.

3.2.2. Nanoporous AAO thin film preparation

1 μm thick Al films were deposited by sputtering on LaSFN9 glass substrates by collaborators at the Institüt für Mikrotechnik Mainz, GmbH.* The Al films were placed in a beaker of 0.3 M oxalic acid in deionised water at 0~2°C, connected as the anode opposite a Pt mesh counter electrode, and anodized at a constant potential of 40 V. These conditions gave an average centre-to-centre pore spacing of 90~100 nm for the film thickness prepared. Anodization was allowed to proceed until a thin Al metal layer ~40 nm thick was left at the interface between the AAO and the glass substrate for optical waveguide coupling. To control the thickness of the Al metal layer thickness, optical transmission through the aluminium thin film was monitored by a laser-photodiode setup as shown in Figure 3.13. Optical transmission through a metal film sensitively depends on the Al film thickness and dielectric constant and can be accurately calculated [77].

When the transmission corresponding to the desired thickness was reached, the power supplied was switched off. The method is illustrated in Figure 3.14 with a sample that was anodized until a 25 nm thick Al layer was left on between the AAO and the glass substrate, indicating a dielectric constant of the Al film in between the values indicated in Figure 3.13. The anodized samples were rinsed in water, and the

* Dipl. Ing. Stefan Schmitt, in the division "Microstructuring Technologies and Sensors: Silicon and Thin Film Applications", under the direction of Dr. P. Detemple.

pores were widened to the desired diameter by immersion in 5 wt % H_3PO_4 in deionised water for a specific amount of time (etch rate ~0.3 nm/min).

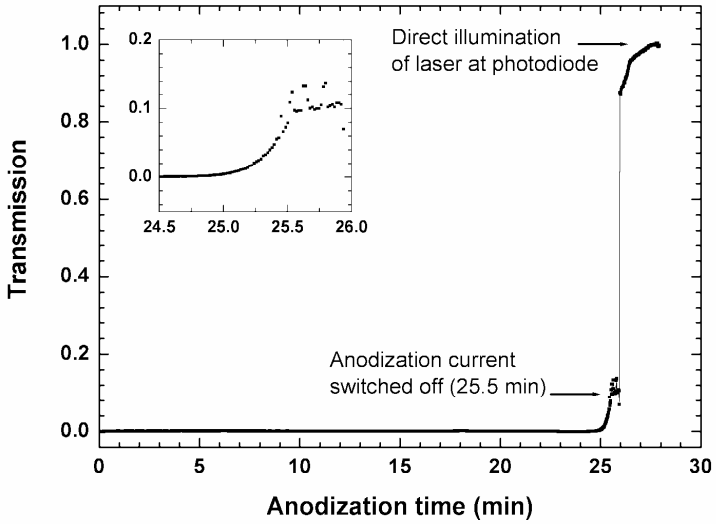

Figure 3.14. Transmitted laser intensity through the AAO/Al thin film during anodization. Anodization started at time 0 min. No transmitted intensity was detected until near the very end of the process, when less than ~50 nm of Al was left on the glass substrate, at which point the transmitted intensity increased exponentially, according to Figure 3.13. In this example, the anodization current was switched off at 25.5 min when the transmitted intensity reached 10%, corresponding to ~25 nm Al left between the glass substrate and the AAO membrane. The inset shows that the intensity can be monitored with reasonably high precision. The jump in transmission at 26 min was caused by removal of the sample, which allowed the direct laser illumination on the photodiode, and illustrates 100% transmission.

3.2.3. SEM characterization of thin film nanoporous AAO

1 μm thick nanoporous AAO thin films prepared on LaSFN9 glass substrate with a 30-40 nm Al interface layer betw 5.4). Pore ordering is not required for this application but pore diameters much smaller than optical wavelengths are essential for the effective medium theory optical description (section 5.1). At the same time, the pores should be much larger than the molecules diffusing through the pores. Thus the basic sample preparation procedure, described in section 2.3, was based on the one-step anodization in oxalic acid (Table 3.2) of 1 μm thick Al films sputtered on glass substrates, to generate pores 30 ~ 70 nm in diameters.

Figure 3.15 shows the SEM cross-section of a sample after the one-step anodization process. The narrow ~20 nm pores could be observed as dense striations oriented generally perpendicular to the substrate surface. The pores are not perfectly parallel to each other, and the misalignment is expected for anodization that has proceeded to only ~10 times $\lambda_{C\text{-}C}$. The AAO layer is brittle and the cross-section shows numerous fracture surfaces. In contrast, the Al metal layer left on the glass is

relatively ductile and show severe, curved deformations along the edge of the film (Figure 3.15a). The metal layer could also be identified by the scalloped surface of the anodization pore front. Part of the grain structure of the original Al film can also be discerned from the rugged top surface of the AAO film, and its details and influence on the AAO morphology will be discussed further below. This roughness is expected to impact on the sharpness of the waveguide coupling resonances to be discussed in Chapter 5.

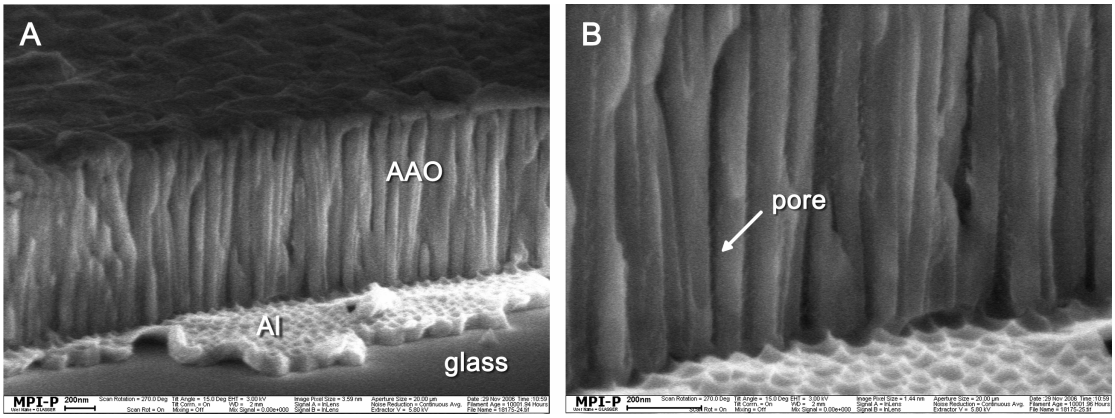

Figure 3.15. SEM cross section of a nanoporous AAO film on glass substrate, prepared from ~1 μm thick sputtered Al thin films anodized in 0.3 M oxalic acid at 40V (standard procedure for AAO with $\lambda_{C\text{-}C}$ ~ 100 nm). The central area in (A) is revealed at a higher magnification in (B). The top surface of the sample retains the overall grain structure of the sputtered Al film and shows a roughness on the order of 100 nm. The cross section shows dense striations oriented generally perpendicular to the substrate surface and are the un-widened pores. Note the Al layer left behind by the laser transmission monitored anodization process. The scalloped imprint of the quasi-spherical pore fronts can be clearly seen.

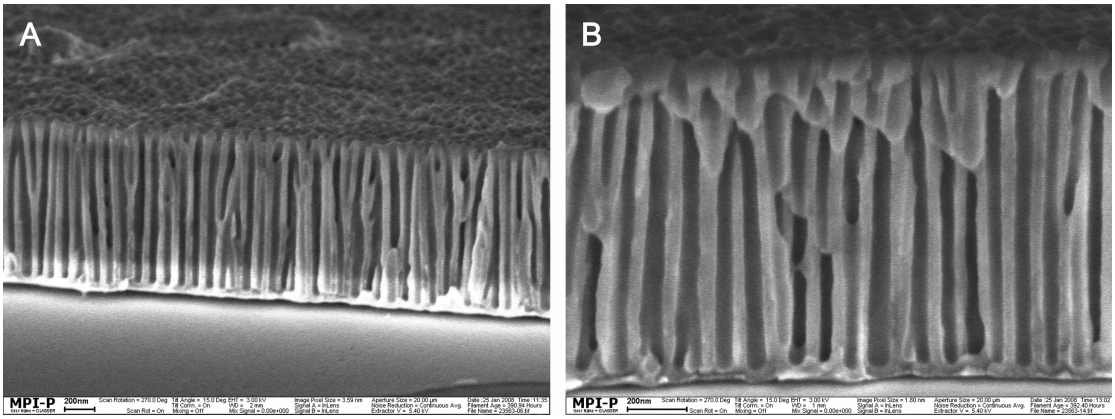

Figure 3.16. SEM cross section of a pore-widened nanoporous AAO sample, anodized under identical conditions as the sample shown in Figure 3.15. The pores were widened for 50 min in 5 wt% H_3PO_4 after the anodization process. The average pore diameter obtained was 60 nm. Note the barrier oxide layer and quasi-spherical (scalloped) pore front near the bottom of the thin films. Merging and diverging of selected pores can be observed, and is typical of the random pore generation process for one-step anodization of such thin layers.

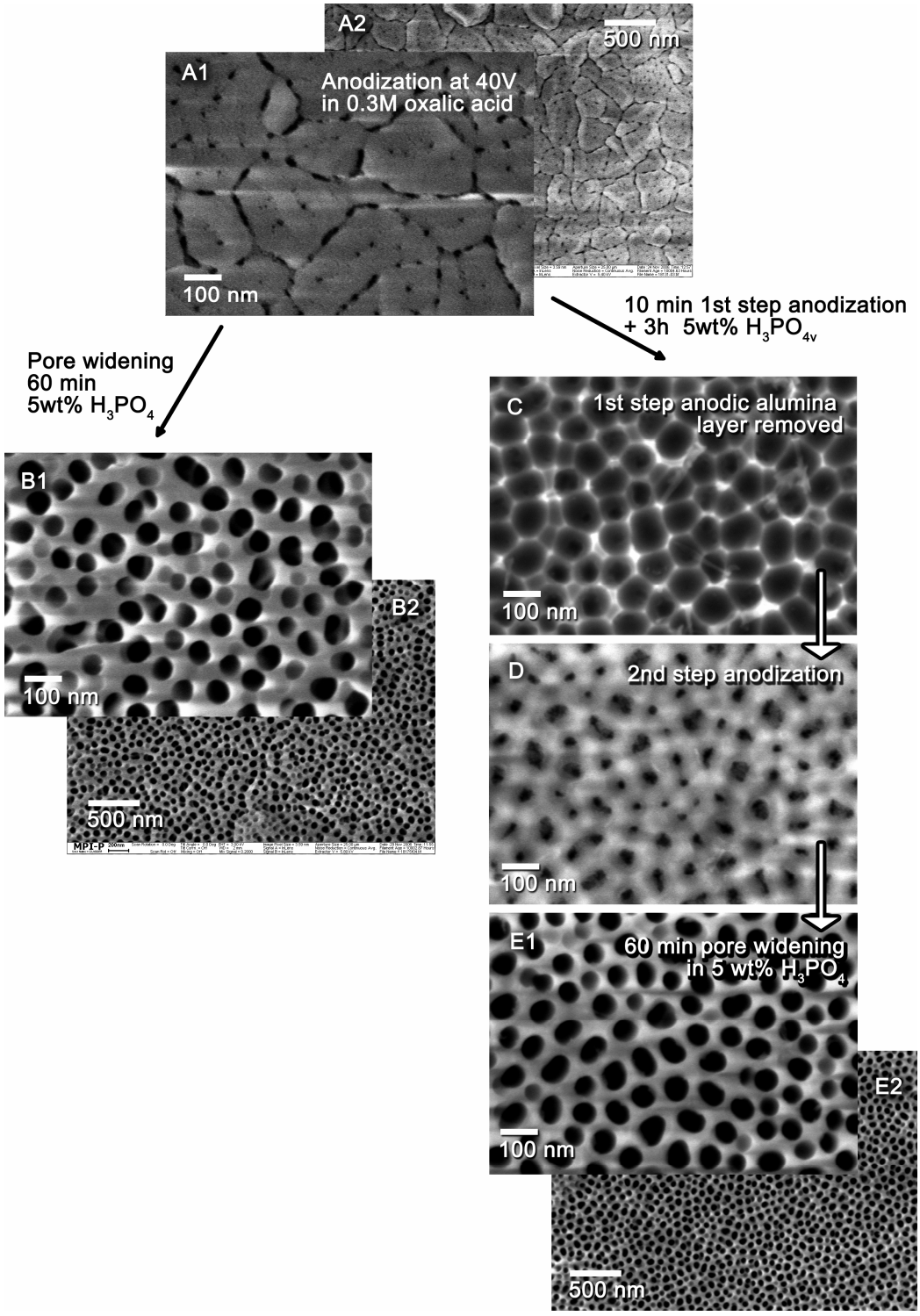

Figure 3.17. SEM top-view images of nanoporous AAO thin films illustrating the process flow of sample preparation. (A) shows the AAO surface morphology after anodization of a 1 μm thick sputtered Al thin film. The grain boundary locations of the original pre-anodized Al thin can be discerned from the network of concentrated pore openings. As shown by the pore widened sample in (B), this preferential pore nucleation along grain boundaries distorts the intrinsic periodicity of the pore arrangement, and leads to numerous pre-mature termination of pores near the surface, and multiple pores originating from a single pore opening. To mitigate the problem, the anodization was split into two steps, as shown in the right column: etching away of the initial distorted layer AAO obtained within the first 10 min of anodization (C), followed by a second anodization on the textured Al surface produces samples (D) improved one-to-one correspondence between pores and their openings, as can be clearly seen after pore widening (E).

The AAO pores can be visualised more clearly after 50 min pore widening (isotropic etching) in 5 wt% H_3PO_4 (Figure 3.16). The general parallel pore arrangement is clearly seen, although some merging and splitting of selected pores can also be observed. Moreover, some pore fronts extend slightly deeper than others, and is suggestive of the initial random pore nucleation process. However, overall, the pores run straight through the film thickness and the pore diameter is quite uniform through the film thickness (Figure 3.16b). Note that the Al metal layer is also present for the sample shown in Figure 3.16, as indicated by the bright charging band near the substrate in Figure 3.16a.

Images of the AAO surface morphology immediately after one-step anodization, corresponding to Figure 3.15, is shown in Figure 3.17a. Although the pore nucleation process is, as expected, non-uniform, there is a strong segregation of the pore openings along surface networks delineating domains 200~300 nm wide. This network corresponds to the grain boundaries present in the original sputtered Al film. As a consequence, the $\lambda_{C\text{-}C}$ is distorted from the native value set by the anodization parameters (Table 3.2), especially along the grain boundaries. Thus multiple pores are seen to lead from the same (enlarged) pore opening. This is seen even more clearly from Figure 3.17b. Moreover, many pores not located along the boundaries did not develop into deep pores and were terminated close to the surface (see discussion relating to Figure 3.12).

This grain boundary induced pore opening segregation is, however, expected to be localised within a thin layer near the film surface, as the cross section images (Figure 3.15 and Figure 3.16) do not show such a pronounced effect. Therefore the optical description of the AAO layer for wavelengths much larger than the pore size (visible wavelengths or longer) is not expected to be unduly affected (see Chapter 5).

A two-step anodization strategy may be used to improve the uniformity of the pore openings. A thin 200~300 nm sacrificial AAO layer was first anodized per the optimised oxalic acid procedure (Table 3.2). This AAO layer was then etched away by 3h's immersion in 5 wt% H_3PO_4 to leave behind a textured Al surface that can direct the pore nucleation process (Figure 3.17c). The remaining 800 nm Al film was then anodized using the same oxalic acid procedure (Figure 3.17d), and then pore widened in 5 wt% H_3PO_4. Figure 3.17e shows that the resulting surface exhibited a higher density of pores that more closely resembled a distribution with local quasi-hexagonal packing. However the AAO film thickness was reduced from ~1 μm to ~800 nm, which resulted in a ~20% decrease in pore surface area.

The pore dimensions measured from the SEM top view images of the 1-step and 2-step anodized Al thin film samples are compared in Table 3.3. The pore diameters obtained from Al thin films anodized by both processes were approximately the same at ~60 nm. However, it is seen that the $\lambda_{C\text{-}C}$ is significantly larger for the 1-step anodized film than for the 2-step process. The pore fraction for the 1-step anodized film is correspondingly lower. For example, one can count 64 full pore

openings in Figure 3.17b (1-step process) compared to 90 full pore openings in Figure 3.17e (2-step process). Since the 2-step anodized film surface reflects the cross section of the pore structure *after* the formation of the first 200~300 nm thick layer of AAO, each initial pore opening in Figure 3.17b actually leads to ~1.5 pores on average after the first 200~300 nm anodization. Although quasi-close packing of the pores is already observed in the 2-step anodized surface (Figure 3.17e), the evolution in pore arrangement is expected to continue throughout the rest of the AAO thin film, albeit to a much less dramatic degree. Thus the SEM top views of the thin film AAO may not give definitive pore dimensions representative of the whole AAO film, and the cylindrical pore model is only approximate for the 1-step anodized AAO thin film, although it describes the 2-step anodized films better.

Preparation	**Corresponding SEM image**	**Mean pore diameter (nm ± 1SD in %)**	**Mean $\lambda_{C\text{-}C}$ (nm)**	**Top surface pore fraction**
Thin film 1-step anodization (60 min 5 wt% pore widening)	Figure 3.17b	62 ± 13%	116	0.26
Thin film 2-step anodization (60 min 5 wt% pore widening)	Figure 3.17e	57 ± 15%	98	0.33

Table 3.3. Pore dimensions corresponding to Figure 3.17b and e. The pore diameters, and area and number densities were measured by computer image analysis (Appendix A). $\lambda_{C\text{-}C}$ was then calculated from these parameters assuming a hexagonal pore lattice.

Figure 3.15 to Figure 3.17 show the AAO thin film morphology for the majority of the surface area. AFM characterization shows a root-mean-squared top surface roughness of <20 nm and a maximum height variation of <150 nm (Figure 3.18a). These values are exaggerated due to height convolution with the pores. This roughness is a result of the polycrystalline grain structure of the original sputtered Al films (Figure 3.18b), as mentioned previously. Apart from this average roughness, the AAO film surfaces were also punctuated by ~200 nm tall granular features (i.e. hillocks, Figure 3.19) that also originated from the grain structure of the sputtered Al film. Hillocks are a common feature of sputtered Al films [69, 71, 78, 79]. They arise due to the compressive stress generated in the film during the sputtering process, and are difficult to eliminate in the thick, pure Al films needed for AAO preparation [70, 80, 81]. The pore structure around these hillocks are more disordered, but they cover only 2~3% of the surface area (Figure 3.19b), thus they are not expected to have a significant influence on the overall extent of surface processes occurring in the AAO

pore structure. However, they may be significant scattering centres for light propagating within the AAO thin film (Chapter 5).

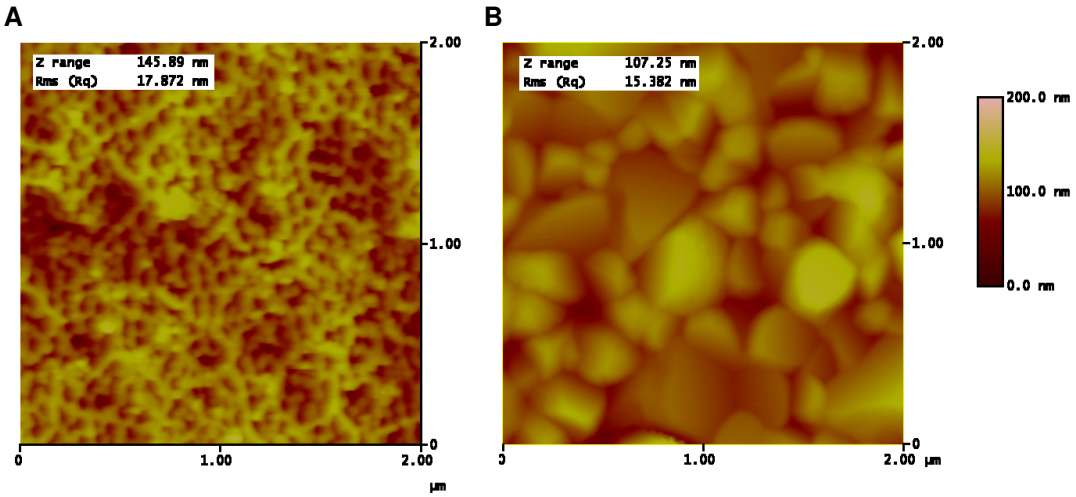

Figure 3.18. AFM height images and roughness analysis of the 2-step anodized thin film AAO surface corresponding to Figure 3.17e (A), and the initial sputtered polycrystalline Al thin film surface (B). For the AAO surface in (A), the pore sizes measured differ from those in Figure 3.17e due to AFM tip convolution effects. The measured roughness (Rq) and the maximum surface height variation (Z range) were also exaggerated due to the depth of the pores.

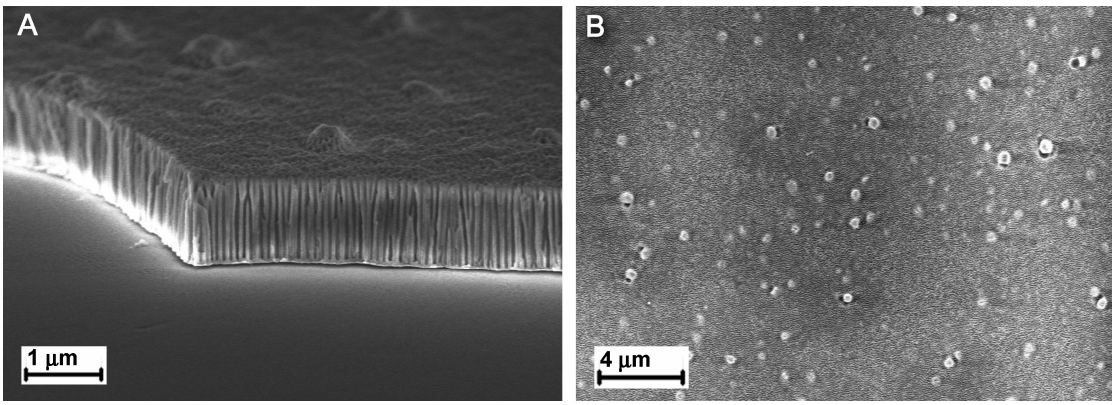

Figure 3.19. Low magnification SEM images showing the distribution of isolated granular structures ~200 nm tall due to hillock formation in the initial sputtered Al thin film. As shown in (B), these cover 2~3 % of the surface area.

3.3. References

[1] Bates FS, Fredrickson GH: Block Copolymer Thermodynamics: Theory and Experiment. *Annual Review of Physical Chemistry* **1990**, *41*, 525.

[2] Fredrickson GH, Bates FS: Dynamics of Block Copolymers: Theory and Experiment. *Annual Review of Materials Science* **1996**, *26*, 501.

[3] Fasolka MJ, Mayes AM: Block Copolymer Thin Films: Physics and Applications. *Annual Review of Materials Research* **2001**, *31*, 323.

[4] Green PF, Limary R: Block Copolymer Thin Films: Pattern Formation and Phase Behavior. *Advances in Colloid and Interface Science* **2001**, *94*, 53.

[5] Matsen MW: The Standard Gaussian Model for Block Copolymer Melts. *Journal of Physics: Condensed Matter* **2002**, R21.
[6] Lazzari M, López-Quintela MA: Block Copolymers as a Tool for Nanomaterial Fabrication. *Advanced Materials* **2003**, *15*, 1583.
[7] Lipic PM, Bates FS, Matsen MW: Non-Equilibrium Phase Behavior of Diblock Copolymer Melts and Binary Blends in the Intermediate Segregation Regime. *Journal of Polymer Science Part B: Polymer Physics* **1999**, *37*, 2229.
[8] Xu T, Kim H-C, DeRouchey J, Seney C, Levesque C, Martin P, Stafford CM, Russell TP: The Influence of Molecular Weight on Nanoporous Polymer Films. *Polymer* **2001**, *42*, 9091.
[9] Guarini KW, Black CT, Yeung SHI: Optimization of Diblock Copolymer Thin Film Self Assembly. *Advanced Materials* **2002**, *14*, 1290.
[10] Jeong U, Kim HC, Rodriguez RL, Tsai IY, Stafford CM, Kim JK, Hawker CJ, Russell TP: Asymmetric Block Copolymers with Homopolymers: Routes to Multiple Length Scale Nanostructures. *Advanced Materials* **2002**, *14*, 274.
[11] Jeong U, Ryu DY, Kho DH, Kim JK, Goldbach JT, Kim DH, Russell TP: Enhancement in the Orientation of the Microdomain in Block Copolymer Thin Films Upon the Addition of Homopolymer. *Advanced Materials* **2004**, *16*, 533.
[12] Simon PFW, Ulrich R, Spiess HW, Wiesner U: Block Copolymer-Ceramic Hybrid Materials from Organically Modified Ceramic Precursors. *Chemistry of Materials* **2001**, *13*, 3464.
[13] Morkved TL, Jaeger HM: Thickness-Induced Morphology Changes in Lamellar Diblock Copolymer Ultrathin Films. *Europhysics Letters* **1997**, 643.
[14] Huinink HP, Brokken-Zijp JCM, van Dijk MA, Sevink GJA: Asymmetric Block Copolymers Confined in a Thin Film. *Journal of Chemical Physics* **2000**, *112*, 2452.
[15] Suh KY, Kim YS, Lee HH: Parallel and Vertical Morphologies in Block Copolymers of Cylindrical Domain. *Journal of Chemical Physics* **1998**, *108*, 1253.
[16] Feng C-L, Zhong XH, Steinhart M, Caminade AM, Majoral J-P, Knoll W: Graded-Bandgap Quantum- Dot-Modified Nanotubes: A Sensitive Biosensor for Enhanced Detection of DNA Hybridization. *Advanced Materials* **2007**, *19*, 1933.
[17] Matsen MW: Thin Films of Block Copolymer. *Journal of Chemical Physics* **1997**, *106*, 7781.
[18] Pickett GT, Balazs AC: Equilibrium Orientation of Confined Diblock Copolymer Films. *Macromolecules* **1997**, *30*, 3097.
[19] Tsarkova L, Knoll A, Krausch G, Magerle R: Substrate-Induced Phase Transitions in Thin Films of Cylinder-Forming Diblock Copolymer Melts. *Macromolecules* **2006**, *39*, 3608.
[20] Kim SH, Misner MJ, Xu T, Kimura M, Russell TP: Highly Oriented and Ordered Arrays from Block Copolymers Via Solvent Evaporation. *Advanced Materials* **2004**, *16*, 226.
[21] Peng J, Gao X, Wei Y, Wang H, Li B, Han Y: Controlling the Size of Nanostructures in Thin Films Via Blending of Block Copolymers and Homopolymers. *Journal of Chemical Physics* **2005**, *122*, 114706.
[22] Morkved TL, Lu M, Urbas AM, Ehrichs EE, Jaeger HM, Mansky P, Russell TP: Local Control of Microdomain Orientation in Diblock Copolymer Thin Films with Electric Fields. *Science* **1996**, *273*, 931.
[23] Thurn-Albrecht T, DeRouchey J, Russell TP, Jaeger HM: Overcoming Interfacial Interactions with Electric Fields. *Macromolecules* **2000**, *33*, 3250.
[24] Thurn-Albrecht T, DeRouchey J, Russell TP, Kolb R: Pathways toward Electric Field Induced Alignment of Block Copolymers. *Macromolecules* **2002**, *35*, 8106.
[25] Genzer J, Kramer EJ: Wetting of Substrates with Phase-Separated Binary Polymer Mixtures. *Physical Review Letters* **1997**, *78*, 4946.
[26] Peters RD, Yang XM, Kim TK, Nealey PF: Wetting Behavior of Block Copolymers on Self-Assembled Films of Alkylchlorosiloxanes: Effect of Grafting Density. *Langmuir* **2000**, *16*, 9620.
[27] Sohn BH, Yun SH: Perpendicular Lamellae Induced at the Interface of Neutral Self-Assembled Monolayers in Thin Diblock Copolymer Films. *Polymer* **2002**, *43*, 2507.
[28] Bandyopadhyay K, Tan E, Ho L, Bundick S, Baker SM, Niemz A: Deposition of DNA-Functionalized Gold Nanospheres into Nanoporous Surfaces. *Langmuir* **2006**, *22*, 4978.
[29] Mansky P, Liu Y, Huang E, Russell TP, Hawker C: Controlling Polymer-Surface Interactions with Random Copolymer Brushes. *Science* **1997**, *275*, 1458.
[30] Ryu DY, Shin K, Drockenmuller E, Hawker CJ, Russell TP: A Generalized Approach to the Modification of Solid Surfaces. *Science* **2005**, *308*, 236.
[31] Kim DH, Lau KHA, Robertson JWF, Lee OJ, Jeong U, Lee JI, Hawker CJ, Russell TP, Kim JK, Knoll W: Thin Films of Block Copolymers as Planar Optical Waveguides. *Advanced Materials* **2005**, *17*, 2442.
[32] Kim DH, Lau KHA, Joo W, Peng J, Jeong U, Hawker CJ, Kim JK, Russell TP, Knoll W: An Optical Waveguide Study on the Nanopore Formation in Block Copolymer/Homopolymer Thin Films by Selective Solvent Swelling. *Journal of Physical Chemistry B* **2006**, *110*, 15381.
[33] Jeong U, Ryu DY, Kho DH, Lee DH, Kim JK, Russell TP: Phase Behavior of Mixtures of Block Copolymer and Homopolymers in Thin Films and Bulk. *Macromolecules* **2003**, *36*, 3626.

[34] Jeong U, Ryu DY, Kim JK, Kim DH, Wu X, Russell TP: Precise Control of Nanopore Size in Thin Film Using Mixtures of Asymmetric Block Copolymer and Homopolymer. *Macromolecules* **2003**, *36*, 10126.

[35] Mayes AM, Russell TP, Satija SK, Majkrzak CF: Homopolymer Distributions in Ordered Block Copolymers. *Macromolecules* **1992**, *25*, 6523.

[36] Xu T, Goldbach JT, Misner MJ, Kim S, Gibaud A, Gang O, Ocko B, Guarini KW, Black CT, Hawker CJ, Russell TP: Scattering Study on the Selective Solvent Swelling Induced Surface Reconstruction. *Macromolecules* **2004**, *37*, 2972.

[37] Wu S: *Surface and Interfacial Tension of Polymers, Oligomers, Plasticizers, and Organic Pigments*. In *Polymer Handbook*, J. Brandrup; E.H. Immergut; E.A. Grulke; A. Abe; D.R. Bloch, eds.; Wiley: New York, 1999, pp. VI/521.

[38] Kim H-C, Russell TP: Ordering in Thin Films of Asymmetric Diblock Copolymers. *Journal of Polymer Science Part B: Polymer Physics* **2001**, *39*, 663.

[39] Schrader D: *Physical Constants of Poly(Styrene)*. In *Polymer Handbook*, J. Brandrup; E.H. Immergut; E.A. Grulke; A. Abe; D.R. Bloch, eds.; Wiley: New York, 1999, pp. V/91.

[40] Wunderlich W: *Physical Constants of Poly(Methyl Metahcrylate)*. In *Polymer Handbook*, J. Brandrup; E.H. Immergut; E.A. Grulke; A. Abe; D.R. Bloch, eds.; Wiley: New York, 1999, pp. V/87.

[41] Magonov SN, Reneker DH: Characterization of Polymer Surfaces with Atomic Force Microscopy. *Annual Review of Materials Science* **1997**, *27*, 175.

[42] McLean RS, Sauer BB: Tapping-Mode Afm Studies Using Phase Detection for Resolution of Nanophases in Segmented Polyurethanes and Other Block Copolymers. *Macromolecules* **1997**, *30*, 8314.

[43] Wang Y, Song R, Lib Y, Shen J: Understanding Tapping-Mode Atomic Force Microscopy Data on the Surface of Soft Block Copolymers. *Surface Science* **2003**, *530*, 136.

[44] Wang H, Djurišić AB, Chan WK, Xie MH: Factors Affecting Phase and Height Contrast of Diblock Copolymer Ps–B-Peo Thin Films in Dynamic Force Mode Atomic Force Microscopy *Applied Surface Science* **2005**, *252*, 1092.

[45] Feng CL, Vancso GJ, Schonherr H: Interfacial Reactions in Confinement: Kinetics and Temperature Dependence of the Surface Hydrolysis of Polystyrene-Block-Poly(Tert-Butyl Acrylate) Thin Films. *Langmuir* **2005**, *21*, 2356.

[46] Sadaie M, Nishikawa N, Kumashiro Y, Ikezawa Y, Kumagai Y, Makino K, Ohnishi S, Tamada K, Hara M: Quantitative Friction Map on Surface Composed of B-Cyclodextrin Monolayer. *Japanese Journal of Applied Physics* **2007**, *46*, 7838.

[47] van Dijk MA, van den Berg R: Ordering Phenomena in Thin Block Copolymer Films Studied Using Atomic Force Microscopy. *Macromolecules* **1995**, *28*, 6773.

[48] Sun Z, Kim DH, Wolkenhauer M, Bumbu GG, Knoll W, Gutmann JS: Synthesis and Photoluminescence of Titania Nanoparticle Arrays Templated by Block-Copolymer Thin Films. *Chemphyschem* **2006**, *7*, 370.

[49] Hillmyer M: *Nanoporous Materials from Block Copolymer Precursors*. In *Block Copolymers Ii*; Springer: Berlin / Heidelberg, 2005; Vol. *190*, pp. 137.

[50] Diggle JW, Downie TC, Goulding CW: Anodic Oxide Films on Aluminum. *Chemical Reviews* **1969**, *69*, 365.

[51] O'Sullivan JP, Wood GC: The Morphology and Mechanism of Formation of Porous Anodic Films on Aluminium. *Proceedings of the Royal Society of London. Series A, Mathematical and Physical Sciences (1934-1990)* **1970**, *317*, 511.

[52] Jessensky O, Muller F, Gosele U: Self-Organized Formation of Hexagonal Pore Arrays in Anodic Alumina. *Applied Physics Letters* **1998**, *72*, 1173.

[53] Li F, Zhang L, Metzger RM: On the Growth of Highly Ordered Pores in Anodized Aluminum Oxide. *Chemistry of Materials* **1998**, *10*, 2470.

[54] Li AP, Muller F, Birner A, Nielsch K, Gosele U: Hexagonal Pore Arrays with a 50-420 Nm Interpore Distance Formed by Self-Organization in Anodic Alumina. *Journal of Applied Physics* **1998**, *84*, 6023.

[55] Nielsch K, Choi J, Schwirn K, Wehrspohn RB, Gosele U: Self-Ordering Regimes of Porous Alumina: The 10 Porosity Rule. *Nano Letters* **2002**, *2*, 677.

[56] Chu S-Z, Wada K, Inoue S, Isogai M, Yasumori A: Fabrication of Ideally Ordered Nanoporous Alumina Films and Integrated Alumina Nanotubule Arrays by High-Field Anodization. *Advanced Materials* **2005**, *17*, 2115.

[57] Martin CR: Nanomaterials: A Membrane-Based Synthetic Approach. *Science* **1994**, *266*, 1961.

[58] Li AP, Muller F, Gosele U: Polycrystalline and Monocrystalline Pore Arrays with Large Interpore Distance in Anodic Alumina. *Electrochemical and Solid-State Letters* **2000**, *3*, 131.

[59] Sander MS, Tan LS: Nanoparticle Arrays on Surfaces Fabricated Using Anodic Alumina Films as Templates. *Advanced Functional Materials* **2003**, *13*, 393.

[60] Lau KHA, Tan LS, Tamada K, Sander MS, Knoll W: Highly Sensitive Detection of Processes Occurring inside Nanoporous Anodic Alumina Templates: A Waveguide Optical Study. *Journal of Physical Chemistry B* **2004**, *108*, 10812.

[61] Masuda H, Yamada H, Satoh M, Asoh H, Nakao M, Tamamura T: Highly Ordered Nanochannel-Array Architecture in Anodic Alumina. *Applied Physics Letters* **1997**, *71*, 2770.

[62] Kriha O, Zhao L, Pippel E, Gösele U, Wehrspohn RB, Wendorff JH, Steinhart M, Greiner A: Organic Tube/Rod Hybrid Nanofibers with Adjustable Segment Lengths by Bidirectional

Template Wetting. *Advanced Functional Materials* **2007**, *17*, 1327.
[63] Ono S, Saito M, Ishiguro M, Asoh H: Controlling Factor of Self-Ordering of Anodic Porous Alumina. *Journal of The Electrochemical Society* **2004**, *151*, B473.
[64] Lee W, Ji R, Gosele U, Nielsch K: Fast Fabrication of Long-Range Ordered Porous Alumina Membranes by Hard Anodization. *Nature Materials* **2006**, *5*, 741.
[65] Asoh H, Nishio K, Nakao M, Tamamura T, Masuda H: Conditions for Fabrication of Ideally Ordered Anodic Porous Alumina Using Pretextured Al. *Journal of The Electrochemical Society* **2001**, *148*, B152.
[66] Mikulskas I, Juodkazis S, Tomasiunas R, Dumas JG: Aluminum Oxide Photonic Crystals Grown by a New Hybrid Method. *Advanced Materials* **2001**, *13*, 1574.
[67] Liu NW, Datta A, Liu CY, Wang YL: High-Speed Focused-Ion-Beam Patterning for Guiding the Growth of Anodic Alumina Nanochannel Arrays. *Applied Physics Letters* **2003**, *82*, 1281.
[68] Dieter GE: *Stress and Strain Relationships for Elastic Behavior*. In *Mechanical Metallurgy*; MacGraw-Hill: Boston, 1986, pp. 53.
[69] Smith U, Kristensen N, Ericson F, Schweitz J-A: Local Stress Relaxation Phenomena in Thin Aluminum Films. *Journal of Vacuum Science & Technology A: Vacuum, Surfaces, and Films* **1991**, *9*, 2527.
[70] Voutsas AT, Hibino Y, Pethe R, Demaray E: Structure Engineering for Hillock-Free Pure Aluminum Sputter Deposition for Gate and Source Line Fabrication in Active-Matrix Liquid Crystal Displays. *Journal of Vacuum Science & Technology A: Vacuum, Surfaces, and Films* **1998**, *16*, 2668.
[71] Lita AE, Sanchez JJE: Characterization of Surface Structure in Sputtered Al Films: Correlation to Microstructure Evolution. *Journal of Applied Physics* **1999**, *85*, 876.
[72] Rabin O, Herz PR, Lin YM, Akinwande AI, Cronin SB, Dresselhaus MS: Formation of Thick Porous Anodic Alumina Films and Nanowire Arrays on Silicon Wafers and Glass. *Advanced Functional Materials* **2003**, *13*, 631.
[73] Thompson GE, Wood GC: Porous Anodic Film Formation on Aluminium. *Nature* **1981**, *290*, 230.
[74] Ono S, Masuko N: The Duplex Structure of Cell Walls of Porous Anodic Films Formed on Aluminum. *Corrosion Science* **1992**, *33*, 503.
[75] Mardilovich PP, Govyadinov AN, Mukhurov NI, Rzhevskii AM, Paterson R: New and Modified Anodic Alumina Membranes Part I. Thermotreatment of Anodic Alumina Membranes. *Journal of Membrane Science* **1995**, *98*, 131.
[76] Thompson GE, Xu Y, P. S, K. S, S.H. H, Wood GC: Anodic Oxidation of Aluminium. *Philosophical Magazine B* **1987**, *55*, 651.
[77] Born M, Wolf E: *Optics of Metals*. In *Principles of Optics*; Cambridge University Press, 1999, pp. 735.
[78] Chaudhari P: Hillock Growth in Thin Films. *Journal of Applied Physics* **1974**, *45*, 4339.
[79] Thornton JA: The Microstructure of Sputter-Deposited Coatings. *Journal of Vacuum Science & Technology A: Vacuum, Surfaces, and Films* **1986**, *4*, 3059.
[80] Verkerk MJ, van der Kolk GJ: Effects of Oxygen on the Growth of Vapor-Deposited Aluminium Films. *Journal of Vacuum Science & Technology A: Vacuum, Surfaces, and Films* **1986**, *4*, 3101.
[81] Onishi T, Iwamura E, Takagi K: Morphology of Sputter Deposited Al Alloy Films. *Thin Solid Films* **1999**, *340*, 306.

4. Protein adsorption on PS-b-PMMA nanopatterns

4.1. Protein interactions with PS/PMMA surface interfaces

4.1.1. Surface interfaces, adsorption and bio-surface studies

The ability to define surface structures on the nanoscale has the potential to significantly advance the fields of biosensing, biomaterials and cell-surface studies. Nanoarrays of biomolecular elements are important for high-throughput biosensing [1-3]. Cell-surface studies with nanopatterns of biochemical or topographic cues may offer mechanistic insights to biochemical pathways that regulate cell-surface interactions [2, 4-6], and provide knowledge for designing biomaterials that mimic the biological system [7, 8]. The introduction of nanoscale features brings with it a high density of surface interface boundaries, and effectively introduces an additional interface material that may exhibit properties different from the surrounding surfaces. Investigation of protein interactions with these interfaces may inform the design of protein-based biosensors and, since adsorbed proteins mediate the interaction of cells with a surface [4, 9, 10], complement our understanding of cell-surface interactions.

Experimental investigation of protein-surface interactions usually proceeds by immersing a surface into a protein solution and measuring the amount of protein adsorbed over time. The phenomenon may be characterised by a dynamic sequence of processes [11-14]: transport to the surface, initial binding, followed by relaxation and conformation changes (denaturation). Various parameters can significantly influence the amount of protein adsorbed [11-13, 15], including pH, protein solution concentration, temperature, and importantly, the nature of the protein and the material properties of the surface. In general, the strength of the protein-surface interaction is higher for larger proteins, because the higher number of amino acid residues provide more “attachment points” for surface interactions [16, 17]. Study of the adsorption (and desorption) kinetics may provide information on the adsorption process, and on the change in protein conformation on the surface (e.g. spreading and re-orientation) [11, 18-21], but contributions from different effects may be difficult to distinguish. The nature of the protein-surface interaction may be electrostatic, such as on oxide surfaces, or be mediated by hydrophobic interactions on uncharged surfaces [12, 13, 16, 17, 22, 23]. The depletion of the hydration layer from the surface can also be a significant driving force for protein adsorption on hydrophobic surfaces [17].

Therefore for an uncharged surface, the amount of protein adsorbed is generally higher on more hydrophobic surfaces [16, 17, 22]. Higher degrees of conformation rearrangement may also accompany adsorption on such surfaces [12, 17, 19, 23].

Protein adsorption studies, such as those discussed above, have concentrated on homogeneous solid surfaces. On the other hand, the nanoscale arrangement of biochemical or topographic cues is characteristic of biological processes [2, 4-6], and new advances in biomaterials may be expected to come from the successful tailoring of surfaces on the nanoscale [7, 8]. Protein adsorption studies on micropatterns [24-26] and on nano-textured materials have been reported [7, 8], but only a small number of studies have been carried out on well-defined nanopatterns [27, 28]. Also, the latter have been focused on the fabrication of protein micro/nanopatterns for sensing purposes (see section 4.2).

Within the context of investigating the nanoscale influence of surface features on protein adsorption, BCP's provide a convenient material system to systematically vary the size of the nanopattern over the entire nanoscale range of 10~100 nm [29-33], down to the length-scale of individual proteins [34, 35]. Therefore nanopatterned BCP surfaces may be a valuable, and conveniently accessible, platform for exploring the length-scale dependent properties of protein/cell-surface interactions. The PS-b-PMMA copolymer nanopatterned surfaces prepared in section 3.1 have been designed with such a purpose in mind, and nanodomain dimensions and density of surface interfaces have been systematically varied by more than an order of magnitude. Significantly, the nanopattern with the highest interface density (84 $\mu m/\mu m^2$) exhibited surface features with dimensions (13 nm) corresponding to individual proteins. To these tailored 2-dimensional nanopatterned surfaces, the adsorption of immunoglobulin-G (IgG) was investigated and compared to the adsorption on PS and PMMA surfaces lacking interfaces. The nanopatterns were characterised with atomic force microscopy (AFM), and related protein adsorption monitored in situ by surface plasmon resonance spectroscopy (SPR). IgG was chosen because their binding capacity for antigens after they have been adsorbed on the surface is suggestive of the amount of denaturation induced during the adsorption process. Unlike previous studies that employed an extreme contrast in hydrophobicity to generate a biomolecular response, such as a preferred adsorbed protein orientation on alkyl/poly(ethylene-oxide) nanopatterns [3, 36], the contrast in hydrophobicity between PS and PMMA is relatively low (both polymers are considered hydrophobic [37, 38], with water contact angles $\theta_{PS} \sim 90^o$ and $\theta_{PMMA} \sim 60^o$) [37, 39]. Thus the present results represent an effort towards highlighting the unique interactions that may arise due simply to the presence of surface interfaces.

4.1.2. Enhanced IgG adsorption along PS-b-PMMA surface interfaces

AFM phase measurements of the nanopatterned PS-*b*-PMMA thin films described in section 3.1 are summarised here as Figure 4.1 for convenient referencing. As mentioned earlier, the domain centre-to-centre spacing ($\lambda_{C\text{-}C}$) was varied over an order of magnitude from 29 nm to ~300 nm, corresponding to characteristic domain widths (w_{PS}) of 13 nm to ~200 nm. The surface area fraction of PS domains (f_{PS}) was ~0.5 for the symmetric PS-b-PMMA showing striped nanopatterns, and ~0.35 for the asymmetric PS-b-PMMA with minor PS cylindrical morphology. As the nanopattern feature density increased, the surface interface density separating the PS and PMMA domains ($l_{interf.}$) also increased from 8 μm/μm^2 to 84 μm/μm^2.

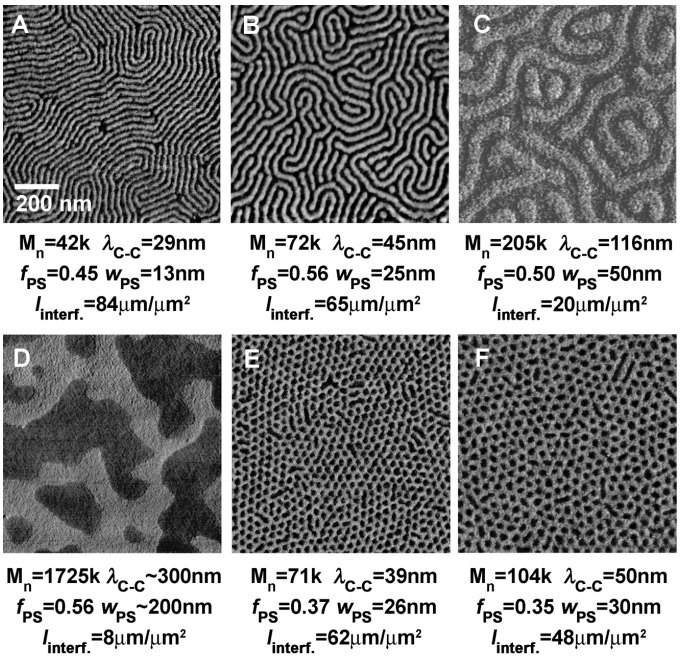

Figure 4.1. AFM phase measurements of PS-b-PMMA nanopatterns. All images show a 1x1 μm^2 scan area and 20º in phase difference. PS and PMMA surfaces are indicated by dark and light shading, respectively (see section 3.1.3). (A)-(D) show striped patterns of increasing $\lambda_{C\text{-}C}$. (E)-(F) show PS dot patterns with local hexagonal ordering. The corresponding M_n, $l_{interf.}$, w_{PS} and f_{PS} are also shown.

In situ SPR results of IgG adsorption on the nanopatterns are shown in Figure 4.4. Adsorption on pure PS and PMMA surface were also performed and compared with the adsorption on the nanopatterns. Adsorption was measured by reflectivity (R) tracking of the SPR minimum (θ_{SPR}, see section 2.3). We take a value of n = 1.53 (corresponding to dried protein layers) and a protein refractive index increment of 0.182 cm^3/g for calculations of the protein layer thickness and the surface mass density of proteins adsorbed [13]. The IgG was dissolved in phosphate buffer saline (PBS) at pH 7.4, and the concentration was fixed at 17 μg/ml. Two kinds of IgG—mouse anti-goat (MxG-IgG, shown in Figure 4.4a) and biotinylated goat anti-rabbit (GxR-IgG, shown in Figure 4.4b)—were used, and both exhibited similar adsorption behaviour.

As expected from adsorption studies on homogeneous surfaces, large increases in the amount of IgG adsorbed are seen in when the protein solutions were first introduced onto the polymer surfaces (Figure 4.4). The adsorption rates then slowed and the adsorbed amounts were seen to approach asymptotic values, with the final amounts adsorbed depending on the nature of the surface (PS/PMMA/nanopattern). It has generally been observed that the amount of IgG adsorbed on PS (Γ_{PS}) is higher than on PMMA (Γ_{PMMA}), indicating the difference in hydrophobicity discussed earlier [37, 40]. Indeed, after 3 h adsorption, Γ_{PS} was 2~3 times higher (1.9 ± 0.2 ng/mm^2) than the amounts adsorbed on pure PMMA surfaces (Γ_{PMMA}): 0.9 ± 0.1 ng/mm^2 for GxR-IgG adsorption; and 0.6 ± 0.1 ng/mm^2 for MxG-IgG adsorption.

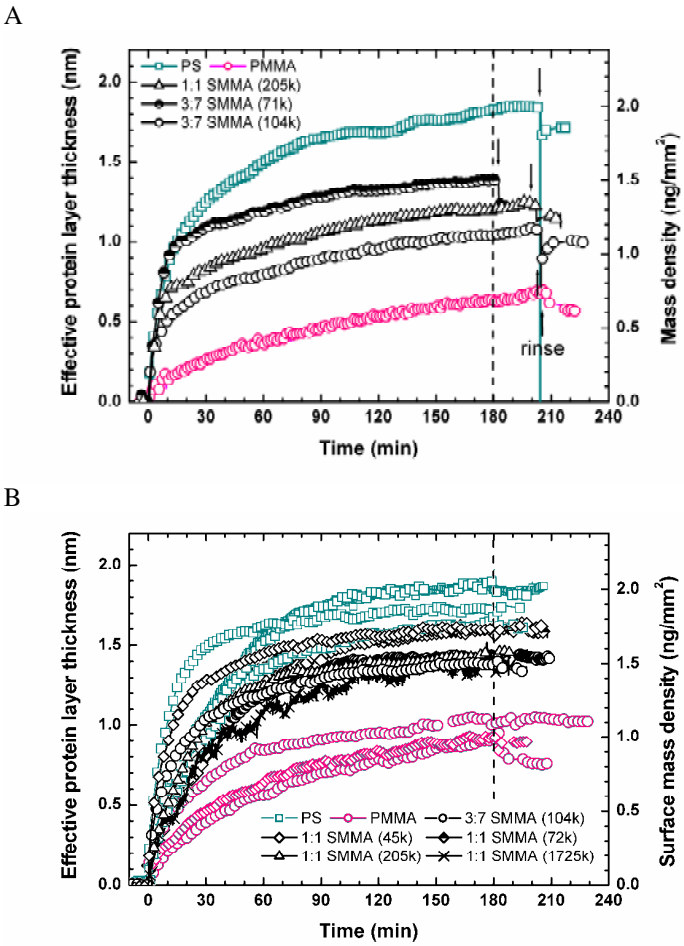

Figure 4.2. IgG adsorption on PS, PMMA, and PS-b-PMMA nanopatterns. (A) shows MxG-IgG adsorption while (B) shows adsorption of biotinylated GxR-IgG. 1:1 SMMA indicates symmetric PS-b-PMMA while 3:7 SMMA indicates the asymmetric PS-b-PMMA with ~30% PS volume fractions. The values in parentheses indicate the M_n of the PS-b-PMMA. The amounts adsorbed at 180 min is indicated by the vertical dashed line.

The amounts adsorbed on the nanopatterns ($\Gamma_{PS\text{-}b\text{-}PMMA}$), which consisted of both PS and PMMA areas, all fell in between Γ_{PS} and Γ_{PMMA}. The experiments were performed in a Teflon liquid cell, and liquid exchange was achieved by injection and extraction of the cell contents with a syringe. A flow system was not used because

proteins can be displaced by the shear stress of flowing liquid [17], and hydrodynamic effects [17, 41, 42] were not considered in this experiment.* Adsorption on all surfaces (except the two symmetric PS-b-PMMA's at 72 and 1725 kg/mol) were repeated to establish the uncertainties of the experiment (approximately ±10%, as indicated by the values of Γ_{PS} and Γ_{PMMA} given above). One also notes that the initial adsorption rates sometimes differed for the same types of surfaces, and likely reflected the influence of diffusion transport to the polymer surface (different measurement positions within the liquid cell). Nonetheless, the final adsorbed amounts were consistent within the bounds of uncertainties measured.

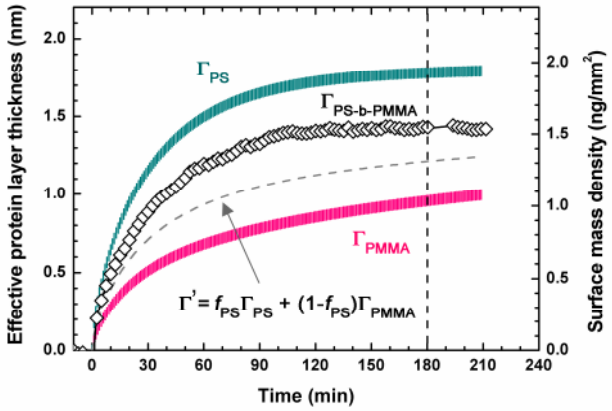

Figure 4.3. GxR-IgG adsorption on PS, PMMA, and the PS-b-PMMA dot nanopattern corresponding to Figure 4.1f. Γ_{PS} and Γ_{PMMA} are the averages of the multiple experiments shown in Figure 4.2b. The dashed line shows the hypothetical amount of IgG adsorbed (Γ') calculated from the f_{PS} weighted-average of Γ_{PS} and Γ_{PMMA}. Short arrows indicate rinsing with PBS.

As mentioned above, the nanopatterned surface consisted of both PS and PMMA domains, and values of $\Gamma_{PS\text{-}b\text{-}PMMA}$ were observed to fall in between Γ_{PS} and Γ_{PMMA}. Indeed, one might expect $\Gamma_{PS\text{-}b\text{-}PMMA}$ to follow the surface fraction weighted average of Γ_{PS} and Γ_{PMMA} (i.e. the linear additive rule: $\Gamma' = f_{PS}\Gamma_{PS} + f_{PMMA}\Gamma_{PMMA}$). As example, Figure 4.3 directly compares the kinetics of a GxR-IgG adsorption measurement on the hexagonally arrayed PS domain nanopattern (Figure 4.1f), with adsorption on pure PS and PMMA surfaces (the averaged trends from all the respective measurements on PS and PMMA surfaces are shown). Moreover, the presumed value (Γ') is also plotted and is shown as the dashed curve. Interestingly, it is seen that $\Gamma_{PS\text{-}b\text{-}MMA}$ was significantly higher than Γ'. Furthermore, this anomaly was observed, to different degrees, for all the nanopatterns for all the IgG tested. Normalizing $\Gamma_{PS\text{-}b\text{-}MMA}$ by Γ' characterises the "excess" amount of protein adsorbed ($\Gamma_{norm.}$), which is plotted against $\lambda_{C\text{-}C}$ in Figure 4.4a. For consistency, $\Gamma_{norm.}$ was calculated for the amount of proteins adsorbed at 180 min before rinsing (i.e. desorption and protein exchange effects were not considered).

* Hydrodynamic effects are exploited in the following section 4.2 to create protein nanopatterns.

In Figure 4.4a, a dramatic enhancement in protein adsorption is seen as the domain size decreases and $\lambda_{C\text{-}C}$ approaches the dimensions of an individual IgG (14.5 x 8.5 x 4 nm) [43, 44]. In contrast, no apparent relationship could be discerned between $\Gamma_{PS\text{-}b\text{-}MMA}$ and f_{PS}, or between $\Gamma_{PS\text{-}b\text{-}MMA}$ and the nanopattern morphology, and those plots are not shown. However, a straightforward interpretation of the enhancement effect with the domain size is suggested by plotting $\Gamma_{norm.}$ against $l_{interf.}$ (Figure 4.4b). It shows that the observed enhancement in protein adsorption is directly related to the length of PS/PMMA surface interface present. Note that the error bars in Figure 4.4b and c span 4 standard deviations (± 2 SD) and serve to illustrate the strength of the enhancement effect.

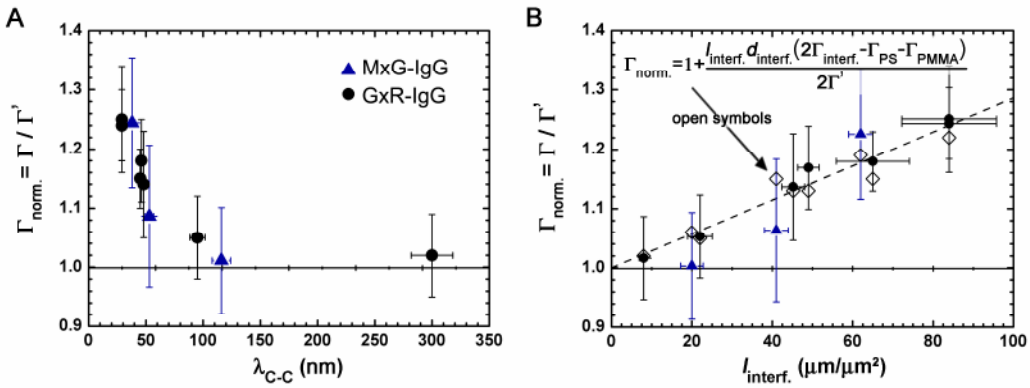

Figure 4.4. (A) and (B) show $\Gamma_{norm.}$ after 180 min adsorption plotted against $\lambda_{C\text{-}C}$ and $l_{interf.}$, respectively. The dashed line in (B) shows the $\Gamma_{norm.}$ predicted from an enhanced adsorption affinity along the PS/PMMA boundary. The fitted $d_{interf.}$ ~ 2 nm and $\Gamma_{interf.}$ ~ 1.67 Γ_{PS}. The error bars show ± 2 standard deviations.

A differentiated affinity for protein adsorption along surface boundaries of nanopatterns may have both surface chemical and geometric origins, if the enhancement effect were indeed correlated with $l_{interf.}$. First, the surface boundaries are not atomically sharp and an IgG adsorbing on the PS/PMMA interface has the possibility to interact with both PS and PMMA surfaces as well as a continuum of surface chemistries between PS and PMMA. This might have allowed residues of a protein to form adsorption attachment points [12, 17, 20, 21, 45] with different regions of the boundary and contribute to, in the case of IgG, a more favourable overall physical interaction. (The opposite effect might apply for different proteins.) Second, the jamming limit to protein adsorption [11] may be higher at the interface between two surfaces with different rates of adsorption. (The jamming limit is the highest density of proteins that can be adsorbed on flat surface by random sequential adsorption.) In the present experiment, the lower adsorbed protein density on PMMA effectively decreased the protein density along the PS side of the PS/PMMA interface, thus increased the number of adsorption sites on the interface large enough to accommodate further adsorption.

To describe the adsorption behaviour on the nanopatterns, $\Gamma_{norm.}$ may be fitted by a two-variable model, where it is assumed, simplistically, that the interface has an effective width ($d_{interf.}$) and a differentiated adsorption affinity ($\Gamma_{interf.}$), which is different from and independent of both Γ_{PS} and Γ_{PMMA}. Then the amount of protein adsorbed, normalized by Γ', can be calculated by summing the amounts adsorbed on respectively the PS, PMMA and interface areas:

Equation 4.1 $$\Gamma_{norm.} = 1 + l_{interf.}d_{interf.}(2\Gamma_{interf.} - \Gamma_{PS} - \Gamma_{PMMA})/(2\Gamma')$$

Fitting of the data shown in Figure 4.4b gave $d_{interf.}$ = 2 nm and $\Gamma_{interf.}$ = $1.67\Gamma_{PS}$. In comparison, adsorption experiments on a random copolymer surface with styrene and methyl methacrylate monomers mixed in a 58:42 ratio showed an IgG adsorption affinity that is only 20% higher than Γ_{PS} (Figure 4.5). (This copolymer was the same as used for balancing PS and PMMA substrate interfacial energies for PS-b-PMMA self-assembly.) On the nanopatterned PS-b-PMMA surfaces, although the fitted $d_{interf.}$ is relatively narrow, the $\Gamma_{interf.}$ enhancement effect resulted in ~25% increase in the amount of IgG adsorbed for the nanopattern with the smallest d_{PS} = 13 nm. At this scale, for the striped morphology, the surface area fraction of the 2 nm wide interfaces = $d_{interf.}/\lambda_{C\text{-}C}$ = 2/29 = 7%. Since $\Gamma_{interf.} > \Gamma_{PS} > \Gamma_{PMMA}$, nanopatterns with even smaller periodicity would be expected to have proportionally higher surface fractions of interfaces. This underscores how surface interfaces can begin to have a significant impact on protein-surface interactions as the feature size of a nanostructure approaches the bio-macromolecular scale.

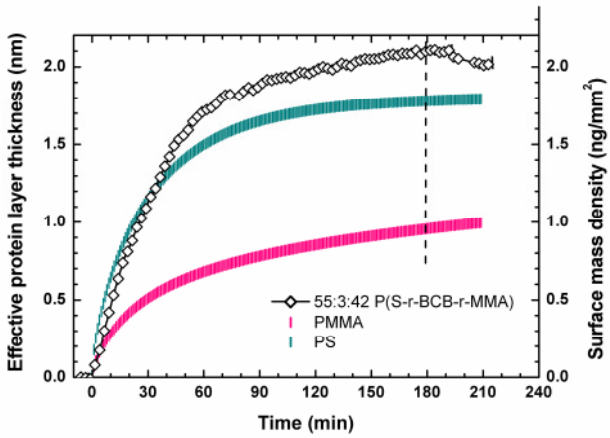

Figure 4.5. Biotinylated GxR-IgG adsorption on the random copolymer P(S-r-BCB-r-MMA) compared with adsorption on PS and PMMA surfaces. Adsorptions on PS and PMMA are the averages of the multiple experiments shown in Figure 4.2b. The amount adsorbed at 180 min is indicated by the vertical dashed line.

Apart from the modification of the total amount of proteins adsorbed, preliminary results on the antigen binding capacity of the adsorbed IgG suggest that the protein activity may also be altered by the density of surface interfaces. Figure 4.6a shows the SPR measurement of specific binding of GxR-IgG to the MxG-IgG

antibody layer adsorbed on the nanopatterned PS-b-PMMA substrates on the smallest dot pattern with w_{PS} = 26 nm (Figure 4.1e). To ensure that only specific binding was measured, bovine serum albumin (BSA) was adsorbed after MxG-IgG adsorption to cover any exposed polymer surfaces not already covered by the initial MxG-IgG layer. BSA is a smaller protein (66 kDa; 8 x 7 x 4 nm) [46, 47] than IgG (150 kDa; 14 x 9 x 4 nm) [43, 48], and adsorbs efficiently to PS and PMMA surfaces [12, 37]. Thus it can adsorb on surfaces not yet covered by the IgG layer. These surfaces might have been exposed by rinsing, or might represent recessed spaces in between neighbouring proteins too small for effective IgG adsorption. After BSA passivation, re-exposure to MxG-IgG did not show significant non-specific adsorption (Figure 4.6a). GxR-IgG was then introduced to the surface, and the amount bound was compared with the initial MxG-IgG layer.

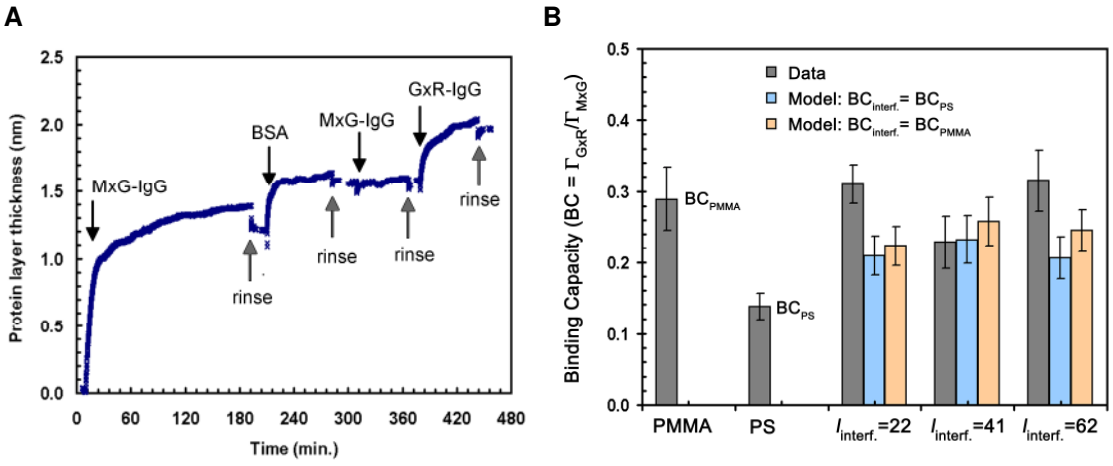

Figure 4.6. (A) shows the SPR measurement of, first, MxG-IgG adsorption on the symmetric PS-b-PMMA corresponding to Figure 4.1e (M_n = 71 kg/mol, and $l_{interf.}$ = 62 μm/μm^2). Then BSA was adsorbed to fill any polymer surfaces not already covered by IgG. MxG-IgG was again introduced to test if any non-specific IgG adsorption could occur on the MxG-IgG/BSA layer: none was observed. Finally, GxR-IgG was introduced and specific binding monitored. (B) compares the antigen binding capacity (the adsorbed amount of GxR-IgG relative to the MxG-IgG layer) of the IgG layers adsorbed on the nanopatterned PS-b-PMMA to the pure PS and PMMA layers.

The ratios between GxR-IgG bound and MxG-IgG adsorbed (i.e. binding capacities—BC) on three different PS-b-PMMA nanopatterns, as well as on PS (BC_{PS}) and PMMA (BC_{PMMA}), are shown in Figure 4.6b. Each IgG has two copies of the antigen binding site [49]. However, since the MxG-IgG were adsorbed on a flat surface, and the antigen—GxR-IgG—is identical in size to MxG-IgG, steric hindrance of neighbouring, bound GxR-IgG would reduce the maximum binding capacity of a *fully covered* MxG-IgG *layer* to ~1. Figure 4.6b shows that BC_{PMMA} (~ 0.3) was much less than the theoretical maximum, and BC_{PS} was even lower (~0.15). These lower capacities may be attributed to improper orientations for binding and protein denaturation [50-52], and the difference between BC_{PMMA} and BC_{PS} may reflect the

influences of both higher levels of denaturation and closer protein packing (hence steric hindrance to binding sites) of the MxG-IgG layer adsorbed on PS surfaces.

Figure 4.6b also shows the predicted binding capacities on the nanopatterned surfaces, based on BC_{PMMA} and BC_{PS}, and on the amounts of MxG-IgG adsorbed on the PS, PMMA and interface regions predicted from the interface model introduced previously (pg. 50). Since the binding capacity on the interface ($BC_{interf.}$) was not known, two cases were considered: $BC_{interf.} = BC_{PS}$ and $BC_{interf.} = BC_{PMMA}$. Interestingly, except for the intermediate nanopattern dimension $l_{interf.} = 41$ μm/μm^2, the binding capacities on the nanopatterned PS-b-PMMA were much higher than would be expected from the surface fractions of PS, PMMA and interface regions. This was true even if the MxG-IgG adsorbed on the interface were assumed to have a binding capacity equal to the higher value of BC_{PMMA}. The limited data set at present does not permit general trends with respect to the dimensions of the nanopatterns to be drawn, but the results suggest that the MxG-IgG adsorbed along the PS-b-PMMA interfaces might have retained a different adsorbed configuration (hence higher binding capacity) than on either the PS or PMMA surfaces.

4.1.3. Summary

We have demonstrated that protein adsorption on topographically flat surfaces nanopatterned with chemical heterogeneity can be modulated by the length density of surface interfaces delineating the nanopattern. We were able to access periodic nanopatterns spanning an order of magnitude in feature size and interface density by PS-b-PMMA self-assembly. Protein adsorption on the nanopatterns could be described by an enhanced adsorption rate along the interface. Moreover, the adsorbed protein configuration on the surface also appeared to be influenced by the nanopatterned surface. Due to the intrinsic high density of surface interfaces on nanopatterns and structures, the interaction of proteins with such interfaces might bear particular relevance to cell-surface studies, and to biomaterial and biosensor applications involving nanoscale features.

4.2. Protein nanoarrays templated by PS-b-PMMA nanopatterns

4.2.1. Introduction to protein nanoarrays and biosensing

Development of protein and peptide arrays on the micro- and nano-scales has been under intense investigation. The success of solid-supported array technology for high throughput nucleic acid analysis [53, 54] has prompted many to envision analogous protein-based arrays for proteome analysis, immunoassays, and

investigations in protein expression and drug screening [50, 55-58]. Multiplexation and miniaturization of protein sensor arrays would dramatically increase the amount of information gathered per volume of sample [2, 43, 50, 59, 60]. This is especially relevant for protein samples since, unlike nucleic acids, they cannot be amplified [57]. Moreover, new phenomena relevant to sensing or protein immobilization may arise [1, 3], and studies concerning the biomolecular interactions between biological structures may be made enabled [4, 60], when the size of array features are on the same length scale as proteins.

Protein microarrays have conventionally been patterned by spotting and inkjet printing [55, 61-64] or by lithography techniques [6, 55, 65]. But these top-down approaches are inadequate at the micron and sub-micron scales. Serial techniques like dip-pen [1, 2, 66-68] and ion- or electron-beam lithographies [3, 36, 69] achieve nanoscale pattern definition but are limited in their ability to define large area patterns [5, 43]. In comparison, self-assembled templates, such as block copolymers (BCP's), can form ordered nanostructures over large areas. Hence BCP's have been gaining momentum as a nanopatterning approach [31, 70-72].

An important issue in patterning protein arrays is to maintain protein activity after surface immobilization [9, 50-52, 63, 69]. In general, covalent immobilization via a suitable linker molecule is used to ensure structural integrity and proper protein orientation [44, 52, 73]. However, the chemistry of covalent immobilization may involve multiple steps and may not be fully efficient, thus effectively limiting the surface protein density and/or protein activity [52, 59]. On the other hand, protein immobilization by physical adsorption leads to varying degrees of denaturation and a random orientation of proteins on the surface, both of which reduce protein activity [50-52]. Nonetheless, this simple technique is still widely employed [44, 64, 74-76], and high densities of proteins may be immobilised [50, 55].

Taking advantage of BCP self-assembly and the simplicity of physical adsorption, we comprehensively explored the preparation and application of physisorbed protein nanoarrays based on BCP templates. There have been recent reports on creating micro- and nano-patterns defined by areas of different protein densities based on the difference in adsorption behaviour on chemically distinct surfaces (preferential adsorption) [24-28]. In this contribution, we show that geometric restrictions derived from preferential adsorption on a nanopattern, and coupled with hydrodynamic effects, provide a framework for creating protein patterns on the nanoscale with high definition. Using this approach, we prepared hexagonally ordered nanoarrays of immunoglobulin (IgG) and bovine serum albumin (BSA) by exclusively adsorbing proteins on the polystyrene (PS) domains of topographically flat polystyrene-block-poly(methyl methacrylate) (PS-b-PMMA) templates. We investigated the pattern formation mechanism with AFM, SPR and through experiments with a set of striped PS-b-PMMA templates with PS line widths ranging from 13 to 200 nm, and verified the nano-nature of the observed exclusive adsorption

behaviour. Our procedure is entirely self-assembly based, and is therefore an approach involving fewer processing steps and equipment than protein nanopatterning based on using BCP as lithography masks [77]. To examine the applicability of our technique, we investigated the antigen binding capacity of an IgG nanoarray and its activity at the level of individual IgG clusters. To illustrate how our technique can function as a platform for patterning other biomolecules and molecular complexes, we also demonstrated DNA sensing based on a streptavidin-PNA (peptide nucleic acid) architecture built on a biotinylated protein nanoarray.

4.2.2. Block Copolymer Template and Protein Nanoarray Formation

The copolymer template used for preparing the protein nanoarray is the PS-b-PMMA with M_n = 104 kg/mol self-assembled into the upright cylindrical morphology with hexagonally arranged 30 nm PS domains with λ_{C-C} = 50 nm surrounded by a PMMA matrix exposed on the film surface corresponding to Figure 3.6c, Both silicon and gold-coated glass substrates were used. This structure is schematically shown in Figure 4.7a. Figure 3.6c is reproduced here as Figure 4.7 b and c for convenient referencing. As described in section 3.1.3, the AFM phase image (Figure 4.7b) reveals PS domains as dark regions surrounded by a light colored PMMA matrix surface. The simultaneously recorded height image (Figure 4.7c) shows a flat topography (R_{rms} = 0.4 nm).

To create protein nanopatterns, the PS-b-PMMA templates were first immersed in protein solution for several minutes to allow for protein adsorption, and then rinsed for ~10 s in an open stream of pure phosphate buffered saline (PBS) or deionised water (Figure 4.7d). Pattern formation was not sensitive to the force or to the length of rinsing in the range of a few seconds to a few minutes. For characterization of the resulting pattern by AFM in air, the protein nanoarrays were rinsed in water and dried under a nitrogen flow. Figure 4.7e shows the height image of the resulting BSA nanoarray prepared from 10 μg/ml IgG in PBS after 4 min. immersion, and Figure 4.7f shows an IgG nanoarray prepared from 14 μg/ml IgG in PBS after 10 min. immersion. Unless otherwise stated, goat anti-rabbit IgG, and PBS at pH 7.4, were used throughout this study. The effects of solution concentration and immersion time on pattern definition are discussed in section 2.3. By comparing the flat topography of the initial PS-b-PMMA template (Figure 4.7c) with the height clusters after protein adsorption (Figure 4.7 e and f), and by recognizing that the array pattern of the initial template (Figure 4.7b) and the height clusters, share the same domain/cluster diameter and repeat period, it is clear that the proteins had adsorbed exclusively on the PS domains and protein nanoarrays had been templated by the BCP hexagonal ordering.

After immersion in the protein solution and rinsing, the wet protein nanoarrays may be used directly to minimise denaturation. We also characterised the nanoarrays

in their "native" state by liquid-AFM. Nonetheless, we show AFM results of patterns imaged in air due to the better resolution achieved, and a comparison with liquid AFM data is given in Appendix B.

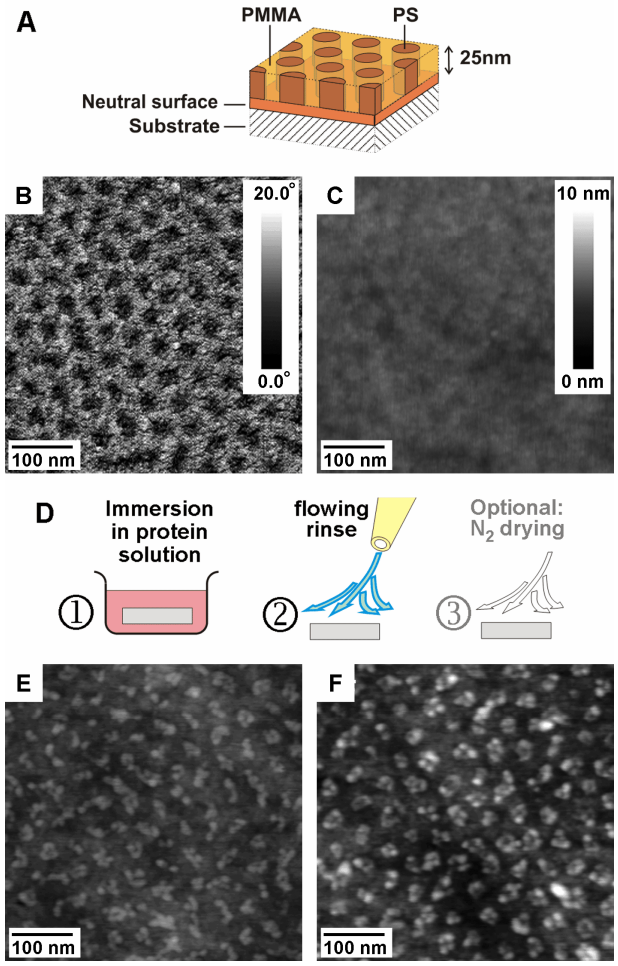

Figure 4.7. (A) Schematic of the ordered, cylindrical PS domain structure of the PS-b-PMMA template used for protein nanopatterning. (B) AFM phase image of the circular top surfaces of the PS domains (dark regions) separated by the PMMA matrix (light areas). (C) AFM height image of the same area. (D) Steps for generating protein nanopatterns: 1) protein adsorption by immersing the template in protein solution; 2) rinsing in an open stream of PBS or water; 3) optional drying under nitrogen flow. (E) and (F): AFM height images of the resulting BSA (E) and IgG (F) nanoarrays. The phase and height scale bars in (B) and (C) apply to all AFM images throughout the article.

In Figure 4.7f, the IgG clusters are 2~5 nm tall and the IgG appeared to have adsorbed with their long axes parallel to the surface. BSA is a smaller protein (66 kDa; 8 x 7 x 4 nm) [46, 47] compared to IgG (150 kDa; 14 x 9 x 4 nm) [43, 48] and the adsorbed BSA clusters were correspondingly shorter in height. However the measured heights should be taken as a lower bound due to mechanical compression by the AFM tip, and as a result of adsorption and exposure to the ambient [50, 52]. Individual

height protrusions within each protein cluster in Fig. 1F are 11~19 nm in diameter, roughly corresponding to the long axis of IgG, and may indicate individual IgG. The variations in measured diameters and heights may indicate a variety of adsorbed orientations, and we estimate that there are 5 or more IgG per nanocluster [78].

4.2.3. Mechanism of Protein Patterning

BSA and IgG are known to adsorb on many polymer surfaces, and the amounts of these proteins adsorbed has been observed to be higher on PS than on PMMA [12, 37, 40]. The amounts of many proteins adsorbed on uncharged surfaces are higher on more hydrophobic surfaces [12, 13, 16, 17, 22, 23], due to dispersion forces [16, 17, 22] and the depletion of the hydration layers from hydrophobic surfaces [17]. The PS surface is more hydrophobic, and exhibits higher water contact angles, than PMMA [37, 39]. We also quantified the amounts of proteins adsorbed on pure PS and PMMA surfaces with SPR measurements. We prepared films of pure PS and PMMA on 45 nm gold coated glass substrates in order to measure IgG adsorption kinetics in situ by SPR. The samples were mounted in a liquid flow cell filled with PBS, and the SPR signal was monitored in situ as the PBS was exchanged with protein solution by the liquid handling system (flow rate = 600 μl/min). SPR monitors the protein layer thickness by measuring the increased optical density on a surface as a result of an adsorbed protein layer [79]. Multilayer adsorption is not possible in the case of BSA or IgG under our conditions [12, 40], and the measured protein layer thickness is an effective value indicating the protein coverage, because both the adsorbed proteins and the spaces between them contribute to the optical signal [13]. Maximum (full) coverage is reached when the kinetics of protein adsorption show no further increase in layer thickness.

As an example, Fig. 2 shows the adsorption kinetics of IgG from an 8.5 μg/ml solution. As the protein solution was introduced, an increase in adsorbed protein layer thickness with time (left axis) was recorded for both the PS and PMMA samples. After 38 min adsorption, the surfaces were rinsed by exchanging the protein solution with pure PBS. More IgG was adsorbed on pure PS than on pure PMMA surfaces, and the adsorbed layer thickness ratio PS to that on PMMA (right axis) was ~2 at all stages of adsorption, testifying the preferential adsorption on PS. This ratio was moderately sensitive to the concentration of IgG, and increased to 3.8 at 17 μg/ml (data not shown). If this preferential adsorption is considered together with the fact that only 30% of the surface was composed of PS (see section I), then, theoretically, roughly equal numbers of IgG should have adsorbed on PS as on PMMA. Furthermore, Figure 4.8shows that after 10 min. adsorption, the effective IgG layer thickness on PS was only half of its final value at 40 min., and indicated a low surface coverage. A similar trend is shown for PMMA. Therefore, many sites on *both* PS and PMMA should still have been unoccupied after the 10 min. adsorption time used for

preparing the IgG nanoarray. However, Fig. 1F shows essentially no IgG adsorbed on the PMMA matrix and roughly complete IgG coverage on PS domains. Thus one may not explain the observation of exclusive nanopatterning of proteins on PS domains based on a single parameter, i.e., the preferential adsorption on PS domains.

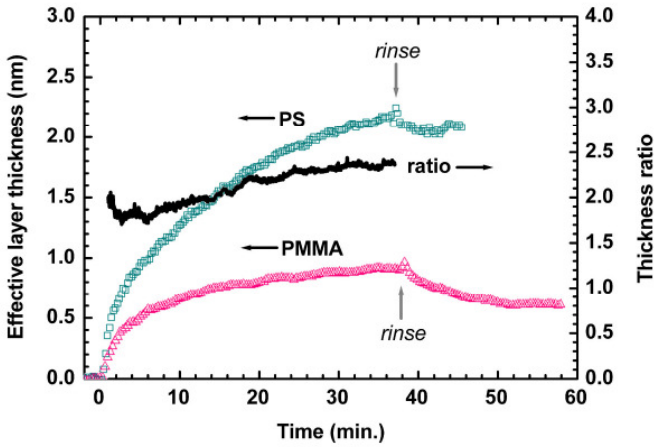

Figure 4.8. Effective IgG layer thickness adsorbed on pure PS (squares) and on pure PMMA (triangles) measured by SPR (left axis). The black line shows the corresponding PS:PMMA layer thickness ratio (right axis). Gray arrows indicate the start of rinsing with pure PBS.

To further explore the patterning mechanism and to test the dimensional limits of our technique, we tested our patterning procedure on the same set of PS-b-PMMA templates already used in the previous section (Figure 4.1) and described in section 3.1.3. In particular, we used PS-b-PMMA with M_n of 42 kg/mol, 204 kg/mol and 1725 kg/mol, and w_{PS} of 13 nm, 55 nm and ~200 nm, and $\lambda_{C\text{-}C}$ of 29 nm, 116 nm and ~300 nm, respectively. The phase images of these nanopatterns are reproduced here as Figure 4.9 a, c, and e for reference. Moreover, to illustrate the potential for adding functional groups to the protein nanopatterns, we show in Figure 4.9 the adsorption behaviour of biotinylated IgG. Unfunctionalised IgG showed analogous results.

AFM height measurements of the protein patterns prepared from 8.5 µg/ml IgG solutions are shown in Figure 4.9 b, d, and f. The respective PS-b-PMMA nanopatterns are revealed through the height protrusions of the adsorbed IgG. If w_{PS} narrowed to 13 nm (Figure 4.9a), around the dimensions of individual IgG, continuous rows of ~16 nm wide dots were observed (Figure 4.9b), and possibly indicated single rows of IgG. Figure 4.7 already demonstrated IgG adsorbed exclusively on 30 nm wide PS domains. For larger w_{PS} (Figure 4.9 d and f), although IgG adsorbed predominantly on PS, some IgG were also observed on the mostly bare PMMA domains. We were not able to find adsorption conditions for these patterns for which no proteins were deposited on PMMA and yet full coverage was achieved on PS areas. Moreover, unoccupied surfaces also remained in the IgG-rich PS domains

on the larger templates. Therefore, the exclusivity of protein adsorption on PS was correlated with the feature size of the PS-b-PMMA template.

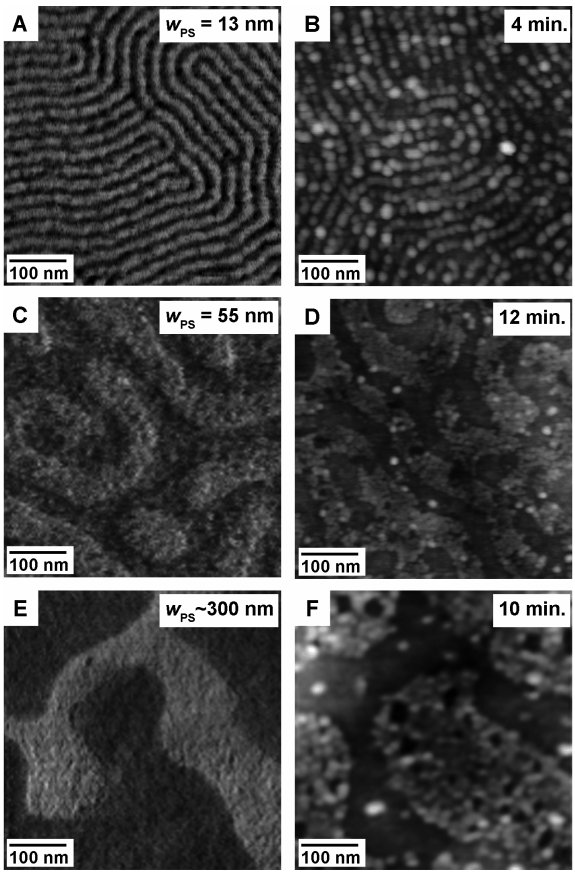

Figure 4.9. AFM images showing the size range of BCP templates investigated. (A), (C) and (E): phase images showing the distribution of PS (dark areas) and PMMA phases (light areas). (B), (D) and (F): height images of IgG patterns prepared on the corresponding BCP templates to the left. All patterns were adsorbed from 8.5 µg/ml biotinylated IgG. The respective adsorption times are indicated on the images. Refer to Fig. 1 for the respective phase and height scales.

Next, we investigated the effect of rinsing. We subjected the PS-b-PMMA templates to two rinsing procedures after the allowed protein adsorption time: regular 10 s rinsing under a flowing, open stream of deionised water (flowing rinse); and the slow dilution of the protein solution with deionised water (static wash). The flow rate of the PBS for flowing rinse was ~500 ml/min and the flow was supplied by a squeeze bottle. The samples were then dried and characterised by AFM in air. We present in Figure 4.10 quantitative AFM results for the template with repeat period ~300 nm. The outlines of the PS domains in Figure 4.10 a and b were identified by computer image analysis, which also identified the IgG clusters on the relatively bare PMMA domains (see supplementary information). The compiled results (Figure 4.10c) show

that the IgG coverage on PMMA after flowing rinse was ~10%, while ~3 times higher coverage was observed for the template subjected to static wash. Similar results were obtained for successive 10 s flowing rinses, and for the smaller templates. Therefore, hydrodynamic forces associated with a flowing rinse were major factors in dramatically reducing the observed IgG coverage on PMMA.

In addition, we subjected the protein nanoarrays (Figure 4.7) to longer periods of flowing rinse up to a few minutes but the nanopatterns remained intact, and the IgG adsorbed on PS were not removed. (In theory, a sufficiently large shear force due to liquid flow can displace proteins from a surface.) Moreover, SPR measurements (Figure 4.8) showed preferential IgG adsorption, faster adsorption kinetics and less desorption on PS than on PMMA, and indicated a stronger interaction of IgG with PS than with PMMA. At the same time, Figure 4.8 also shows that the amount of IgG desorbed from PMMA after a short rinse commensurate with our 10s flowing rinse procedure would be small (e.g., 2% desorbed after 1 min. rinsing). Consequently there was essentially no desorption from the entire PS-b-PMMA nanoarray template surface after a short flowing rinse.

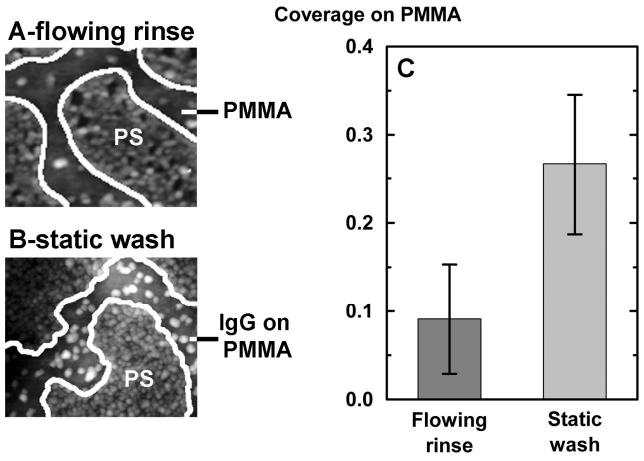

Figure 4.10. 400 x 500 nm AFM height images after (A) flowing rinse and reproduced from Fig. 3F, with PS areas masked by computer image analysis, and (B) after static wash, also with PS domains identified by computer image analysis. (C) Measurements over different regions of the samples totaling ~10 um^2 were analyzed to compute the IgG coverage on PMMA surfaces for the two rinsing procedures. Both (A) and (B) show a 10 nm height scale. (For comparison, the size of IgG is 14 x 9 x 4 nm.)[43, 48]

We have already shown that preferential adsorption on PS, together with the higher fractional surface area of PMMA, would result in roughly equal amounts of adsorbed IgG on PS and on PMMA domains. Moreover, the amount of IgG adsorbed after 10 min. adsorption would yield significantly less than complete coverage on both surfaces. Taken together with the observations that – 1) desorption was not significant

after a short rinse; 2) adsorbed IgG on PS were securely immobilised; and 3) flowing rinse could dramatically reduce the IgG density on PMMA – the observed exclusive patterning of adsorbed protein on PS indicates that the IgG originally adsorbed on PMMA must have migrated to the unoccupied PS surfaces during rinsing. This may be possible via a series of detachments and reattachments of some of the interaction points [12, 16, 17] comprising the physical adsorption. It is known that adsorption is a sequence of processes [11-13, 15, 17], and that the initial adsorbed conformation represents a metastable state [17], which can relax over time to maximise the number of interaction points [12, 17, 20, 21]. Thus the relatively short adsorption times used for patterning and the weak protein-PMMA interactions (compared with on PS), may represent adsorbed states that allowed disruption and formation of different interaction points to result in, with PBS rinsing, nanoscale movement (but not complete desorption) of the protein on PMMA. As mentioned earlier, displacement of proteins from a surface is possible at a sufficiently large flows [17].

The inability to exclusively pattern IgG on templates with PS domains wider than ~50 nm provides further details on the patterning process. (In comparison, the size of IgG is 14 x 9 x 4 nm.) [43, 48]. First, this might indicate the spatial limit to IgG migration during flowing rinse. Second, we also observed unoccupied regions in the interior of the PS domains for the templates with larger PS domains (Figs. 3D and F). Keeping in mind that IgG desorption was negligible, and that SPR measurements indicated incomplete IgG coverage on PS after 10 min. adsorption (Fig. 2), it is likely that once an IgG migrating on PMMA had encountered an unoccupied area of PS along the PS/PMMA boundary, it would adsorb, be immobilised, and would block the passage of other migrating IgG to still unoccupied PS areas in the interior of the PS domains. Correspondingly, Figs. 3D and F show that the boundaries between PS and PMMA domains can be readily identified by the presence of adsorbed IgG.

As the scale of the BCP nanopattern decreases, the length per unit area of the PS/PMMA boundary increases. Thus the fraction of unoccupied PS sites adjacent to PMMA available for reattachment of the migrating IgG would increase with decreasing domain size of the PS-b-PMMA nanopattern. In fact, if the width of PS domains equals 2 times the size of the protein, all PS adsorption sites would be adjacent to the PS/PMMA boundary and potentially be available for reattachment. Considering the dimensions of IgG (14 x 9 x 4 nm) and that the IgG probably adsorbed with the long axes parallel to the surface to maximise the number of attachment points, exclusive patterning by adsorption and rinsing on nanopatterns with PS domain widths up to 18~28 nm would be possible, as long as the PS domains were not already completely covered during the initial adsorption. Practically, unfilled PS surfaces of areas smaller than the size of individual IgG would not severely degrade the protein pattern definition, and slightly wider domain widths of, e.g., ~3 times the size of the protein may also be used.

Other than rinsing and IgG migration on PMMA surfaces, surface tension as the aqueous meniscus passes over the template surface during drying for AFM measurement may also be partially responsible for the nanoscale movement of proteins towards PS regions. This force was demonstrated, e.g., for alignment of DNA molecules on a BCP surface [80]. Notwithstanding, our experiment with different rinsing procedures showed that IgG remained on PMMA after static wash regardless of the drying procedure, and that an external hydrodynamic force was required for patterning IgG exclusively on PS domains.

4.2.4. Optimizing Nanoarray Formation and Demonstration of Nanoarray Function

Our observations concerning the migration of proteins during rinsing suggests that, other than the dimensional constraint relating the BCP nanotemplate feature size and the size of the protein, the total amount of proteins adsorbed also plays a critical role in obtaining optimal registry of the protein nanoclusters with the underlying template. This is because, in the case of PS-b-PMMA, the combined amount of IgG initially adsorbed on PS and PMMA must be just enough to occupy all adsorption sites on the PS domains in order to achieve optimal registry of the IgG clusters with the PS nanoarray. When too many IgG had adsorbed, because desorption is not important in our procedure, the proteins would also have to fill the less favourable PMMA surfaces, leading to reduced nanoarray definition. Too few IgG adsorbed would lead to incomplete patterns. Apart from the adsorption time, the solution concentration used for adsorption is another major influence on the amount adsorbed on the templates. More time would be needed to adsorb the same amount of proteins at lower concentrations, and vice versa. At the same time, the strength of the interaction between an adsorbed protein and a surface evolves over time due to transitions in adsorbed conformation [12, 13], and, among other effects [15], generally increases over time after initial adsorption [11, 12]. Thus long adsorption times would be unfavourable for protein nanoarray formation if proteins did not retain sufficient mobility on PMMA, and very short adsorption times might confer a mobility too high on both PS and PMMA for optimal pattern definition.

This tradeoff between protein solution concentration and adsorption time was experimentally explored to find the conditions for optimal IgG nanoarray formation. The match between protein nanoarray and the underlying PS-b-PMMA nanopattern was quantified by image analysis (see Appendix A), wherein the differences in area and shape between individual adsorbed protein nanoclusters and PS domains, and the difference between the surface coverage of the protein nanoarray and the underlying PS domains, were measured. These outcomes are plotted in Figure 4.11 as averaged, absolute percentage deviations from the ideal PS-b-PMMA template pattern: the

smaller the percentage deviation, the closer the protein nanoarray match the ideal, hexagonally ordered PS-b-PMMA template.

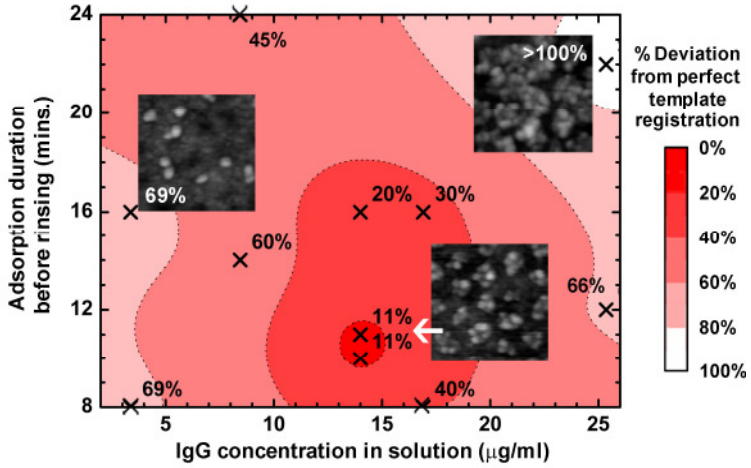

Figure 4.11. Percentage deviations quantifying the geometric mismatch of the IgG nanoarrays, prepared using various IgG solution concentrations and adsorption times, with the ideal hexagonal BCP nanotemplate. Crosses are measured data while the contour map is a fitted surface for guiding the eye only. Three example AFM height images are inset to illustrate how the deviations calculated by computer image analysis can identify optimal pattern registration (middle), and both incomplete (upper left) and over-filled (upper right) nanoarrays. All insets show a 200 x 200 nm scan size and a 10 nm height scale.

Figure 4.11 shows that the optimal conditions centre around intermediate adsorption times (10 min.) and protein solution concentrations (14 μg/ml). The AFM images inset illustrate that our analysis was able to distinguish both incomplete and overfilled templates from a properly formed IgG nanoarray. For example, the upper right inset shows that when more IgG than was necessary to provide full coverage on the PS domains had adsorbed, IgG also adsorbed on PMMA regions, especially on areas adjacent to the PS domains. This resulted in poorly separated protein clusters, and the "excess" IgG decorating the PS-templated IgG clusters reflect the underlying geometric restrictions and IgG migration during flowing rinse. Note also in Figure 4.11 the trend in relatively low deviations (< 40 %) extending along the diagonal of the graph from lower concentrations and longer adsorption times, to higher concentrations and shorter adsorption times. This underscores the fundamental influence of the total amount of protein adsorbed on achieving good pattern definition.

IgG nanoarrays prepared under the optimal conditions were employed directly in an immunoassay to test the adsorbed protein activity. Rabbit anti-mouse IgG (RxM-IgG) were used as the antigen and their capture by the IgG nanoarray from solutions of different concentrations was measured in situ by SPR (Figure 4.12). (To emphasise the anti-rabbit specificity of the goat IgG comprising the nanoarrays, we

denote them as GxR-IgG in this section.) First, the nanopatterned sample was mounted on the liquid flow cell for measurement with SPR—the effective layer thickness of the GxR-IgG nanoarray was 1.0 nm. Then, BSA (100 µg/ml) was introduced into the flow cell and allowed to adsorb for 60 min, (similar to the assay shown in Figure 4.5a) in order to cover all remaining unoccupied polymer surfaces and to prevent non-specific adsorption of RxM-IgG antigens [1, 2, 55, 62]. This also resulted in a topographically flat sensing surface fully covered by proteins (Figure 4.12, left inset), where the nanoarray was solely defined by biochemical heterogeneity and where the topography could not interfere with IgG binding. RxM-IgG was then introduced and the amount bound relative to the amount of nanoarrayed GxR-IgG (binding ratio, i.e., antigen binding capacity) was calculated. Figure 4.13a summaries these experimental steps. Control experiments in which a high concentration of GxR-IgG at 170 µg/ml was reintroduced after BSA adsorption showed no further adsorption and demonstrated the efficacy of BSA passivation. Although GxR-IgG in the IgG nanoarray were adsorbed with random orientation and closely packed by BSA, antigen binding for a RxM-IgG concentration of 17 µg/ml (~1 µM) was observed at a ratio of 0.04 after 30 min. binding. At 5 times higher antigen concentration, the binding ratio increased by 3 times to 0.13, and at 10 times higher antigen concentration, the binding ratio increased 5 times to 0.2. Considering that there were > 5 GxR-IgG per protein cluster in the nanoarray (see section I), AFM height measurements revealed that this last result was high enough to achieve binding activity at each element in the IgG nanoarray—the left inset in Figure 4.12 shows the topographically flat GxR-IgG/BSA sensing surface, and the inset on the right shows a hexagonal arrangement of RxM-IgG bound to the underlying GxR-IgG nanoarray after the assay.

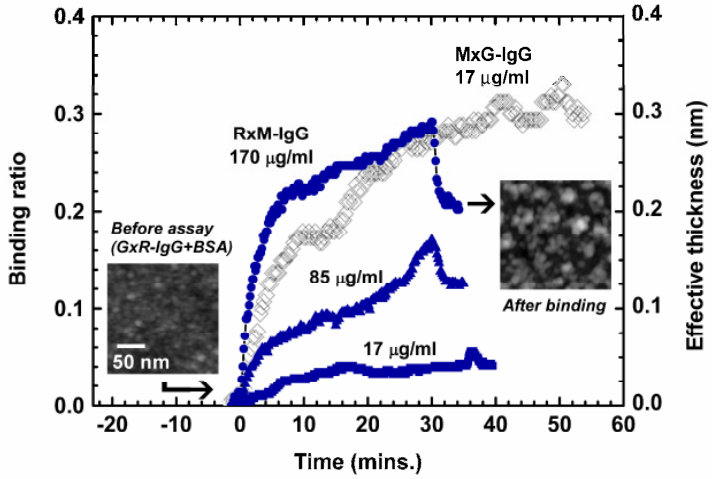

Figure 4.12. Binding of RxM-IgG and MxG-IgG to the nanoarrayed GxR-IgG, measured by SPR. The left axis indicates the binding ratio and the right axis shows the measured protein layer thickness corresponding to the binding. Gray arrows indicate the start of rinsing with pure PBS. The inset on the left shows the flat topography of the BSA in-filled GxR-IgG nanoarray. The inset on the right shows

the reappearance of the nanoarray pattern after RxM-IgG binding from 170 µg/ml solution. The length scale bar in the left inset is common to both AFM images, and both images have a 10 nm height scale.

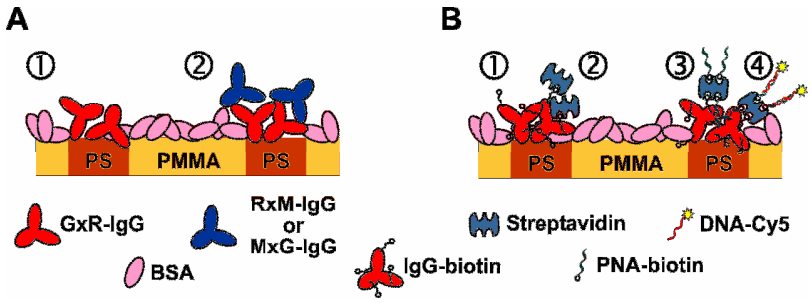

Figure 4.13. Schematics of cross-sections of the IgG/BSA nanoarrays used for immunoassay (A) and for tethering streptavidin and PNA for DNA sensing (B). In (A), (1) indicates GxR-IgG patterning on PS followed by BSA adsorption on PMMA; and (2) indicates IgG binding on the GxR-IgG nanoclusters. In (B), (1) indicates IgG-biotin array formation on PS followed by BSA adsorption on PMMA; (2) streptavidin binding on the IgG-biotin nanoarray; (3) immobilization of PNA-biotin probes to the IgG-streptavidin complexes; and (4) detection of DNA target via fluorescence labeling.

Figure 4.12 also shows the inverse assay, in which the nanopatterned GxR-IgG was the antigen and a mouse anti-goat IgG (MxG-IgG) was introduced in the solution. A binding ratio of 0.3 was measured at a comparatively low MxG-IgG concentration of 17 µg/ml. This was expected as the MxG-IgG in solution were free to seek the optimal orientation for binding. We also used polyclonal MxG-IgG, which could bind to the GxR-IgG immobilised in various orientations.

To further explore the potential of our protein nanoarray created on BCP templates, we built a streptavidin-PNA (peptide nucleic acid) architecture for DNA sensing in a nanoarray format. Our group had previously demonstrated the streptavidin-PNA architecture on homogeneous biotinylated-thiol self-assembled monolayer (SAM) surfaces [81]. To prepare the nanoarray sensor architecture, biotinylated IgG (IgG-b) was patterned with adsorption conditions of 6 min. at 8.5 µg/ml and, as outlined earlier, BSA was subsequently used* to passivate all remaining polymer surfaces, as in the previous immunoassay experiment (Figure 4.12). In the second step, streptavidin (6 µg/ml) was introduced and were bound to the IgG-b clusters. At this point, the nanoarray pattern reappeared in AFM height images as the streptavidin clusters rose above the flat IgG-b/BSA background, demonstrating

* Optionally, the BSA layer on the template could be crosslinked by a bifunctional linker molecule (e.g. ethylene glycol bis(succinimidyl succinate), i.e. EGS, purchased from Pierce Biotechnology, USA) to completely stabilize the physisorbed protein nanostructure. The protected protein nanoarray could then be used under high flow velocities of 30 cm/min. or more for extended periods without loss in nanoarray ordering. Otherwise, we have used the uncrosslinked protein nanoarrays at flow velocities of ~2 cm/min. for a couple of hours without issue. To perform the crosslinking, the sample was immersed in 500 ml of an EGS mixture for 90 min, then rinsed in deionsed water. EGS was dissolved at a concentration of 2 mM, in a sulfoNHS-EDC amine coupling solution mixture purchased from Biacore (GE Healthcare Europe, Freiburg, Germany). The amine coupling mixture consisted of 750 mg 1-ethyl-3-(3-dimethylaminopropyl)carbodiimide hydrochloride (EDC), 115 mg N-hydroxysuccinimide (NHS), 10.5 ml 1.0 M ethanolamine-HCl pH 8.5.

the integrity and activity of the biotinylated nanoarray. In the third step, 15-mer, single-stranded, biotinylated-PNA probes (1 μM) were immobilised on top of the IgG-b/streptavidin clusters. The PNA was the active DNA-sensing element: single-stranded DNA target sequences complementary to the immobilised PNA would hybridise whereas mismatched sequences would not, or would hybridise with reduced efficiency, depending on the degree of mismatch. The single-stranded target DNA sequences were also fluorescent labeled and hybridization kinetics was measured by surface plasmon field-enhanced fluorescence spectroscopy (SPFS) [81]. Figure 4.13b illustrates the preparation of the molecular architecture, and Figure 4.14 shows one such experiment. AFM images of the surface before (flat topography with BSA passivation) and after the experiment are also shown in the figure insets.

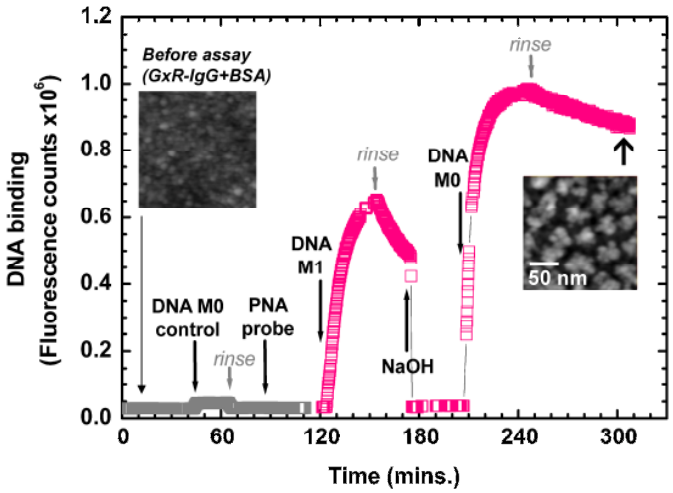

Figure 4.14. SPFS kinetics of DNA binding on an IgG-biotin/BSA/streptavidin/PNA nanoarray. M1 refers to the 15-mer DNA with a single nucleotide mismatch with respect to the arrayed PNA probes, and M0 is the 15-mer DNA with no mismatch. Gray arrows indicate the start of rinsing with pure buffer. "Control" refers to the addition of M0 before PNA immobilization and shows no non-specific binding on the IgG-biotin/BSA/streptavidin platform. The DNA concentration used was 44 nM. The AFM height image inset shows the nanoarray pattern of the final IgG-streptavidin-PNA-DNA architecture. The height scale is 10 nm.

A background control was first performed by introducing the complementary DNA target (44 nM) after streptavidin binding but before PNA probe immobilization. No hybridization occurred without the PNA probe and the measured fluorescence intensity rose barely above and returned to the background level after rinsing. After PNA probe immobilization, a DNA target sequence with a single nucleotide mismatch at 44 nM (M1) was introduced. This resulted in a relatively slow rise in binding kinetics and rinsing caused rapid dissociation of the mismatched PNA-DNA. The nanoarray-sensor architecture was "regenerated" by the addition of 10 μM NaOH, which completely dissociated and rinsed away all bound DNA [81]. Next, introducing

the complementary DNA at 44 nM (M0), resulted in 40% higher fluorescence and much faster kinetics, indicating efficient hybridization. Rinsing caused a comparatively slow dissociation of the PNA-DNA. Thus the present nanoarray based sensor architecture was able to distinguish single nucleotide mismatches, from the amount of DNA hybridised, and from both the binding and dissociation kinetics. The signal-to-noise ratio was also very high throughout the experiment (>100). The AFM inset in Figure 4.14 shows the nanoarray pattern of the full architecture (in air) after the experiment and additional experiments showed that the BCP-based IgG-streptavidin-PNA nanoarray was able to withstand multiple NaOH regeneration for the reuse of the sensor. Furthermore, the tethering of other molecules could be accomplished by suitable functionalization of the protein comprising the adsorbed nanoarray. Thus it is possible to construct nanoarrays of more complex or fragile biomolecular assemblies based on the present simple and efficient protein nanopatterning generated by selective adsorption on self-assembled BCP templates.

4.2.5. Summary

We have demonstrated a simple method for creating protein nanoarrays based on self-assembled block copolymer thin film templates, and comprehensively explored its formation mechanism and applicability as a platform for immunoassays and building biomolecular architectures. Both IgG and BSA nanoarrays were created on PS-b-PMMA templates, and patterning of protein patterns down to a line width of 13 nm was demonstrated. On the chemically heterogeneous PS-b-PMMA template surface, it was shown that exclusive protein adsorption on PS domains surrounded by a PMMA matrix was due to a combination of rinsing effects and the geometric restrictions imposed by a nanopattern with a difference in protein adsorption behaviour on adjacent, chemically distinct surfaces. This was found to be a nanoscale effect applicable to patterns with a characteristic dimension of the domains of higher adsorption affinity < 3 times the size of the protein. For example, we were able to achieve IgG adsorption exclusively on PS domains < 50 nm with the PS/PMMA system. The patterning process took less than 15 min. to complete. At the other size extreme, if the domains shrank to below the nanoscale such that the surface comprised effectively of a random PS-PMMA copolymer, the surface would be more appropriately described as a single material and no patterning would be expected. Thus the present patterning scheme truly reflects the confluence of factors at the nanoscale.

Antigen binding to an IgG nanoarray prepared by our approach was demonstrated by complementary surface plasmon resonance (SPR) and AFM measurements. After patterning the IgG on the PS domains, BSA was adsorbed on the adjacent PMMA regions to prevent non-specific adsorption of antigens, and to create a topographically flat protein layer with nanoarrayed biochemical heterogeneity.

Although the adsorbed IgG were randomly oriented, they retained sufficient activity that the array nanopattern reappeared in AFM height images after antigen binding on top of the flat sensor surface, indicating binding on most if not all IgG clusters at sufficiently high antigen concentrations.

We also demonstrated DNA sensing and the building of a moderately complex streptavidin-PNA probe architecture tethered to individual biotinylated IgG nanoarray clusters. AFM showed the integrity of the nanoarray format of the biomolecular complex, and SPR field-enhanced fluorescence measurements showed that single nucleotide mismatch on a 15-mer DNA target could be clearly distinguished from the matching sequence by both the binding amount and kinetics. Nanoarrays of other biomolecules, such as peptide fragments or other proteins necessitating covalent immobilization for proper function, could potentially be patterned with this linker approach.

In summary, we have demonstrated a simple "bottom-up" technique for creating large area protein nanoarrays and determined the mechanistic framework for extending this patterning approach to other proteins and material systems. We also demonstrated that this nanoarray platform provides additional flexibility in nanoarraying other biomolecules if the biomolecules could bind to a suitably functionalised adsorbed protein array. Our approach may enable protein-based nanoarray sensors, and may also be of use in investigations which require an understanding of the arrangement of cell and biological functions on the nanoscale.

4.3. References

[1] Lee KB, Park SJ, Mirkin CA, Smith JC, Mrksich M: Protein Nanoarrays Generated by Dip-Pen Nanolithography. *Science* **2002**, *295*, 1702.

[2] Lee KB, Kim EY, Mirkin CA, Wolinsky SM: The Use of Nanoarrays for Highly Sensitive and Selective Detection of Human Immunodeficiency Virus Type 1 in Plasma. *Nano Letters* **2004**, *4*, 1869.

[3] Pallandre A, De Meersman B, Blondeau F, Nysten B, Jonas AM: Tuning the Orientation of an Antigen by Adsorption onto Nanostriped Templates. *Journal of the American Chemical Society* **2005**, *127*, 4320.

[4] Arnold M, Cavalcanti-Adam EA, Glass R, Blummel J, Eck W, Kantlehner M, Kessler H, Spatz JP: Activation of Integrin Function by Nanopatterned Adhesive Interfaces. *Chemphyschem* **2004**, *5*, 383.

[5] Agheli H, Malmstrom J, Larsson EM, Textor M, Sutherland DS: Large Area Protein Nanopatterning for Biological Applications. *Nano Letters* **2006**, *6*, 1165.

[6] Senaratne W, Sengupta P, Jakubek V, Holowka D, Ober CK, Baird B: Functionalized Surface Arrays for Spatial Targeting of Immune Cell Signaling. *Journal of the American Chemical Society* **2006**, *128*, 5594.

[7] Park H, Cannizzaro C, Vunjak-Novakovic G, Langer R, Vacanti CA, Farokhzad OC: Nanofabrication and Microfabrication of Functional Materials for Tissue Engineering. *Tissue Engineering* **2007**, *13*, 1867.

[8] Engel E, Michiardi A, Navarro M, Lacroix D, Planell JA: Nanotechnology in Regenerative Medicine: The Materials Side. *Trends in Biotechnology* **2007**, *26*, 39.

[9] Mrksich M: What Can Surface Chemistry Do for Cell Biology? *Current Opinion in Chemical Biology* **2002**, *6*, 794.

[10] Stevens MM, George JH: Exploring and Engineering the Cell Surface Interface. *Science* **2005**, *310*, 1135.

[11] Talbot J, Tarjus G, Van Tassel PR, Viot P: From Car Parking to Protein Adsorption: An Overview of Sequential Adsorption Processes. *Colloids and Surfaces A: Physicochemical and Engineering Aspects* **2000**, *165*, 287.

[12] Nakanishi K, Sakiyama T, Imamura K: On the Adsorption of Proteins on Solid Surfaces, a Common but Very Complicated Phenomenon. *Journal of Bioscience and Bioengineering* **2001**, *91*, 233.

[13] Voros J: The Density and Refractive Index of Adsorbing Protein Layers. *Biophysical Journal* **2004**, *87*, 553.

[14] Sousa A, Sengonul M, Latour R, Kohn J, Libera M: Selective Protein Adsorption on a Phase-Separated Solvent-Cast Polymer Blend. *Langmuir* **2006**, *22*, 6286.

[15] Kim J, Somorjai GA: Molecular Packing of Lysozyme, Fibrinogen, and Bovine Serum Albumin on Hydrophilic and Hydrophobic Surfaces Studied by Infrared-Visible Sum Frequency Generation and Fluorescence Microscopy. *Journal of the American Chemical Society* **2003**, *125*, 3150.

[16] Sethuraman A, Han M, Kane RS, Belfort G: Effect of Surface Wettability on the Adhesion of Proteins. *Langmuir* **2004**, *20*, 7779.

[17] Raffaini G, Ganazzoli F: Understanding the Performance of Biomaterials through Molecular Modeling: Crossing the Bridge between Their Intrinsic Properties and the Surface Adsorption of Proteins. *Macromolecular Bioscience* **2007**, *7*, 552.

[18] Wertz CF, Santore MM: Adsorption and Reorientation Kinetics of Lysozyme on Hydrophobic Surfaces. *Langmuir* **2002**, *18*, 1190.

[19] Santore MM, Wertz CF: Protein Spreading Kinetics at Liquid-Solid Interfaces Via an Adsorption Probe Method. *Langmuir* **2005**, *21*, 10172.

[20] Toscano A, Santore MM: Fibrinogen Adsorption on Three Silica-Based Surfaces: Conformation and Kinetics. *Langmuir* **2006**, *22*, 2588.

[21] Clark AJ, Kotlicki A, Haynes CA, Whitehead LA: A New Model of Protein Adsorption Kinetics Derived from Simultaneous Measurement of Mass Loading and Changes in Surface Energy. *Langmuir* **2007**, *23*, 5591.

[22] Silin V, Weetall H, Vanderah DJ: Spr Studies of the Nonspecific Adsorption Kinetics of Human Igg and Bsa on Gold Surfaces Modified by Self-Assembled Monolayers (Sams). *Journal of Colloid and Interface Science* **1997**, *185*, 94.

[23] Wertz CF, Santore MM: Effect of Surface Hydrophobicity on Adsorption and Relaxation Kinetics of Albumin and Fibrinogen: Single-Species and Competitive Behavior. *Langmuir* **2001**, *17*, 3006.

[24] Neto C: A Novel Approach to the Micropatterning of Proteins Using Dewetting of Polymer Bilayers. *Physical Chemistry Chemical Physics* **2007**, *9*, 149.

[25] Li L, Hitchcock AP, Robar N, Cornelius R, Brash JL, Scholl A, Doran A: X-Ray Microscopy Studies of Protein Adsorption on a Phase-Segregated Polystyrene/Polymethyl Methacrylate Surface. 1. Concentration and Exposure-Time Dependence for Albumin Adsorption. *Journal of Physical Chemistry B* **2006**, *110*, 16763.

[26] Morin C, Hitchcock AR, Cornelius RM, Brash JL, Urquhart SG, Scholl A, Doran A: Selective Adsorption of Protein on Polymer Surfaces Studied by Soft X-Ray Photoemission Electron Microscopy. *Journal of Electron Spectroscopy and Related Phenomena* **2004**, *137-40*, 785.

[27] Kumar N, Hahm JI: Nanoscale Protein Patterning Using Self-Assembled Diblock Copolymers. *Langmuir* **2005**, *21*, 6652.

[28] Kumar N, Parajuli O, Hahm J: Two-Dimensionally Self-Arranged Protein Nanoarrays on Diblock Copolymer Templates. *Journal of Physical Chemistry B* **2007**, *111*, 4581.

[29] Bates FS, Fredrickson GH: Block Copolymer Thermodynamics: Theory and Experiment. *Annual Review of Physical Chemistry* **1990**, *41*, 525.

[30] Fredrickson GH, Bates FS: Dynamics of Block Copolymers: Theory and Experiment. *Annual Review of Materials Science* **1996**, *26*, 501.

[31] Fasolka MJ, Mayes AM: Block Copolymer Thin Films: Physics and Applications. *Annual Review of Materials Research* **2001**, *31*, 323.

[32] Green PF, Limary R: Block Copolymer Thin Films: Pattern Formation and Phase Behavior. *Advances in Colloid and Interface Science* **2001**, *94*, 53.

[33] Matsen MW: The Standard Gaussian Model for Block Copolymer Melts. *Journal of Physics: Condensed Matter* **2002**, R21.

[34] Simon PFW, Ulrich R, Spiess HW, Wiesner U: Block Copolymer-Ceramic Hybrid Materials from Organically Modified Ceramic Precursors. *Chemistry of Materials* **2001**, *13*, 3464.

[35] Napoli A, Sebök D, Senti A, Meier W: *Potential Applications of Polymer Vesicles*. In *Block Copolymers in Nanoscience*, Massimo Lazzari; Guojun Liu; Sébastien Lecommandoux, eds.; Wiley-VCH: Weinheim, 2006, pp. 64.

[36] Denis FA, Pallandre A, Nysten B, Jonas AM, Dupont-Gillain CC: Alignment and Assembly of Adsorbed Collagen Molecules Induced by Anisotropic Chemical Nanopatterns. *Small* **2005**, *1*, 984.

[37] Hasegawa M, Kitano H: Adsorption-Kinetics of Proteins onto Polymer Surfaces as Studied by the Multiple Internal-Reflection Fluorescence Method. *Langmuir* **1992**, *8*, 1582.

[38] Knoner G, Rolfe BE, Campbell JH, Parkin SJ, Heckenberg NR, Rubinsztein-Dunlop H: Mechanics of Cellular Adhesion to Artificial Artery Templates. *Biophysical Journal* **2006**, *91*, 3085.

[39] *We also measured static water contact angles of 88+/-1 deg, and 60.4+/-2.1deg, on our PS and PMMA surfaces, respectively.*

[40] Ayhan F, Rad AY, Ayhan H: Investigation of in Vitro Interactions between Different Polymeric Surfaces and Blood Proteins Via Phagocytosis Phenomena. *Journal of Biomaterials Science, Polymer Edition* **2003**, *14*, 1427.

[41] Elgersma AV, Zsom RLJ, Lyklema J, Norde W: Kinetics of Single and Competitive Protein Adsorption Studied by Reflectometry and Streaming Potential Measurements. *Colloids and Surfaces* **1992**, *65*, 17.

[42] Kalasin S, Santore MM: Hydrodynamic Crossover in Dynamic Microparticle Adhesion on Surfaces of Controlled Nanoscale Heterogeneity. *Langmuir* **2008**, *24*, 4435.

[43] Lynch M, Mosher C, Huff J, Nettikadan S, Johnson J, Henderson E: Functional Protein Nanoarrays for Biomarker Profiling. *Proteomics* **2004**, *4*, 1695.

[44] Xu H, Lu JR, Williams DE: Effect of Surface Packing Density of Interfacially Adsorbed Monoclonal Antibody on the Binding of Hormonal Antigen Human Chorionic Gonadotrophin. *Journal of Physical Chemistry B* **2006**, *110*, 1907

[45] Douillard R, Daoud M, Aguie-Beghin V: Polymer Thermodynamics of Adsorbed Protein Layers. *Current Opinion in Colloid & Interface Science* **2003**, *8*, 380.

[46] Carter DC, Ho JX: Structure of Serum Albumin. *Advances in Protein Chemistry* **1994**, *45*, 153.

[47] Ferrer ML, Duchowicz R, Carrasco B, de la Torre JG, Acuna AU: The Conformation of Serum Albumin in Solution: A Combined Phosphorescence Depolarization-Hydrodynamic Modeling Study. *Biophysical Journal* **2001**, *80*, 2422.

[48] Harris LJ, Larson SB, Hasel KW, Day J, Greenwood A, McPherson A: The Three-Dimensional Structure of an Intact Monoclonal Antibody for Canine Lymphoma. *Nature* **1992**, *360*, 369.

[49] Lesk A: *Antibody Structure*. In *Introduction to Protein Science: Architecture, Function, and Genomics*; Oxford University Press: New York, 2004, pp. 270.

[50] Wilson DS, Nock S: Functional Protein Microarrays. *Current Opinion in Chemical Biology* **2002**, *6*, 81.

[51] Giacomelli CE, Bremer M, Norde W: Atr-Ftir Study of Igg Adsorbed on Different Silica Surfaces. *Journal of Colloid and Interface Science* **1999**, *220*, 13.

[52] Peluso P, Wilson DS, Do D, Tran H, Venkatasubbaiah M, Quincy D, Heidecker B, Poindexter K, Tolani N, Phelan M, Witte K, Jung LS, Wagner P, Nock S: Optimizing Antibody Immobilization Strategies for the Construction of Protein Microarrays. *Analytical Biochemistry* **2003**, *312*, 113.

[53] Schena M, Shalon D, Heller R, Chai A, Brown PO, Davis RW: Parallel Human Genome Analysis: Microarray-Based Expression Monitoring of 1000 genes. *Proceedings of the National academy of Sciences of the United States of America* **1996**, *93*, 10614.

[54] Lockhart DJ, Winzeler EA: Genomics, Gene Expression and DNA Arrays. *Nature* **2000**, *405*, 827.

[55] Xu QC, Lam KS: Protein and Chemical Microarrays - Powerful Tools for Proteomics. *Journal of Biomedicine and Biotechnology* **2003**, 257.

[56] Zhu H, Snyder M: Protein Chip Technology. *Current Opinion in Chemical Biology* **2003**, *1*, 55.

[57] Wilson DS, Nock S: Recent Developments in Protein Microarray Technology. *Angewandte Chemie-International Edition* **2003**, *42*, 494.

[58] Zhou C, Friedt JM, Angelova A, Choi KH, Laureyn W, Frederix F, Francis LA, Campitelli A, Engelborghs Y, Borghs G: Human Immunoglobulin Adsorption Investigated by Means of Quartz Crystal Microbalance Dissipation, Atomic Force Microscopy, Surface Acoustic Wave, and Surface Plasmon Resonance Techniques. *Langmuir* **2004**, *20*, 5870.

[59] Lee M, Kang DK, Yang HK, Park KH, Choe SY, Kang C, Chang SI, Han MH, Kang IC: Protein Nanoarray on Prolinker (Tm) Surface Constructed by Atomic Force Microscopy Dip-Pen Nanolithography for Analysis of Protein Interaction. *Proteomics* **2006**, *6*, 1094.

[60] Mirkin CA: *Protein Nanoarrays*. In *Nanobiotechnology Ii*, Chad A. Mirkin; Christof M. Niemeyer, eds.; Wiley-VCH: Weinheim, 2007, pp. 242.

[61] Frank R: Spot-Synthesis: An Easy Technique for the Positionally Addressable, Parallel Chemical Synthesis on a Membrane Support. *Tetrahedron* **1992**, *48*, 9217–9232.

[62] MacBeath G, Schreiber SL: Printing Proteins as Microarrays for High-Throughput Function Determination. *Science* **2000**, *289*, 1760.

[63] Zhu H, Bilgin M, Bangham R, Hall D, Casamayor A, Bertone P, Lan N, Jansen R, Bidlingmaier S, Houfek T, Mitchell T, Miller P, Dean RA, Gerstein M, Snyder M: Global Analysis of Protein Activities Using Proteome Chips. *Science* **2001**, *293*, 2101.

[64] Fang Y, Frutos AG, Lahiri J: Membrane Protein Microarrays. *Journal of the American Chemical Society* **2002**, *124*, 2394.

[65] Fodor SP, Read JL, Pirrung MC, Stryer L, Lu AT, Solas D: Light-Directed, Spatially Addressable Parallel Chemical Synthesis. *Science* **1991**, *251*, 767.

[66] Hyun J, Ahn SJ, Lee WK, Chilkoti A, Zauscher S: Molecular Recognition-Mediated Fabrication of Protein Nanostructures by Dip-Pen Lithography. *Nano Letters* **2002**, *2*, 1203.

[67] Lee H, Park J, Kim J, Jung H, Kawai T: Well-Oriented Nanowell Array Metrics for Integrated Digital Nanobiosensors. *Applied Physics Letters* **2006**, *89*.

[68] Salazar RB, Shovsky A, Schonherr H, Vancso GJ: Dip-Pen Nanolithography on (Bio)Reactive Monolayer and Block-Copolymer Platforms: Deposition of Lines of Single Macromolecules. *Small* **2006**, *2*, 1274.

[69] Bruckbauer A, Zhou DJ, Kang DJ, Korchev YE, Abell C, Klenerman D: An Addressable Antibody Nanoarray Produced on a Nanostructured Surface.

Journal of the American Chemical Society **2004**, *126*, 6508.

[70] Hamley IW: Nanostructure Fabrication Using Block Copolymers. *Nanotechnology* **2003**, R39.

[71] Lazzari M, López-Quintela MA: Block Copolymers as a Tool for Nanomaterial Fabrication. *Advanced Materials* **2003**, *15*, 1583.

[72] Segalman RA: Patterning with Block Copolymer Thin Films. *Materials Science and Engineering R-Reports* **2005**, *48*, 191.

[73] Bonroy K, Frederix F, Reekmans G, Dewolf E, De Palma R, Borghs G, Declerck P, Goddeeris B: Comparison of Random and Oriented Immobilisation of Antibody Fragments on Mixed Self-Assembled Monolayers. *Journal of Immunological Methods* **2006**, *312*, 167.

[74] Ge H: Upa, a Universal Protein Array System for Quantitative Detection of Protein-Protein, Protein-DNA, Protein-Rna and Protein-Ligand Interactions. *Nucleic Acids Research* **2000**, *28*, e3.

[75] Wang D, Liu S, Trummer BJ, Deng C, Wang A: Carbohydrate Microarrays for the Recognition of Cross-Reactive Molecular Markers of Microbes and Host Cells. *Nature Biotechnology* **2002**, *20*, 275.

[76] Martin BD, Gaber BP, Patterson CH, Turner DC: Direct Protein Microarray Fabrication Using a Hydrogel "Stamper". *Langmuir* **1998**, *14*, 3971.

[77] Jung J-M, Kwon KY, Ha T-H, Chung BH, Jung H-T: Gold-Conjugated Protein Nanoarrays through Block-Copolymer Lithography: From Fabrication to Biosensor Design. *Small* **2006**, *2*, 1010.

[78] *The number of IgG to each cluster could not be directly counted because AFM only provides a top view and, although both BSA and IgG only form monolayers when adsorbed under our conditions,[12, 40] tip convolution also limits the spatial definition of the measured features. By considering the PS nanodomain diameter, and assuming that each IgG occupied an area equivalent to a circle with the IgG's longest axis as the diameter, we arrive at a lower bound estimate of 5 IgG per nanoclusters*.

[79] Knoll W: Interfaces and Thin Films as Seen by Bound Electromagnetic Waves. *Annual Review of Physical Chemistry* **1998**, *49*, 569.

[80] Liu G, Zhao J: Guided Alignment and Positioning of Single DNA Molecules by a Structured Contact Line on a Block Copolymer Surface. *Langmuir* **2006**, *22*, 2923.

[81] Yao D, Yu F, Kim J, Scholz J, Nielsen PE, Sinner E-K, Knoll W: Surface Plasmon Field-Enhanced Fluorescence Spectroscopy in Pcr Product Analysis by Peptide Nucleic Acid Probes. *Nucleic Acids Research* **2004**, *32*, e177.

5. Nanostructured optical waveguides and their application

In this chapter, the application of self-assembled BCP and nanoporous AAO thin films as optical waveguides in the visible wavelengths is explored. Due to the sub-wavelength nature of the BCP and AAO nanostructures, the dielectric responses of the BCP and nanoporous AAO thin films are well described by effective medium theory (EMT), and they are conveniently measured by optical waveguide spectroscopy (OWS). The investigation of thin film block copolymer waveguides is based on self-assembled PS-b-PMMA/PMMA with PMMA cylindrical morphology oriented normal to the substrate surface. Therefore the optical analyses of the BCP and AAO thin films are linked by a common structural morphology, as shown in Figure 5.1, that exhibits cylindrical nanodomains (PMMA or pores) that run through the thickness of the film, are oriented normal to the substrate surface, and are isolated from each other by a matrix material (PS or anodic alumina). This cylindrical morphology exhibits a distinct structural anisotropy between the directions normal and parallel to the substrate surface, and effects a corresponding anisotropy in optical response that will prove valuable in the characterization of the nanostructures.

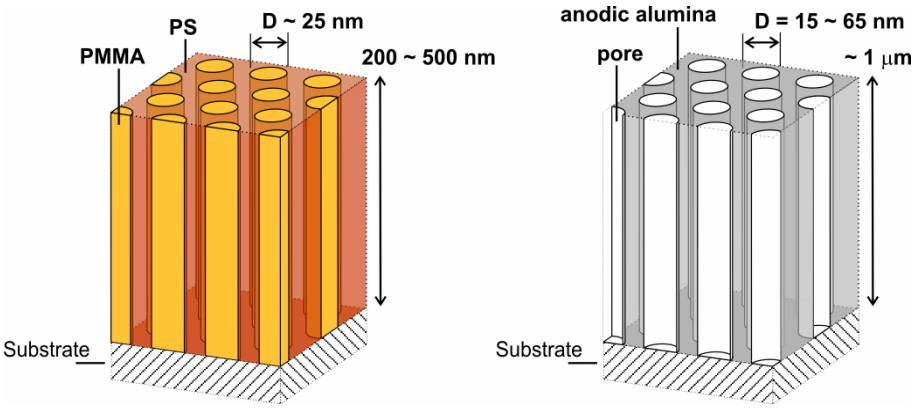

Figure 5.1. Schematics of the cylindrical morphologies of the nanostructured PS-b-PMMA/PMMA and nanoporous AAO thin films analyzed by EMT and waveguide experiments. D is the characteristic nanodomain dimension, which is the diameter of the cylindrical domains in these structures. The centre-to-centre domain spacing ($\lambda_{C\text{-}C}$) for the BCP samples are ~46 nm, and are 90 ~100 nm for the AAO samples. The interfacial layers between the nanostructured films and the substrate, as described in Chapters 2 and 3, are omitted for clarity.

The chapter is organised as follows: first, introductions to EMT and OWS are presented; then the novel concept of a block copolymer waveguide is demonstrated, and it is shown that the morphology of the BCP thin film can be characterised by its dielectric response as measured by waveguide analysis; finally, based on a previous demonstration of nanoporous AAO waveguides, the application of the AAO waveguide as a highly sensitive and versatile sensor of surface processes, and macromolecular nanostructure formation within the pores, is explored.

5.1. Effective medium theory (EMT)

A structure composed of discrete domains of different materials may appear homogeneous to incidence optical radiation, and acquire an averaged, effectively homogeneous dielectric response (ε), if the characteristic size of the domains is much smaller than the wavelength of the light. The value of ε should then be related in some way to the dielectric responses of the materials comprising the individual domains, to their respective volumes, and also to the individual spatial arrangement and shapes of the domains. Effective Medium Theory (EMT) characterises such a heterogeneous structure by simple, macroscopic variables (i.e., bulk material dielectric constants, domain morphology and volume fractions) that in effect define a uniform, prototypical composite structure with a dielectric response that is, on average, equivalent to ε. Nanostructures have features sizes much smaller than visible or longer wavelengths, therefore EMT may be used to study their optical responses. The theory has been applied to analyzing AAO [1-3], numerous phase separated and nano morphologies [4-8], and also surface roughness [9].

The Maxwell-Garnett (MG) formula [10, 11] is the first EMT that derives the effective dielectric response (ε_{eff}) based on the macroscopic variables discussed above. It was derived from the Clausius-Mossotti relation [9, 12], by considering the polarizability of a macroscopically small but atomically large inclusion (i.e. nanodomain) in the presence of an external field [9, 12]:

Equation 5.1a
$$\frac{\varepsilon_{eff} - \varepsilon_{matrix}}{\varepsilon_{matrix} + (\varepsilon_{eff} - \varepsilon_{matrix})P} = f_{domain} \frac{\varepsilon_{domain} - \varepsilon_{matrix}}{\varepsilon_{matrix} + (\varepsilon_{domain} - \varepsilon_{matrix})P}$$

Equation 5.1b
$$\varepsilon_{eff} = \varepsilon_{matrix} \frac{\varepsilon_{matrix} + (f_{domain} + f_{matrix}P)(\varepsilon_{domain} - \varepsilon_{matrix})}{\varepsilon_{matrix} + f_{matrix}P(\varepsilon_{domain} - \varepsilon_{matrix})}$$

where there are nanodomains (with dielectric constant ε_{domain}) occupying a volume fraction f_{domain}, which are embedded in a continuous matrix material (characterised by ε_{matrix}) of the corresponding volume fraction $f_{matrix} = 1 - f_{domain}$. P is the depolarization factor, a parameter that biases ε_{eff} according to the shape and orientation of the nanodomains ($0 \leq P \leq 1$) [1, 2, 5, 9], the details of which will be discussed further

below. Equation 5.1a is the MG formula in the form traditionally presented, and rearrangement of Equation 5.1a to express ε_{eff} explicitly gives Equation 5.1b. Thus given a certain nanodomain shape (P) and the assumption that the nanodomains are isolated from each other, the sizes of individual nanodomains can be calculated from f_{domain} if the spatial distribution of the nanodomains is known. Since the material values ε_{domain} and ε_{matrix} may be separately measured in the bulk, EMT provides an approach to deduce nanostructural information (f_{domain} and P) from measured optical properties (ε_{eff}) [9], even though the nanostructure cannot be directly resolved by light at wavelengths much larger than the nanodomains. Some theoretical assumptions must, naturally, be satisfied.

As stated at the beginning of the section, EMT analysis is concerned with the situation in which the characteristic size of the nanostructure/nanodomains (D) is much smaller than the wavelength of the incidence light (λ). A value of $D/\lambda < 0.1$ is usually held to be sufficient for the EMT approximation to be valid [9, 13]. For example, $D/\lambda < 0.1$ is easily satisfied by the BCP and AAO nanostructures (Figure 5.1) when probed with a red laser at λ = 633 nm. A more sophisticated discussion concerning the required relative "smallness" of D should also take into account the dielectric contrast across the nanodomains interfaces. Estimations that appeal to Mie scattering have been considered [4, 9, 12], and D is regarded as sufficiently small if the scattered intensity is considerably smaller than the transmitted intensity. For a ratio of $D/\lambda = 0.05 \sim 0.1$ found in the BCP and the AAO systems, a scattering loss in the range 2 ~ 10% is calculated. The size requirement also stems from other simplifying assumptions in deriving the MG formula.

Equation 5.1 was derived by considering the electrostatic response of the embedded nanodomains that are completely isolated from each other by the matrix material due to an external electric field [9, 12]. The electrostatic description is valid only if the domain and matrix materials are not electrical conductors, and this is evidently the case for the PS-b-PMMA and the AAO nanostructures. In the case of dielectrics, the electrostatic description is identical with the quasi-static limit, which allows a wavelength dependence of the dielectric response [8, 9, 12-14]. More specifically, in the quasi-static limit, the dielectric response induced by the incidence field is assumed to be instantaneous and in phase over the entire nanodomain. This description is also more easily observed if the nanodomains are small in terms of the incidence wavelength. In summary, the (quasi-)static analysis would apply for optical or longer wavelengths for the dielectric nanostructures considered in this study.

A consequence of assuming that the nanodomains are embedded within a matrix that completely isolates the domains from one another (even in the unphysical case of a f_{domain} so large that the nanodomains must start interpenetrating each other) is that equation 5.1 is not symmetric [12]. That is, if the positions of ε_{domain} and ε_{matrix}, and f_{domain} and f_{matrix} were exchanged, the ε_{eff} calculated from equivalent values of f_{domain} and $f_{matrix} = 1 - f_{domain}$ do not agree. This discrepancy grows larger as the

dielectric contrast increases (ε_{matrix} /ε_{domain} >> 1, for $\varepsilon_{matrix} > \varepsilon_{domain}$) and as f_{domain} approaches f_{matrix}. This problem was first considered by Bruggeman, who assumed that the local electrostatic response inside and outside a nanodomain should exactly balance each other [9, 12]. But this symmetric formulation implies, for intermediate f_{domain}, an interpenetrating two-phase geometry [9, 12]. Such a distribution of nanodomains is contrary to the arrayed, isolated cylindrical nanodomains of the PS-b-PMMA and the nanoporous AAO thin film morphologies. Moreover, the dielectric contrast for the PS-b-PMMA and the nanoporous AAO thin films considered are relatively small, from ε_{matrix} /ε_{domain} < 3 in the most "extreme" case of air-filled AAO pores to ε_{matrix} /ε_{domain} ~ 1 in the case of PS-b-PMMA (see later sections for discussions on the material dielectric constants). Thus the MG formula is the most appropriate to the optical investigations of the present nanostructures.

The depolarization factor P specifies the degree of polarizability, hence the charges induced, on the surfaces of the nanodomains relative to the strength of the incidence electric field. Consideration of Maxwell's equations across a material interface tells us that only the component of the electric field normal to the interface can induce surface charges. Therefore the value of P depends on the shape and orientation of the nanodomains with respect to the polarization of the incidence electric field. The limits $0 \leq P \leq 1$ accompanying Equation 5.1 may be understood in terms of a flat infinite interface. In the case of an applied electric field that is polarised normal to the interface, the entire strength of the field can be directed to induce polarization across the interface, and $P = 1$. In the case that the applied electric field is polarised parallel to the interface, no part of the field can induce polarization and $P = 0$. For a three dimensional nanodomain with interfaces oriented at intermediate angles to the incidence field, P may assume different, intermediate values along the principal spatial coordinates. As a matter of course, the sum of all components of P cannot exceed the maximum that can be applied by the incidence field, i.e. (in Cartesian coordinates) [6, 12, 15]:

Equation 5.2 $$P_x + P_y + P_z = 1$$

Accordingly, regarding the BCP or AAO nanodomains under discussion (Figure 5.1), different P's should be inserted into Equation 5.1 depending on whether the incidence electric field is polarised normal or parallel to the long axis of the cylindrical domains. That is, the cylindrical morphology acquires an anisotropic dielectric response. Since the BCP and AAO cylinders considered have a high aspect ratio larger than 10 (Figure 5.1), the polarizability contributions at the narrow ends of the cylinders may be neglected. Therefore, identifying the z-axis with the normal of the substrate surface, P_z ~ 0 along the long axis of the cylinders. Moreover, the cylinders are hexagonally ordered only locally (see Chapter 3) and may be considered

to be randomly arranged over a macroscopic area (such as the width of a laser beam ~1 mm wide). Therefore, according to Equation 5.2, $P_x = P_y = 1/2$ in the plane of the film (parallel to the substrate surface). In contrast, for an isotropic morphology (such as randomly distributed spherical nanodomains), P must be equal in all directions, i.e. $P_x = P_y = P_z = 1/3$. Analytical values of P have also been derived for ellipsoids of revolution (with semi-axes $a \neq b = c$) [12, 16-18]. In fact, the case of infinitely elongated ellipsoids of revolution models the case of cylindrical nanodomains [1, 7, 8, 13]. Numerical solutions of P applicable to complex shapes have also been calculated [8]. The basic variations in P are summarised in Table 5.1.

	x, parallel to substrate surface	y, surface parallel, orthogonal to x	z, perpendicular to substrate surface	$\Sigma_i(P_i)$
Nanocylinders oriented normal to substrate surface	1/2	1/2	0	1
Randomly distributed spherical nanodomains	1/3	1/3	1/3	1
Lamellae parallel to the substrate surface	0	0	1	1

Table 5.1. Summary of depolarization factors, P, along the principal axes of thin films with different nanostructures.

Examination of Equation 5.1 shows that ε_{eff} increases monotonically with decreasing P for real values of ε_{domain} and ε_{matrix} (i.e. for any combination of dielectric materials). In fact, ε_{eff} achieves its highest possible value for $P = 0$, and becomes the volume fraction weighted average of ε_{domain} and ε_{matrix}. Conversely, ε_{eff} achieves its lowest value for $P = 1$, and becomes the volume fraction weighted geometric average of ε_{domain} and ε_{matrix}. These are the Wiener absolute bounds, which can be compared to electrical capacitors connected in series and in parallel [9], and they specify the maximum anisotropy possible for any nanostructure.

In case that the cylindrical nanodomains possess internal structures of their own, such as when the pore surfaces in AAO are functionalised with a layer of material, Equation 5.1 may be applied step-wise to approximate ε_{eff} for the entire film [19]:

Equation 5.3a
$$\varepsilon_{eff}^{\text{entire film}} = \varepsilon_{\text{alumina}} \frac{\varepsilon_{\text{alumina}} + (f_{pore} + f_{\text{alumina}} P)(\varepsilon_{eff}^{\text{pore}} - \varepsilon_{\text{alumina}})}{\varepsilon_{\text{alumina}} + f_{\text{alumina}} P(\varepsilon_{eff}^{\text{pore}} - \varepsilon_{\text{alumina}})}$$

Equation 5.3b
$$\varepsilon_{eff}^{\text{pore}} = \varepsilon_{\text{unfilled pore}} \frac{\varepsilon_{\text{unfilled pore}} + (f_{\text{deposited material}} + f_{\text{unfilled pore}} P)(\varepsilon_{\text{deposited material}} - \varepsilon_{\text{unfilled pore}})}{\varepsilon_{\text{unfilled pore}} + f_{\text{unfilled pore}} P(\varepsilon_{\text{deposited material}} - \varepsilon_{\text{unfilled pore}})}$$

In this approach, ε_{eff} in the different orientations are substituted independently (cross terms are not considered). Moreover, there does not appear to be any experimental benefit to treating the multiple phases simultaneously within the MG formalism, as the theory is not symmetric with respect to the volume fractions. The approximation is also expected to be valid as long as the fraction of deposited material within the cylindrical pores is not too large. Fully anisotropic models are also available [7] but the numerical differences calculated from such models compared to the results from Equation 5.3 are not significant in the present context of dielectric nanodomains with a relatively low dielectric contrast to the matrix material to justify the additional theoretical complexity.

5.2. Optical waveguiding and Optical Waveguide spectroscopy (OWS)

OWS refers to the analysis of optical waveguide modes that are excited in a thin film slab waveguide in order to (independently) measure with high sensitivity, the thickness and the (anisotropic) dielectric function of the thin film. In the Kretschmann configuration [20] (shared with the SPR, see section 2.3), the dielectric waveguiding film is positioned at the base of a prism coated with a semi-transparent metal layer. Through this metal layer, optical coupling occurs, at specific combinations of incidence angles and wavelengths, between the incidence light directed through the prism and resonant waveguide modes propagating in the film. That is, the incidence light is channelled through the metal coupling layer into the dielectric thin film, where it is confined and is waveguided (propagated) throughout the film (Figure 5.2).

To enable convenient sample handling, the waveguiding film is actually prepared on top of a glass substrate which is pre-coated with the metal layer, and which has a dielectric constant identical to that of the prism. The glass substrate is then temporarily joined to the base of the prism with optical index-matching oil to form an optically homogeneous assembly during the OWS measurement.

Adjustment of the incidence angle (θ) controls the propagation constant, hence the momentum, of the incidence light parallel to the thin film surface ($k_x = k \sin\theta$, Figure 5.2), which is the component relevant to waveguiding in the planar thin film. To qualify as a waveguide, the thin film material must be optically transparent at the wavelength of the guided light. As we have already seen in section 5.1, the nanostructured BCP and AAO layers are effectively optically homogeneous with limited scattering losses at visible wavelengths, which make them suitable waveguide materials. (A He-Ne laser at λ = 632.8 nm is used throughout this study, unless otherwise stated.) Moreover, the dielectric constant ($\varepsilon = n^2$, where n is the refractive index[*]) of the waveguide must be higher than that of the top covering medium (e.g. air)

[*] $\varepsilon = n^2$ applies in the case of non-magnetic materials in the infinite frequency limit, such as for the insulating materials considered here, and at visible wavelengths.

so that light can be confined within the film thickness by total internal reflection (TIR) at the top interface. At the bottom, light is reflected from the metal coating on the glass substrate. In the Kretschmann setup, the dielectric constant of the prism is designed to be higher than the waveguide film, as will be further discussed below. Therefore light is totally reflected at the metal-prism interface at an incidence angle $\theta > \theta_{TIR} = \sin^{-1}(n_{cover}/n_{prism})$.* However, at specific angles when the momentum of the incidence light matches that the propagation properties of a waveguide mode, light is channeled into the waveguide and light is not reflected. Hence waveguide modes are measured as reflection minima in the reflected intensity (R) vs. θ scan. Figure 5.2 shows the prism-sample setup and the detection scheme.

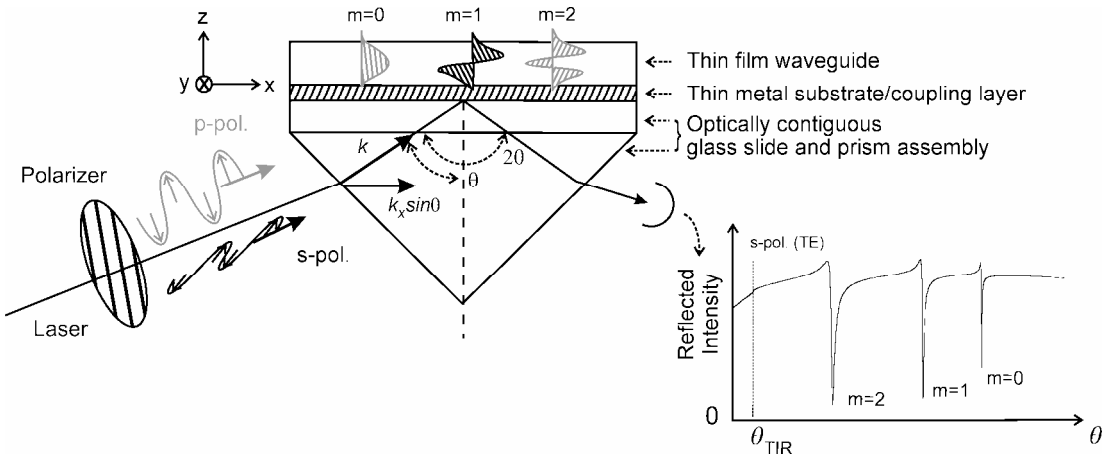

Figure 5.2. Schematic of prism coupling in the Kretschmann configuration and the waveguide mode detection scheme. $z = 0$ is at the interface between the thin film waveguide and the metal substrate. θ_{TIR} is the critical angle for total internal reflection. Schematics of the waveguide mode electric field distributions (E_y) are overlaid on the waveguiding film model. Only one waveguide mode is excited at any one time as the incidence angle θ is scanned between 0º and 90º. The R vs. θ trace on the lower right shows TE modes for a model thin film of thickness h = 840 nm and ε = 2.4. The number of waveguide modes excited and their angle positions depend on the exact values of h and ε.

The momentum of a waveguide mode can be determined by analysis of Maxwell's equations and by matching the phase shifts acquired as the light propagates within the waveguide, and as it interacts with the interfaces [20-22]. The phase matching condition is specified by the waveguide film thickness (h) and in terms of a propagation constant (β), which specifies the momentum of the waveguided light. Therefore β is dependent on the dielectric constants of the system (ε_i) and the polarization of the light. The polarization may have principal components parallel to the surface (s-polarization, along the y-direction) and perpendicular to it (p-polarization, along the z-direction). These are also known as TE (transverse electric)

* By Snell's law of refraction: $n_{prism}\sin\theta_{prism} = n_{metal}\sin\theta_{metal} = n_{film}\sin\theta_{film} = n_{cover}\sin\theta_{cover}$. Total internal reflection occurs when $\theta_{cover} > 90°$. Note that n_{metal} is complex, therefore so is θ_{metal}.

and TM (transverse magnetic) modes, respectively. Accordingly, these modes are represented by the fields: **E** = (0, E_y, 0) or equivalently **H** = (H_x, 0, H_z) for the TE modes, and **H** = (0, H_y, 0) or equivalently **E** = (E_x, 0, E_z) for the TM modes. To illustrate how the propagation modes are influenced by ε and h, the case of the asymmetric slab waveguide shown in Figure 5.3 is examined below.

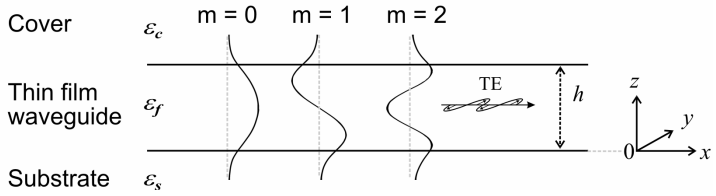

Figure 5.3. Light propagation in a thin film waveguide of thickness h in the 3-layer slab waveguide model considered. z = 0 is at the interface between the thin film and the substrate. The electric field amplitudes of Ey(z) for the first three TE modes are shown schematically. The evanescent tails emanating from the interfaces give rise to the Goos-Hänchen shift. (Adapted from Knoll [20].)

For the planar geometry under discussion, the guided light propagating in the x-direction is only confined in the thickness (z) direction. Moreover, for the principal polarizations, only the y-components in the electric field for TE modes, and the y-component in the magnetic field for TM modes, are non-zero. Furthermore, for field solutions consistent with Maxwell's equations, the propagating modes should be oscillatory within the thickness of the waveguide, and confinement further specifies that the fields should decay exponentially into the cover and substrate layers. Thus the field solutions of the propagation modes are of the forms (omitting the time dependence and propagation in the x-direction) [20, 21]:

Equation 5.4a $A_y = A_c e^{-\alpha_c (z-h)}$ $\qquad \alpha_c = \sqrt{\beta^2 - \varepsilon_c \omega^2 / c^2}$ $\qquad$ for $h \le z$

Equation 5.4b $A_y = A_f \cos(\kappa_f z - \phi)$ $\qquad \kappa_f = \sqrt{\varepsilon_f \omega^2 / c^2 - \beta^2}$ $\qquad$ for $0 \le z \le h$

Equation 5.4c $A_y = A_s e^{\alpha_s z}$ $\qquad \alpha_s = \sqrt{\beta^2 - \varepsilon_s \omega^2 / c^2}$ $\qquad$ for $z \le 0$

where the subscripts c, f, and s stand for, respectively, the cover, the thin film and the substrate layers; A stands for either E (TE modes) or H (TM modes); α and κ are the decay and propagation constants in the y-direction, respectively; ϕ is the phase shift; and β is the waveguide mode propagation constant. Incidentally, $\sqrt{\varepsilon}\omega/c$ specifies the momentum of freely traveling light in a material with dielectric constant ε (c is the speed of the light in vacuum, and ω is its frequency). To specify the solutions, ϕ and β can be obtained by appealing to the boundary conditions: i) the fields are matched at z = 0, and z = h, and ii) the phase shift across the thickness of the film is a multiple of π:

Equation 5.5a $$\kappa_f h - \phi_s - \phi_c = \mathrm{m}\pi \quad (\mathrm{m} = 0, 1, 2\ldots)$$

Equation 5.5b **for TE modes:** $$\phi_s = \tan^{-1}\frac{\alpha_s}{\kappa_f} \quad \textbf{and} \quad \phi_c = \tan^{-1}\frac{\alpha_c}{\kappa_f}$$

Equation 5.5c **for TM modes:** $$\phi_s = \tan^{-1}\frac{\varepsilon_f}{\varepsilon_s}\frac{\alpha_s}{\kappa_f} \quad \textbf{and} \quad \phi_c = \tan^{-1}\frac{\varepsilon_f}{\varepsilon_c}\frac{\alpha_c}{\kappa_f}$$

To impose phase shifts (left hand side of Equation 5.5a) that sum to integer multiples of π (right hand side of Equation 5.5a) means that only discrete values of the propagation constants β are allowed for given combinations of ε_f, ε_s, ε_c, and h. The value m specifies the waveguide mode number, and the permitted values β_m can be obtained graphically or numerically. These are drawn for different values of h, ε_f and m in Figure 5.4 for TE modes, but the discussion also applies directly to TM modes. The waveguide modes are also referred, according to m, as TE_0, TE_1,… and TM_0, TM_1, etc. The schematics of the corresponding TE field amplitude distributions $E_y(z)$ are shown in Figure 5.3. An important point to note is that the higher order modes are more "leaky", i.e. larger portions of the waveguide mode optical fields actually reside outside the film, in the evanescent parts of the field. Thus the higher order modes are more sensitive to the properties at the fringes of the waveguide.

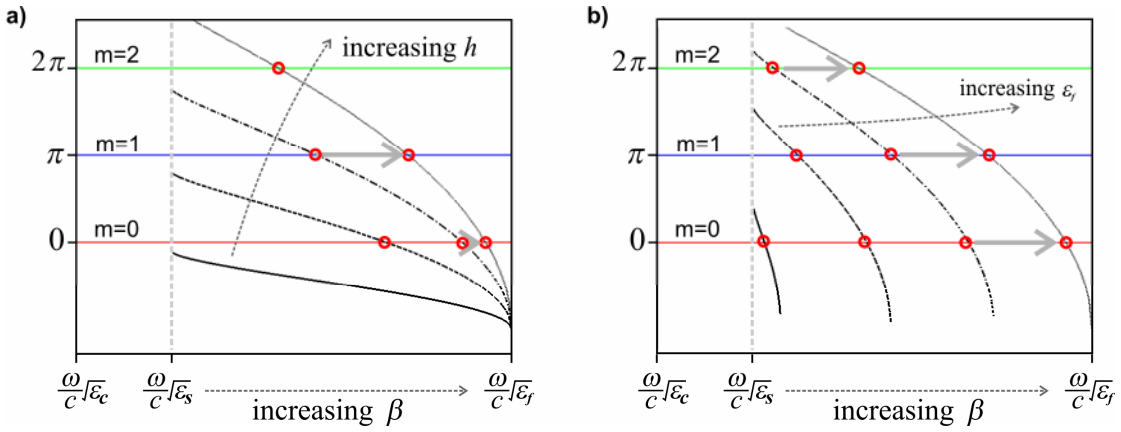

Figure 5.4. Graphical solutions of β. The curves in black indicate the left hand side of Equation 5.5a, plotted with increasing h at constant ε_f (a), or with increasing ε_f at constant h (b). The right hand side of Equation 5.5a are the constants 0, π, and 2π, representing the modes m = 0, 1, and 2, respectively. The solutions β_m are indicated by the red circles. The horizontal arrows in (a) indicate that the shifts in β_m with increasing h for the different modes are highly asymmetric, while in (b) the shifts with increasing εf for the different modes are more comparable. The curves were calculated for TE modes, with ε_s = 1.7, ε_c = 1.7, ε_f = 1.76 to 2.51, and h = 1 to 6 µm, but the basic trends also apply to TM modes.

Other than the discrete nature of β, Figure 5.4a shows that Equation 5.5a can be satisfied up to higher integers m as the film thickness increases. That is, thicker waveguides support more waveguide modes (discrete solutions β_m), and the same

modes are shifted to higher β (arrows in Figure 5.4a). However, a minimum (cut-off) thickness is required for solutions to β to exist, due to the fact that real values of Equation 5.5 and Equation 5.4 are obtained only for $\beta > \sqrt{\varepsilon_s}\omega/c$ (for $\varepsilon_s > \varepsilon_c$). Moreover, since only the first term on the left hand side of Equation 5.5a is dependent on h, the left hand side value is not affected by h in the limit $\beta \rightarrow \sqrt{\varepsilon_f}\omega/c$ as $\kappa_f \rightarrow 0$. Thus increases in h shift the permitted values of β more for higher mode numbers m (Figure 5.4a). Figure 5.4b shows that Equation 5.5a can also be satisfied for higher mode numbers m with increases in ε_f. That is, increasing ε_f supports more waveguide modes, and the same modes are shifted to higher β (arrows in Figure 5.4b). In this case, all terms on the left hand side of Equation 5.5a increase with ε_f. Therefore the increases in β with increases in ε_f for the different modes are relatively similar to each other. Careful examination of the mode shifts in fact shows slightly larger shifts for *lower* mode numbers m, which is opposite in behaviour to changes due to h. Consequently, inspection of the relative shifts in β between different modes can distinguish changes in ε_f from those in h.

In the foregoing discussion, the source of the guided light has been omitted to simplify the analysis and to emphasise the roles of ε_f and h in determining the waveguide response. It is also shown that β, which specifies the momentum of the propagating light, is always larger than $\sqrt{\varepsilon_s}\omega/c$, where $\varepsilon_s > \varepsilon_c \geq \varepsilon_{air}$. Thus β is also larger than momentum of light of the same frequency travelling in free space (i.e. air: $\sqrt{\varepsilon_{air}}\omega/c$). Consequently, a coupling device is needed to increase the momentum of an external (monochromatic) source above $\sqrt{\varepsilon_{air}}\omega/c$ up to the value β in order to excite waveguide modes [20, 23]. In the Kretschmann configuration (Figure 5.2), a high index prism with $\varepsilon_p > \varepsilon_f$, and therefore a propagation constant for light traveling in the prism $k_p = \omega\sqrt{\varepsilon_p}/c > \beta$, is used. Since $\varepsilon_p > \varepsilon_f > \varepsilon_c$, total internal reflection occurs at the base of the prism at incidence angles $\theta \geq \theta_{TIR} = \sin^{-1}(n_c/n_p)$ according to Snell's law of refraction ($n = \sqrt{\varepsilon}$, is the refractive index). The total internal reflection (TIR) is also characterised by an evanescent, exponential field that decays away from the base of the prism. Moreover, in the Kretschmann configuration, the waveguide substrate layer is a metal coating prepared directly on the base of the prism, and its thickness is reduced to such an extent that the energy of the TIR evanescent field can tunnel through the metal into the thin film waveguide via momentum coupling with a waveguide mode, at a specific mode excitation angle θ_m that satisfies $k_p \sin(\theta_m) = \beta_m$ [23]. In other words, the incidence angle θ at the base of the prism controls the momentum of the incoming light in the direction parallel to the substrate (higher θ correspond to higher β), and selects the waveguide mode to be excited (Figure 5.2).

The advantage of using a metal substrate/coupling layer is that its thickness, hence the coupling efficiency, can be controlled with high precision by vacuum deposition of the metal layer. The consequence for waveguide mode propagation is

that the propagation length is considerably reduced* due to optical damping by the metal [28, 29]. At the same time, the symmetric prism characteristic of the Kretschmann configuration leads to the back-coupling of the waveguide modes propagating in the thin film out into the prism, simultaneous with the excitation of waveguide modes. The destructive interference between the incidence and back-coupled waves leads to a minimum in the reflected intensity around the waveguide mode coupling angles, and enables the direct detection of waveguide mode coupling: as the incidence angle is scanned from θ_{TIR} up to 90º, the incidence light is reflected except at angles θ_m where mode coupling and the associated destructive interference result in minima in the reflected intensity, R (Figure 5.2, lower right). Analysis of these angle minima (R vs. θ measurements) with respect to the thin film waveguide ε_f and h constitutes optical waveguide spectroscopy.

The use of a metal coupling layer also leads to the excitation of a surface plasmon mode (section 2.3) as the fundamental guided mode in p-polarization (TM mode m = 0, i.e. TM_0). However, the surface plasmon is sensitive only to the dielectric response adjacent to the metal layer, and is not sensitive to the "bulk" response through the thickness of the waveguide (or external stimuli). The surface plasmon mode is also often excited at very high momentum and (grazing) incidence angles. Therefore this mode is often not used for waveguide analysis.

A further effect of the metal coupling layer is that higher order modes have broader mode minima than lower order modes. As discussed on page 81, a large part of the fields for higher order modes reside outside the waveguiding film. Thus the metal substrate/coupling layer can interact more with the guided light and damps the higher order modes to a greater extent, broadening the minima.

The R vs. θ results are most conveniently analyzed quantitatively by the Fresnel equations without explicitly solving for the optical fields and β in Equation 5.4 and Equation 5.5 [20, 30, 31]. The Kretschmann configuration is just a multilayer system composed of infinite (with respect to the laser beam ~1 mm wide) slabs of material, and the Fresnel equations are exact solutions to Maxwell's equations derived explicitly to calculate the reflected intensity as functions of ε (or equivalently n) and h for such a multilayer geometry [31, 32]:

Equation 5.6a $$R = \left|r_{0123\ldots n}\right|^2 = \left|\frac{r_{01} + r_{123\ldots n}e^{i2h_1k_1}}{1 + r_{01}r_{123\ldots n}e^{i2h_1k_1}}\right|^2 \quad ; \quad r_{ij} = \frac{n_j^{2\gamma}k_i - n_i^{2\gamma}k_j}{n_j^{2\gamma}k_i + n_i^{2\gamma}k_j}$$

* Optical damping by the metal layer also results in broadening of the waveguide mode excitation conditions. This reduces the sharpness of the reflected intensity minima in the measurements, and results in a corresponding loss in precision in determining ε_f and h from the waveguide mode response. Thus Ag or Au, which have the lowest damping loses among the metals, are usually used as coupling layers. ε_f is commonly measured only up to parts per 10^3 ~ 10^4 in OWS, which can be a few orders of magnitude lower than for other dielectric waveguide sensing schemes [24-27].

Equation 5.6b $$n_i \sin\theta_i = n_j \sin\theta_j \quad ; \quad k_i = \frac{\omega}{c} n_i \cos\theta_i \quad ; \quad \gamma = \begin{cases} 0 & \text{TE modes} \\ 1 & \text{TM modes} \end{cases}$$

where the numbered subscripts 0,1,2,3… denote consecutive layers of a general multilayer system with up to n layers prepared on top of prism base in the Kretschmann configuration. Layer 0 refers to the prism, layer n refers to the top-most unbounded cover layer (e.g. air), and θ_0 refers to the incidence angle at the base of the prism. Trial values of ε_i and h_i may then be substituted into Equation 5.6 to calculate the expected R vs. θ response, which is compared with the OWS measurement. The best fit then corresponds to the ε_i and h_i describing the actual waveguide system. This methodology has been used extensively to analyze both OWS and SPR results [20, 30, 31].

As discussed in section 5.1, the nanostructured BCP and AAO thin films possess anisotropic dielectric constants, and the above analysis of waveguide mode propagation and the Fresnel equations can be expanded to describe anisotropic films [32]. In particular, TE modes, which have an electric field component only in the *y*-direction, are sensitive primarily to ε_y (= ε_x), and TM modes are sensitive primarily to ε_z. At the same time, as discussed within the context of Figure 5.4, the influences of ε_f and h on the waveguide mode response may be distinguished by examining the relative positions of the excitation angles θ_m (where $k_p \sin(\theta_m) = \beta_m$) corresponding to different waveguide modes. In an analogous way, the contributions from the different components of $\varepsilon_f = \{\varepsilon_x , \varepsilon_y , \varepsilon_z\}$ and h of the anisotropic waveguide are distinguished from each other by the relative angle positions of the TE and TM modes. Evidently, $\{\varepsilon_x , \varepsilon_y , \varepsilon_z\}$ and h may only be measured independently if there are at least as many waveguide modes as variables, which means that the waveguide should be thick enough to support a sufficient number of modes to adequately analyze the optical properties of the waveguide. Fresnel calculations were implemented with the program WINSPALL [33]. Further information on the Kretschmann configuration and OWS, are given in several reviews [20, 22, 30].

5.3. PS-b-PMMA thin film waveguides and BCP nanostructure characterization

BCP films have not been explored in the field of optical elements, in particular, waveguiding layers, although polymer-based optical materials have been widely applied [34]. Since the domain size and chemical nature of BCP's can be tailored by controlling their molecular weights and by incorporating specific functionality, BCPs may act as waveguiding layers with tunable dielectric constants and optimised physicochemical properties in integrated optical devices. Here, we demonstrate that thin films of BCPs with controlled microdomain orientation can be employed as planar optical waveguides and investigate their optical response by OWS. Although

the propagating light in a planar thin film (slab) waveguide is only confined in the thickness direction of the film, the analysis of the slab waveguide is theoretically and experimentally simple, and provides the full information necessary for characterizing the nanostructured BCP thin film.

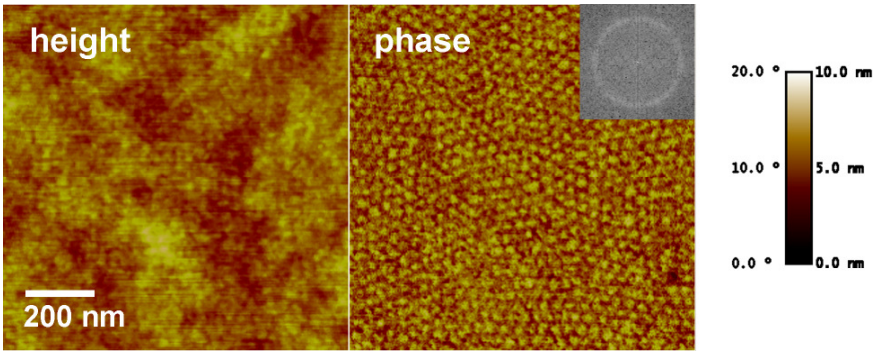

Figure 5.5. AFM height and phase images of the surface nanopattern self-assembled from PS-b-PMMA/PMMA blend with total PS-b-PMMA M_n = 56 kg/mol and homopolymer PMMA M_n = 13.8 kg/mol. In the phase image, PS surfaces appear as darker areas. $\lambda_{C\text{-}C}$ (46 nm) was measured from the FFT shown as the greyscale inset. (PS-b-PMMA/PMMA sample was prepared courtesy of Prof. Dr. Juan Peng, now at Fudan University, Shanghai, China.)

As discussed in the previous section, a sufficiently thick film is needed to support multiple waveguide modes for analysis of the film's anisotropic dielectric response. Therefore we focused on the "thick" films of asymmetric PS-b-PMMA blended with PMMA homopolymer with $h > 10\lambda_{C\text{-}C}$, described in section 3.1, for the demonstration of BCP waveguides. These samples were prepared on Ag coupling coatings functionalised with surface energy neutral P(S-r-MMA) brush layers. The AFM surface measurement of such a sample, reproduced from Figure 3.9 for convenient referencing, is shown in Figure 5.5. $\lambda_{C\text{-}C}$ between the PMMA minor cylindrical domains is 46 nm and films were prepared with h between 200 ~ 500 nm (section 3.1.5).

Figure 5.6a shows the OWS R vs. θ measurement* for a PS-b-PMMA/PMMA film. Two waveguide mode minima were observed when measured with incidence light under s-polarization at ~35° (TE_1) and ~59° (TE_0), and one mode was observed in p-polarization at ~49° (TM_1). The surface plasmon mode (TM_0) was expected to appear at grazing angles according to Fresnel calculations and was not measured within the current angle range. The minimum at θ_{TIR} under p-polarization was not an independent waveguide mode but was convoluted with the reflectivity change due to

* Note that, for experimental convenience, the incidence angles shown in the R vs. θ measurements throughout this report refer to the external angle defined by the goniometer setup in the Kretschmann configuration, not the internal incidence angle within the prism. The internal angle θ', relevant to Fresnel calculations, is related to the external angle θ by: $\sin(45°-\theta) = n_{prism}\sin(45°-\theta')$.

total internal reflection, and was not used for analysis. Figure 5.5 indicates that over a large area, such as the ~1 mm wide incidence laser beam, the domains can be considered disordered in the plane of the film, that is, the dielectric response in the plane of the film is isotropic, and $\varepsilon_x = \varepsilon_y$ (z is along the surface normal). Thus the three modes suitable for analysis could be used to measure the three parameters describing the film— $\{\varepsilon_x = \varepsilon_y, \varepsilon_z\}$ and h —independently. Fitting by Fresnel calculations gave $\varepsilon_{film} = \{2.4047, 2.4047, 2.4100\}$ and $h = 464$ nm. The thickness and dielectric constant of the Ag coupling layer was: $h_{Ag} = 44$ nm and $\varepsilon_{Ag} = -17+0.5i$.* The dielectric constant of air ($\varepsilon_{air} = 1.0000$) was also verified independently by the reflected intensity disturbance at the critical angle of total internal reflection, $\theta_{TIR} = \theta_{air} = \sin^{-1}(n_{air}/n_{prism})$. Actually, since ε_{air} has a fixed value at room temperature and pressure, and $\varepsilon_{prism} = 3.406$ is specified by the glass manufacturer, θ_{air} was used as the angle calibration for the OWS setup.

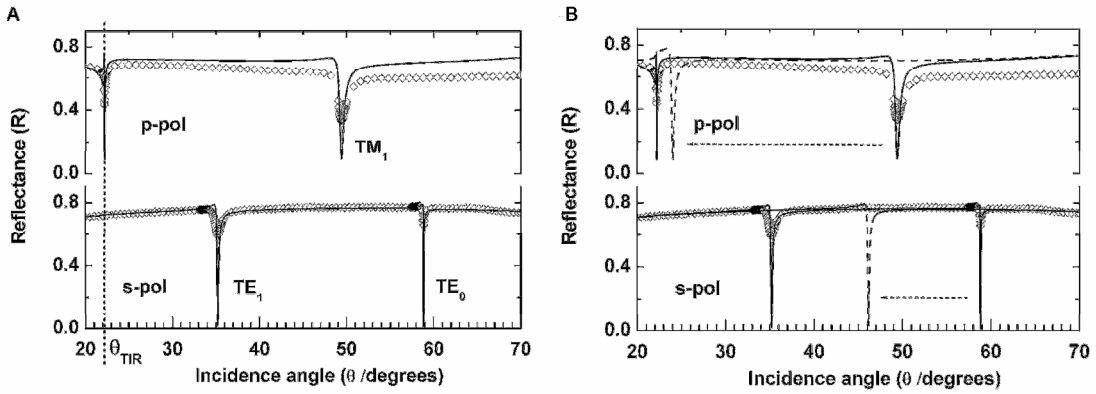

Figure 5.6. (A) OWS R vs. θ measurement of a PS-b-PMMA/hPMMA waveguide sample (symbols) with the following parameters measured by Fresnel calculations (solid lines): $\varepsilon_{film} = \{2.4047, 2.4047, 2.4100\}$ and $h = 464$ nm. One waveguide mode plus the reflectivity disturbance near θ_{TIR} can be observed for the measurement in p-polarization (top), and 2 waveguide modes could be observed under s-polarization (bottom). (B) The R vs. θ measurement of the same sample shown alongside the waveguide response of a hypothetical PS-b-PMMA/PMMA film with the same ε_{film} but half the thickness. The modes are shifted to lower angles for the thinner film, and only one mode could be observed under each polarization.

The angle positions for the measured and calculated waveguide mode minima could be matched accurately using the fitted values of ε_{film} and h (Figure 5.7), although significant broadening of the measured reflectivity minima compared to the calculations were observed. This is a common phenomenon for actual thin film samples, and is generally caused by surface roughness and lateral heterogeneity of the

* ε_{Ag} used was based on the literature value [30, 35]. The thickness of the adhesion and neutral surface energy layers (section 3.1.2): 3-MPS (2 nm), SiO_2 (33nm), and PS-r-PMMA (4 nm), were measured separately by SPR after each preparation step. Note that deposition parameters, aging, annealing and other factors can significantly alter thin film optical values.

samples [22, 30, 36]. The fitted film thickness was verified by measurement with a line profiler, and showed agreement to within the uncertainty of the profilometer (~10 nm). Also, the measured components of ε_{film} are reasonable values because, for a film that has both PS and PMMA components, they fall in between the dielectric constants of pure PS and PMMA (ε_{PS} = 2.53 and ε_{PMMA} = 2.22) [37, 38]. The measured waveguide response was also compared to that of a hypothetical PS-b-PMMA/PMMA film with the same ε_{film} but half the thickness in Figure 5.6b. The modes are seen to shift to lower angles for the thinner film, and only one mode could be observed under each polarization, and as such would be insufficient to independently characterise {$\varepsilon_x = \varepsilon_y$, ε_z} and h.

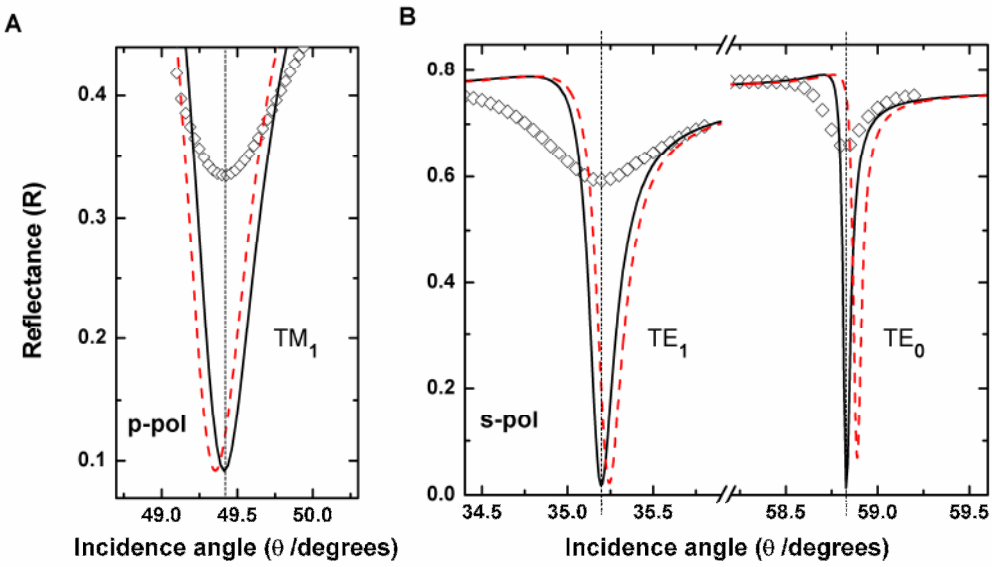

Figure 5.7. Detailed views of the waveguide modes shown in Figure 5.6. The Fresnel fitting (solid curves, which coincide with the EMT calculations corresponding to the perpendicular cylindrical morphology) matches the measured angle minima (symbols) accurately. The corresponding isotropic EMT model (red dashed curves) predicts too low angle minima for the measurement in p-polarization, and too high minima in the s-polarization measurement.

In the present example of PS-b-PMMA/PMMA films, although the locally ordered PMMA domains observed by AFM (Figure 5.5) already suggest that the intended perpendicular cylindrical morphology was successfully prepared, such surface measurements do not provide direct evidence for the interior structure of the sample. Therefore OWS measurements of the BCP film's dielectric response, which is a "bulk" measurement of the film, combined with effective medium theory (EMT) analysis (section 5.1), can fill an important gap for the (quantitative) non-destructive optical characterization of the film's nanostructure.

First, the anisotropic dielectric response ($\varepsilon_y \neq \varepsilon_z$) measured already indicates the presence of an anisotropic nanostructure within the BCP film. The difference (ε_z –

ε_y) > 0.005, and is much larger than effects of molecular packing, such as the intrinsic anisotropy of α-helical poly(γ-benzyl-L-glutamate), which is < 0.001 (see section 5.4.2). Furthermore, the measured dielectric constants can be compared with the prediction from the EMT cylindrical model. In fact, we can consider a number of specific questions concerning the BCP waveguide system: is the volume fraction of PMMA (and of PS) in the film prepared the same as intended during PS-b-PMMA synthesis and PMMA blending? Are the literature values for ε_{PS} and ε_{PMMA} directly applicable to the polymers thin films? How well does the cylindrical model describe the BCP film given the uncertainties in the volume fraction of PMMA (f_{PMMA}) and ε_{PS} and ε_{PMMA}? As a matter of course, the analysis is always bounded by the fact that information on the nanostructure was derived only from the two measured dielectric parameters: $\varepsilon_x = \varepsilon_y$ and ε_z.

In the EMT model for the perpendicular cylindrical morphology, the anisotropic dielectric response is found by substituting in Equation 5.1 P = 1/2 for $\varepsilon_x^{eff} = \varepsilon_y^{eff}$, and P = 0 for ε_z^{eff} (Table 5.1). Given literature values ε_{PS} = 2.53 and ε_{PMMA} = 2.22 [37, 38], values for $\{\varepsilon_x^{eff}, \varepsilon_y^{eff}, \varepsilon_z^{eff}\}$ may be calculated for different $f_{PMMA} = f_{cylinder} = 1 - f_{PS}$ to find the best fit with the OWS measurement $\{\varepsilon_x, \varepsilon_y, \varepsilon_z\}$. Both the difference between ε_{film} and ε_{film}^{eff} and the degree of anisotropy should be taken into account in such a fitting procedure:

Equation 5.7 $$\text{Fitting error} = \left|\varepsilon_x^{eff} - \varepsilon_x\right| + \left|\varepsilon_z^{eff} - \varepsilon_z\right| + \left|(\varepsilon_x^{eff} - \varepsilon_z^{eff}) - (\varepsilon_x - \varepsilon_z)\right|$$

Using Equation 5.7, a best fit value of $\varepsilon_{film}^{eff} = \{\varepsilon_x^{eff}, \varepsilon_y^{eff}, \varepsilon_z^{eff}\} = \{2.047, 2.047, 2.094\}$ was obtained and corresponded to f_{PMMA} = 0.39, which is close to the intended value of = 0.35 ± 0.02. (The uncertainty assumed is due to measurement errors during blending of the PMMA and PS-b-PMMA and solution preparations.) Note that the fitting error between the EMT model and the OWS measurement calculated by Equation 5.7 is only 0.0012, which is less than the degree of anisotropy, and less than 0.1% of $\{\varepsilon_x, \varepsilon_y, \varepsilon_z\}$. The calculated and measured film dielectric constants and volume fractions are shown in Table 5.2 for comparison (rows A and B).

Preparation conditions can induce significant changes to the dielectric constant of a thin film [39], as can polymer molecular weight and sample purity. Therefore the literature values may not be strictly applicable to the present BCP films. On the other hand, it is possible to measure the ε_{PS} and ε_{PMMA} specific to the PS-b-PMMA/PMMA thin film by assuming that $f_{PMMA} = f_{cylinder}$ = 0.35 ± 0.02, corresponding to the intended PS-b-PMMA/PMMA blending ratio. In this case, the best fit $\{\varepsilon_x^{eff}, \varepsilon_y^{eff}, \varepsilon_z^{eff}\}$ were calculated by varying ε_{PS} and ε_{PMMA} while f_{PMMA} was kept constant at 0.35 to minimise the difference with the OWS measurement $\{\varepsilon_x, \varepsilon_y, \varepsilon_z\}$. The fitted results, also shown in Table 5.2 (row C), are ε_{PS} = 2.528 ± 0.005 and ε_{PMMA} = 2.192 ± 0.009, and the fitting error approached zero. These fitted values of ε_{PS} and ε_{PMMA} are actually in

agreement with the literature values, given the uncertainties arising from the original uncertainty in f_{PMMA}. Therefore, taken together, the analyses based on literature values of ε_{PS} and ε_{PMMA} and that based on a fixed f_{PMMA}, show that the dielectric response of the BCP film measured by OWS is in excellent agreement with the perpendicular cylindrical morphology.

	f_{PMMA} ($f_{cylinder}$)	$\varepsilon_x = \varepsilon_y$	ε_z	Error	ε_{PS}	ε_{PMMA}	$P_x = P_y$	P_z
(A) OWS measurement	/	2.4047	2.4100	/	/	/	/	/
(B) EMT best fit to cylindrical morphology	0.389	2.4047	2.4094	0.0012	2.530	2.220	1/2	0
(C) EMT best fit assuming fixed f_{PMMA}	0.350	2.4047	2.4100	0.0000	2.528	2.192	1/2	0
(D) EMT calculated for a isotropic structure	0.350	2.4065	2.4065	0.0106	2.530	2.220	1/3	1/3

Table 5.2. Measured (A) and fitted (B)-(D) dielectric constants for the PS-b-PMMA/PMMA thin film with cylindrical morphology oriented normal to the substrate surface.

The dielectric response predicted from the cylindrical model can also be compared with EMT predictions for different morphologies in order to gauge the model's suitability. For example, if the PS-b-PMMA/PMMA self-assembly failed for some reason, and the PS and PMMA microphase separated in a disordered fashion to form randomly distributed PMMA domains embedded in a PS matrix, the dielectric response would also be isotropic and is predicted from Equation 5.1 by substituting P = 1/3 (Table 5.1). Using the values ε_{PS} = 2.528 and ε_{PMMA} = 2.192 obtained from the previous analysis, ε_{film} = 2.4065 is calculated for such an isotropic film (Table 5.2, row D). The corresponding R vs. θ waveguide response calculated by Fresnel equations is compared with the measured OWS results and the fitted EMT cylindrical model in Figure 5.7. Since the isotropic model predicts a dielectric constant that is lower than ε_z and higher than $\varepsilon_x = \varepsilon_y$ in the fitted cylindrical model, the waveguide mode angles predicted for the isotropic model can be expected, respectively, to be lower than the OWS data for the measurement in p-polarization and higher than the data for the s-polarization measurement. As seen in Figure 5.7, the R vs. θ responses for isotropic EMT model are clearly distinguishable from the OWS measurements, even though the absolute differences in the mode minima angles between the cylindrical and isotropic models are small. Moreover, the fitting error for the isotropic model is an order of magnitude higher than for cylindrical model (Table 5.2). Indeed,

any EMT model that predicts a degree of anisotropy between the components of the dielectric response in the directions normal and parallel to the film surface lower than the cylindrical model simply cannot explain the measured optical anisotropy. Furthermore, for a nanostructure that is macroscopically uniform in different directions within the plane of the film ($\varepsilon_x = \varepsilon_y$), the constraint in depolarization factors imposed by Equation 5.2 means that the perpendicular cylindrical morphology is the structure with the highest degree of anisotropy with $\varepsilon_z > \varepsilon_x = \varepsilon_y$. In other words, the measured anisotropic dielectric response is best described by the perpendicular cylindrical morphology within the context of EMT.

The cylindrical domain diameter (D) of the PS-b-PMMA/PMMA film can also be approximated from the f_{PMMA} estimated from EMT analysis and the $\lambda_{C\text{-}C}$ measured from AFM surface measurements, if the cylindrical nanodomains are assumed to form a close-packed hexagonal arrangement throughout the plane of the film:

Equation 5.8
$$D = \lambda_{C-C}\sqrt{\frac{4 f_{PMMA}\sin 60^0}{\pi}} \;;\; f_{PMMA} = \frac{\pi\left(D/2\right)^2}{{\lambda_{C-C}}^2 \sin 60^0}$$

Taking values of $\lambda_{C\text{-}C}$ = 46 nm and f_{PMMA} = 0.35 ~ 0.39, D was estimated to be 29 ~ 30 nm, which is in good agreement with the AFM measurement (Figure 5.5).

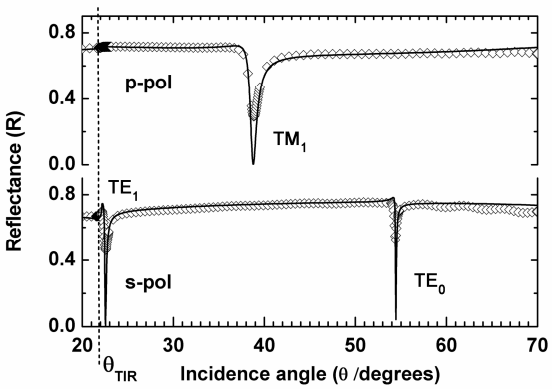

Figure 5.8. OWS R vs. θ measurement of a PS-b-PMMA/PMMA waveguide sample (symbols) with the following parameters measured by Fresnel calculations (solid lines): ε_{film}= {2.4047, 2.4047, 2.4100} and h = 345 nm. One waveguide mode near θ_{TIR} can be observed for the measurement in p-polarization (top), and 2 waveguide modes could be observed under s-polarization (bottom).

The waveguide response of another PS-b-PMMA/PMMA film was also measured by OWS (Figure 5.8) and could also be fitted with ε_{film} = {2.4047, 2.4047, 2.4100}. But the film thickness was thinner in this case: h = 345 nm. Three waveguide modes were still observed, but the s-polarization mode at ~23º was already

very close to the observable limit of at θ_{TIR} = 22.1°. Thus this film thickness represents the limit below which OWS characterization of the PS-b-PMMA/PMMA film would not provide the full information on the ε_{film} and h characteristics. Further experiments on changing the PS-b-PMMA/PMMA waveguide properties by solvent treatment and subsequent thermal annealing are described in Appendix C.

5.4. Nanoporous AAO waveguide sensing

In an earlier report [19], the sub-wavelength nature of the nanoporous AAO thin films has been shown to enable optical waveguiding at visible wavelengths, and enable the EMT description of the anisotropic dielectric constants of the nanoporous structure. This description is analogous to the BCP waveguide characterization just discussed in the previous section. Other groups have also applied the concept to a variety porous waveguide systems [40-43]. Moreover, high sensitivity sensing, by the EMT analysis of the dielectric constant changes of the nanostructure during uniform deposition of materials on the pores walls, was demonstrated in the earlier report. In this section, this sensing concept based on the optical anisotropy generated by the film nanostructure is further explored.

The basic methodology in analyzing the nanoporous AAO waveguide response is presented in section 5.4.1 through the example of the uniform functionalization of the anodic alumina surface with a silane layer. In section 5.4.2, the ability of the waveguide-nanoporous AAO sensing to distinguish processes within the pores and on the top surface of the AAO film is demonstrated with an example of layer-by-layer deposition of dendrimer polyelectrolytes. It was observed that the LbL process within the pores ceased after a number of layers while that on the top surface proceeded unabated. In section 5.4.3, the in situ characterization of surface initiated polymerization of a polypeptide, poly(γ-benzyl-L-glutamate), is presented. EMT analysis of the AAO film dielectric constants was able to discern the development of an anisotropic polymeric nanostructure with the AAO pores. Lastly, in section 5.4.4, excitation of fluorophores by the guided light within the nanoporous AAO, and sensing based on the fluorescence signal are demonstrated.

5.4.1. EMT description and uniform deposition of silane layers

The surface functionalization of the AAO film with an oxysilane was performed to enable the preparation of the macromolecular film structures to be described in later sections. The EMT analysis is similar to that already introduced in section 5.3 to describe the PS-b-PMMA/PMMA waveguide. The differences are that the dielectric constant of the nanoporous film can change as different materials are introduced into the pores, and that there are now three components in the films system:

alumina, the material deposited on the pore walls, and the medium filling the rest of the pore (air or solvent).

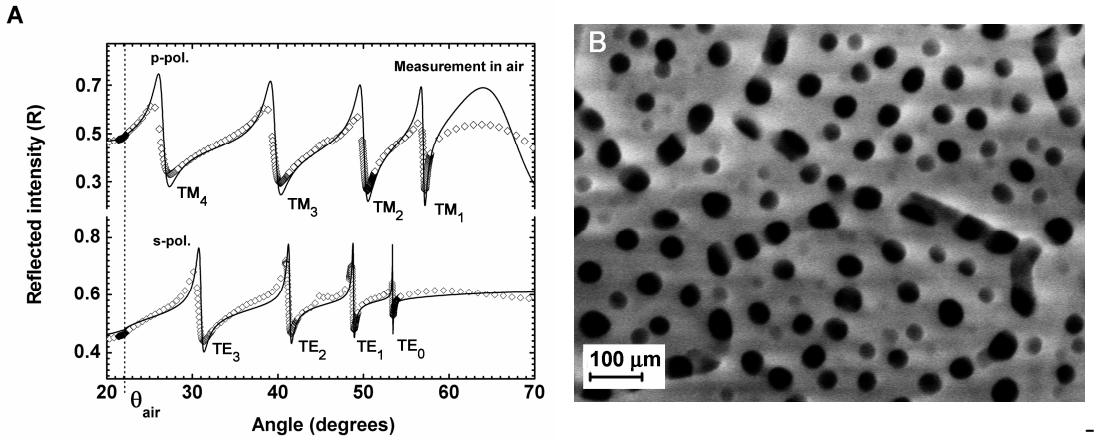

Figure 5.9. (A) R vs. θ measurement of an AAO film, the SEM top view of which is shown in (B). Symbols in (A) show the OWS data and the solid lines show the fitted Fresnel calculations. θ_{air}, is the critical angle of total internal reflection in air.

Figure 5.9a shows the R vs. θ waveguide response of a 1-step anodized AAO film in air, and Figure 5.9b shows the corresponding top surface morphology observed in SEM. Fitting of the waveguide mode minimum angles by Fresnel calculations gave a film thickness h = 1261 nm and ε_{film} = {2.021, 2.021, 2.163}. The optical model also included the Al coupling layer (h_{Al} = 19 nm and ε_{Al} = 35 + 30i) and an alumina barrier layer in between the Al and AAO layers ($h_{barrier}$ = 50 nm and $\varepsilon_{barrier}$ = 2.7). This multilayer model* of the AAO film has also been used to describe ellipsometry measurements of the film [3, 45].

The sample shown in Figure 5.9 was actually mounted on a liquid flow cell, sealed by elastomeric o-rings, and fitted with a peristaltic pump to control the flow of liquid in and out of the cell (Figure 2.1). If a liquid, e.g. ethanol, is introduced, the cover medium would be changed from air to ethanol. Since $\varepsilon_{ethanol} > \varepsilon_{air}$, the critical angle of total internal reflection would also increase from θ_{air} to $\theta_{ethanol}$. Thus all waveguide modes would also be shifted to above $\theta_{ethanol}$. Moreover, if the ethanol filled the pores, the overall dielectric constant of the nanoporous film would also increase, and shift the waveguide modes to even higher angles (see the discussion relating to Figure 5.4 for details). Figure 5.10 illustrates this analysis. In Figure 5.10a,

* The approximate thickness value of the Al layer was already measured during the anodization process by the film's optical transmittance (section 2.3), and that of the barrier layer could be estimated from the formation mechanism of the AAO. The value of ε_{Al} used for Fresnel calculations was based on reported bulk Al values: ε_{Al} = -39+24i [44]. The value of $\varepsilon_{alumina}$ used was obtained the EMT model to be described. Note that deposition parameters, aging, annealing and other factors can have a tremendous effect on thin film optical values. As the OWS measurement has a redundancy of mode minima for fitting the two independent components of the dielectric constants in the ε_{film}, more accurate values of h_{Al}, $h_{barrier}$ and ε_{Al} were also fitted by the OWS response.

the hypothetical response of the air-filled waveguide with an ethanol cover medium is shown: two modes can be observed in both p- and s-polarizations. In contrast, the actual OWS measurement with pore filling is shown Figure 5.10b. With an increased ε_{film} three modes could be observed in both p- and s-polarizations. The fitted film parameters are: ε_{film} = {2.392, 2.392, 2.427} and h = 1266 nm.

Since the value $\varepsilon_{pore} = \varepsilon_{air}$ (or $\varepsilon_{ethanol}$) is known from measurements of θ_{air} and $\theta_{ethanol}$, fitting of ε_{film} with the EMT cylindrical model in the manner analogous to the analysis of the PS-b-PMMA/PMMA waveguide can give both $\varepsilon_{alumina}$ and the pore fraction f_{pore}.* In fact, since there are two independently measured components in ε_{film} = {$\varepsilon_x = \varepsilon_y$, ε_z}, $\varepsilon_{alumina}$ and f_{pore} may, in principle, be independently determined by either set of ε_{film} measured in air or in ethanol. However, simultaneous fitting of both sets of film dielectric constants offers a check on the suitability of the EMT cylindrical model, and on whether the pores were completely filled with ethanol. The fitting results are given in Table 5.3 below:

	In air		**In ethanol**	
	$\varepsilon_x = \varepsilon_y$	ε_z	$\varepsilon_x = \varepsilon_y$	ε_z
Measurement	2.021	2.163	2.392	2.427
EMT best fit	2.020	2.164	2.394	2.425
Fitting results: $\varepsilon_{\text{alumina}} = 2.681$; $f_{\text{pore}} = 0.308$ Fitting parameters: $P_x = P_y = 0.5$; $P_z = 0$; $\varepsilon_{ethanol} = 1.8485$ (measured from θ_{ethanol}); $\varepsilon_{air} = 1$				

Table 5.3. Comparison of $\varepsilon_{\text{film}}$ from OWS measurements with the corresponding EMT best fit.

Excellent agreement between the OWS measurement and the EMT model was found, and a single set of model parameters, $\varepsilon_{\text{alumina}} = 2.681$ and $f_{pore} = 0.308$, could fit both measurements in air and in ethanol, thus verifying the model and the fact that ethanol should wet the anodic alumina surface. The fitting error (Equation 5.7) corresponding to each of the four measured dielectric constants was 0.002 or less, and indicates the level of uncertainty in the EMT characterization of the nanoporous AAO. Note, however, that Fresnel calculations fitting the OWS R vs. θ data gave slightly different film thickness values in air (1261 nm) and in ethanol (1266 nm). This may be attributed to uncertainties in the measurement, or could reflect the fact that the optical thickness measured is dependent on the dielectric constant of the waveguide [21]. The fitted value for $\varepsilon_{\text{alumina}}$ is smaller than for crystalline Al_2O_3 ($\varepsilon_{\text{sapphire}} = 3$) but this is not unreasonable for the present amorphous, ion incorporated anodic alumina. Assuming hexagonal packing of the cylindrical pores, the diameter of the pores (Equation 5.8), D_{pore} was found to be 57 nm, based on f_{pore} and the pore centre-to-

* $\varepsilon_{alumina}$ differs from bulk values of crystalline Al_2O_3 because of the amorphous nature and non-stoichiometry of the anodic alumina.

centre periodicity $\lambda_{C\text{-}C}$ = 98 nm (Table 3.3), which is in reasonable agreement of D_{pore} with SEM top surface characterization shown in Figure 5.9b.*

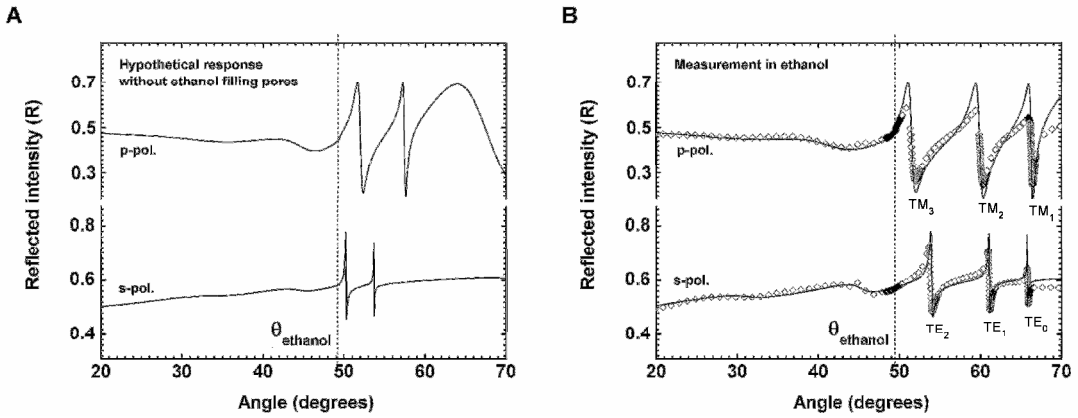

Figure 5.10. (A) Hypothetical R vs. θ response of the AAO film shown in Figure 5.9 immersed in ethanol *without* ethanol penetration into the pores. (B) The measured R vs. θ response of the same film *with* ethanol pore filling. Symbols show the OWS data and the solid lines show the fitted Fresnel calculations. $\theta_{ethanol}$, is the critical angle of total internal reflection in ethanol.

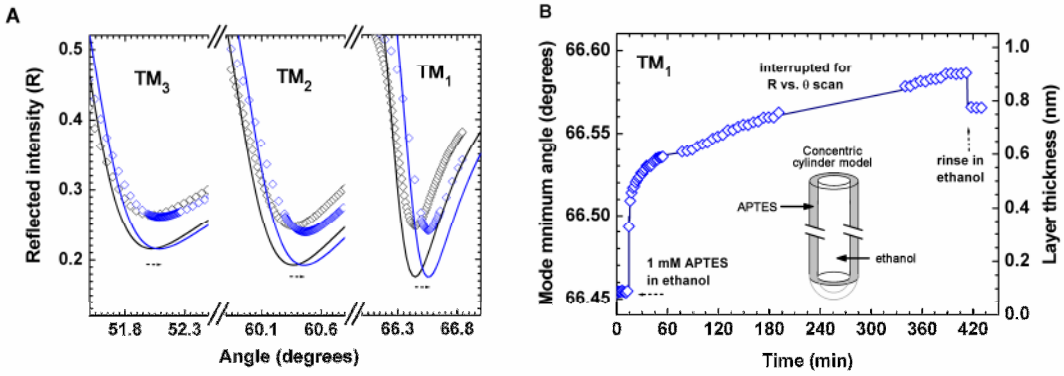

Figure 5.11. (A) The angle shifts in the p-polarization R vs. θ response (in ethanol) of the film shown in Figure 5.9 and Figure 5.10. The shifts were caused by the deposition of a 0.7 nm thick APTES layer on the pore walls. Symbols show the OWS data and the solid lines show the fitted Fresnel calculations. (B) shows the corresponding in situ angle tracking of the TM_1 waveguide mode at the highest incidence angle.

Functionalization of the AAO surface with silanes is a common procedure for modifying its surface chemistry, and may be performed by immersing the AAO in a silane solution or by gas phase deposition [46]. Silane layers have a dielectric constant higher than air and many common solvents. Thus the deposition of a silane layer, which displaces a corresponding volume of air or solvent, would increase the overall

* As discussed in section 3.2.2, the top surface of the 1-step anodized AAO observed in SEM is not representative of the pore structure in the bulk of the film, but D_{pore} should not deviate as much through thickness of the film because the pore etching mechanism is not affected by how the pores split or coalesce to achieve the equilibrium $\lambda_{C\text{-}C}$.

dielectric constant of the AAO. In the AAO waveguide, this would shift the waveguide modes to higher angles. Therefore the AAO waveguide can be used to monitor the silanization process (in situ) by tracking the angle shifts of the waveguide mode minima.

The chemisorption of 1 mM 3-aminopropyl-triethoxysilane (APTES) in dry ethanol, on the sample already described in Figure 5.9, is shown in Figure 5.11. Details of the R vs. θ measurements in p-polarization in ethanol before and after ~7 h immersion in the APTES solution are compared in Figure 5.11a. The TM_1 waveguide mode minimum at the highest mode coupling angle (~66.45º) was the sharpest, because it was damped the least by the Al metal coupling layer (see section 5.2). Therefore the angle position of this mode was tracked in real time to indicate the kinetics of chemisorption, as shown in Figure 5.11b. The chemisorption process was most rapid within the first hour, which was followed by what appeared to be a slow linear deposition process. The sample was rinsed with pure ethanol within the liquid cell after ~410 min and a (possibly physisorbed) portion of the layer was removed. R vs. θ measurements performed between 240-300 min were very similar to that after rinsing, and are not shown.

To estimate the thickness of the APTES layer deposited, the expected increase in ε_{film} was modeled by replacing $\varepsilon_{\text{pore}} = \varepsilon_{\text{ethanol}}$ with an effective ε_{pore}^{eff} describing the nanostructure of the pore plus the APTES layer (Equation 5.3). Since APTES deposition was expected to be uniform throughout the cylindrical pore (ethanol was already shown to completely fill the pores) the pore + APTES structure was modelled by concentric cylinders, as also shown in Figure 5.11b. That is, the pores were modelled also by the cylindrical morphology, and $P_x = P_y = 1/2$ and $P_z = 0$ were substituted into Equation 5.3b. Within the pores, $\varepsilon_{\text{matrix}} = \varepsilon_{\text{ethanol}} = 1.845$ and $\varepsilon_{\text{APTES}} = 2.019$ [47]. The APTES layer thickness h_{APTES} is then related to its volume fraction by:

Equation 5.9
$$h_{\text{APTES}} = \frac{\text{D}_{\text{pore}}}{2}\left(1-\sqrt{1-f_{\text{APTES}}}\right) \quad ; \quad f_{\text{APTES}} = 1-\left(\frac{\text{D}_{\text{pore}}-2h_{\text{APTES}}}{\text{D}_{\text{pore}}}\right)^2$$

The expected increase in $\varepsilon_{\text{film}}$ with increasing h_{APTES} can then be calculated through the concentric cylinder pore model nested within the AAO film cylindrical morphology model (Equation 5.3). The corresponding angles shifts were then obtained by substituting the calculated $\varepsilon_{\text{film}}$ into Fresnel calculations (Equation 5.6). The predicted values can be compared with the TM_1 angle tracking measurement, as shown on the right axis in Figure 5.11b.

Tracking of only one angle minimum actually cannot independently measure both ε_y and ε_z of the film. Therefore the R vs. θ measurement after rinsing (Figure 5.11a) was necessary to confirm the actual angle changes with the EMT model. Fitting of ε_{film} gave $h_{\text{APTES}} = 0.78$ nm, which is a reasonable value given the

theoretical APTES monolayer thickness [47, 48] of ~1 nm; the fitting results are shown in Table 5.4. Note that only one variable h_{APTES} (hence f_{APTES}) was used to simultaneously fit both ε_y and ε_z; $\varepsilon_{alumina}$ and f_{pore} were taken from the previous analysis of the blank AAO. The total fitting error of the APTES functionalised film was on the same level as for the blank AAO, and gave a relatively large uncertainty in the *absolute* value of h_{APTES} equal to approximately ~0.5 nm. However, the sensitivity in detecting *relative* changes during the deposition of the APTES layer by waveguide mode angle tracking, as seen in Figure 5.11b, depended on the sharpness of the mode minimum and the angular precision of the instrumentation, and was much higher. In the present example, deposition of ~1 nm APTES resulted in more than 0.1º in angle shift, compared with an angular precision of 0.001º limited by the mechanical specifications of the waveguide setup. Thus sub-angstrom sensitivity is achieved in the in situ monitoring of surface processes with the AAO waveguide, while the uncertainty in absolute thickness determination from EMT modelling is in the range of 0.5 ~ 1 nm.

	Blank AAO in ethanol		**AAO with APTES layer In ethanol**	
	$\varepsilon_x = \varepsilon_y$	ε_z	$\varepsilon_x = \varepsilon_y$	ε_z
Measurement	2.392	2.427	2.396	2.430
EMT best fit	2.394	2.425	2.397	2.428
Fitting results: $f_{\mathrm{APTES}} = 0.054$ ($h_{\mathrm{APTES}} = 0.78$ nm) Fitting parameters: $P_x = P_y = 0.5$; $P_z = 0$; $\varepsilon_{ethanol} = 1.8485$; $\varepsilon_{alumina} = 2.681$; $f_{\mathrm{pore}} = 0.308$				

Table 5.4. Comparison of ε_{film} from OWS measurements with the corresponding EMT best fit after APTES deposition.

Naturally, the characterization of the silanization process can also be performed ex situ. This was performed in the case of high temperature gas phase deposition* of APTES and 3-aminopropyl-dimethylethoxysilane (APDMES) of the silanes in vacuum according to established protocols [46]. The waveguide responses of the AAO films were measured before and after silanization in air. These AAO films were prepared by the 2-step anodization described in Figure 3.17, and were only 860 nm (Figure 5.12a) and 704 nm (Figure 5.12b) thick, as measured from the Fresnel calculations. EMT analyses of the measured ε_{film} indicated average pore diameters of 76 nm and 70 nm, respectively, which were larger than the previous AAO sample shown in Figure 5.9. The larger pores also implied a lower alumina volume fraction. Thus only two waveguide modes were observed in each polarization in Figure 5.12. EMT analysis of ε_{film} before and after silanization indicated h_{APDMES} ~ 1 nm and h_{APTES} ~ 2.5 nm. The latter was considerably thicker than the liquid silanization

* The AAO sample was kept in a glass container next to a small reservoir of the neat silane and heated at 135ºC in < 0.01 mbar for 3 h. The samples were then cooled and rinsed and sonicated in acetone for ~5 min.

process considered in Figure 5.11, and may reflect the crosslinked formation of multilayers.

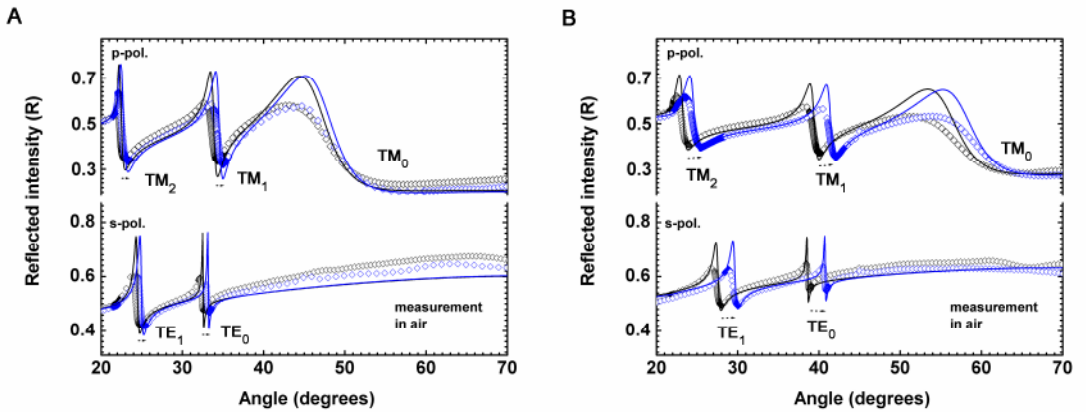

Figure 5.12. Comparisons of the R vs. θ response in air before and after gas phase silanization of the AAO film with (A) APDMES and (B) APTES. The broad drops in reflected intensity in p-polarization at angles > 50° are the broad plasmon resonances on the Al coupling film. The film thickness was 860 nm in (A) and 704 nm in (B), as measured by Fresnel calculations. EMT model fitting indicated pore diameters of 76 nm in (A) and 70 nm in (B), and h_{APDMES} ~ 1 nm and h_{APTES} ~ 2.5 nm.

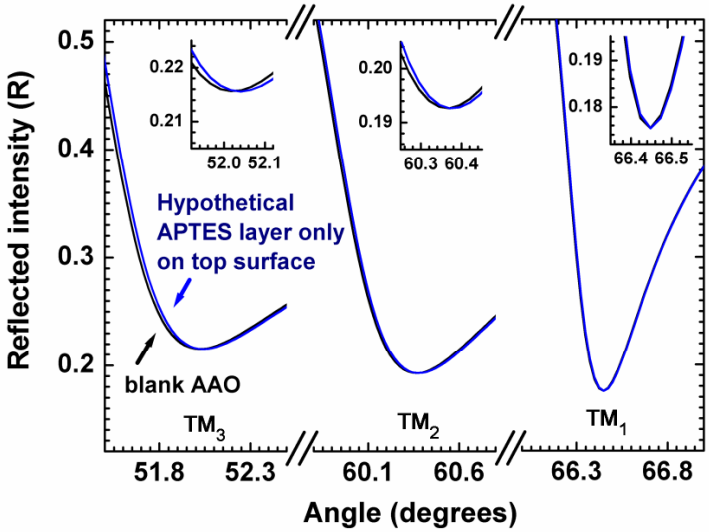

Figure 5.13. Hypothetical angle shifts of the waveguide modes in p-polarization due to APTES deposition only on the top surface of the AAO film. Calculations were based on the blank AAO measurement shown in Figure 5.10b. The insets show the miniscule expected angle shifts, and the higher shifts for the modes at lower incidence angles.

The high sensitivity in AAO-waveguide sensing was achieved due to the sharp resonances of waveguide modes, and because the nanoporous structure amplified the optical response by providing a vast internal surface area over which the surfaces processes can occur and the signal integrated. Moreover, as discussed in the context of

Figure 5.4 and observed in Figure 5.11a, the increase in ε_{film} due to the addition of a silane layer throughout the film thickness resulted in similar angle shifts for all the waveguide modes. Careful examination of the shifts reveals slightly larger shifts for lower order modes. In other words, the quasi-parallel shifts indicate a uniform, conformal APTES coating of the AAO film. In contrast, in case the deposition process only occurred on the top surface of the AAO waveguide, the angle shifts would be much smaller and more asymmetrical, with larger shifts for modes at lower angles. This is shown in Figure 5.13. Therefore the asymmetry in mode minimum angle responses can be used to discriminate the deposition processes occurring within the pores and on the top surface of the AAO film, and this capability is explored in the following chapter, for characterizing the layer-by-layer deposition of dendrimer polyelectrolyte "nanotubes" templated by the AAO film.

5.4.2. Dendrimer polyelectrolyte LbL deposition within and outside of the porous AAO waveguide

A strategy for surface modification that has gained significant attention is the layer-by-layer (LbL) deposition of polyelectrolyte multilayers. In this process [49-51], a charged substrate surface is immersed, in an alternating fashion, in solutions of polyelectrolytes with anionic and cationic characters. If during each step, adsorption of the polyelectrolyte to the oppositely charged surface leads to charge overcompensation and inversion, then adsorption of the next layer of oppositely charged polyelectrolyte can occur, and the process is repeated until the desired thickness or layer configuration is achieved. The layered complex is stabilised by electrostatic interactions, and the physico-chemical properties are determined by the polyelectrolytes chosen. The LbL process is versatile [49], and deposition of such functionalised multilayers in a nanoporous AAO thin film results in polyelectrolyte nanotubes. Such a geometry has been explored as nano test tubes for drug delivery [52] and has been suggested for separation processes [53]. If the nanotubes remained immobilised in the nanoporous AAO matrix, sensing configurations with high lateral resolution may also be envisioned [53].

We prepared LbL assemblies from alternating depositions of N,N-disubstituted hydrazine phosphorus-containing dendrimers of the fourth generation (G_4) having 96 terminal functional groups with either cationic or anionic character (Figure 5.14) [54-56]. One-step anodized AAO thin films were used and were 1.3 μm thick, with pores ~70 nm in diameter. The dendrimers have an unperturbed diameter of ~4 nm and were dissolved in deionised water (with 50 mM NaCl) at a concentration of 1 mg/ml. The pH of the solution was neutral. LbL deposition was preceded by functionalization of the AAO surface with 3-aminopropyl-dimethylethoxysilane (APDMES) from the gas phase to give a positively charged surface in water, as described in the previous section. An attempt to deposit the

dendrimers without the APDMES layer was unsuccessful. The increase in total dendrimer thickness was monitored in situ by TM_1 waveguide mode angle tracking and R vs. θ measurements, in the same way the liquid phase silanization was monitored, also shown in the previous section. This method of preparing dendrimer "nanotubes" has already been reported in 2005 [53] using ordered AAO templates 80 μm thick and much larger pore diameters at 400 nm. Up to 20 bilayer deposition steps were performed in those early experiments. Although the LbL process has been characterised separately on a flat surface by SPR (up to 6 bilayers [57]), which indicated a linear growth in total dendrimer layer thickness (~4 nm/layer), the in situ characterization of the LbL process in the cylindrical nanopore geometry has not been possible until now. Indeed, the LbL deposition of charged species within the AAO as the pore diameter becomes smaller may be challenging.

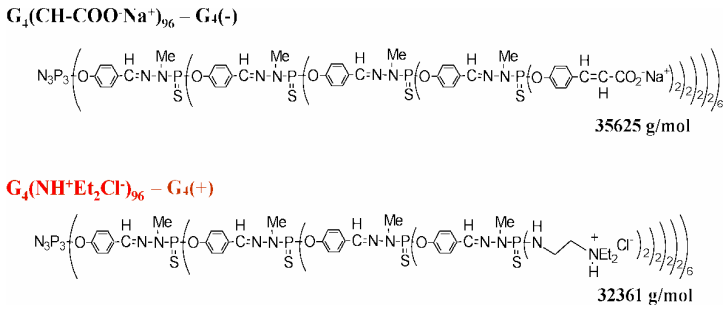

Figure 5.14. Schemes of the N,N-disubstituted hydrazine phosphorus-containing dendrimers having 96 terminal functional groups with either cationic (G_4(-)) or anionic (G_4(+)) character used for LbL deposition.

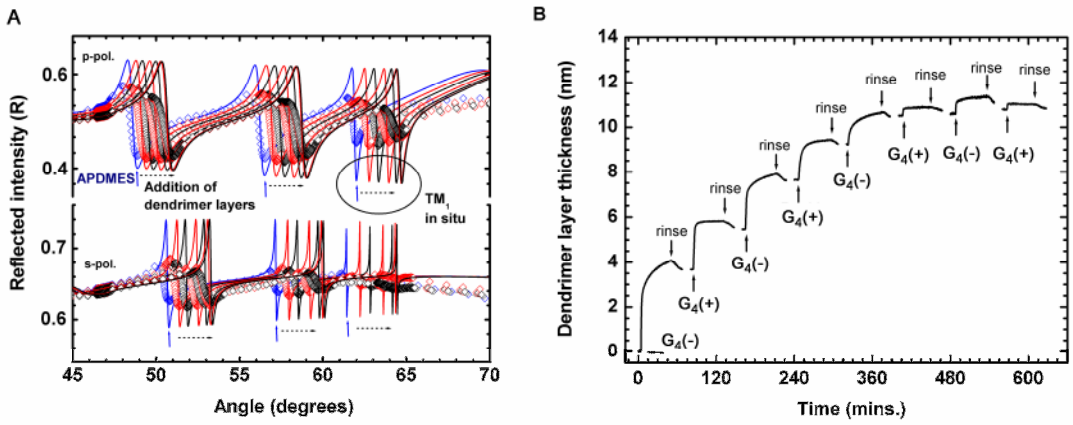

Figure 5.15. (A) R vs. θ measurements showing successive steps of G_4(-) and G_4(+) LbL deposition from 1 mg/ml solution with 50 mM NaCl added. Rinsing indicates exchange of the liquid cell contents with copious amount of deionised water. The TM_1 mode angle position was tracked in situ between each R vs. θ measurement, and was plotted as (B). The angle changes were fitted by EMT to give the dendrimer layer thickness increase on the pore walls indicated by the vertical axis.

Figure 5.15a shows the R vs. θ measurements of the AAO film after each successive G_4(-) and G_4(+) deposition step. As with the silanization experiment described earlier, the angle position of the TM_1 waveguide mode was tracked to monitor the deposition process in situ, and the dendrimer layer thickness increase with adsorption time is shown in Figure 5.15b. The dendrimer thickness was calculated from the measured angle shifts using the same EMT analysis as used for analysing APTES deposition in Figure 5.11b. Note that this EMT modelled thickness refers, more specifically, to the deposition within the pores that induces a "bulk" change in the dielectric constant of the nanoporous film ε_{film}. This is because the TM_1 angle position is the least sensitive to film thickness changes (Figure 5.4 and Figure 5.13).

As shown in Figure 5.15b, the thickness of the first layer of negative dendrimer, G_4(-) was ~3.5 nm, while the next layer of the oppositely charged G_4(+) was ~2 nm. The following layer of G_4(-) was also ~2 nm, while the next layer of G_4(+) decreased to ~1.5 nm. In fact, the layer thickness deposited within the pores continued to decrease for successive layers until no additional angle shift of the TM_1 mode was observed by the third bilayer steps (i.e. G_4(-):3 and G_4(+):3) by which point the total thickness deposited was ~10.5 nm. This thickness would also imply that the original 70 nm diameter pores are now less than 50 nm wide.

Analysis of the R vs. θ waveguide modes, however, show that the angle shifts for the higher order modes at lower angles (i.e. TM_3, TM_2, and correspondingly TE_2, TM_1) continued to increase with further LbL deposition steps. Details of the TM_3 and TM_1 R vs. θ responses, and the cumulative angles shifts for all TM modes after each deposition step, are shown in Figure 5.16. It is seen that, although the total angle shift for TM_1 approached an asymptotic value of 2.6°, the TM_3 angle position, and to a lesser extent also that of TM_2, steadily increased (at a slow rate). Similar trends were observed for the TE modes.

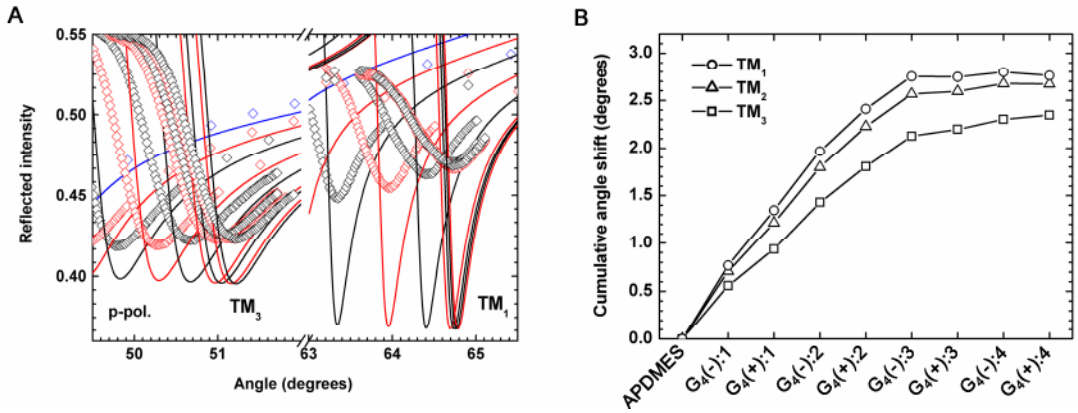

Figure 5.16. Details of the R vs. θ measurements shown in Figure 5.15. (A) plots the TM_1 and TM_3 modes for successive depositions steps. It is seen that the TM_3 minimum angle shifted to higher angles for all deposition steps, while the TM_1 angle essentially remained stationary for the third and fourth bilayer steps. (B) compares the angle shifts in detail for all three TM modes and highlights the continued increase in the TM_2 and TM_3 angle positions, while the TM_1 mode remained stationary for later deposition steps.

As discussed in section 5.2, film thickness increases (deposition on the film's top surface) induces larger mode shifts for higher order modes, while increasing ε_{film} (bulk deposition within pores) induces quasi-parallel shifts with slightly larger shifts for lower order modes. Careful fitting of the R vs. θ measurements by Fresnel calculations can deconvolute changes in ε_{film} and film thickness (h). Combined with EMT fitting, this analysis gives independent measurements of the dendrimer deposition process on the top surface (assumed to be equal to the change in h) and within the pores (the identical EMT analysis of ε_{film} for uniform pore coatings). These fitted thickness values are presented in Figure 5.17.

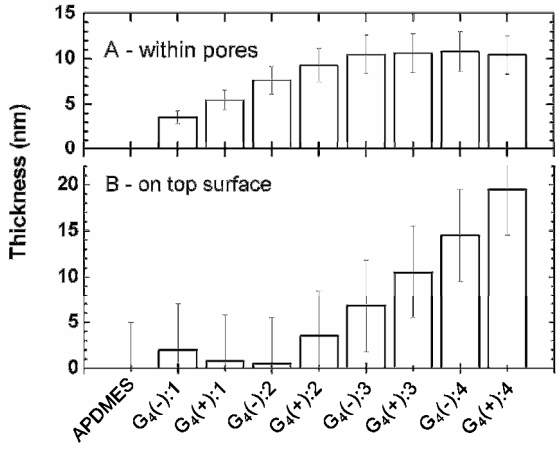

Figure 5.17. Comparison of the LbL deposition process within the pores (A) and on the top surface of the AAO film (B). (A) was obtained by EMT fitting of ε_{film} measured from the R vs. θ data and corresponding Fresnel calculations, while (B) was obtained directly from the change in film thickness obtained from the same Fresnel calculations. The uncertainty plotted in (A) is ±20%, and is ±5 nm in (B).

Similar to the trend in TM_1 angle shifts shown in Figure 5.16, Figure 5.17 shows that dendrimer deposition within the pores had essentially ceased after 2 bilayers. At the same time, the thickness increase on the top surface followed a linear increase for the later bilayer deposition steps. The thickness increment was ~4 nm/layer, and was comparable to the 3.5 nm first layer of G_4(-) measured within the pores. The absence of thickness changes on the top surface for the first 2 bilayers may be an artefact of the fitting procedure—in the absence of TM_1 angle mode shifts, the only fitting variable for the R vs. θ measurements for the later deposition steps was the film thickness. Moreover, the detection of thickness changes involves a degree of uncertainty higher than for detection within the pores, because this is a local, top surface effect, and the induced waveguide mode angle shifts are correspondingly small (as demonstrated in Figure 5.13). One should also bear in mind that there should exist an interface region near the pore openings that may be better described by a combination of the measured top surface and bulk pore effects. The spatial resolution

of the changes in ε_{film} with respect to the height position through the thickness of the film is limited by the spatial distributions of the waveguide mode amplitude maxima (Figure 5.3), which span significant fractions of the film thickness. Therefore ε_{film} (hence the dendrimer layer thickness within the pores) should be taken as an average measurement within the bulk of the AAO film. Surface roughness also adds to the complexity of the actual interface region.

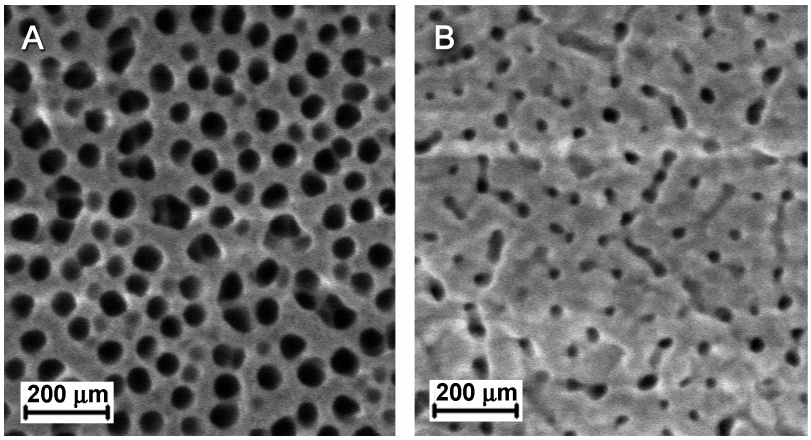

Figure 5.18. Top surface SEM micrographs of the blank AAO film (A) and that after the dendrimer LbL deposition (B). The average pore diameter of the blank AAO film corresponds reasonably well to the EMT modelled 70 nm, while the final pore diameter appeared to be smaller than the 50 nm indicated by the 10 nm dendrimer layer covering the pore walls.

The OWS-EMT analysis of the LbL process was complemented with SEM characterization of the top surfaces of the AAO samples. Figure 5.18a shows the pore morphology of the blank AAO film while Figure 5.18b shows the top surface after the 4 bilayer deposition steps were performed. While the pores of the blank AAO match well with the 70 nm diameter deduced from EMT analysis, the dendrimer coated film show significantly smaller pores than the 50 nm diameter inferred from the 10.5 nm layer measured within the pores. Indeed, some of the pore openings appeared to be completely covered with deposited material. In fact, because the vacuum environment of the SEM should have completely dried the polyelectrolyte film, the dendrimer multilayer structure might have been partially collapsed, and even more of the pores might have been blocked in situ than is suggested by Figure 5.18b. Moreover, the deposition process near the pore openings might be more similar to the deposition process on the top surface than for the process deep within the AAO film. Taking the 20 nm top layer thickness at face value (Figure 5.17) would imply a constriction of the pore openings from the original 70 nm to ~30 nm, which appears to be more consistent with the SEM observation. This pore blocking might explain the observed premature termination of the deposition process within the pores.

The constriction of the pore openings observed might also imply a preferential adsorption of the dendrimer polyelectrolytes in the top portion of the AAO nanoporous structure. It is expected that as the dendrimer solution was first introduced, deposition would initially occur near the pore openings. Further diffusion of dendrimers is then supposed to allow deposition in the interior of the AAO film. Apparent 1D diffusion was reported for AAO templates 35 μm thick with 35-40 nm diameter pores [58], with non-interacting pore surfaces. This led to molecule dwell times in the pores 10~20 times longer than normal diffusion within a corresponding volume in unbounded solution, but diffusion through the pores appeared otherwise unhindered. Thus molecules can in principle diffuse throughout the length of the present, much shorter 1.3 μm AAO pores. Also, at 50 mM NaCl concentration in the dendrimer solution, consideration of the Debye screening length [*] indicates that charges should be completely screened over a distance of ~1.5 nm [59]. On the other hand, as the polyelectrolytes adsorb near the pore openings, the charge inverted pore surfaces in the top part of the AAO film assume a repulsive interaction with the polyelectrolytes in solution. Thus a small repulsive field is introduced at the pore openings commensurate with the screening length. Also the actual sizes of the pore openings are reduced by the thickness of the adsorbed dendrimer layer. For a 3~4 nm thick first layer and a screening length of ~1.5 nm, the 70 nm pore openings are effectively reduced to only ~60 nm in diameter, corresponding to a reduction in cross sectional area by 27%. The rate of polyelectrolyte entry into the pores may correspondingly decrease. Although the adsorption time for each deposition was allowed to proceed for 40 min in our experiments, the decreased diffusion rate into the pores might have been sufficient to result in a slight decrease in adsorbed thickness of the polyelectrolyte towards the bottom of the pores. For the following layer of oppositely charged dendrimers, the pore opening constriction also occurs as the polyelectrolyte initially adsorbed near the pore openings. Moreover, the effect of the reduced diffusion rate into the pore could have been compounded by a reduced adsorption affinity near the bottom of the pores, if the charge overcompensation from the previous polyelectrolyte layer had already been reduced due to a decreased amount of the first dendrimer layer adsorbed. Thus the adsorption of successive layers of polyelectrolytes towards the bottom of the AAO film may become increasingly less efficient, leading to a decreasing per layer thickness within the pores, averaged through the bulk of the film, as indicated by the OWS-EMT measurement.

In summary, two mechanisms could have led to the constriction of the pore openings, thus terminating the adsorption within the ~70 nm diameter pores before

---

[*] The Debye length is [59]: $\lambda_D = 1/\sqrt{4\pi l_B \sum_i z_i \rho_i}$

where z and ρ are the number densities and valences of the dissolved ion species *i*, and where l_B ~ 0.7 nm is the Bjerrum length, the range at which two single electron charges have the thermal energy kT in pure water at room temperature and pressure: $kT = e^2/(4\pi\varepsilon_0\varepsilon_{water} l_B)$, where ε_0 and ε_{water} are the dielectric constants of vacuum and water (static value).

they were completely filled with polyelectrolytes. First, LbL deposition on the top surface of the AAO film adds not only to the vertical thickness of polyelectrolyte multilayer, but also contributes to a lateral thickness increase at the edges of the pore openings, thereby constricting them. Furthermore, deposition on the pore surfaces nearest to the pore openings was expected to occur before the dendrimer polyelectrolytes had a change to diffuse further into the film. This would lead to earlier charge reversal nearer the pore openings within the porous structure, and induce a repulsive pore wall interaction that induces a barrier to further transport into the pores. Combined, these two effects could lead to less and less efficient deposition within the pores over successive depositions steps. Note that there is a range of pore diameters for the 1-step anodized AAO films used, and the effect due to pore opening constriction appeared to have been very large for the smaller pores—the smaller pore openings were completely blocked (Figure 5.18b).

LbL deposition was also performed for dendrimers dissolved in pure water, also at a concentration of 1 mg/ml, but without additional NaCl added. Taking the simplistic view that no counterion condensation [60, 61] occurred, and all 96 charged groups on the surface of each dendrimer acted as individual ions when the dendrimers were dissolved in water, ion concentration in the solution would be ~5 mM in water. The associated (lower bound) screening length was then ~6 nm.

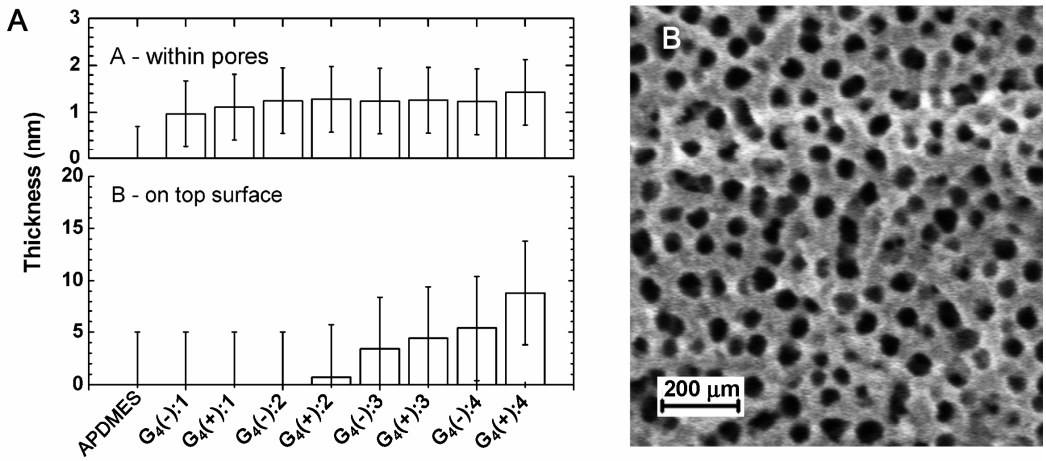

Figure 5.19. (A) Comparison of the LbL deposition process within the pores and on the top surface of the AAO film for adsorption from 1 mg/ml dendrimers in pure water. The uncertainty plotted in is ±0.7 nm on top, and ±5 nm below. (B) Top surface SEM micrographs of the AAO film after LbL deposition.

Figure 5.19a shows the comparison of the dendrimer layer thickness adsorbed within the pores and on the top surface, obtained from OWS-EMT analysis as before, and Figure 5.19b shows the corresponding SEM micrograph of the sample after the deposition process. From the OWS measurement, the contrast in adsorption behaviour

within the pores and on the surface was qualitatively similar to the case of adsorption from salted solutions (Figure 5.17). However, deposition within the pores appeared to have stopped after only 1 bilayer of dendrimers deposited, and may indicate the influence of the nearly 4 times larger screening length. (Note that the cross sectional area of the pores go as the square of the pore radius.) Moreover, the average thickness increment on the top surface was 1.8±0.7 nm/layer, and was ~50% smaller than for the previous experiment with 50 mM NaCl. This lower value matches previous studies using flat substrates [53], and the decrease is consistent with the reported influence of ionic strength on LbL polyelectrolyte deposition [50, 60]. The large pores in the top surface morphology measured by SEM is also consistent with the lower adsorbed amounts measured by OWS. Although no pore constriction is apparent (which is consistent with influence of the large screening length), it is difficult to ascertain the actual changes in pore diameters due to the small amounts of dendrimers deposited. Further experiments with 2-step anodized AAO films and cross-sectional SEM measurements are underway to further investigate and quantify the relationship between pore size, the effective size of the dendrimers (according to the screening length), and the LbL deposition process.

5.4.3. Characterization of anisotropic polymer nanostructures within AAO pores

The modification of the nanoporous AAO film with smooth layers of materials, and their characterization by combined waveguide and EMT analysis, has been discussed in the previous sections. On the other hand, how might the optical response of the AAO film be altered if the deposited layer possessed its own anisotropy? This issue is explored in this section with the example of the surface grafting of the polypeptide, poly(γ-benzyl-L-glutamate) (PBLG).

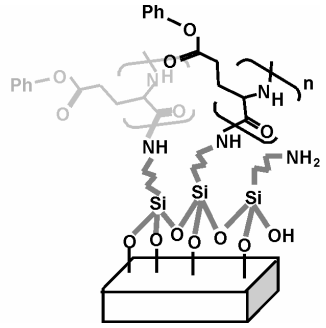

Figure 5.20. Schematic of the PBLG system on the APTES functionalised substrate (AAO).

PBLG is an interesting polypeptide because it and related polypeptides have already been proposed for a range of applications in biosensing [62, 63], chiral

separation [64, 65], and optics [66, 67]. Moreover, the ester side chains of a grafted PBLG brush may be conveniently modified. In biosensing, high sensitivity and selectivity are desired. For high sensitivity, it is desirable to maximise the number of binding sites in order to enhance sensing capabilities. The use of the nanoporous AAO matrix to provide an internal surface for binding is one step towards that goal. Functionalization of the AAO surface with a polymer brush with multiple binding sites along the polymer backbone represents a natural extension towards creating 3D architectures with an enhanced number binding sites per unit area. In the course of realizing this strategy, interesting nanostructures and their associated waveguide responses, were observed.

To prepare PBLG brushes, the AAO surface was first functionalised by gas phase APTES deposition (section 5.4.1) to provide a high density of primary amine surface groups. These then acted as surface initiators for the ring opening polymerization of N-carboxy anhydride (NCA) to form PBLG [48, 68, 69]. A schematic of the polypeptide system is shown in Figure 5.20. The polymerization process was carried out in anhydrous tetrahydrofuran (THF), and the concentration of NCA in THF was 100 mM. The surface grafting process was monitored in situ, as in earlier sections, by R vs. θ measurements and by angle tracking of the TM_1 waveguide mode minimum. The ability to characterise a surface initiated polymerization process within the nanoporous AAO template is unprecedented. It is also expected to yield information on the development of the PBLG brush architecture, and lead to control of the functional group density in the 3D polypeptide brush/nanoporous AAO architecture.

An all-Teflon, sealed liquid flow cell adapted to a peristaltic pump was used together with the OWS setup in the present PBLG experiments. This was used to prevent THF evaporation from the liquid cell, and to prevent the introduction of water impurities (which could cleave an anhydride ring and lead to formation of unbounded polymer in the solution [68]). In contrast to the LbL process described in the previous section, preferential brush growth near the pore openings towards the top part of the AAO film is not expected, because the NCA monomer never acquires a repulsive interaction with the pore surfaces. Also the experiment was a long, continuous polymerization process that is expected to allow equilibrium concentrations of NCA species to be reached throughout the sample.

Figure 5.21 shows the in situ R vs. θ measurements in THF before and after 25 h surface initiated polymerization on AAO films (APTES functionalised) for two samples. The polymerization process was stopped by rinsing the NCA solution filled flow cell with pure THF. Figure 5.21a shows the results for a 640 nm thick 2-step anodized AAO film with D_{pore} ~ 76 nm, as characterised by OWS-EMT analysis, and Figure 5.21b shows a 1110 nm thick 1-step anodized AAO film with D_{pore} ~ 60 nm. Due to both the higher film thickness and the higher ε_{film} (smaller pores led to higher

alumina content), more modes could be observed* in Figure 5.21b than in Figure 5.21a. As in previous sections, addition of polymeric material within the nanoporous AAO increased ε_{film} and shifted all waveguide modes to higher angles. Since the sample with the larger pore diameters had a higher internal surface area, more material could be grafted *per unit volume* of the AAO film, thus the angle shifts were correspondingly larger in Figure 5.21a than in Figure 5.21b. The total angle shift for the TM_1 mode after 25 h surface initiated polymerization in Figure 5.21a was 4.6º, and was 3.5º in Figure 5.21b. Also seen in Figure 5.21 for both samples was the appearance of an additional waveguide mode in s-polarization by the end of the experiment due to the large increase in ε_{film} during the PBLG grafting process. Both samples showed qualitatively the same behaviour, and the following quantitative discussion refers to the sample with the larger 76 nm pores.

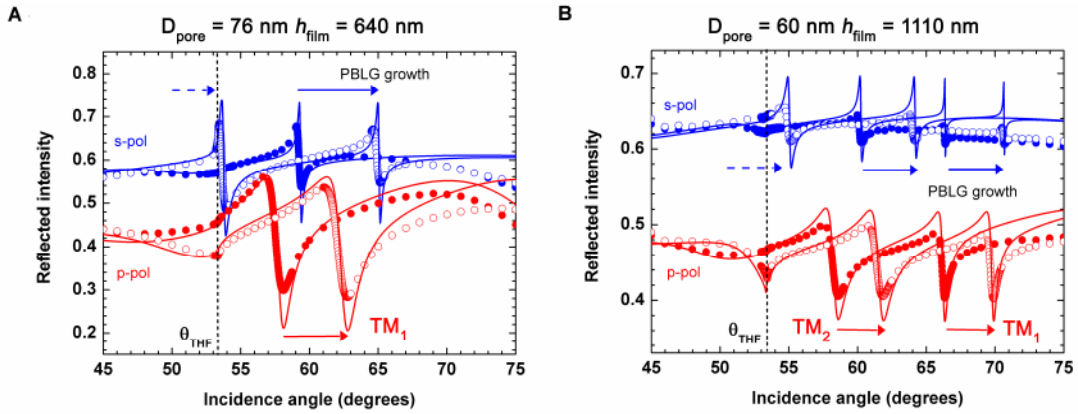

Figure 5.21. R vs. θ measurements of nanoporous AAO thin film samples before and after PBLG grafting on the APTES functionalised surface. (A) shows the angle shifts for a 640 nm thick 2-step anodized AAO sample with 76 nm pores, while (B) shows the angle shifts for a 1110 nm thick 1-step anodized AAO sample with 60 nm pores.

Figure 5.22a shows the TM_1 mode angle minimum tracking corresponding to Figure 5.21a, and measurements of $\varepsilon_{film} = \{\varepsilon_x = \varepsilon_y , \varepsilon_z\}$ throughout the polymerization process. As the following discussion will show, it was necessary to track not only the TM_1 mode, but also to measure the full R vs θ waveguide response during the course of the polymerization process. From these measurements, the full dielectric response $\varepsilon_{film} = \{\varepsilon_x = \varepsilon_y , \varepsilon_z\}$ was monitored.

Before the introduction of NCA solution, EMT analysis of the R vs. θ baseline measurements in THF indicated a ~1.8 nm thick APTES layer, and the measured $\varepsilon_x = \varepsilon_y$ was smaller than ε_z (time = 0 h, Figure 5.22a). When the 100 mM NCA solution

* The amplitudes of the waveguide mode minima were also smaller in Figure 5.21b because this film had a thicker Al coupling layer h_{Al} = 30 nm, as opposed to h_{Al} = 20 nm in Figure 5.21a. As in previous sections, ε_{Al} = 35 + 30i was used.

was introduced, a rapid initial increase in the angle shift (~0.2º) was observed, indicating adsorption of the monomers. (Note that the change in THF solution dielectric constant due to the high NCA concentration was already corrected for in Figure 5.22a.) The angle shift then continued to increase slowly until after 2~3 h, the slope of the θ vs. time trace increased to a quasi-linear region for the period 3~15 h. This change in slope might have origins in a change in PBLG layer dielectric constant during the chain conformational change to α-helices as the degree of polymerization increased beyond the oligomer length [68]. However, as polymerization proceeded further, the rate of angle increase decreased, and appeared to approach an asymptotic value beyond ~15 h. This might have been a consequence of carrying out the polymerization process within a nanoscale pore geometry, as the discussion below suggests.

Corresponding to the angle shift, the measured values $\varepsilon_{\text{film}} = \{\varepsilon_x = \varepsilon_y\ ,\ \varepsilon_z\}$ followed the same general trend with time. However, although both ε_y and ε_z increased in value with time, as time progressed, their values became more similar until after ~20 h, ε_x (= ε_y) became larger than ε_z: after THF rinsing $\varepsilon_{\text{film}}$ = {2.460, 2.460, 2.458}. This anisotropy was opposite to the initial anisotropy of the AAO film (at time = 0 h, $\varepsilon_{\text{film}}$ = {2.282, 2.282, 2.303}). Recalling the optical description of the AAO film, TM waveguide modes with electric fields polarised in the direction of the long axes of the cylindrical pores (p-polarization), are essentially undisturbed by the AAO pore structure due to the alignment of the polarization with the pore surfaces. On the other hand, TE modes with electric fields oriented in the plane of the film are screened by the cylindrical pore interfaces. Therefore in the EMT model ε_z^{eff} (P_z = 0) > ε_x^{eff} (P_x = 1/2) for all pore fractions and dielectric material constants (Equation 5.1). Clearly, the measured anisotropy of $\varepsilon_x = \varepsilon_y > \varepsilon_z$ after 25 h NCA polymerization is in contradiction to the predicted anisotropy of the AAO cylindrical pore structure, and also to the model of a uniform PBLG coating on the pore walls. This discrepancy is shown graphically in Figure 5.22b, in which the predicted $\varepsilon_{\text{film}}^{eff}$ and the measured $\varepsilon_{\text{film}}$ are plotted against the best fit PBLG layer thickness ($\varepsilon_{\text{PBLG}}$ = 2.403 [70]). The fitting simply identifies the best match between the averages of the predicted $\varepsilon_{\text{film}}^{eff} = \{\varepsilon_x^{eff}\ ,\ \varepsilon_z^{eff}\}$ and the measured $\varepsilon_{\text{film}} = \{\varepsilon_x\ ,\ \varepsilon_z\}$. So the average $\varepsilon_{\text{film}}$, hence the amount of PBLG grafted, as expected in this polymerization process, appeared to increase monotonically with time. However, the evolution of the measured optical anisotropy was in a direction opposite to the EMT model for the addition of a uniform PBLG layer.

Figure 5.22b also shows that the increase in predicted $\varepsilon_{\text{film}}^{eff}$ with PBLG layer thickness followed a parabolic trajectory. This is due to the cylindrical pore geometry, for which the pore/PBLG surface area decreased as the layer thickness of PBLG increased. At the same time, the EMT model also predicts a decreasing anisotropy between ε_x^{eff} and ε_z^{eff} with an increase in the amount of PBLG grafted (the solid curves approach each other with increasing layer thickness). This is because the dielectric

contrast between 100 mM NCA in THF ($\varepsilon_{100mM\ NCA}$ = 1.98) and alumina ($\varepsilon_{alumina}$ = 2.68) is higher than that between PBLG (ε_{PBLG} = 2.403 [70]) and alumina, and the anisotropy naturally decreases with the displacement of THF with PBLG. In spite of this, ε_x^{eff} is always smaller than ε_z^{eff} (the pores become completely filled before ε_x^{eff} approaches ε_z^{eff}). In comparison, the discrepancy in the optical anisotropy between the measured ε_{film} and the model became larger with increasing "thickness" of PBLG grafted (inset, Figure 5.22b).

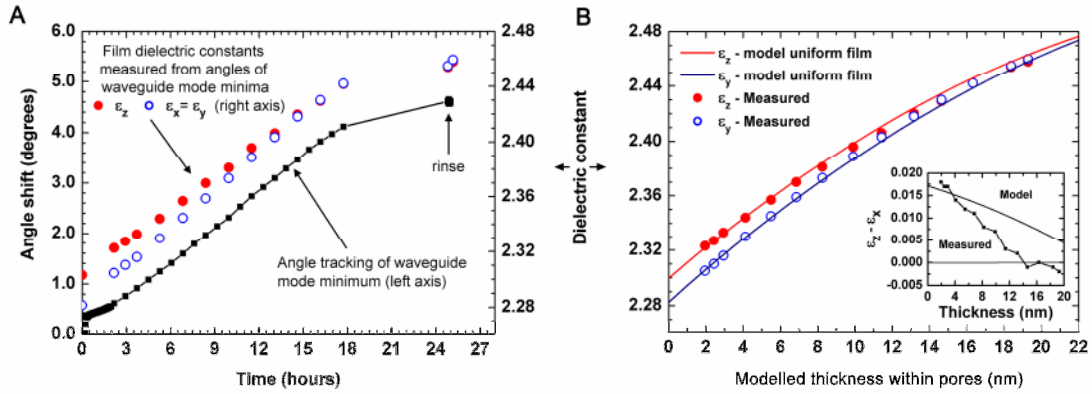

Figure 5.22. (A) Angle shift of the TM_1 mode shown in Figure 5.21 (black symbols and line, left axis), and the corresponding ε_{film} measured from repeated R vs. θ measurements performed over the 25 h time period of the polymerization process (coloured circles, right axis). Note that ε_y became larger than ε_z towards the end of the polymerization process. (B) The measured ε_{film} plotted against the best fit PBLG layer thickness based on the model of a conformal coating on the pore walls. The reversal in order between ε_y and ε_z towards the end of the polymerization process is in disagreement with the optical model (inset).

For the other sample with smaller pores, ε_x (= ε_y) also became closer in value to ε_z but remained slightly smaller. In this case, after THF rinsing, ε_{film} = {2.541, 2.541, 2.545}. Since the fraction of pores in this sample was smaller, whatever process within the pores that led to the increase of ε_x (= ε_y) relative to ε_z made a smaller contribution to the overall dielectric response of the film, and resulted in the smaller amount of anisotropy reversal observed.

The long term stability of the AAO film in THF at room temperature and pressure is proven from experience (SEM characterization, to be discussed later, verified this assertion). That is, the optical anisotropy arising from the oriented porous oxide structure was expected to remain constant throughout the experiment. Therefore there must have developed within the pores a structure with an anisotropy opposite in orientation, and large enough to equalize, then reverse the optical anisotropy of the nanoporous AAO structure.

As mentioned earlier, PBLG assumes an α-helical secondary structure [68], which imparts an intrinsic birefringence to the macromolecule [70, 71]. Indeed, post-

polymerization, ex situ FTIR measurements of the PBLG modified AAO films confirmed the presence of α-helices by the shifts in the amide absorption bands.* Nonetheless, this intrinsic optical anisotropy arising from the molecular structure contributes only a difference of <0.001 † in the orthogonal components of the macromolecule's dielectric constants. This anisotropy is much smaller than the anisotropy reversal measured (the difference between the model and measurement $\Delta\varepsilon \sim 0.005$, Figure 5.22b inset). Thus the measured anisotropy cannot be explained by the intrinsic birefringence alone, even if all the α-helices were aligned with each other parallel to the plane of the film, and imparted anisotropy orthogonal to that of the AAO pore structure.

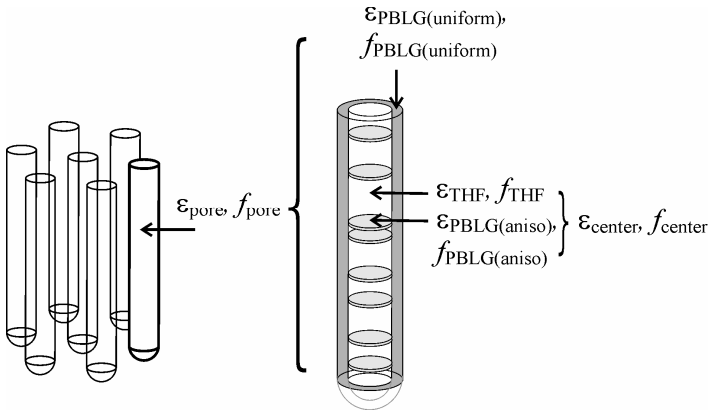

Figure 5.23. Schematic showing the idealised cylindrical pore array on which the original EMT model is based (left, the hemi-spherical bottom is ignored), and the 2-component structured cylinder model with a uniform coating on the pore walls and random lamellae lying perpendicular to the cylindrical axis and parallel to the substrate surface (right).

On the other hand, a larger, nanostructured arrangement of the PBLG material within the pores that has elements aligned normal to the pore walls, may generate an optical anisotropy of the magnitude required to explain the measurement. This optical anisotropy would be generated in the same way that the cylindrical pore morphology imparts anisotropy to the AAO film. Also like the AAO structure, such a hypothetical PBLG nanostructure within the pores is at a scale suitable for the EMT description of its optical response.

As the AAO film structure is unaltered, the basic cylindrical pore model is retained. The PBLG material within the pores, however, is assumed to consist of not just a cylindrical layer uniformly coating the pore walls, but also take up a certain volume of the central reservoir of the THF solvent/NCA solution, in the form of

* FTIR measurements and analysis were performed by Dr. Hatice Duran from the MPI-P. See Appendix D.

† The reported anisotropy was 0.01 in the orthogonal components of the refractive index, n ($\varepsilon = n^2$). The exact degree of anisotropy depends on the solvent environment [70-71], reminiscent of the anisotropy of the AAO filled with different solvents.

nanodomains oriented normal to the pore walls. No information is available at this point in the discussion to specify the shape of this anisotropic structure intruding into the central pore space. Also, the new model has to be fitted by only two measurable quantities $\varepsilon_x = \varepsilon_y$ and ε_z. Therefore the simplest possible configuration, with randomly positioned lamellae within the pores, was assumed for the proposed anisotropic PBLG model. Figure 5.23 shows a schematic illustrating the concept of the anisotropic PBLG structure within the pores. The EMT model, based on the same procedure used in previous sections of nesting EMT descriptions of different parts of the film (Equation 5.3), is:

Equation 5.10a
$$\varepsilon_{eff}^{\text{entire film}} = \varepsilon_{\text{alumina}} \frac{\varepsilon_{\text{alumina}} + (f_{\text{pore}} + f_{\text{alumina}} P_{\text{cylinder}})(\varepsilon_{eff}^{\text{pore}} - \varepsilon_{\text{alumina}})}{\varepsilon_{\text{alumina}} + f_{\text{alumina}} P_{\text{cylinder}} (\varepsilon_{eff}^{\text{pore}} - \varepsilon_{\text{alumina}})}$$
$$\textbf{where } f_{\text{pore}} + f_{\text{alumina}} = 1$$

Equation 5.10b
$$\varepsilon_{eff}^{\text{pore}} = \varepsilon_{eff}^{\text{center}} \frac{\varepsilon_{eff}^{\text{center}} + (f_{\text{PBLG(uniform)}} + f_{\text{center}} P_{\text{cylinder}})(\varepsilon_{\text{PBLG}} - \varepsilon_{eff}^{\text{center}})}{\varepsilon_{eff}^{\text{center}} + f_{\text{center}} P_{\text{cylinder}} (\varepsilon_{\text{PBLG}} - \varepsilon_{eff}^{\text{center}})}$$
$$\textbf{where } f_{\text{PBLG(uniform)}} + f_{\text{center}} = 1$$

Equation 5.10c
$$\varepsilon_{eff}^{\text{center}} = \varepsilon_{\text{THF}} \frac{\varepsilon_{\text{THF}} + (f_{\text{PBLG(aniso)}} + f_{\text{THF}} P_{\text{lamellae}})(\varepsilon_{\text{PBLG}} - \varepsilon_{\text{THF}})}{\varepsilon_{\text{THF}} + f_{\text{THF}} P_{\text{lamellae}} (\varepsilon_{\text{PBLG}} - \varepsilon_{\text{THF}})}$$
$$\textbf{where } f_{\text{PBLG(aniso)}} + f_{\text{THF}} = 1$$

where $P_{\text{cylinder}} = 1/2$ and 0 for the x- and z-directions, respectively, and $P_{\text{lamellae}} = 0$ and 1 for the x- and z-directions, respectively. Note that the description is isotropic in the plane of the film, as in the original model, so that the x and y components are equivalent. Note also that Equation 5.10a and b are analogous to Equation 5.3a and b, which was used to describe the previous silane and dendrimer examples. The crucial difference is that the medium filling the centres of the pores is now occupied by a nanostructured arrangement of solvent and pore-spanning PBLG. This $\varepsilon_{eff}^{\text{center}}$ is calculated in Equation 5.10c. Note also that there are only two independent variables in Equation 5.10a through c: $f_{\text{PBLG(aniso)}}$ and $f_{\text{PBLG(uniform)}}$ to fit the two measurable quantities $\varepsilon_x = \varepsilon_y$ and ε_z. All other parameters have already been measured or are known from reported values. Moreover, as before, the thickness of the uniform coating of PBLG, $h_{\text{PBLG(uniform)}}$, can be calculated from $f_{\text{PBLG(uniform)}}$ using Equation 5.9.

$\varepsilon_{eff}^{\text{entire film}}$ can be fitted almost perfectly to $\varepsilon_{\text{film}} = \{\varepsilon_x = \varepsilon_y, \varepsilon_z\}$ by varying $f_{\text{PBLG(aniso)}}$ and $f_{\text{PBLG(uniform)}}$. Not factored into this fitting was the intrinsic birefringence of α-helical PBLG, as the alignment of the PBLG chains is uncertain. Thus $f_{\text{PBLG(aniso)}}$ was likely to be overestimated and $f_{\text{PBLG(uniform)}}$ (hence $h_{\text{PBLG(uniform)}}$) underestimated. Figure 5.24a compares the fitted $h_{\text{PBLG(uniform)}}$ with the averaged best fit PBLG thickness calculated from Figure 5.22, while Figure 5.24b shows directly the pore

volume fractions of both the uniform PBLG coating and anisotropic PBLG spanning the pores fitted by Equation 5.10.

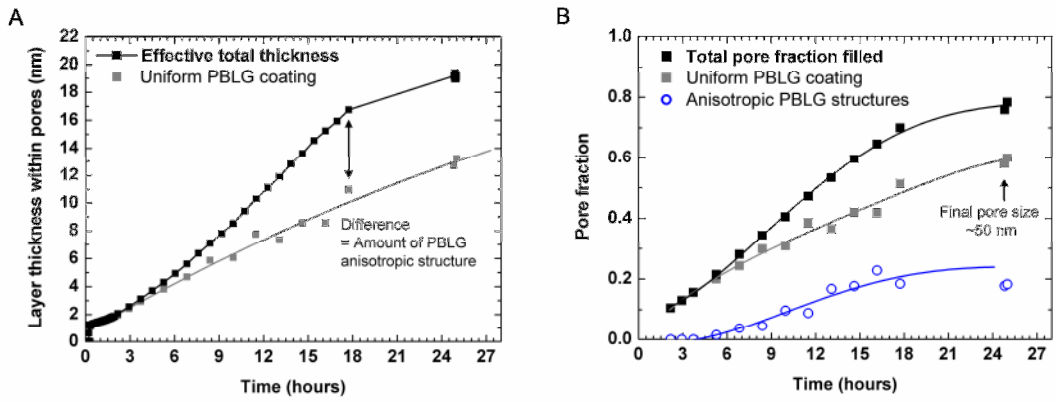

Figure 5.24. (A) The best fit amounts of PBLG material contained in the uniform coating (grey symbols) and within the entire pore (black symbols). The difference between the two data sets indicates the amount of PBLG material arranged across the central space of the pore. (B) The amount of PBLG growth as a uniform coating on the pore walls (grey), and as pore spanning anisotropic structures (blue), are expressed in terms of the pore fraction filled. The corresponding solid curves are only for guiding the eye. According to the thickness of the uniform coating, the final modelled pore size should be ~50 nm.

Altogether, Figure 5.24 indicates that the pores were modified with a uniform PBLG brush layer until 5 h into the polymerization process, when a 3~4 nm uniform layer of material had already been grafted, representing a ~20% filling of the cylindrical pore volume. Also at this point, the rate of the amount of PBLG polymerised increased. It is not clear with the present data how the evolution of the PBLG chain to the α-helical structure with the increase in the degree of polymerization, and the growth of PBLG into the centre of the pores, may be related. Further FTIR measurements focusing on the conformation evolution of the grafted PBLG are in progress. At later times, the rate for the growth of the uniform PBLG brush coating was almost linear, but the anisotropic pore spanning component of PBLG growth appeared to slow considerably after ~18 h, leading to an overall decrease in the rate of PBLG material added. At the end of the 25 h measurement, the model suggests (Figure 5.24b) that the original 76 nm diameter pores have been reduced to ~50 nm in diameter by the ~13 nm thick uniform PBLG coating, and that around half of this central pore volume was occupied by the anisotropic component of the PBLG structure. A 13~20 nm thick layer of PBLG would indicate a degree of polymerization = 160~250 (assuming a PBLG α-helix tilt angle of ~32° with respect to the surface) [69, 72].

SEM characterization of the dried AAO films after 25 h polymerization supports the EMT-OWS analysis of the anisotropy reversal, and the suggestion of a pore-spanning component to the growth of PBLG. Figure 5.25 shows the top surface of the sample with 76 nm diameter pores before and after the 25 h polymerization

process. A clear reduction in the pore diameters was observed, commensurate with the ~50 nm pore diameters implied by the ~13 nm uniform PBLG brush layer. In particular, cross section characterization of the AAO samples, shown in Figure 5.26, reveals the presence of structures spanning the width of the pores within the nanoporous films, as anticipated by the anisotropy reversal characterised by the in situ (and non-destructive) optical analysis. These structures were observed in both the samples with 76 nm (Figure 5.26a) and 60 nm pores (Figure 5.26b). These structures appeared like ribbed undulations on the pore walls in the 76 nm pores, and as filamentary/lamellae features in the 60 nm wide pores. However, these nanostructures might have been de-swelled in the SEM vacuum chamber and might have appeared even more extensive in the native solvent environment. Due to the change in environment, the SEM images were not quantified to determine the amount of PBLG material grown. In any case, the pore spanning structures might have decreased the diffusion rate within the pores, and might have contributed to the decrease in PBLG growth rate observed after ~15 h polymerization.

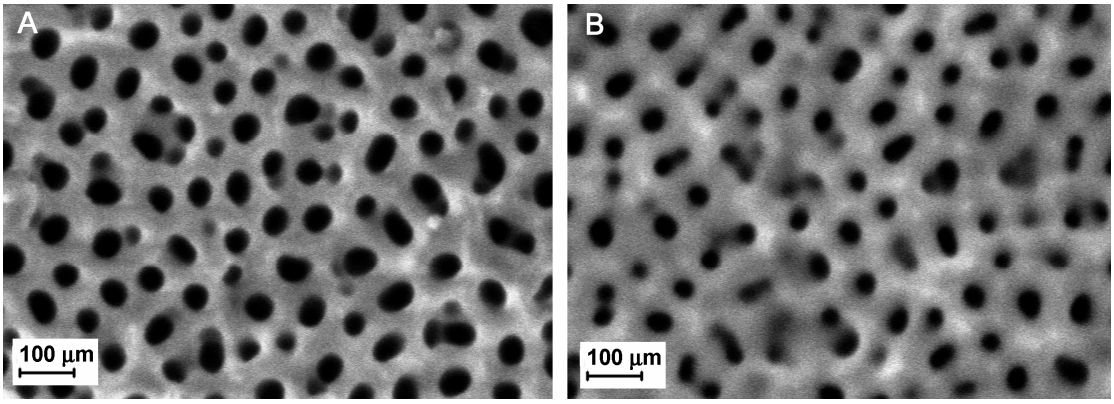

Figure 5.25. (A) SEM micrograph of the top surface of the 640 nm thick 2-step anodized AAO film with 76 nm pores (according to EMT fitting). (B) The top surface of the same sample after 25 h PBLG polymerization, as shown in Figure 5.21 through Figure 5.27.

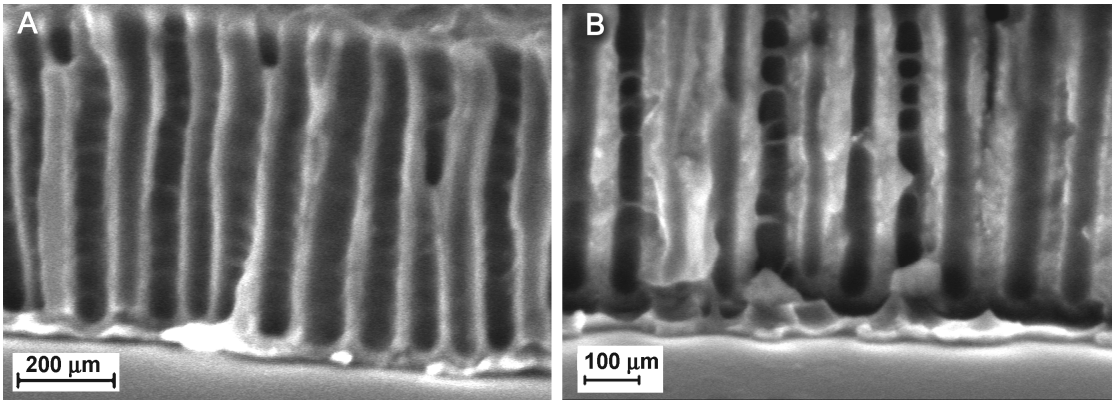

Figure 5.26. SEM cross sectional views of the AAO/PBLG structure after 24~25 h polymerization for the samples with initial pore sizes of 76 nm (A) and 60 nm (B), corresponding to the R vs. θ measurements shown in Figure 5.21.

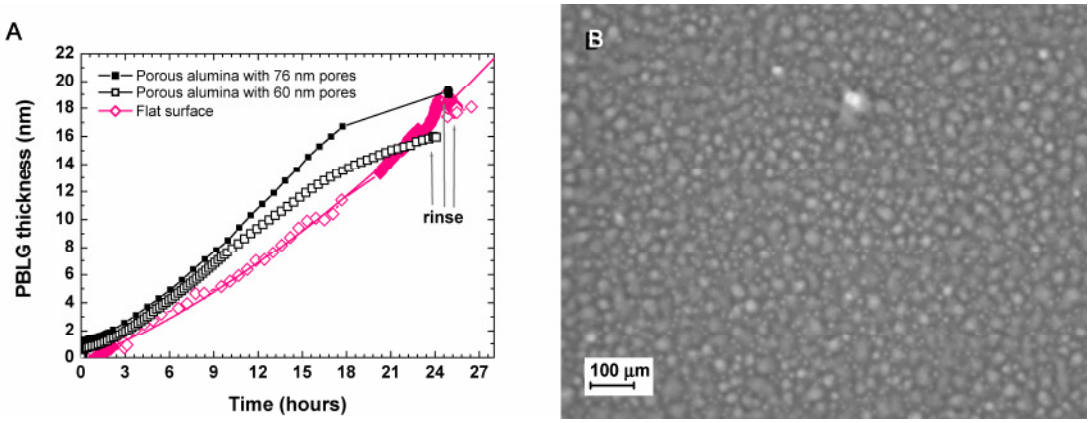

Figure 5.27. (A) The total thickness of PBLG grown within the pores of the AAO film (for both the samples with 60 nm and 76 nm pores) compared with the thickness grown on top of a flat SiO_2 film. The trends in PBLG growth for all three samples were similar for the first ~15 h, after which the growth within the pores slowed. (B) SEM characterization of the PBLG modified SiO_2 surface after the polymerization process.

To verify the extent to which the nanopore geometry had influenced the rate of polymerization, the experiment was repeated on a flat substrate. A 1060 nm thick SiO_2 waveguide* was functionalised with APTES using the procedure identical to that applied on the AAO films. The growth of the PBLG brush layer thickness was measured in situ, as shown for the AAO film with 76 nm pores, by repeated measurements of the R vs. θ waveguide response as well as by tracking of the TM_1 minimum angle. Analysis of the R vs. θ measurements was also carried out using Fresnel calculations. In the case of the solid SiO_2 waveguide, the waveguide film thickness change can be directly identified with the increase in PBLG thickness, while the dielectric constant of the PBLG layer was held constant (ε_{PBLG} = 2.403, as in the corresponding AAO analysis). ε_{SiO2} = 2.1 was used for the waveguide, identical to the value of common SiO_2 glass.

Figure 5.27a compares the PBLG layer thickness increase with time on the flat surface with that on the AAO samples. It is seen that the growth rates for the AAO samples were initially higher. However, the difference is within the bounds of uncertainty in the EMT approximation. On the other hand, the growth rate on the flat surface appeared to be increasing over time, while the growth rates within the AAO pores slowed, as described earlier. Thus the thickness of the PBLG layers on all the samples was similar at ~25 h. Importantly, the growth on the flat surface showed no sign of slowing, and appeared certain to overtake that within the AAO pores at longer

* The layer structure of the SiO2 waveguide was: glass substrate/Cr/Ag/Cr/SiO_2(sputtered)/SiO_2(solgel) at layer thicknesses of 1 nm/30 nm/1 nm/10600 nm/30 nm. The Cr layers were used to promote adhesion between the Ag and glass and SiO_2 layers. The SiO_2 waveguide was deposited by RF-plasma sputtering directly from a SiO_2 target (400W, $8x10^{-2}$ mbar Ar, using an Edwards Autolab 500). An additional SiO_2 solgel layer was prepared on the sputtered SiO_2 to optimize the solvent stability of the waveguide, according to the protocol used for preparing the BCP neutral surface energy brush (section 3.1.2). The dielectric constant of the thin film SiO_2 (ε_{SiO2} = 2.1), measured by baseline OWS measurements, was identical to the value of common SiO_2 glass.

polymerization times. SEM characterization of the PBLG modified flat waveguide (Figure 5.27b) showed a random distribution of islands of materials, but no filamentary structures. At the same time, FTIR measurements* indicated that the brush densities on both the flat and AAO samples were similar (4~5 chains/nm^2), thus indicating the similarity of the APTES layers deposited on all the samples. Interestingly, the decrease in the PBLG growth rate occurred earlier within the 60 nm wide pores than within the larger 76 nm pores, suggesting that the pore size had a fundamental influence on the formation of the anisotropic structure, and the rate of PBLG polymerization. In fact, the overlapping growth trends for both the pore sizes within the first ~9 h indicate that the difference in pores sizes in this range has a minor influence on the transport of monomers. However, the smaller pore sizes could have advanced the onset of the anisotropic pore spanning PBLG structures, which might then have reduced the diffusion in the pores. Further in situ measurements with different monomer concentrations may further elucidate the kinetics of the polymerization process within the confined AAO pore geometry.

5.4.4. Fluorescence detection in AAO thin film waveguides

The concept of fluorescence detection within the context of the nanoporous AAO waveguide is considered in a qualitative manner in this section. Previously in section 5.4.1, the sensitivity of detecting the deposition of a layer of material on the pore surfaces of the nanoporous AAO by waveguide mode minimum tracking was demonstrated. The chemisorption of a monolayer thick layer of APTES was monitored in situ (Figure 5.11), and an angle change on the order of 0.1° was recorded. This detected signal was two orders of magnitude larger than the angular precision of the mechanical setup. Although a high sensitivity was achieved for this label-free detection of a relatively small molecule (M_w = 221), the signal level (TM_1 mode minimum angle change) was dependent on the dielectric contrast between APTES and the pore filling medium (the solvent, i.e. ethanol). Thus for high sensitivity detection of molecules with a low dielectric contrast from the medium, fluorescence detection of the molecule labeled with a fluorophores may be considered.

Assuming there is an overlap between the wavelength of the waveguide modes (i.e. of the incidence laser) and the adsorption band, the guided electric fields confined in the AAO waveguide can be used to excite fluorophores residing within the nanoporous structure. That is, maxima in the fluorescence intensity may be expected at the waveguide mode coupling angles where reflectivity minima are observed during a R vs. θ measurement. Moreover, since the fluorescence intensity emitted depends on

* FTIR measurements and analysis were performed by Dr. Hatice Duran from the MPI-P. The grafting density was estimated from the OWS measured PBLG layer thickness, the known density of PBLG (1.32 g/cm^2), and chain tilt angle measured from FTIR peak ratios. See Appendix D.

the intensity of the excitation field [73], the detected fluorescence intensity can represent the extent of surface reactions of labeled molecules, if the concentration of unbound molecules in solution within the pores is lower than the surface bound concentration.

The fluorescence radiated (at the emission wavelength) can be collected and counted by a photomultiplier mounted on top of the AAO film, in exactly the same manner as for surface plasmon field-enhanced spectroscopy (SPFS, section 2.3) [73]. To minimise the level of background light detected that is unrelated to fluorescence emission, the entire setup is placed in a light-proof box, and optical filters are mounted in front of the photomultiplier to filter out the excitation source and other stray light. The excitation and detection schemes are illustrated in Figure 5.28.

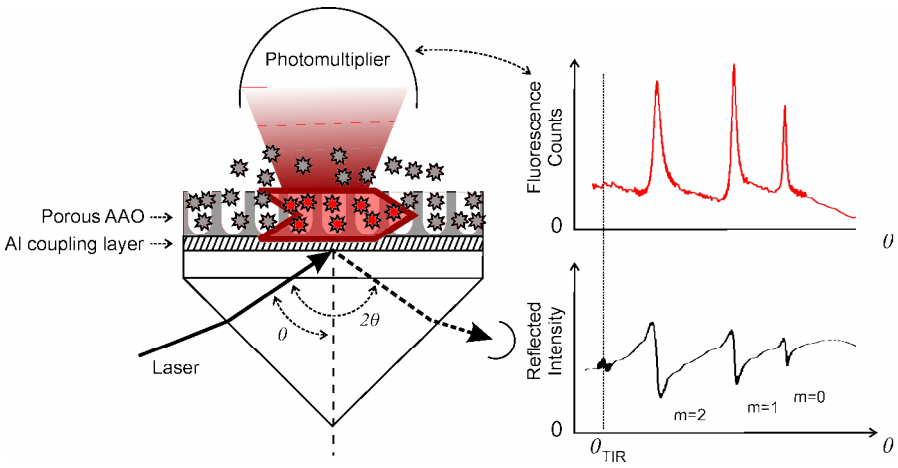

Figure 5.28. Schematic of the OWS nanoporous waveguide-fluorescence setup. (The liquid flow cell is omitted for clarity.) A photomultiplier is attached to the Kretschmann setup on top of the nanoporous film. As light is coupled into the nanoporous waveguide at the mode coupling angles, fluorophores within the nanoporous waveguide are excited by the propagating electric field, and radiate light at their emission wavelength. This fluorescence is detected by the photomultiplier and recorded together with the R vs. θ waveguide mode data.

It has been reported [36] that the light intensity of the propagating modes are enhanced with respect to the incidence light, due to the field confinement within the waveguiding film. Since the fluorescence intensity emitted depends on the intensity of the excitation field [73], this enhancement may lead to an enhanced sensitivity for fluorescence detection. However, the reported waveguide mode enhancement, experimentally measured in the range of 1~20, was dependent on a variety of factors, including film thickness and interface homogeneity. Moreover, in the case of the nanoporous waveguide, fluorescence emission may also be confined within the waveguide by internal reflections.

To demonstrate fluorescence excitation and detection in the nanoporous-AAO system, the binding of labeled streptavidin onto a biotin functionalised AAO from

different solution concentrations was measured. Streptavidin is a 53 kDa protein that exhibits specific, non-covalent binding to biotin (a small molecule, M_w = 244, important in metabolic reactions related to cell growth) with a very high affinity ($K_{association} = 10^{13} \sim 10^{15}\ M^{-1}$) [74, 75]. Moreover, there are four biotin binding pockets to each streptavidin, with two sites arranged on each of the two main opposing faces of the protein. Thus the binding is essentially irreversible above femtomolar concentrations, and simplifies analysis of the binding kinetics. Commercially available streptavidin labeled with the dye Alexa Fluor 647 was used. The absorption of the dye at the wavelength of the laser in the present waveguide setup (632.8 nm) is around half of its maximum at 647 nm, but the dye's emission maximum is located at 670 nm, which is well separated from the laser excitation. Therefore in the fluorescence detection setup (Figure 5.28), a bandstop filter centred at 632.8 nm and a bandpass filter centred at 670 nm, were used to minimise the background intensity detected by the photomultiplier.

Biotin functional groups were introduced on the surface of the AAO film by a LbL deposition strategy based on the well-studied [50, 60, 76] polyelectrolyte pair: PSS-PAH (poly(styrene sulfonic acid sodium salt) and poly(allyl amine hydrochloride)). First, the AAO film was modified with a layer of APDMES by gas-phase deposition, as described in section 5.4.1, to offer an amine terminated and positively charged surface in an aqueous environment. The sample was then immersed for 30 min in 1 mg/ml PSS (M_w ~70,000) dissolved in pH 7.4 phosphate buffered saline with 140 mM NaCl added (PBS). PSS adsorption led to charge overcompensation and a negatively charged surface on the pore surfaces. The sample was then rinsed in pure PBS, followed by immersion for 30 min in 1 mg/ml PAH (M_w ~15,000), also dissolved in PBS, and final sample rinsing in pure PBS. The PAH had 21% of its allylamine units along its backbone functionalised with biotin. This PAH-biotin was recently introduced by collaborators at the MPI-P (see section 2.1.2). This level of biotin incorporation was chosen to retain solubility of the polyelectrolyte in aqueous solutions, and to promote binding of streptavidin, which was shown to require a ~30% biotinylated surface for optimal binding [77, 78]. Finally, the PAH-biotin modified AAO sample, which is mounted within a liquid flow cell, was introduced to labeled streptavidin dissolved in PBS, at successively higher concentrations ranging from 10 fM to 800 nM. The LbL surface modification scheme and streptavidin binding are illustrated in Figure 5.29. Streptavidin binding was detected in situ by R vs. θ waveguide measurements and TM_1 waveguide mode angle tracking, as in previous experiments, and also by monitoring the intensity of the waveguide mode-associated fluorescence maxima. As streptavidin binding to the surface biotin groups occur, the waveguide modes are expected to shift to higher angles because the dielectric constant for streptavidin ($\varepsilon_{streptavidin}$ = 2.1 [73, 77]) is higher than PBS (ε_{PBS} = 1.777, measured by SPR). Also, as higher and higher amounts of streptavidin are bound to the PAH-biotin modified AAO from higher and

higher streptavidin concentrations in solution, the excited fluorescence intensities at the waveguide mode coupling angles are also expected to increase.

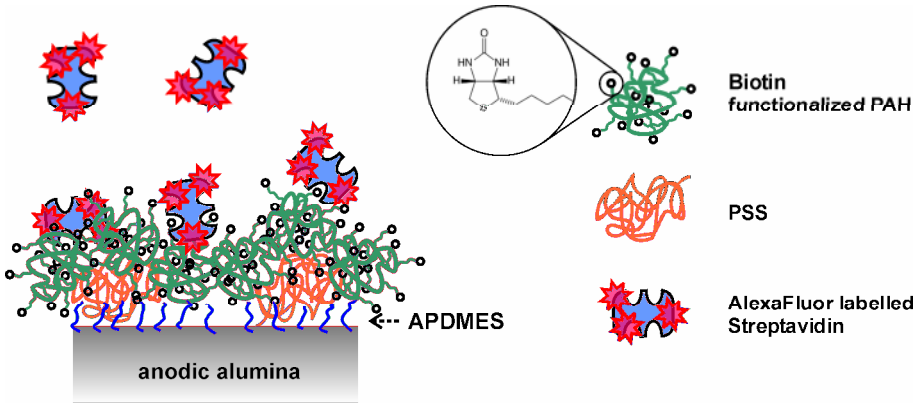

Figure 5.29. Schematic of the LbL surface modification scheme for capturing streptavidin from solution. The AAO film was first functionalised with an APDMES layer. The negatively charged PSS was then adsorbed onto the APDMES layer, followed by adsorption of the positively charged PAH on the PSS. 21% of the monomers along the PAH backbone were biotinylated, enabling binding of the fluorescence labelled streptavidin onto the PAH layer.

Figure 5.30 shows the R vs. θ waveguide response, and the associated fluorescence emission, of an AAO film modified by PAH-biotin before and after streptavidin binding. The AAO sample was prepared by 2-step anodization, was 844 nm thick and had a 76 nm average pore diameter. The angle shift of the TM_1 mode minimum, and the associated fluorescence intensity, during the intermediate steps of introducing labeled streptavidin at increasing concentrations, are shown in Figure 5.31a.

In the top panels of Figure 5.30, the R vs. θ waveguide responses in both the p- and s-polarizations are shown. As described in previous sections, the OWS measurements were quantified by Fresnel calculations and EMT analysis. The total TM_1 angle shift was ~0.8º, corresponding to a uniform streptavidin layer of ~3 nm, and corresponding reasonably to the native dimensions of streptavidin (4~5 nm [74, 79]). Since the protein cannot form close-packed layers, the modeled thickness represents only the average layer height [80].

In the lower panels of Figure 5.30, the fluorescence signals are shown. Before streptavidin binding, the background photon count was at the level of <50,000 counts per second (cps). This background signal originated primarily from detector noise and light that could not be rejected* by the optical filters. Thus small maxima were still

* The background intensity consists primarily of noise from the photomultiplier and scattered intensity from the incidence laser light. When the incidence laser was switched off, the background count (detector noise) was ~500

observed at the waveguide mode coupling angles even though no fluorophores were present in the AAO films. After streptavidin binding, the fluorescence intensity of the maxima increased dramatically as expected. The fluorescence peak associated with the TM_1 mode increased by more than 3 orders of magnitude to 2.2 x 10^7 cps.*

It was also observed that the fluorescence intensity maxima occurred at lower angles immediately to the left of the R vs. θ waveguide mode minima (Figure 5.30b). This difference was a manifestation of the phase shift accompanying waveguide mode coupling that gave rise to the destructive interference between the incidence and back-coupled waves and the reflected intensity minima. The waveguide mode minima corresponded to coupling conditions giving rise to the maximum phase shift, while the maximum waveguide mode field intensities in the film, hence the maximum excited fluorescence intensities, actually corresponded to angles slightly lower than the minima in reflected intensity. A practical consequence of this small angle deviation is that the fluorescence intensity measured during tracking of the TM_1 mode angle minimum, was lower than the actual fluorescence maximum by an amount proportional to angle deviation and the local slope of the fluorescence maximum. The analogous optical description also applies to the case of SPR fluorescence detection [73].

Figure 5.31a shows the in situ TM_1 mode angle shifts and the corresponding increase in intensity of the associated fluorescence maximum, as increasing amounts of streptavidin bound onto the PAH-biotin modified AAO film. Streptavidin was introduced at successively higher concentrations, starting from 10 fM at 20 min. up to 250 nM at 290 min. Binding was allowed to proceed for 30 min before being interrupted by rinsing in pure PBS. The system was then allowed to equilibrate for another 30 min or more in pure PBS before streptavidin at the next concentration was introduced. Around 1 ml of streptavidin solution was used at each concentration, and at least 2 ml pure PBS was used for each rinsing step. In comparison, the liquid flow cell had a volume of only 0.03 ml and 0.75 cm^2 of the AAO sample was exposed to the liquid reagents (Appendix E). The root mean squared (rms) fluctuation of the angle minimum position was 0.0009º (measured during the first 20 min, Figure 5.31a) and the rms fluctuation of the fluorescence signal was 350 cps (measured during the first 120 min, as illustrated in the inset in Figure 5.31a). The International Union of Pure and Applied Chemistry (IUPAC) recommends that the limit of detection (LOD) be defined as 3 times the signal rms plus the mean background [81], i.e. $LOD_{TM1\ shift}$ = 0.0027º and $LOD_{fluoresence}$ = 1050 + 29200 = 30250 cps. Thus streptavidin binding on

---

cps. The efficiency of the optical filters is 99.9~99.99% outside the desired wavelengths, thus most of the background intensity would have originated from the incidence light. The natural fluorescence of the AAO anodized in oxalic acid has been measured and was at the spectrometer's level of noise in the wavelength range ~670 nm. The incidence laser intensity was measured to be 300 nW/cm^2 by a photodiode calibration unit.

* The photomultiplier used to measure the fluorescence intensity actually saturates at ~4 x 10^6 cps. The final fluorescence intensity was measured by decreasing the incidence laser intensity to ~10% of the normal value by cross polarisers. The fluorescence intensity was assumed to be proportional to the incidence intensity.

the surface was observed by the TM_1 angle minimum increase at concentrations at or above 200 fM, and the fluorescence intensity was observed to increase after binding at a concentration at or above 4 pM. However, the determination of $LOD_{TM1\ shift}$ was complicated by irregular binding kinetics, as will be discussed on pg. 124.

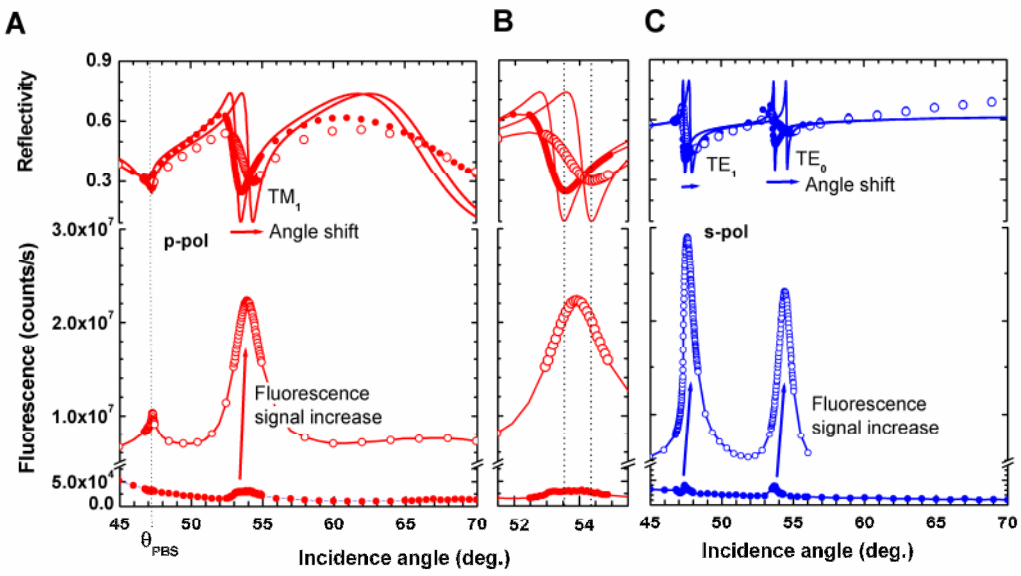

Figure 5.30. OWS R vs θ measurements (top) and the simultaneously recorded fluorescence signal (bottom), of the PAH-biotin functionalised nanoporous AAO waveguiding films, both before (solid symbols) and after (open symbols) binding of streptavidin to the point of saturation. Solid curves show the idealised response according to Fresnel calculations. (A) shows the waveguide response under p-polarised light (TM_1 mode); (B) shows the details of the TM_1 mode angle shifts; and (C) shows the response under s-polarised light (TE_0 and TE_1 modes). Binding of the fluorescence labeled streptavidin caused the waveguide modes to shift to higher angles, and the fluorescence intensity to increase. Note the break on the vertical scale for the fluorescence counts. Note also that the fluorescence maxima occur at angles immediately to the right of the reflected intensity minima, as shown in (B).

Since the biotin-streptavidin binding was virtually irreversible, the equilibrium amount of streptavidin bound is identified with the total number of streptavidin binding sites on the AAO film [82, 83]. As a consequence, the slopes of the binding curves at each concentration (i.e. Figure 5.31) should be linear until all binding sites are occupied, even though the analysis is complicated by the fact that each streptavidin can bind to four biotin groups on the surface [82]. However, the actual binding kinetics appeared to approach an asymptotic value at all concentrations. This effect is exaggerated by the log scales of Figure 5.31 and is especially prominent in the fluorescence signal. Prior R vs. θ measurements and EMT analysis of the PAH-biotin surface modification layer indicated a 1.5 nm thick layer of PAH-biotin, and an upper bound density of 10^{15} biotin/cm^2 on the 840 nm thick AAO sample with a total surface area of 19 cm^2 (Appendix E). In comparison, there are only 6 x 10^6 streptavidin/ml in a 10 fM solution, and 1.5 x 10^{14} streptavidin/ml in a 250 nM

solution. Therefore there were more binding sites than there were streptavidin at all concentrations in the 1 ml of solutions used. Thus the observed decreases in the binding rates were likely due to the depletion of streptavidin in the solution. Additionally, because there were more binding sites than there were streptavidin in the solutions even at the highest concentration used, the amount of streptavidin bound at each concentration was assumed to be independent of the previous binding reactions at lower concentrations. The assumption was also supported by the fact that the concentration intervals between the different streptavidin solutions were separated by an order of magnitude or higher.

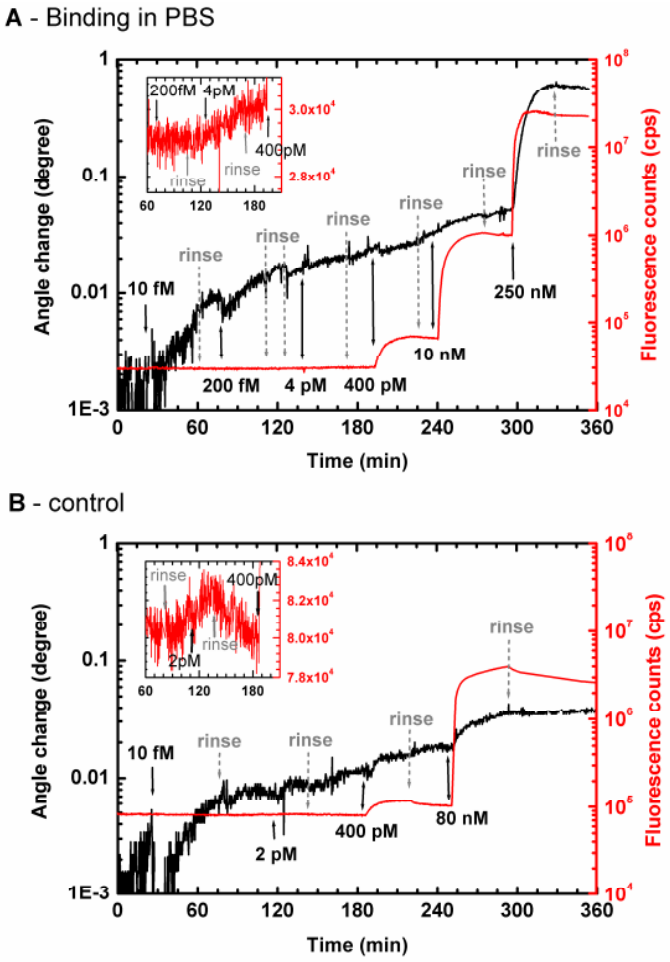

Figure 5.31. Real time responses of the TM_1 angle shifts and changes in the associated fluorescence intensities due to binding of the fluorescence labelled streptavidin on the PAH modified nanoporous AAO film. Note the log10 vertical scales in the main graphs, and the normal scale in the insets. The black curves show the angle changes (left axes), and the red curves show the change in fluorescence intensity (right axes). (A) shows the binding onto biotinylated PAH of streptavidin from PBS at different concentrations. (B) shows the control experiment in which non-specific binding of streptavidin onto *unfunctionalised* PAH without biotinylation was measured. Black arrows indicate when streptavidin was introduced, and grey arrows indicate rinsing with PBS. The insets show the changes in the fluorescence signal when picomolar concentrations of streptavidin were introduced, which cannot be clearly seen in the main graphs.

The isoelectric point of streptavidin is pH 6~6.5 [84], therefore the protein is expected to carry a slight negative charge in the pH 7.4 PBS used. Moreover, the Alex Fluor label is sulfonated [85] which also imparts a slight negative charge to the protein. Therefore significant "non-specific" adsorption unrelated to biotin-streptavidin binding may occur on the positively charged PAH-biotin. This background adsorption was measured by preparing an AAO sample modified with a final layer of *unfunctionalised* PAH (M_w~56,000) instead of the PAH-biotin. Adsorption of the pure PAH also resulted in a ~1.5 nm thick layer, and the measurement of the TM_1 angle minimum due to non-specific streptavidin adsorption on PAH, as well as the associated fluorescence intensity maximum, are shown in Figure 5.31b. Significant angle shifts and fluorescence intensity increases were indeed observed, but the signals were nevertheless smaller in comparison with streptavidin binding on the biotin modified PAH. Incidentally, the fluorescence background in this experiment was higher at 81700 cps, and the background rms was proportionally higher at 870 cps, while the angle shift rms (0.0007º) was comparable to the previous experiment with PAH-biotin. The total angle shift (up to a streptavidin concentration of 80 nM) was 0.03º, while the cumulative fluorescence intensity increase was 2.5 x 10^6 cps. On the other hand, significant desorption was also observed in the fluorescence signal after each PBS rinsing, and indicated the non-specific nature of the binding.

A more direct and quantitative comparison of streptavidin binding on the PAH-biotin and the unfunctionalised PAH modified AAO surfaces is shown in Figure 5.32, by plotting the cumulative adsorbed amounts at each concentration against the streptavidin solution concentration. In particular, the adsorbed amounts were normalised by 3 times the signal rms so that a normalised value of 10^0 on the vertical scale corresponded to the limit of detection (LOD). Also, since there were more binding sites than streptavidin, the concentration axis could also be interpreted as proportional to the amount of streptavidin contained in the solution.

In Figure 5.32a, it is seen that the angle change detected for both the PAH-biotin and the unfunctionalised PAH samples were similar up to a concentration of 10^{-8} M. That is, streptavidin-biotin binding could not be unambiguously distinguished from adsorption at concentrations below 10^{-8} M. Moreover, the slope of log(angle change) vs. log(concentration) was much smaller than unity below 10^{-8} M, although the slope increased at higher concentrations. As discussed earlier, the virtually irreversible binding between streptavidin and biotin leads to linear binding kinetics. It also implies that, within the diffusion-limited regime, the binding shown in a log-log plot should scale directly with the concentration with a slope = 1 [82]:

Equation 5.11. $$\frac{d(binding)}{dt} = kC_{streptavidin} \;;\; \log(\Delta binding) = \log C_{streptavidin} + \log k\Delta t$$

where k is the mass transport coefficient, $C_{streptavidin}$ is the streptavidin concentration in solution, and Δt is the length of the binding step (= 30 min).

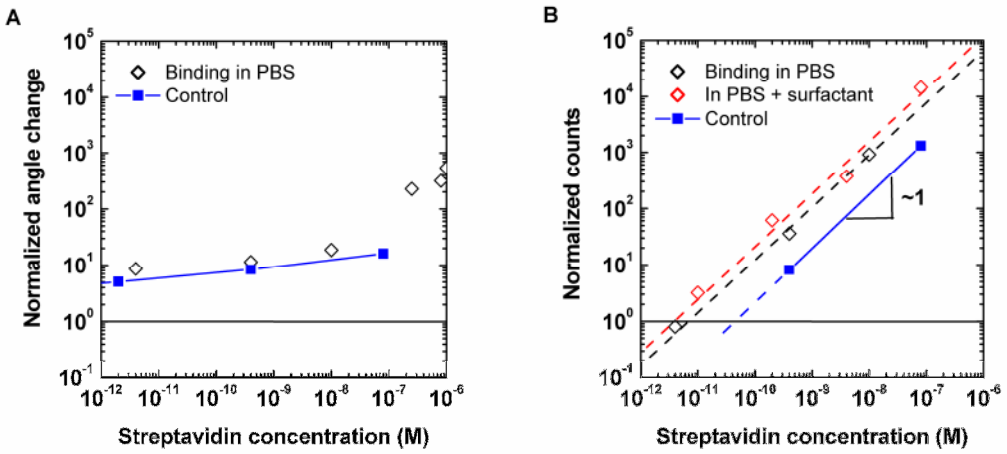

Figure 5.32. Comparison between the cumulative amounts of streptavidin bound to the biotinylated PAH layer ("binding in PBS") and to the un-modified PAH layer (control), as measured by the TM_1 mode angle shift (A) and by the associated fluorescence signal (B). The normalised signals were obtained by dividing the raw signals by 3 times the standard deviation in the baseline measurements. The horizontal lines set at a normalised signal level of 10^0 indicate the level below which, according to IUPAC guidelines, the signal change can no longer be distinguished from the background. In (B) an additional experiment in which a surfactant (Tween-20) was added to the PBS solution at a concentration of 0.05 vol.% is also shown for comparison ("in PBS + surfactant"). The dashed blue line indicates measurements in the "control" experiments performed at concentrations below 10^{-10} M. These results were at the level of noise and were not included in the log-log plot because they could not be properly normalised. The intercepts between the horizontal line indicating the smallest detectable signal (10^0) and the dashed curves fitting the data, indicate the concentration of streptavidin at the limit of detection (3~7 pM). The slopes of all the curves in (B) are ~1, suggesting diffusion-limited binding kinetics.

In contrast to the angle scan results, the normalised fluorescence data shown in Figure 5.32b all have slopes ~ 1, consistent with Equation 5.11, and corresponded to a much more sensitive response than the angle scan data. It is seen that the fluorescence intensity increase on PAH-biotin was approximately an order of magnitude higher than on unfunctionalised PAH. Figure 5.32b also shows an additional experiment in which the PBS was spiked with a surfactant (polyoxyethylenesorbitan monolaurate, i.e. Tween-20) at a concentration of 0.05 vol.% (0.45 mM). The surfactant was expected to prevent the loss of streptavidin to the surfaces of the liquid handling system due to non-specific adsorption, which may have an especially significant effect at low concentrations. However, this benefit was achieved by the sacrificial adsorption of the surfactant, and a surfactant layer ~1 nm thick was measured on the PAH-biotin functionalised AAO when the liquid cell was first flushed with the spiked PBS, prior to streptavidin binding. Subsequently, as streptavidin was introduced, the TM_1 angle minimum was observed to shift to lower values, indicating desorption of material, possibly due to the displacement of the surfactant by streptavidin bound to

biotin (Appendix F). These ambiguous angle shifts were not comparable to the other angle shift data, and were not included in Figure 5.32a. However, the fluorescence signal simply records the amount of streptavidin bound on the surface, regardless of the binding process or the macromolecular architecture. Therefore, the corresponding binding amounts with the surfactant spiked PBS could be compared with the other fluorescence data sets in Figure 5.32b. Indeed, this data set indicated slightly elevated levels of streptavidin binding, which might correspond to the amount of streptavidin otherwise lost to the surfaces of the liquid handling system. Furthermore, the intercepts between the binding data and the LOD horizontal line in Figure 5.32b shows that streptavidin binding could be detected at a concentration of 3~7 x 10^{-12} M.

It is not clear, given the present data, why the binding results, as shown in Figure 5.32a, indicate such a weak dependence of the angle shift with concentration, at concentrations < 10^{-8} M. The corresponding fluorescence data indicates that streptavidin binding was occurring down to at least a concentration of 10^{-12} M. It is possible that the angle change signal was convoluted with a second, non-fluorescence process, such as desorption of molecules in the polyelectrolyte layers. At the same time, any explanation must also explain the similarity in the binding data on both PAH-biotin and unfunctionalised PAH surfaces. For example, displacement of counterions due to streptavidin binding may have been responsible for the small net change in waveguide mode minimum angle. Another possibility is that the initial streptavidin binding led to a rearrangement of the polyelectrolyte layers, which, if it led to a decrease in the layers' dielectric constant, could compensate for the increase in optical density due to increase in thickness of the streptavidin layer. However, no experimental support of either speculation is currently available. Given that the binding process led to the anomalous angle shift data, the corresponding $LOD_{TM1\ shift}$ could also not be specified. Nonetheless, the fluorescence data shows the expected kinetics, that streptavidin binding had definitely occurred, and $LOD_{fluorescence}$ could be determined.

As discussed earlier, $LOD_{fluorescence}$ was 10^{-12} M. This was at the same level reported for SPR fluorescence detection (SPFS) [86]. However, it is expected that fluorescence sensing with nanoporous AAO waveguides should be at least an order of magnitude higher than SPFS. This is because the nanoporous AAO provides at internal surface area at least an order of magnitude higher than the corresponding planar surface, thus correspondingly more fluorophores could be attached to the surface. However, the background intensity measured, at 30,000~80,000 cps, was also an order of magnitude higher than in the case of SPFS [86]. This cold be due to the fact that the incidence light can interact with the entire thickness of the waveguide, compared with only a 50 nm thick Au film than in the case of SPR, thus increasing the possible amount of scattered (background) radiation. Moreover, this scattering may be significant in the case of the AAO film due to ~3% surface coverage by hillock formations (section 3.2.2), which represent grain structures with sizes on the

scale of the wavelength of the waveguided light. Surface roughness of the AAO films may also contribute to the background scattered light (section 3.2.2). Moreover, the fluorescence signal could also be improved by replacing the Al coupling layer with a Au or Ag layer, such as customarily used in SPFS. The lower optical damping inherent in the noble metal layers [30] would increase waveguide mode field intensities, and increase the illumination of the fluorophores. Surface roughness of the Al coupling layer might also have contributed to sub-optimal coupling efficiency for the waveguide modes, and light scattering. Thus a range of improvements to the AAO sample preparation could potentially improve the sensitivity of fluorescence detection using the nanoporous waveguide.

5.5. References

[1] Foss CA, Hornyak GL, Stockert JA, Martin CR: Template-Synthesized Nanoscopic Gold Particles: Optical Spectra and the Effects of Particle Size and Shape. *Journal of Physical Chemistry* **1994**, *98*, 2963.

[2] Hornyak GL, Patrissi CJ, Martin CR: Fabrication, Characterization, and Optical Properties of Gold Nanoparticle/Porous Alumina Composites: The Nonscattering Maxwell-Garnett Limit. *Journal of Physical Chemistry B* **1997**, *101*, 1548.

[3] Galca AC, Kooij ES, Wormeester H, Salm C, Leca V, Rector JH, Poelsema B: Structural and Optical Characterization of Porous Anodic Aluminum Oxide. *Journal of Applied Physics* **2003**, *94*, 4296.

[4] Norrman S, Andersson T, Granqvist CG, Hunderi O: Optical Properties of Discontinuous Gold Films. *Physical Review B* **1978**, *18*, 674.

[5] Granqvist CG, Hunderi O: Optical Properties of Ag-Sio2 Cermet Films: A Comparison of Effective-Medium Theories. *Physical Review B* **1978**, *18*, 2897.

[6] Aspnes DE, Heller A, Porter JD: Microstructurally Engineered, Optically Transmissive, Electrically Conductive Metal Films. *Journal of Applied Physics* **1986**, *60*, 3028.

[7] García-Vidal FJ, Pitarke JM, Pendry JB: Effective Medium Theory of the Optical Properties of Aligned Carbon Nanotubes. *Physical Review Letters* **1997**, *78*, 4289.

[8] Maldovan M, Bockstaller MR, Thomas EL, Carter WC: Validation of the Effective-Medium Approximation for the Dielectric Permittivity of Oriented Nanoparticle-Filled Materials: Effective Permittivity for Dielectric Nanoparticles in Multilayer Photonic Composites. *Applied Physics B: Lasers and Optics* **2003**, *76*, 877.

[9] Aspnes DE: Optical Properties of Thin Films. *Thin Solid Films* **1982**, *89*, 249.

[10] Maxwell-Garnett JC: Colours in Metal Glasses and in Metallic Films. *Philosophical Transactions of the Royal Society of London. Series A, Containing Papers of a Math. or Phys. Character (1896-1934)* **1904**, *203*, 385.

[11] Maxwell-Garnett JC: Colours in Metal Glasses, in Metallic Films, and in Metallic Solutions. Ii. *Philosophical Transactions of the Royal Society of London. Series A, Containing Papers of a Math. or Phys. Character (1896-1934)* **1906**, *205*, 237.

[12] Choy TC: *Effective Medium Theory: Principles and Applications* Oxford University Press: New York, 1999.

[13] Foss CA, Tierney MJ, Martin CR: Template Synthesis of Infrared-Transparent Metal Microcylinders: Comparison of Optical Properties with the Predictions of Effective Medium Theory. *Journal of Physical Chemistry* **1992**, *96*, 9001.

[14] Granqvist CG, Hunderi O: Optical Properties of Ultrafine Gold Particles. *Physical Review B* **1977**, *16*, 3513.

[15] Granqvist CG, Hunderi O: Conductivity of Inhomogeneous Materials: Effective-Medium Theory with Dipole-Dipole Interaction. *Physical Review B* **1978**, *18*, 1554.

[16] Osborn JA: Demagnetizing Factors of the General Ellipsoid. *Physical Review* **1945**, *67*, 351.

[17] Landau LD, Lifshitz EM, Pitaevskii LP: *Electrodynamics of Continuous Media*, Butterworth-Heinemann 1984.

[18] van de Hulst HC: *Light Scattering by Small Particles* Dover Publications, 1981.

[19] Lau KHA, Tan LS, Tamada K, Sander MS, Knoll W: Highly Sensitive Detection of Processes Occurring inside Nanoporous Anodic Alumina Templates: A Waveguide Optical Study. *Journal of Physical Chemistry B* **2004**, *108*, 10812.

[20] Knoll W: Interfaces and Thin Films as Seen by Bound Electromagnetic Waves. *Annual Review of Physical Chemistry* **1998**, *49*, 569.
[21] Kogelink H: *Theory of Dielectric Waveguides*. In *Integrated Optics*, T. Tamir, ed.; Springer: Berlin / Heidelberg, 1979; Vol. *7*, pp. 13.
[22] Hunsperger RG: *Integrated Optics - Theory and Technology*, Springer: Berlin / Heidelberg, 2002.
[23] Tamir T: *Beam and Waveguide Couplers*. In *Integrated Optics*, T. Tamir, ed.; Springer: Berlin / Heidelberg, 1979; Vol. *7*, pp. 83.
[24] Lukosz W: Principles and Sensitivities of Integrated Optical and Surface Plasmon Sensors for Direct Affinity Sensing and Immunosensing. *Biosensors and Bioelectronics* **1991**, *6*, 215.
[25] Heideman RG, Kooyman RPH, Greve J: Performance of a Highly Sensitive Optical Waveguide Mach-Zehnder Interferometer Immunosensor. *Sensors and Actuators B: Chemical* **1993**, *10*, 209.
[26] Potyrailo RA, Hobbs SE, Hieftje GM: Optical Waveguide Sensors in Analytical Chemistry: Today's Instrumentation, Applications and Trends for Future Development. *Fresenius' Journal of Analytical Chemistry* **1998**, *362*, 349.
[27] Weisser M, Tovar G, Mittler-Neher S, Knoll W, Brosinger F, Freimuth H, Lacher M, Ehrfeld W: Specific Bio-Recognition Reactions Observed with an Integrated Mach–Zehnder Interferometer. *Biosensors and Bioelectronics* **1999**, *14*, 405.
[28] Hickel W, Knoll W: Optical Waveguide Microscopy. *Applied Physics Letters* **1990**, *57*, 1286.
[29] Born M, Wolf E: *Optics of Metals*. In *Principles of Optics*; Cambridge University Press, 1999, pp. 735.
[30] Raether H: *Surface-Plasmons on Smooth and Rough Surfaces and on Gratings*, Springer: Berlin / Heidelberg, 1988.
[31] Skivesen N, Horvath R, Pedersen HC: Optimization of Metal-Clad Waveguide Sensors. *Sensors and Actuators B: Chemical* **2005**, *106*, 668.
[32] Born M, Wolf E: *Wave Propagation in a Stratified Medium*. In *Principles of Optics*; Cambridge University Press, 1999, pp. 55.
[33] Worm J; Max Planck Institute for Polymer Research: Mainz, **2001**, pp. Implementation of Fresnel calculations for a layer system with anistropic dielectric and layer thickness values; and the graphical comparison with measured reflectivity data.
[34] Ma H, Jen AKY, Dalton LR: Polymer-Based Optical Waveguides: Materials, Processing, and Devices. *Advanced Materials* **2002**, *14*, 1339.
[35] Winsemius P, van Kampen FF, Lengkeek HP, van Went CG: Temperature Dependence of the Optical Properties of Au, Ag and Cu. *Journal of Physics F: Metal Physics* **1976**, 1583.
[36] Durr M, Menges B, Knoll W, Yasuda A, Nelles G: Direct Measurement of Increased Light Intensity in Optical Waveguides Coupled to a Surface Plasmon Spectroscopy Setup. *Applied Physics Letters* **2007**, *91*, 021113.
[37] Wunderlich W: *Physical Constants of Poly(Methyl Metahcrylate)*. In *Polymer Handbook*, J. Brandrup; E.H. Immergut; E.A. Grulke; A. Abe; D.R. Bloch, eds.; Wiley: New York, 1999, pp. V/87.
[38] Schrader D: *Physical Constants of Poly(Styrene)*. In *Polymer Handbook*, J. Brandrup; E.H. Immergut; E.A. Grulke; A. Abe; D.R. Bloch, eds.; Wiley: New York, 1999, pp. V/91.
[39] Ay F, Kocabas A, Kocabas C, Aydinli A, Agan S: Prism Coupling Technique Investigation of Elasto-Optical Properties of Thin Polymer Films. *Journal of Applied Physics* **2004**, *96*, 7147.
[40] Cameron PJ, Jenkins ATA, Knoll W, Marken F, Milsom EV, Williams TL: Optical Waveguide Spectroscopy Study of the Binding of Cytochrome C in Mesoporous Titanium Dioxide Film Electrodes. *Chemistry of Materials* **2008**, *accepted for publication*.
[41] Awazu K, Rockstuhl C, Fujimaki M, Fukuda N, Tominaga J, Komatsubara T, Ikeda T, Ohki Y: High Sensitivity Sensors Made of Perforated Waveguides. *Optics Express* **2007**, *15*, 2592.
[42] Fujimakia M, Rockstuhla C, Wanga X, Awazua K, Tominagaa J, Ikedab T, Ohkib Y, Komatsubarac T: Nanoscale Pore Fabrication for High Sensitivity Waveguide-Mode Biosensors. *Microelectronic Engineering* **2007**, *84*, 1685.
[43] Reimhult E, Kumar K, Knoll W: Fabrication of Nanoporous Silicon Nitride and Silicon Oxide Films of Controlled Size and Porosity for Combined Electrochemical and Waveguide Measurements. *Nanotechnology* **2007**, 275303.
[44] Smith DY, Shiles E, Inokuti M: *The Optical Properties of Metallic Aluminum*. In *Handbook of Optical Constants of Solids* Edward D. Palik, ed.; Academic Press: New York, 1997.
[45] Stein N, Rommelfangen M, Hody V, Johann L, Lecuire JM: In Situ Spectroscopic Ellipsometric Study of Porous Alumina Film Dissolution. *Electrochimica Acta* **2002**, *47*, 1811.
[46] Jonas U, Krueger C: The Effect of Polar, Nonpolar, and Electrostatic Interactions and Wetting Behavior on the Particle Assembly at Patterned Surfaces. *Journal of Supramolecular Chemistry* **2002**, *2*, 255–270.
[47] Kurth DG, Bein T: Thin Films of (3-Aminopropyl)Triethoxysilane on Aluminum Oxide and Gold Substrates. *Langmuir* **1995**, *11*, 3061.
[48] Wieringa RH, Siesling EA, Geurts PFM, Werkman PJ, Vorenkamp EJ, Erb V, Stamm M, Schouten AJ: Surface Grafting of Poly(L-Glutamates). 1. Synthesis and Characterization. *Langmuir* **2001**, *17*, 6477.
[49] Decher G: Fuzzy Nanoassemblies: Toward Layered Polymeric Multicomposites. *Science* **1997**, *277*, 1232.
[50] Schönhoff M: Self-Assembled Polyelectrolyte Multilayers. *Current Opinion in Colloid and Interface Science* **2003**, *8*, 86.

[51] Hubsch E, Ball V, Senger B, Decher G, Voegel JC, Schaaf P: Controlling the Growth Regime of Polyelectrolyte Multilayer Films: Changing from Exponential to Linear Growth by Adjusting the Composition of Polyelectrolyte Mixtures. *Langmuir* **2004**, *20*, 1980.

[52] Hillebrenner H, Buyukserin F, Kang M, Mota MO, Stewart JD, Martin CR: Corking Nano Test Tubes by Chemical Self-Assembly. *Journal of the American Chemical Society* **2006**, *128*, 4236.

[53] Kim DH, Karan P, Göring P, Leclaire J, Caminade A-M, Majoral J-P, Gösele U, Steinhart M, Knoll W: Formation of Dendrimer Nanotubes by Layer-by-Layer Deposition. *Small* **2005**, *1*, 99.

[54] Launay N, Caminade A-M, Lahana R, Majoral J-P: A General Synthetic Strategy for Neutral Phosphorus-Containing Dendrimers. *Angewandte Chemie International Edition* **1994**, *33*, 1589.

[55] Majoral JP, Caminade AM: Dendrimers Containing Heteroatoms (Si, P, B, Ge, or Bi). *Chemical Reviews* **1999**, *99*, 845.

[56] Loup C, Zanta M-A, Caminade A-M, Majoral J-P, Meunier B: Preparation of Water-Soluble Cationic Phosphorus-Containing Dendrimers as DNA Transfecting Agents. *Chemistry - A European Journal* **1999**, *5*, 3644.

[57] Yu Y-M, Feng C-L: Personal communication, **2008**.

[58] Hohlbein J, Steinhart M, Schiene-Fischer C, Benda A, Hof M, Hübner Christian G: Confined Diffusion in Ordered Nanoporous Alumina Membranes. *Small* **2007**, *3*, 380.

[59] Israelachvili JN: *Intermolecular and Surface Forces*, Academic Press: New York, 1992.

[60] Ball V, Voegel JC, Schaaf P: Effect of Thiocyanate Counterion Condensation on Poly(Allylamine Hydrochloride) Chains on the Buildup and Permeability of Polystyrenesulfonate/Polyallylamine Polyelectrolyte Multilayers. *Langmuir* **2005**, *21*, 4129.

[61] Dobrynin AV, Rubinstein M: Theory of Polyelectrolytes in Solutions and at Surfaces. *Progress in Polymer Science* **2005**, *30*, 1049.

[62] Deming TJ: Polypeptide Materials: New Synthetic Methods and Applications. *Advanced Materials* **1997**, *9*, 299.

[63] Duran H, Lau KHA, Lübbert A, Jonas U, Steinhart M, Knoll W: *Biopolymers for Biosensors: Polypeptide Nanotubes for Optical Biosensing*. In *Polymers for Biomedical Applications*, Anil Mahapatro, ed.; Oxford University Press: New York, 2007; Vol. *977*, pp. 371.

[64] Higashi N, Saitou M, Mihara T, Niwa M: Enantioselective Binding of Alpha-Amino Acids at Poly(L-Glutamic Acid)-Functionalized Monolayer Surfaces. *Journal of the Chemical Society, Chemical Communications* **1995**, 2119.

[65] Lee NH, Frank CW: Separation of Chiral Molecules Using Polypeptide-Modified Poly(Vinylidene Fluoride) Membranes. *Polymer* **2002**, *43*, 6255.

[66] Whitesell JK, Chang HK: Surface Oriented Polymers for Nonlinear Optics. *Molecular Crystals and Liquid Crystals* **1994**, *240*, 251

[67] Machida S, Urano TI, Sano K, Kato T: Response of a Hydrogen-Bonded Liquid Crystal to an Applied Electric Field Accelerated by a Poly(gamma-Benzyl L-Glutamate) Chemical Reaction Alignment Film. *Langmuir* **1997**, *13*, 576.

[68] Block H: *Poly (Gamma-Benzyl-L-Glutamate) and Other Glutamic Acid Containing Polymers*, Gordon & Breach Science Publishers: New York, 1983.

[69] Chang YC, Frank CW: Grafting of Poly(Benzyl-L-Glutamate) on Chemically Modified Silicon Oxide Surfaces. *Langmuir* **1996**, *12*, 5824.

[70] Cassim JY, Taylor EW: Intrinsic Birefringence of Poly-{Gamma}-Benzyl-L-Glutamate, a Helical Polypeptide, and the Theory of Birefringence. *Biophysical Journal* **1965**, *5*, 531.

[71] de Campos Vidal B: Poly-Gamma-Benzyl-L-Glutamate Birefringent Fiber as a Model of Form and Intrinsic Birefringences of Alpha-Helical Polypeptides. *Cellular and Molecular Biology* **1986**, *32*, 109.

[72] Wieringa RH, Siesling EA, Werkman PJ, Angerman HJ, Vorenkamp EJ, Schouten AJ: Surface Grafting of Poly(L-Glutamates). 2. Helix Orientation. *Langmuir* **2001**, *17*, 6485.

[73] Liebermann T, Knoll W: Surface-Plasmon Field-Enhanced Fluorescence Spectroscopy. *Colloids and Surfaces A: Physicochemical and Engineering Aspects* **2000**, *171*, 115.

[74] Weber PC, Ohlendorf DH, Wendoloski JJ, Salemme FR: Structural Origins of High-Affinity Biotin Binding to Streptavidin. *Science* **1989**, *243*, 85.

[75] Freitag S, Trong IL, Chilkoti A, Klumb LA, Stayton PS, Stenkamp RE: Structural Studies of Binding Site Tryptophan Mutants in the High-Affinity Streptavidin-Biotin Complex. *Journal of Molecular Biology* **1998**, *279*, 211.

[76] Lourenco JMC, Ribeiro PA, BotelhodoRego AM, BrazFernandes FM, Moutinho AMC, Raposo M: Counterions in Poly(Allylamine Hydrochloride) and Poly(Styrene Sulfonate) Layer-by-Layer Films. *Langmuir* **2004**, *20*, 8103.

[77] Haeussling L, Ringsdorf H, Schmitt FJ, Knoll W: Biotin-Functionalized Self-Assembled Monolayers on Gold: Surface Plasmon Optical Studies of Specific Recognition Reactions. *Langmuir* **1991**, *7*, 1837.

[78] Knoll W, Zizlsperger M, Liebermann T, Arnold S, Badia A, Liley M, Piscevic D, Schmitt F-J, Spinke J: Streptavidin Arrays as Supramolecular Architectures in Surface-Plasmon Optical Sensor Formats. *Colloids and Surfaces A: Physicochemical and Engineering Aspects* **2000**, *161*, 115.

[79] Darst SA, Ahlers M, Meller PH, Kubalek EW, Blankenburg R, Ribi HO, Ringsdorf H, Kornberg RD: Two-Dimensional Crystals of Streptavidin on Biotinylated Lipid Layers and Their

Interactions with Biotinylated Macromolecules. *Biophysical Journal* **1991**, *59*, 387.
[80] Voros J: The Density and Refractive Index of Adsorbing Protein Layers. *Biophysical Journal* **2004**, *87*, 553.
[81] Thomsen V, Schatzlein D, Mercuro D: Limits of Detection in Spectroscopy. *Spectroscopy* **2003**, *18*, 112.
[82] Karlsson R, Roos H, Fägerstam L, Persson B: Kinetic and Concentration Analysis Using Bia Technology. *Methods* **1994**, *6*, 99.
[83] Myszka DG, Morton TA, Doyle ML, Chaiken IM: Kinetic Analysis of a Protein Antigen-Antibody Interaction Limited by Mass Transport on an Optical Biosensor. *Biophysical Chemistry* **1997**, *64*, 127.
[84] van Oss CJ, Giese RF, Bronson PM, Docoslis A, Edwards P, Ruyechan WT: Macroscopic-Scale Surface Properties of Streptavidin and Their Influence on Aspecific Interactions between Streptavidin and Dissolved Biopolymers. *Colloids and Surfaces B: Biointerfaces* **2003**, *30*, 25.
[85] Panchuk–Voloshina N, Haugland RP, Bishop–Stewart J, Bhalgat MK, Millard PJ, Mao F, Leung W-Y, Haugland RP: Alexa Dyes, a Series of New Fluorescent Dyes That Yield Exceptionally Bright, Photostable Conjugates. *Journal of Histochemistry and Cytochemistry* **1999**, *47*, 1179.
[86] Sato A, Menges B, Knoll W: **2008**. Unsubmitted manuscript.

6. Conclusion

Block copolymer self-assembly and porous alumina fabrication by anodization are two methods for conveniently generating nanostructures by self-organization. As physical structures approach the nanoscale, properties not found in the original materials in macroscopic forms emerge. We have focused on: 1) the ability of diblock PS-*b*-PMMA copolymers to form topographically flat, surface chemical nanopatterns, to explore the protein adsorption behavior on surfaces with a tremendous density of chemical interfaces; 2) the ability of both PS-*b*-PMMA and porous anodic alumina thin films to serve as effective optical waveguides due to the sub-wavelength nature of their nanostructures; and 3) the exploitation of these waveguides for the in situ sensing of surface processes with high sensitivity, by analysis of the films' optical anisotropy generated as a result of the oriented nanostructures.

Concerning protein adsorption on nanopatterned PS-b-PMMA, BCP self-assembly was shown to be a convenient platform for adjusting the domain size and surface interface density over the entire nanoscale, and to investigate the influence of interface densities on protein-surface interactions. First, we demonstrated that the amount of protein adsorbed on a surface can be modulated by the length density of surface interfaces delineating the BCP chemical nanopattern. Due to the intrinsic high densities of surface interfaces on nanopatterns and structures, the interaction of proteins with such interfaces may inform the design of relevant biomaterials, biosensors, and cell-surface experiments.

Motivated by the effect of high surface interface densities demonstrated, we also developed a simple method for the directed assembly of adsorbed protein nanoarrays on the PS-b-PMMA thin films, and explored its formation mechanism and applicability. We performed immunoassays on these nanoarrays, and used them as nanotemplates for arraying other biomolecules. The patterning mechanism was based on a combination of rinsing effects and the geometric restrictions imposed by a nanopattern with a difference in protein adsorption behaviour on adjacent, chemically distinct surfaces. Templates surfaces possessing domains with the higher adsorption affinity and a characteristic dimension up to 2~3 times the size of the protein may be used. At the other size extreme, no patterning effect would be expected if the domains shrank significantly below the size of individual proteins. Thus the patterning scheme is truly a nanoscale effect.

Optical waveguiding with thin films of PS-b-PMMA and nanoporous alumina have been demonstrated, and the effective medium theory description of the optical responses of the thin films was shown to be a versatile tool for the characterization of their nanostructures. Analysis of the anisotropic dielectric response of the PS-*b*-PMMA film could discern the domain morphology in the interior of the nanostructured film. Moreover, nanoporous alumina waveguides have been applied as a discriminating and highly sensitive platform to investigate a host of surface processes *in situ*. Deposition of molecules on the pore surfaces was detected as an overall shift in the dielectric constant (optical density) of the nanoporous AAO, and complementary waveguide mode fluorescence detection was also demonstrated using the nanoporous waveguide. In addition, LbL polyelectrolyte deposition occurring on the top surface and inside the pores of the waveguide, and anisotropy in PBLG polypeptide nanostructures developing inside the pores, could be distinguished by the analysis of waveguide mode shifts and the dielectric response in combination with effective medium theory. In particular, the oriented nanoporous AAO structure generated a unique optical anisotropy upon which the analyses of the surface processes could be based. Furthermore, high sensitivity was achieved due to the very sharp coupling resonances intrinsic to the waveguiding phenomenon, and because the nanoporous structure amplified the optical response by providing a vast internal surface area over which surface processes could occur and over which the optical signal could be integrated.

7. Appendices

A. Computer image analysis of AFM and SEM images

Images were analysed by the software ImageJ [1], which was originally developed at the US National Institutes of Health (NIH) to identify and quantify island-like features in digital images. It is freely available for download for use in research at http://rsb.info.nih.gov/ij/.

A1. Measuring PS-b-PMMA nanopattern parameters: f_{PS}, w_{PS}, l_{interf}.

Analysis was based on the phase contrast of PS and PMMA domains in tapping mode AFM phase images. As discussed in the text, PS domains appear as regions darker in shading (lower phase offset) than PMMA regions. Thus the first and key step in identifying the PS domains (or equivalently the PMMA domains) was to set a threshold shading level that corresponded to the spatial extent of PS domains in a phase image. This was done using the "Threshold" function in ImageJ, and was justified by the bimodal distribution of the phase offsets contained in the AFM image—PS and PMMA regions exhibit separate and distinct average phase offsets. Figure 7.1 illustrates this process with the example of the 3:7 PS-b-PMMA sample corresponding to Figure 3.8 (pg. 25).

The phase offset histogram plots the number of data points corresponding to each phase offset level. Thus if there are two distinct types of domains in the phase measurement (distinctly darker and lighter shaded domains), corresponding to two types of materials (i.e. PS and PMMA in the present case), they can be identified by their histogram peaks. The taller the peaks, the more data points correspond to that type of domain, and the larger the surface fraction in the AFM image is composed of that material (Figure 7.1a). The same applies to height data for domains with distinct height levels, such as for proteins adsorbed on a flat surface (see section A.3). For imageJ analysis, the AFM phase data (a continuous range in phase offsets) is first converted (i.e. bitmap export) into greyscale values (levels 0 to 255) by the AFM controller software (NanoScope III software version 5.30r1, 2004).

A greyscale histogram corresponding to the original phase data is found in the converted greyscale image opened in ImageJ (Figure 7.1b). The "Threshold" filter is then used for identifying the domains (midpoint between histogram peaks). Figure 7.1c shows the resulting black and white image after application of the threshold filter,

and the black PS domains can be counted and measured by the "analyze particles" routine (Figure 7.1d). The routine counts the number of image pixels comprising each domain, as well as the number of pixels making up the perimeter of the domains.

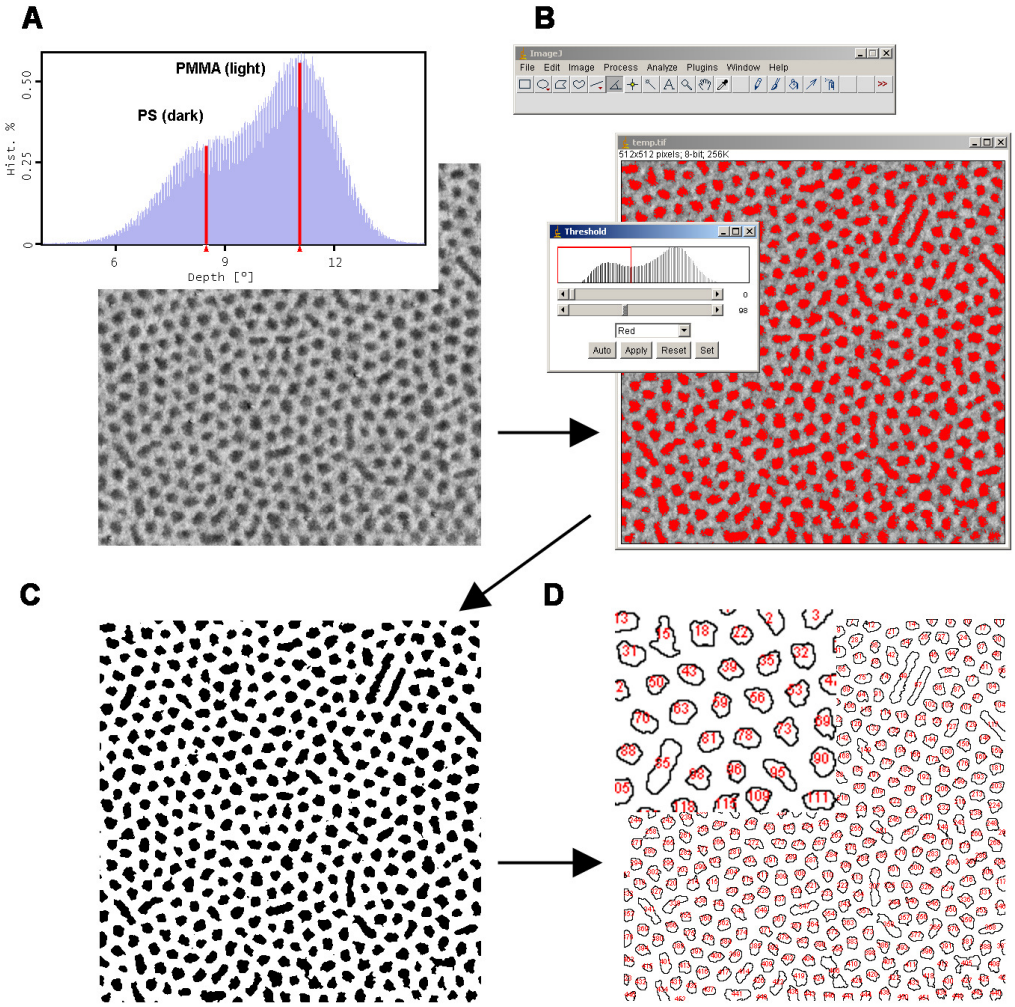

Figure 7.1. Computer image analysis of AFM phase measurement with ImageJ (3:7 PS-b-PMMA sample corresponding to Figure 3.8). (A) shows the phase offset histogram of the original AFM measurement, and the equivalent greyscale image converted from the AFM phase data. (B) shows the image opened in ImageJ and the greyscale "threshold filter" dialogue window for identifying the domains (midpoint between histogram peaks). The PS domains are identified in red. Slight differences between the phase offset histogram in (A) and the greyscale histogram in (B) were caused by the AFM data to greyscale conversion algorithm. (C) shows the resulting black and white image after application of the threshold filter (black now identifies PS), and (D) shows the domains identified, counted and measured by the "analyze particles" routine.

The domain parameters are defined as follows: 1) the ratio between the aggregate number of all pixels corresponding to the PS domains and the number of pixels comprising the entire image gives the PS surface fraction (f_{PS}); 2) The modal average of the domain diameters (defined as the diameter of a circle with an area

equal to the domain's) is identified as the characteristic width of the domains (w_{PS}); and 3) Summing the number of pixels making up the domain perimeters, relative to the AFM image magnification, gives the PS/PMMA surface interface density ($l_{interf.}$).

For striped domains (symmetric PS-b-PMMA), w_{PS} was measured by inspection of AFM image cross-sections taken perpendicular to the stripe direction, and by averaging several such measurements.

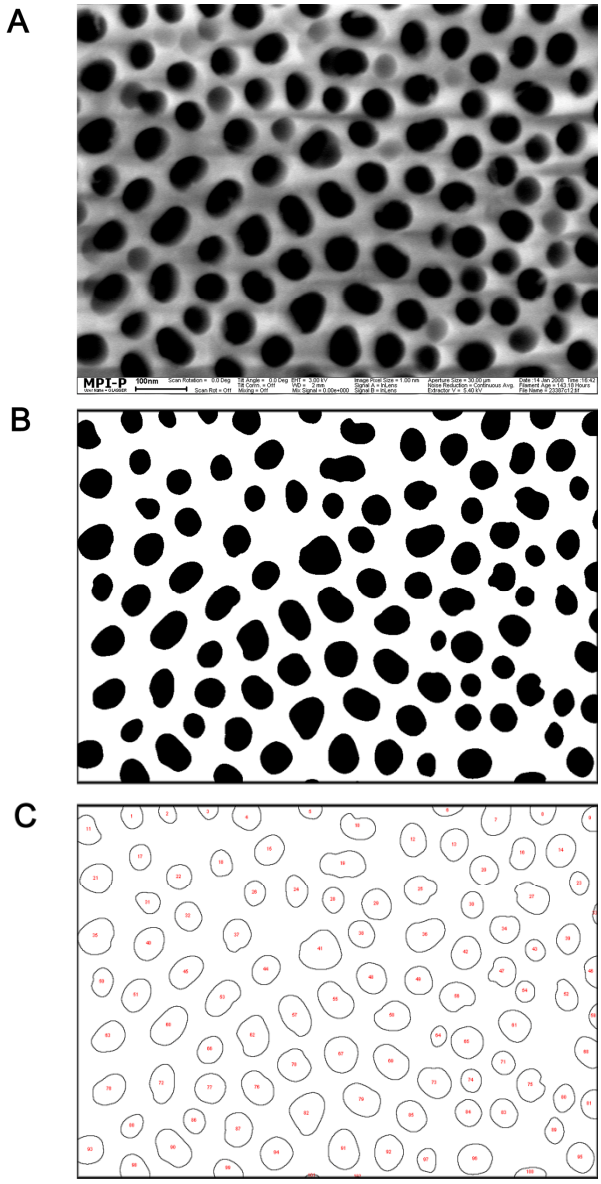

Figure 7.2. Images illustrating the procedure for measuring pore sizes and pore surface area fractions by ImageJ. The procedure is identical to that for identifying PS-b-PMMA dot domains (Figure 7.1). (A) shows the original SEM image (corresponding to Figure 3.17e1 on pg. 37). (B) shows the black and white image obtained after applying the threshold filter. Pores are identified by the black regions. (C) shows the domain counting by imageJ. The small red dots at the centres of the domains are actually the number labels in a small font size added automatically by ImageJ.

A2. Measuring AAO f_{pore} and D_{pore} from SEM images

These are measured by ImageJ using exactly the same procedure as described in the previous section for identifying the PS-b-PMMA dot nanopatterns and is not elaborated here again. Figure 7.2 illustrates the successive steps in this process. Figure 7.2a was previously introduced as Figure 3.17e1 (pg. 37) and shows the surface pore distribution of a 2-step anodized AAO.

A3. Identifying coverage of IgG on PMMA domains

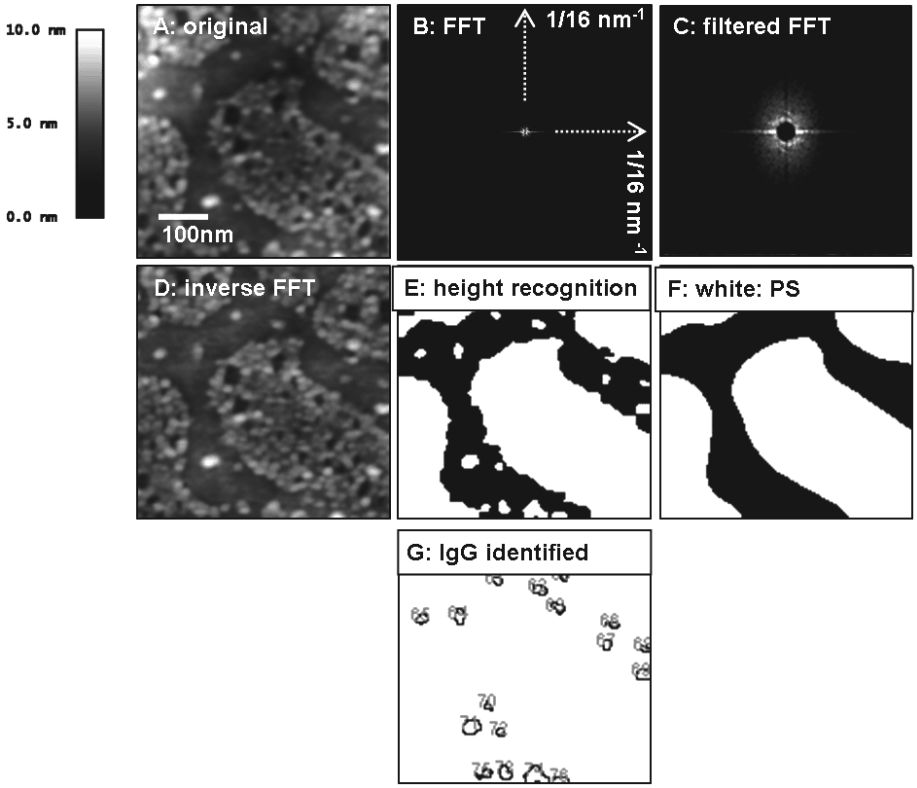

Figure 7.3. Sequence of AFM images illustrating the computer analysis used for identifying IgG on PMMA domains.

Figure 7.3a shows the IgG covered symmetric PS-b-PMMA template ($\lambda_{C\text{-}C}$ ~ 300 nm) after flowing rinse, previously introduced as Figure 4.9f (pg. 59). IgG's were identified by their height differences from the PS-b-PMMA template surface. However, the surface had a macroscale waviness in topography in the same height range as the adsorbed IgG over periods of hundreds of nanometers. This was clearly seen in the Fast Fourier transform (FFT) of the height image (Figure 7.3b) as a low frequency peak centered at the origin. The waviness was easily filtered by applying a high pass filter to the FFT with a band edge at 100 nm. The filtered FFT (Figure 7.3c) shows a void in the center, which indicates the removal of spatial information

correlated with each other over surface distances greater than 100 nm. The flattened height image, shown in Figure 7.3d, was obtained by the inverse transform of Figure 7.3c. The IgG could then be unambiguously distinguished by their height difference with the surrounding bare PMMA areas. The IgG were identified in white against a black background (Figure 7.3e) by the thresholding filter in ImageJ (Appendix A.1).

In section 4.2.3, we were only interested in the sparsely separated IgG adsorbed on PMMA. Since most of the PMMA surface was bare, we assumed that the PMMA domains, shown in black in Fig. S3F, were defined by the extent of these IgG deficient surfaces, and we ignored the unoccupied regions in the interior of the PS domains without IgG adsorbed, by applying an edge-smoothing function to Figure 7.3e. The IgG features within the PMMA region are shown in Figure 7.3g, and were defined as features < 10000 nm^2 in Figure 7.3e. These IgG features on PMMA were automatically numbered and outlined in Figure 7.3g by ImageJ, as described in Appendix A.1. The fractional area of the IgG on PMMA calculated from AFM measurements areas totaling ~10 μm^2 were plotted in Figure. 4.10 in section 4.2.3. Note that to illustrate the process clearly at a high magnification, images in Figure 7.3 were cropped from a measurement originally measuring 2x2 μm. The FFT was calculated from the original 2x2 μm image.

A4. Quantifying the match between the adsorbed protein and the original PS-b-PMMA template nanopatterns.

The first row of images in Figure 7.4 shows the raw AFM measurements, the second row the flattened images, and the third row the outlines of the PS domains or IgG clusters identified by computer image analysis. The first column is a phase measurement that illustrates the analysis of the bare PS-b-PMMA nanotemplate Figure 7.4a shows a magnified view of the central region in Figure 7.1a), and Figure 7.4b to d show height measurements corresponding to IgG adsorption experiments. These columns correspond, from left to right, to preparation conditions of 10 min adsorption from 3.4 μg/ml, 16 min adsorption from 17 μg/ml, and 22 min adsorption from 25.5 μg/ml, respectively. The image analysis routine used was similar to that used in section A.3, except that a lower band edge (40 nm) corresponding to the smaller PS-b-PMMA dot pattern (cylindrical morphology) was applied, and that all clusters in an image were counted. Figures 7.4f to h show the flattened height images with IgG adsorbed. The phase image of the bare PS-b-PMMA template (Figure 7.4a) did not need to be flattened, and is reproduced in Figure 7.4e. The IgG clusters/PS domains in Figure 7.4e-h were then identified by setting a threshold height level corresponding to the PMMA background. The results (Figure 7.4i to l) were then identified and analyzed, as described in previous sections, by the “analyse particles” routine in ImageJ.

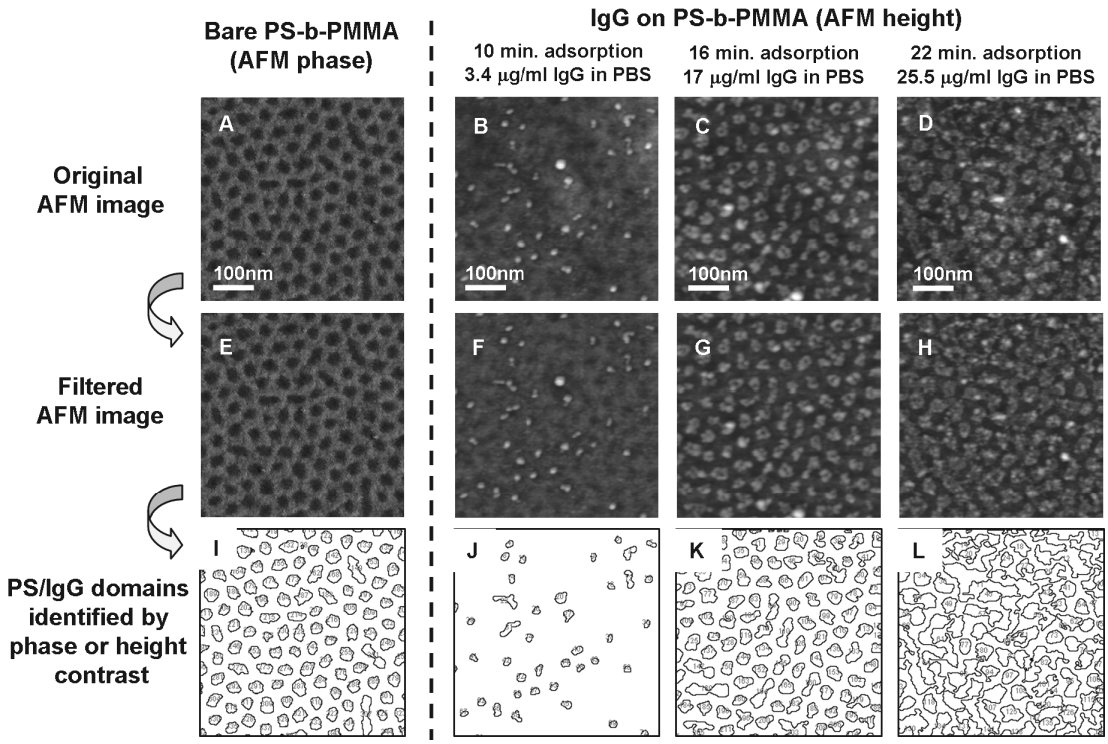

Figure 7.4. AFM height and phase images illustrating the computer image analysis used for quantifying the match between the IgG nanoarrays and the underlying PS-b-PMMA nanotemplate.

Two parameters measured for each IgG cluster/domain were especially important: the area and the Feret's diameter (also known as the caliper length—the longest distance between any two points along the cluster/domain perimeter). These two parameters were used to calculate three metrics that defined the match between the IgG clusters and the PS-b-PMMA nanopattern:

1) The **percentage deviation in area** between individual IgG clusters and the modal average area of a bare PS domain was calculated. This is a measure of whether a PS domain was completely covered by IgG.
2) The **percentage deviation in Feret's diameter** between individual IgG clusters and the modal average diameter of the bare PS domains was calculated. The shape of the IgG cluster was also important, and the Feret's diameters, instead of the perimeter lengths of individual IgG clusters, was used to characterize the overall cluster shape. The Feret's diameter was used because it gives consistent values for IgG arrangements of roughly the same shape regardless of whether voids or gaps along the periphery of the IgG cluster exist. These sub-protein scale details along the periphery of an IgG cluster are not important for good nanoarray definition.

3) Lastly, the **percentage deviation of the total coverage of IgG clusters** from the PS surface fraction of the bare template was also measured (summed from all measured cluster areas). A well defined IgG nanoarray requires not only close matching of the individual size and shape of the IgG clusters with the PS domains, but also that every PS domain be completely covered with IgG.

The absolute values of all three percentage deviations were averaged and resulted in a score characterizing the perfection of the IgG nanoarray. These averages were plotted in Figure 4.11 in section 4.2.4 (pg. 62). The corresponding data values are shown in Table 7.1 below.

Protein solution concentration (ug/ml)	Adsorption time (min)	RMS % difference in area between IgG clusters and the average PS domain	RMS % difference in Feret's diameter between IgG cluster and the average PS domain	% difference in surface coverage between IgG clusters and the PS nanoarray	Average of the three parameters
3.4	8	38%	65%	87%	63%
3.4	16	35%	60%	87%	61%
8.5	14	20%	28%	71%	39%
8.5	24	21%	32%	54%	36%
14.0	10	11%	20%	4%	12%
14.0	11	10%	16%	13%	13%
14.0	16	28%	51%	40%	40%
16.9	8	14%	23%	81%	39%
16.9	16	60%	50%	40%	50%
25.4	12	62%	75%	57%	65%
25.4	22	95%	97%	105%	99%

Table 7.1. Absolute percentage deviations from a perfect registry between adsorbed IgG clusters and the PS domain nanopattern of the PS-b-PMMA template, for the data points plotted in Figure 4.11 (pg. 63).

B. Comparison of AFM measurements of protein nanopatterns in air and in liquid (PBS)

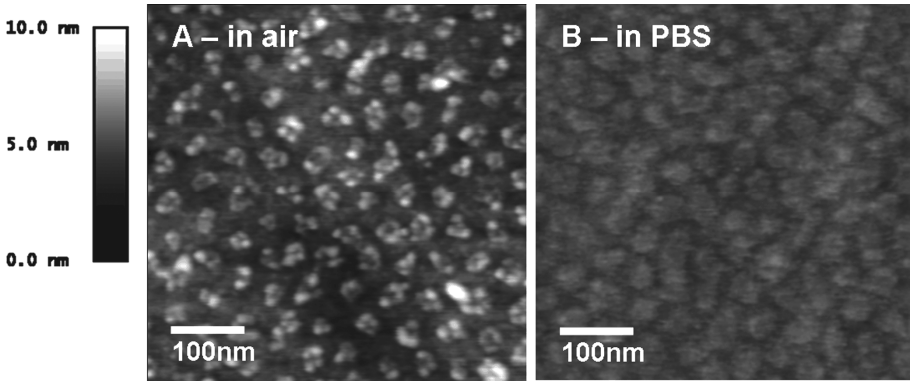

Figure 7.5. Comparison of AFM height measurements in air and in liquid. (A) is reproduced from Figure 4.7f and shows an IgG nanoarray imaged by AFM in air. (B) shows a nanoarray prepared under the same conditions, but imaged in PBS buffer. Much finer resolution was obtained in air than in PBS. The same type of 1.8 N/m silicon cantilever was used for both measurements. In (B), the sample was placed in the AFM liquid cell directly after flowing rinse without drying under a nitrogen stream.

C. Optical waveguide characterization of PS-b-PMMA/PMMA film after swelling and re-annealing

The 464 nm thick PS-b-PMMA/PMMA film with perpendicular cylindrical morphology, introduced in Figure 5.6, was rinsed in acetic acid and then re-annealed at a high temperature, in order to explore the morphological effects of such a process. It has been previously demonstrated [2, 3] that swelling of the PS-b-PMMA/PMMA film in acetic acid preferentially dissolves the PMMA homopolymer embedded in the centres of the PMMA cylindrical domains and swells the surrounding copolymer PMMA blocks. After drying the sample of acetic acid, a nanoporous BCP film with ordered arrays of cylindrical pores that penetrate the length of the original PMMA domains was reported. Reannealing the film above the glass transition temperatures of PS and PMMA (both ~100ºC) then resulted in the rearrangement of the PMMA copolymer blocks and physical closing of the pores. However, relatively thin films of thickness h ~ 2 times $\lambda_{C\text{-}C}$ were used in those studies. Therefore we followed the swelling and reannealing process to investigate the processing effects with a thick PS-b-PMMA/PMMA film of thickness h > ~10 times $\lambda_{C\text{-}C}$. (The following experiments were performed by Prof. Dr. Dong Ha Kim, now at Ewha Women's University, Korea, Seoul. The present author was responsible for the waveguide data analysis.)

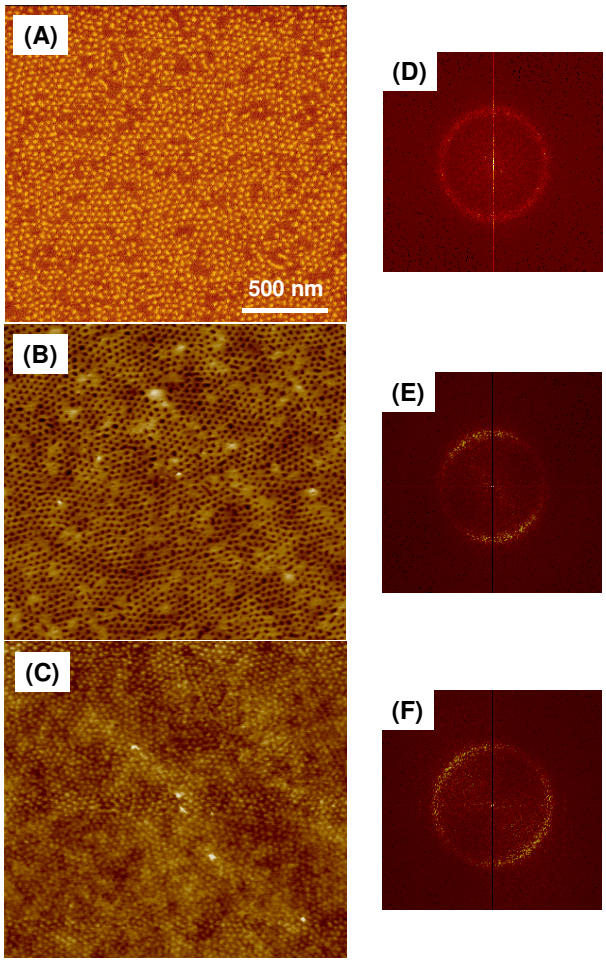

Figure 7.6. AFM height measurements of the PS-b-PMMA/PMMA film as prepared (A), after acetic acid swelling (B), and after reannealing at 155ºC for 2 days (C). (D)-(F) show the FFT of the corresponding image to the left. All indicated $\lambda_{C\text{-}C}$ ~ 46 nm.

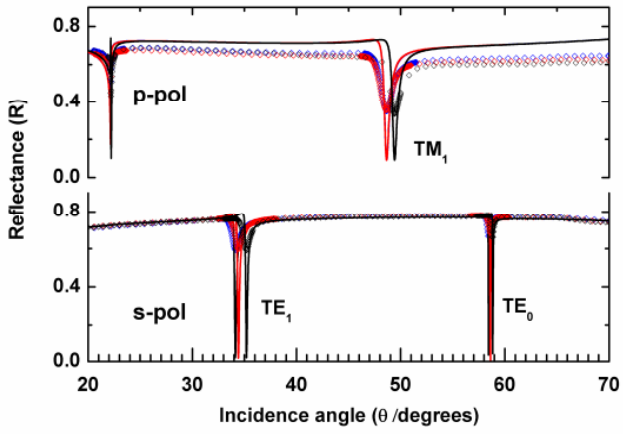

Figure 7.7. R vs. θ waveguide measurements of the PS-b-PMMA/PMMA film before swelling (black), after swelling (blue), and after reannealing (red). Symbols are measured data. Lines are Fresnel calculations. The angle shifts after swelling are quite small, and the blue and red data points appear to overlap in the Figure. Detailed views of the mode shifts are shown in Figure 7.8.

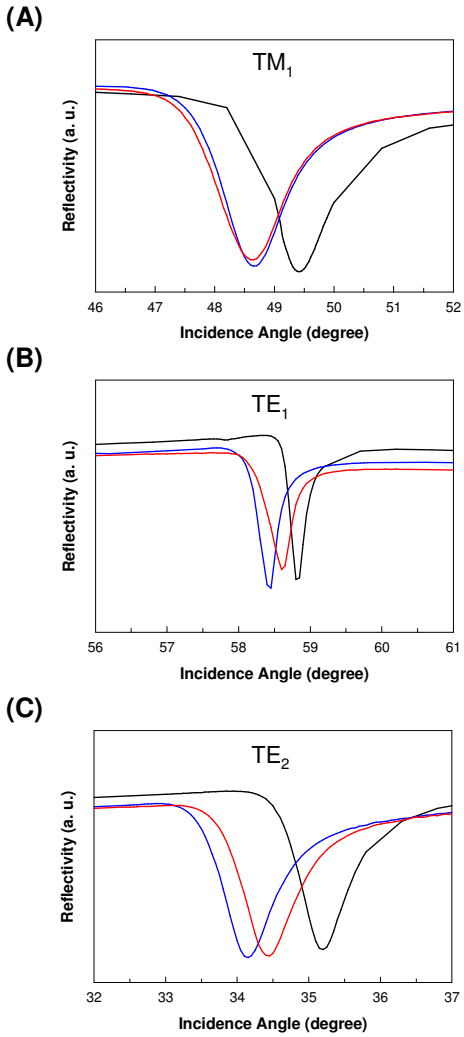

Figure 7.8. Detailed views of the waveguide mode responses shown in Figure 7.7. All curves represent data points and the Fresnel calculations are not shown. The curves show the PS-b-PMMA/PMMA film before swelling (black), after swelling (blue), and after reannealing (red).

The initial PS-b-PMMA/PMMA film morphology has already been characterized by EMT-waveguide analysis in section 5.3. The film was then immersed in pure acetic acid for 30 min and directly dried in a stream of compressed air. The surface morphologies before and after swelling were characterized by AFM and shown in Figure 7.6a and b. It is apparent that the acetic acid treatment resulted in a nanoporous top surface as reported in the literature. The pores were caused not only by the removal of PMMA homopolymer material, but also by the wetting of the top surface of the PS matrix with the PMMA copolymer blocks near the surface [2, 3]. $\lambda_{C\text{-}C}$ did not change, as indicated by the FFT analysis (Figure 7.6d and e). Reannealing was then performed at 155ºC for 2 days in vacuum, and AFM characterization (Figure 7.6c) showed that the pores were closed off, caused by the re-assembly of the PMMA copolymer blocks [2, 3]. FFT of the AFM image (Figure 7.6f) suggests that $\lambda_{C\text{-}C}$ decreased slightly, but the change was within the uncertainty of the measurement. R

vs. θ waveguide measurements were also performed after the swelling and reannealing steps. These are shown in Figure 7.7 and Figure 7.8. The dielectric constants (ε_{film} = {$\varepsilon_x = \varepsilon_y$, ε_z }) and film thickness (h) measured from Fresnel calculation fittings for all stages of processing are shown in Table 7.2.

As expected from the removal of the PMMA homopolymer, the film's ε_{film} decreased after rinsing in acetic acid (Table 7.2). Interestingly, the best fit between the R vs. θ waveguide response and the Fresnel calculations "measurement" indicated that the film thickness (h) decreased from 464 nm to 454 nm after the swelling step (Table 7.2). Swelling by acetic acid was performed at room temperature, significantly below the glass transition temperature of PS. Thus large scale film deformations were not expected and this thickness decrease appeared anomalous. It was also close to the experimental uncertainty in thickness determination (±5 nm), and could have been due to thickness inhomogeneity across the sample (i.e. different position on the film measured). Thus another set of Fresnel calculation fittings were performed with the constraint that h remained constant. The resulting ε_{film} measured are also shown in Table 7.2 (in parenthesis), and indicated larger decreases in ε_{film}.

		Film thickness	**$\varepsilon_x = \varepsilon_y$**	**ε_z**
Initial film (see Table 5.2, pg. 89)	**Measurement**	**464 nm**	**2.4047**	**2.4100**
	EMT fit (PS + PMMA)	n/a	2.4047	2.4094
After acetic acid swelling	**Measurement**	**454 nm (464 nm)**	**2.4010 (2.379)**	**2.4090 (2.382)**
	EMT fit (PS + PMMA + air filled pores)	n/a	2.4010 (2.379)	2.4094 (2.392)
	EMT fit (PS + PMMA + acetic acid filled pores)	n/a	2.4012 (2.379)	2.4094 (2.387)
After reannealing	**Measurement**	**456 nm (464 nm)**	**2.4047 (2.384)**	**2.4000 (2.384)**

Table 7.2. Anisotropic dielectric constants (ε) and film thickness values (h) measured by Fresnel calculation fitting of the R vs. θ waveguide responses (Measurement), and the corresponding EMT best fits, before swelling, after swelling, and after reannealing.

EMT calculations analogous to those discussed in section 5.4 (now with each cylindrical domain represented by a concentric layer of PMMA and a central air pore) were also used to estimate the amount of PMMA removed. The original PMMA homopolymer volume fraction was 7 % of the entire film. Based on the best fit film thickness and ε_{film} values, EMT calculations indicated that only ~3 % of this 7 %

homopolymer addition was removed by acetic acid swelling. On the other hand. assuming that h remained constant (i.e. the difference was assumed to be due to measurement uncertainty), EMT calculations indicated that ~18 % of the 7 % homopolymer addition was removed.

These fractions calculated are clearly significantly lower than the original PMMA content. However, it is possible that the acetic acid within the nanopores was not completely removed by drying in air. This would imply a higher fraction of PMMA homopolymer removed, because the higher than expected ε_{film} might have been caused by a higher than expected dielectric constant of the material filling the pores ($\varepsilon_{acetic\ acid} = 1.8796 > \varepsilon_{air} = 1$). Such an analysis indicated that ~12 % (or, assuming constant h, up to 84%) of the original PMMA domains were displaced by acetic acid.

If the 10 nm decrease in film thickness after swelling was not due to measurement uncertainty or a difference in sample area being measured (film inhomogeniety), then it could have represented the removal of some of the PMMA content in the film. Under such an assumption, 2.1% of the film's original volume was removed during the swelling process, which would have represented 31 % of the original PMMA homopolymer added. Combined with the possibility of acetic acid filling the generated pores, up to a maximum of 43% of the homopolymer fraction could have been removed. Alternatively, assuming a constant h in the Fresnel fitting, up to 84% of PMMA content was removed.

In the original report [2, 3], all the PMMA homopolymer content was removed by acetic acid rinsing, and cylindrical pores were formed in the 50~60 nm thick films characterized by X-ray scattering and photoelectron spectroscopy. It the present case of much thicker films (~460 nm), it is possible that some of the PMMA homopolymer dissolved by acetic acid was unable to diffuse out of the PS-b-PMMA polymer matrix. Nevertheless, the decrease in waveguide mode angles (Figure 7.8) and EMT analysis (Table 7.2) indicated that some of PMMA (homopolymer) material was indeed removed during the pore generation process seen in AFM characterization (Figure 7.6b), although the amount removed could be not quantified with certainty.

The 2 day reannealing step at 155ºC was an interesting process that tested the self-assembly properties of the PS-b-PMMA/PMMA system. The original perpendicular cylindrical morphology was enabled by the precise engineering of the homopolymer content [4]. Thus it is possible that annealing above the glass transition temperature after removal of some homopolymer would shift the equilibrium arrangement of the PS and PMMA domains to another morphology. (Any remaining acetic acid would also have been removed; boiling point of acetic acid = 118ºC.) At the same time, as indicated by the waveguide-EMT discussion on swelling behavior above, the exact amount of PMMA removed could not be determined quantitatively by the optical waveguide characterization. Thus a qualitative description of the waveguide data is given below.

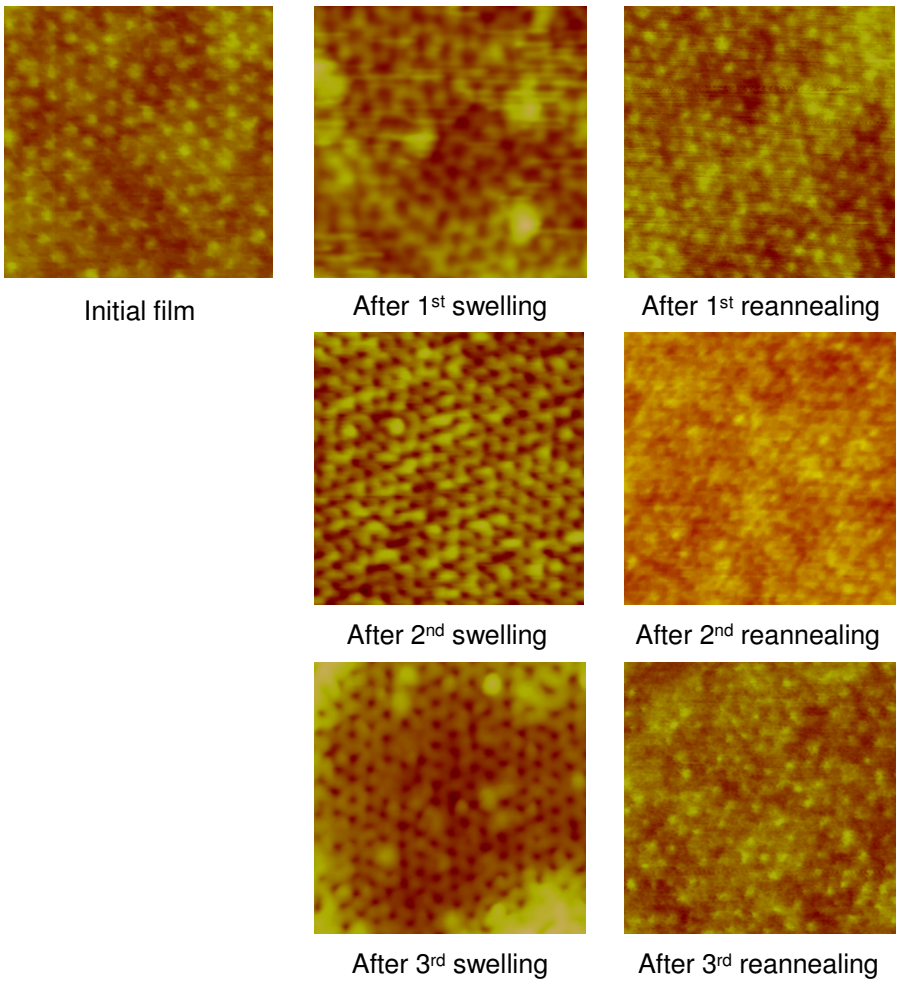

Figure 7.9. AFM images of the surfaces of a PS-b-PMMA/PMMA mixture film for each step of the repeated swelling/re-annealing procedure. The film was treated with acetic acid for 30 min and annealed for 2 days, respectively, for each step of swelling and annealing experiments.

As mentioned earlier, AFM characterization (Figure 7.6c) showed that the nanoporous domains indeed closed up after reannealing. However, comparison of the waveguide mode minima before and after reannealing (Figure 7.8) revealed that the modes in s-polarization (TE modes) shifted back to higher angles while the mode in p-polarization (TM modes) essentially remained at the same angle position. Furthermore, the ε_{film} measured (Table 7.2) showed that the anisotropy of the film reversed in order. If the film thickness (h) had decreased after the earlier swelling step, then Fresnel calculations gave $\varepsilon_x = \varepsilon_y > \varepsilon_z$. In the case that h was actually constant, $\varepsilon_x = \varepsilon_y \sim \varepsilon_z$ was obtained (Table 7.2, in parenthesis). In either case, there was a decrease in anisotropy in the system. Therefore a structural change must have accompanied the reannealing process. (The situation is reminiscent of the discussion in section 5.4.3., where PBLG surface grafting reversed the anisotropy in the AAO thin film.) Since neither the atactic PS nor the PMMA used had any intrinsic (crystalline) anisotropy, and both polymers had an elevated mobility at the annealing temperature, if

anisotropy reversed in order, i.e. $\varepsilon_x = \varepsilon_y > \varepsilon_z$, then the cylindrical morphology must have (at least partially) reoriented to a surface parallel configuration. If $\varepsilon_x = \varepsilon_y \sim \varepsilon_z$, then an isotropic distribution of PMMA domains in a PS matrix could be expected.

In the case of an isotropic distribution of PMMA/pore domains, all orientational components of ε_{film} were equally sensitive to the film composition. In contrast, in the original perpendicular cylindrical film morphology consistent with the as-prepared and swelled films ($\varepsilon_x = \varepsilon_y < \varepsilon_z$), the electric fields of TM modes were oscillating parallel to the long cylinder/pore axis, thus probing the average composition of the film. Therefore, the relative constancy of the TM_1 mode angle after reannealing, shown in Figure 7.8a, could indicate relatively little change in the average chemical composition after re-annealing, and that some pores remained (trapped) after reannealing.

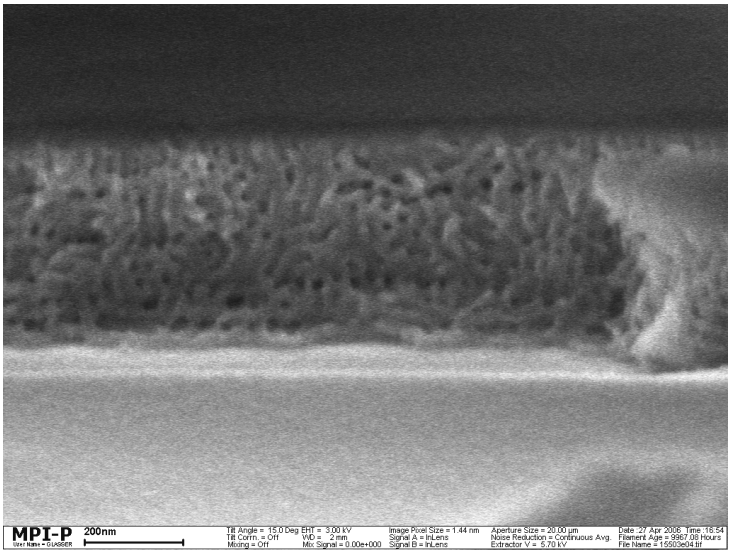

Figure 7.10. SEM cross section of the PS-b-PMMA/PMMA film after three swelling-reannealing cycles. To generate sufficient image contrast, the entire PMMA fraction, including components not removed by swelling, was removed by UV treatment followed by acetic acid rinsing. The scale bar indicates 200 nm.

Several successive cycles of these swelling and reannealing steps were also performed [5], and AFM surface characterization always showed the opening and closing of a nanoporous structure (Figure 7.9). The corresponding waveguide measurements were also similar to the initial swelling-reannealing cycle. At the end of the process, SEM cross section images of the nanostructured BCP film were taken by cleaving the sample (Figure 7.10), and showed the loss of structure already indicated by the non-destructive waveguide characterization (Figure 7.7 and Table 7.2) Thus the domain ordering processes occurring simultaneously inside and near the top surface of a thin film of block copolymer with homopolymer addition, during swelling and

reannealing steps, were characterized by complementary waveguide, AFM and SEM measurements. In particular, the optical waveguide characterization was able to reveal processes not discerned by conventional non-destructive microscopy analysis (AFM) alone.

D. FTIR measurements and analysis of PBLG modified AAO

FITR measurements and analysis were the work of Dr. Hatice Duran at the Max Planck Institute for Polymer Research. A brief summary of the results are given below:

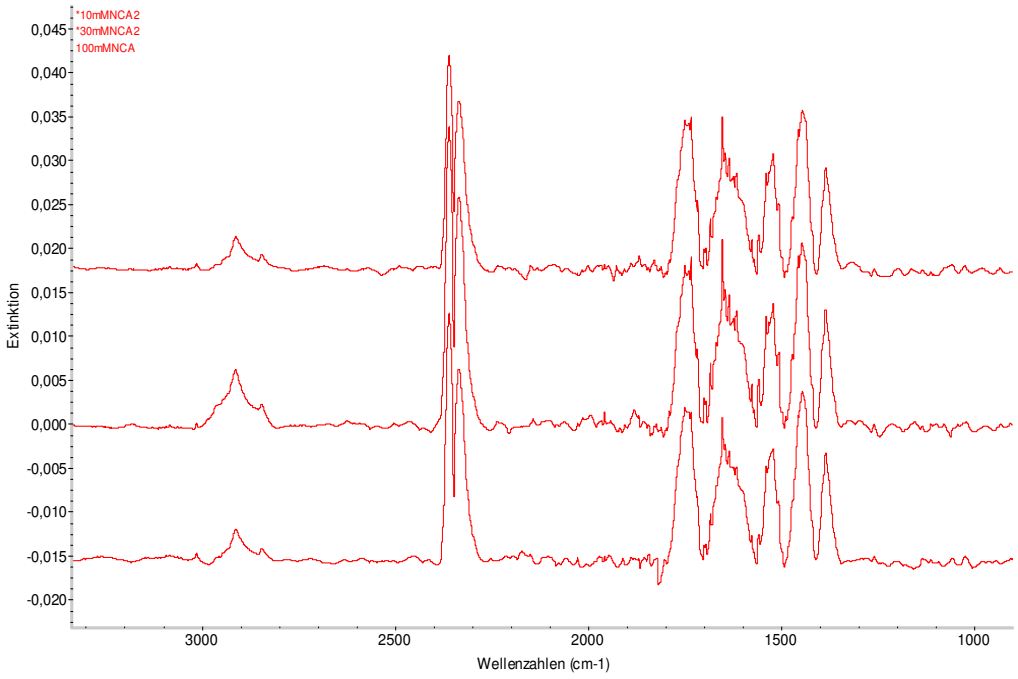

Figure 7.11. FT-IR scans for NCA polymerized on nanoporous alumina thin films at NCA concentrations of 10, 30 and 100mM in THF for 24h.

The positions of the amide I and amide II bands of PBLG backbone are characteristic of the secondary structure of the polypeptide [6], i.e. α-helix (amide I ~ 1650 cm^{-1}, amide II~ 1546 cm^{-1}), β-sheet (amide I ~1630 cm^{-1}, amide II ~ 1530 cm^{-1}), and random coil (amide I ~1656 cm^{-1}, amide II ~ 1535 cm^{-1}). A sample may possess components of all three PBLG structures. Therefore the measured amide bands were fitted to peaks with the known wavenumbers listed above to calculate their respective volume fractions. Since the amide II region also includes the contribution from the aromatic ring, their contributions at 1498 cm^{-1} and 1516 cm^{-1} were subtracted from the amide II peak. Figure 7.11 shows FT-IR scans of PBLG growth at various concentration of NCA monomer (10, 30 and 100 mM in THF) on the nanoporous

AAO thin films. The amide peak assignments confirmed the presence of PBLG α-helices.

As mentioned in section 5.4.3, the PBLG α-helix tilt angle is ~32º with respect to the surface [7, 8]. This was also verified from the measured FTIR spectra by examining the peak ratio between the amide I and II bands, since these resonances represent different vibrational orientations of the amide groups with respect to the axis of the α-helix [8]. Since the geometry of the α-helix is known, the chain density can be estimated from the tilt angle by assuming densely packed chains. A value of 4~5 chains/nm was obtained. The degree of polymerization can also be estimated from the tilt angle and the film thickness obtained from OWS-EMT analysis, by, again assuming densely packed chains, and a monomer length of 0.15 nm. A degree of polymerization ~200 was calculated for a 20 nm thick film.

E. AAO sample surface area, PAH-biotin adsorption, and biotin surface density calculation

The **sample surface area** exposed to the liquid reagent is given by the cut-out of the liquid cell's PDMS (polydimethylsiloxane) soft seal = π x 0.3 x 0.8 cm = 0.75 cm^2 (the cut-out is an ellipse). Correspondingly, the **volume** inside the ~0.5 mm thick flow cell is 0.03 ml.

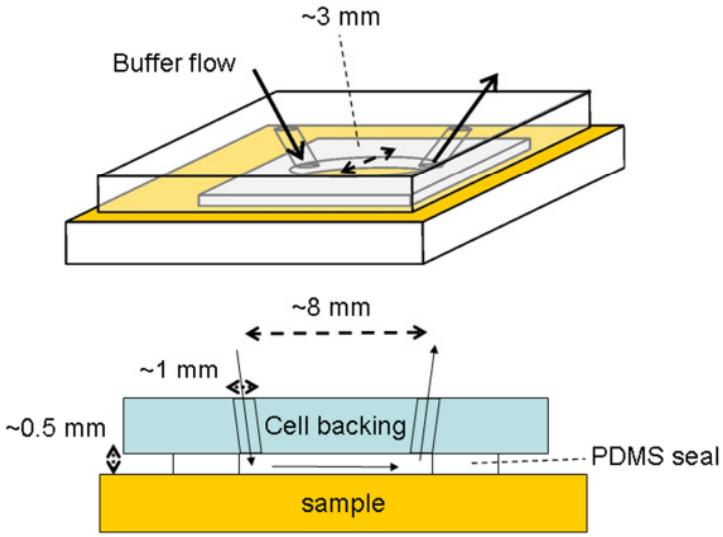

Figure 7.12. Schematics of the liquid flow cell, with dimensions, used for SPR and OWS experiments in which a continuous liquid flow was applied (using a peristaltic pump).

The **total surface area** of the nanoporous AAO thin film was calculated as follows:

Total area = Top area x (1 + density of pores x cylindrical internal area)

$= 0.75\ cm^2 \times (1 + (\lambda_{C\text{-}C}^2 \sin 60^o)^{-1} \times (\pi \times D_{pore} \times h))$

$= 0.75\ cm^2 \times (1 + ((98\ nm)^2 \sin 60^o)^{-1} \times (\pi \times 76\ nm \times 800\ nm))$

$= 0.75\ cm^2 \times (1 + 23)$

$= 18\ cm^2$

where the top area is the sample surface area calculated above, and $\lambda_{C\text{-}C}$, D_{pore} and h, are the pore centre-to-centre spacing, pore diameter and the film thickness, respectively.

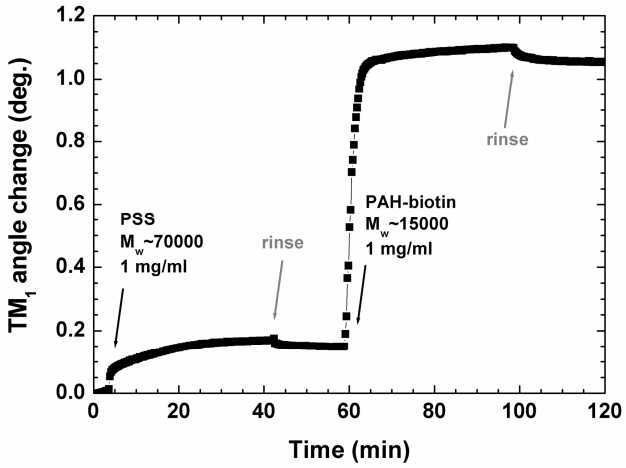

Figure 7.13. TM_1 angle shift associated with the adsorption of PSS and PAH-biotin on the APDMES functionalized 2-step nanoporous AAO thin film (pore diameter ~76 nm and film thickness 803 nm).

Figure 7.13 shows the TM_1 mode angle shift due to PSS and PAH-biotin adsorption on an APDMES functionalized nanoporous AAO thin film waveguide, with 76 nm pores and film thickness of 803 nm (2-step anodized, for details, see Figure 5.25, and sections 3.2.3 and 5.4). PBS was used to dissolve both polyelectrolytes, both at a concentration of 1 mg/ml. The net angle shifts due to PSS and PAH-biotin adsorptions, were 0.15º and 0.9º degree, respectively. These corresponded to thickness increases of ~0.2 nm and ~1.3 nm, for the PSS and PAH layers, respectively. The same sample preparation was used for all experiments described in section 5.4.4. It is not immediately clear why PSS adsorption was only one-sixth of PAH-biotin's. It could be related to the higher molar concentration of the PAH-biotin, or the charge density of the APDMES functionalized AAO surface.

The upper bound biotin surface site density was estimated as:

Site density = <u>percentage of biotin functionalization along PAH chain</u>
(volume of PAH monomer / PAH layer thickness)

The percentage of functionalization was 21% (see section 2.1.2) and the volume of a PAH monomer unit was estimated as a cubic volume equal to $(2.5Å)^3$. The PAH layer thickness was, as measured above, 1.3 nm. The upper bound site density is therefore 2 x 10^{15} cm^{-2}. The corresponding **total number of biotin sites** is then simply the site density times the total AAO area = 18 cm^2 x 2 x 10^{15} cm^{-2} ~ 4 x 10^{16}.

F. Streptavidin binding on PAH-biotin modified AAO from solutions made in PBS spiked with 0.45 mM Tween-20

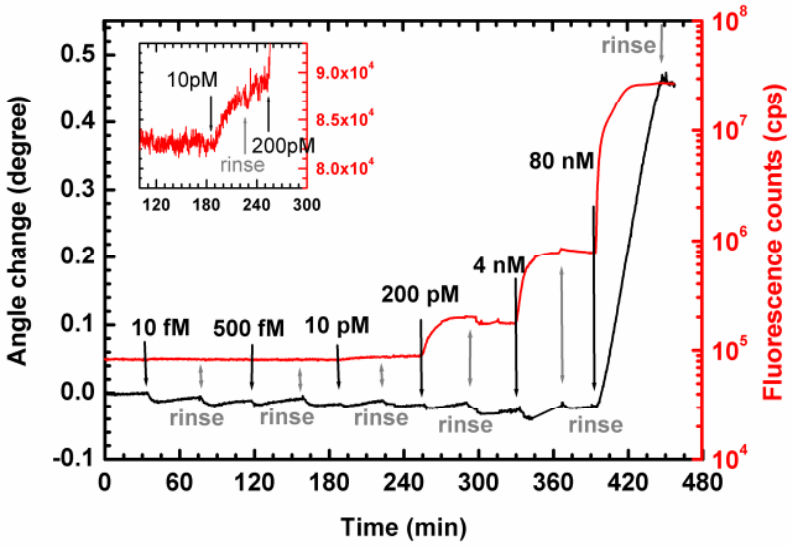

Figure 7.14. Real time responses of the TM_1 angle shift and change in the associated fluorescence intensities due to binding of the fluorescence labelled streptavidin dissolved in PBS + 0.05% Tween-20, on the PAH-biotin modified nanoporous AAO film. The black curve shows the angle changes (left axes), and the red curves show the change in fluorescence intensity (right axes, log10). Black arrows indicate when streptavidin was introduced, and grey arrows indicate rinsing with PBS (with Tween-20). The inset shows the change in the fluorescence intensity at the lowest streptavidin concentration when a signal was detected, which cannot be clearly seen in the main graphs. Note the small negative angle changes, up until a concentration of 4 nM, whenever either streptavidin or buffer was introduced.

G. References

[1] Rasband WS: Imagej. U. S. National Institutes of Health, Bethesda, Maryland, USA, http://rsb.info.nih.gov/ij/.

[2] Xu T, Stevens J, Villa JA, Goldbach JT, Guarini KW, Black CT, Hawker CJ, Russell TP: Block Copolymer Surface Reconstuction: A Reversible Route to Nanoporous Films. *Advanced Functional Materials* **2003**, *13*, 698.

[3] Xu T, Goldbach JT, Misner MJ, Kim S, Gibaud A, Gang O, Ocko B, Guarini KW, Black CT, Hawker CJ, Russell TP: Scattering Study on the Selective Solvent Swelling Induced Surface Reconstruction. *Macromolecules* **2004**, *37*, 2972.

[4] Jeong U, Ryu DY, Kho DH, Kim JK, Goldbach JT, Kim DH, Russell TP: Enhancement in the Orientation of the Microdomain in Block Copolymer Thin Films Upon the Addition of Homopolymer. *Advanced Materials* **2004**, *16*, 533.

[5] Kim DH, Lau KHA, Joo W, Peng J, Jeong U, Hawker CJ, Kim JK, Russell TP, Knoll W: An Optical Waveguide Study on the Nanopore Formation in Block Copolymer/Homopolymer Thin Films by Selective Solvent Swelling. *Journal of Physical Chemistry B* **2006**, *110*, 15381.

[6] Block H: Poly (Gamma-Benzyl-L-Glutamate) and Other Glutamic Acid Containing Polymers, Gordon & Breach Science Publishers: New York, 1983.

[7] Chang YC, Frank CW: Grafting of Poly(Benzyl-L-Glutamate) on Chemically Modified Silicon Oxide Surfaces. *Langmuir* **1996**, *12*, 5824.

[8] Wieringa RH, Siesling EA, Werkman PJ, Angerman HJ, Vorenkamp EJ, Schouten AJ: Surface Grafting of Poly(L-Glutamates). 2. Helix Orientation. *Langmuir* **2001**, *17*, 6485.

List of Figures

List of Tables

Publications

Lau KHA, Bang J, Kim DH, Knoll W: Protein interactions with surface interfaces of nanopatterns. *Submitted.*

Lau KHA, Bang J, Kim DH, Knoll W: Self-assembly-based protein nanoarrays on block copolymer templates. *Accepted for publication in Adv. Func. Mater.*

Lau KHA, Cameron PJ, Duran H, Abou-Kandil AI, Knoll W: Nanoporous waveguides as versatile, high-sensitivity biosensors. To appear in *Advanced surface design for biomaterial and life science applications*. Edited by Förch R, Schoenherr H, Jenkins ATA; Wiley-VCH, 2008: chapter 4.5.

Duran H, Lau KHA, Lübbert A, Jonas U, Steinhart M, Knoll W: Biopolymers for biosensors: Polypeptide Nanotubes for optical biosensing. In *Polymers for Biomedical Applications*. Edited by Mahapatro A, Kulshrestha AS; American Chemical Society, 2007: 371-390.

Lau KHA, Knoll W, Kim DH: Theoretical optical waveguide investigation of self-organized polymer thin film nanostructures with nanoparticle incorporation. *Macromol. Res.* 15, 211-215 (2007)

Kim DH, Lau KHA, Joo W, Peng J, Jeong U, Hawker CJ, Kim JK, Russell TP, Knoll W: An optical waveguide study on the nanopore formation in block copolymer/homopolymer thin films by selective solvent. *J. Phys. Chem. B* 110, 15381-15388 (2006)

Kim DH, Lau KHA, Robertson JWF, Lee OJ, Jeong U, Lee JI, Hawker CJ, Russell TP, Kim JK, Knoll W: Thin films of block copolymers as planar optical waveguides. *Adv. Mater.* 17, 2442-2446 (2005)